RICE UNIVERSITY

Synthesis, Characterization, and Functionalization of Transition Metal Phosphide Nanomaterials from Single Source Molecular Precursors

by

Anna Therese Kelly

A THESIS SUBMITTED
IN PARTIAL FULFULLMENT OF THE
REQUIREMENTS FOR THE DEGREE

Doctor of Philosophy

APPROVED, THESIS COMMITTEE:

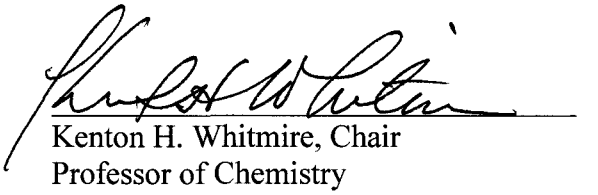

Kenton H. Whitmire, Chair
Professor of Chemistry

Lon J. Wilson
Professor of Chemistry

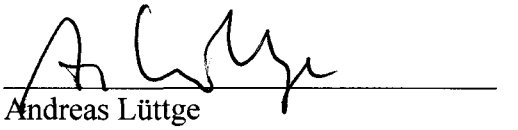

Andreas Lüttge
Professor of Earth Science and
Chemistry

HOUSTON, TEXAS
NOVEMBER 2009

UMI Number: 3421150

All rights reserved

INFORMATION TO ALL USERS
The quality of this reproduction is dependent upon the quality of the copy submitted.

In the unlikely event that the author did not send a complete manuscript
and there are missing pages, these will be noted. Also, if material had to be removed,
a note will indicate the deletion.

UMI 3421150
Copyright 2010 by ProQuest LLC.
All rights reserved. This edition of the work is protected against
unauthorized copying under Title 17, United States Code.

ProQuest LLC
789 East Eisenhower Parkway
P.O. Box 1346
Ann Arbor, MI 48106-1346

Abstract

Synthesis, Characterization, and Functionalization of Transition Metal Phosphide Nanomaterials from Single Source Molecular Precursors

by

Anna Therese Kelly

This thesis details the synthesis, characterization, and functionalization of transition metal phosphide nanomaterials from single source molecular precursors. The decomposition of the organometallic cluster, $H_2Fe_3(CO)_9P^tBu$, yielded iron phosphide (Fe_2P) nanomaterials of various morphologies depending on the surfactants used for the decomposition. Branched nanostructures were observed as a result of crystal splitting in a few of the surfactant systems. Cross-shaped structures were also observed and attributed to the twinning of two individual bundles during growth as the result of an interrupted growth process. The role of the solvents, in particular the use of oleic acid for the formation of nanorods, in the formation of Fe_2P nanoparticles will be discussed. Magnetic measurements taken of a variety of different morphologies of these iron phosphide nanoparticles will also be presented. Fe_2P nanoparticles were also isolated via the decomposition of other clusters, including $Fe_3(CO)_9(P^tBu)_2$, $Fe_2(CO)_6(PH^tBu)_2$, $Fe_4(CO)_{11}P^tBu_2$, and $Fe_3(CO)_{10}P^tBu$. In order to study the mechanism by which the clusters decompose, the decompositions were monitored using infrared spectroscopy. For all of the systems studied, the clusters rearranged in the surfactant solutions, ultimately resulting in $Fe_2(CO)_6(PH^tBu)_2$ prior to decomposition. This rearrangement is

believed to be a result of the interaction of the clusters with the surfactants employed, supported by the finding that the solid state decomposition of $H_2Fe_3(CO)_9P^tBu$ was found to result in a combination of Fe_3P, Fe_2P, and Fe_3O_4.

In addition to the formation of the binary phases of transition metal phosphide nanomaterials, investigation into the formation of mixed metal phosphides of iron and manganese were also performed. For these experiments, $H_2Fe_3(CO)_9P^tBu$ with a manganese source, either $Mn_2(CO)_{10}$ or $Mn(CO)_5Br$, were decomposed in a variety of surfactant systems. The resulting nanoparticles were only doped with manganese; pure stoichiometric phases were not isolated.

Finally, the functionalization of Fe_2P split rods, T-shapes, and crosses with a gold shell was performed. Their optical properties were studied, and a redshift in the extinction maximum was seen as the shell thickness increased. This plasmon peak shift, as opposed to the trends seen in silica-Au core-shell structures as shell thickness increases, is attributed to the high permittivity of the Fe_2P core.

DEDICATION

In Loving Memory of both of my Grandmothers.
They are missed each and every day.

Nora Kelly
1925 - 2008

Margaret Mary McDonnell
1924 – 2004

Acknowledgements

I would first like to thank my advisor, Dr. Kenton Whitmire. Without his support and guidance, I wouldn't be at this point. He is a great advisor, always available and encouraging. I would also like to thank my committee members, Dr. Andreas Lüttge and Dr. Lon J. Wilson.

I am grateful for all of the great collaborators I have had the pleasure to work with over the years. Without their help, my thesis wouldn't be what it is. First of all, I would like to thank Dr. Irene Rusakova at the University of Houston for all of her help with obtaining amazing TEM images (all of the SAED patterns and most of the HR-TEM images presented were obtained by Dr. Rusakova). I am in awe of her knowledge and expertise. Thanks also to Dr. Naomi Halas, Dr. Emilia Morosan for her assistance with collecting SQUID measurements, and Dr. Akhilesh Tripathi at Rigaku for his guidance with X-ray powder diffraction data and checking over my WPF analyses. Thanks to Dr. Cristina Hofmann and Trina Mandal for their help in obtaining SEM images. Also special thanks to Dr. Carly Levin for her help with the gold-coating project (she obtained the UV-Vis spectra and synthesized the colloidal gold solution used for the experiments) as well as for her friendship and Dr. Carrie McNeil for her help in acquiring GC-MS data. To the funding agencies that providing funding for the research I have conducted: the Robert A. Welch Foundation and the National Science Foundation.

To all of the Whitmire group members, who have been there for the times when things actually worked and the times when nothing would work! The post doctoral researchers, especially Dr. Teyeb Ould-Ely, who helped me get started when I first joined

the lab and performed SQUID measurements for me, Dr. Vitalie Stavila, Dr. Eva Machnikova, and to visiting scientist Dr. Ion Bulimestru. A special thanks to Dr. Cristina Hofmann, for her friendship and support; she is always able to make me laugh, even in times when I didn't feel much like laughing. To all the other graduate students in the Whitmire lab: Trina Mandal, Adam Colson, Sean Walsh, and Radu Racovita. Also to the visiting graduate students we have had, John Gibbons and Damian Synnott. To all the undergraduate students that have worked with me: Sheela Ramanan, J.L. Kiappes, Christopher Lam, Ryan Tait, and Megan Johnson. I hope they enjoyed working with me as much as I enjoyed working with them. And to all the other undergraduate students that have worked in the lab during my time here: Darío Prieto-Centurión, Page Sigman, Felipe Serrano, Diana Wu, Brian Henderson, Vu Nguyen, and Christine Sun.

To all the other graduate students that I was fortunate to become friends with over the years: Dr. Sean Pheasant, Dr. Jennifer Jamison, Dr. Keith Hartman, and Dr. Merlyn Pulikkathara. To all the scientists and staff in the Chemistry Department, especially to Dr. Wenhua Guo, Dr. Bo Chen, Dr. Lawrence B. Alemany, and Richard Crouse, for their willingness to help whenever I needed them. To all the staff of the Chemistry Department, especially to Sue Friend, Naomi Duval, Sofía Medrano-Correa, Dr. Mary McHale, and Virginia Wairegi, all of whom were always so welcoming and helpful. Also to Dave Cervantes, the custodian for our lab for the majority of the time that I was here, who did a great job and was an extremely caring person; he will be greatly missed.

Finally, to all of my family, who were probably beginning to think that this day would never come. Especially to my mom and dad, who have always supported me in whatever I set my mind to and loved me unconditionally. To my brother, Michael, who

at one time was an expert at annoying me, and who is now someone that I don't know what I would do without. To my dance family; it is partially due to them that I was able to stay sane throughout my years as a graduate student. And to all my other friends who have supported me over the years, I am extremely thankful for your love and friendship.

Table of Contents

Abstract ii
Acknowledgements v
Table of Contents viii
List of Figures xi
List of Tables xx
List of Schemes xx
Chapter 1. General Introduction 1
Chapter 2. Synthesis of a variety of Fe_2P nanostructures via the decomposition of $H_2Fe_3(CO)_9P^tBu$ 8
2.1. Introduction 8
2.2. Experimental Procedure 9
2.2.1. Characterization. 9
2.2.2. Synthesis of $H_2Fe_3(CO)_9P^tBu$. 10
2.2.3. Synthesis of Iron Phosphide Nanofibers (1). 11
2.2.4. Synthesis of Nanofiber "Bundles" (2). 12
2.2.5. Synthesis of Dumbbell-Shaped Nanofiber "Bundles" (3). 12
2.3. Results & Discussion 12
2.4. Conclusions 29
Chapter 3. Effects of variations in precursor, surfactant system, and other reaction parameters on the synthesis of iron phosphide nanomaterials 31
3.1. Introduction 31
3.2. Experimental Procedure 33
3.2.1. Heating Rate Experiments. 34
3.2.2. Varying solvent/surfactant system 35
3.2.3. Varying the Functional Groups of the Surfactants 37
3.2.4. Varying Trialkylamines 39
3.2.5. Synthesis of iron-phosphorus clusters. 40
3.2.6. Decomposition of Various Precursors 43
3.3. Results & Discussion 44

3.3.1. Varying Heating Rates 44
3.3.2. Changing the Solvent System 46
3.3.3. Changing the Precursor 73
3.4. Conclusions 79
Chapter 4. Investigation of the mechanism of decomposition for the formation of iron phosphide nanoparticles 80
4.1. Introduction 80
4.2. Experimental Procedure 81
4.2.1. Monitoring IR spectra of decompositions 82
4.2.2. Quenching of the decomposition 85
4.2.3. Decompositions in a single solvent 85
4.2.4. Bulk Decompositions 86
4.3. Results & Discussion 88
4.3.1. IR studies of the decompositions. 88
4.3.2. Quenching of the decomposition. 96
4.3.3. Decompositions in a single solvent 97
4.3.4. Bulk Decompositions 101
4.4. Conclusions 106
Chapter 5. Synthesis of iron-manganese phosphide nanomaterials 108
5.1. Introduction 108
5.2. Experimental Procedure 110
5.2.1. Decompositions of $H_2Fe_3(CO)_9P^tBu + Mn_2(CO)_{10}$ 110
5.2.2. Decompositions of $H_2Fe_3(CO)_9P^tBu + Mn(CO)_5Br$ 112
5.2.3. Decomposition of $H_2Fe_3(CO)_9P^tBu$ & manganese formate 113
5.2.4. Decompositions of $HMn_2(CO)_8PPh_2$ 113
5.3. Results & Discussion 114
5.3.1. $H_2Fe_3(CO)_9P^tBu + Mn_2(CO)_{10}$ 114
5.3.2. $H_2Fe_3(CO)_9P^tBu + Mn(CO)_5Br$ 120
5.3.3. $H_2Fe_3(CO)_9P^tBu + Mn(O_2CH)_2$ 124
5.3.4. Decompositions of $HMn_2(CO)_8PPh_2$ 127
5.4. Conclusions 128

Chapter 6. Gold coated iron phosphide core-shell nanostructures 129
6.1. Introduction 129
6.2. Experimental 131
6.3. Results & Discussion 134
6.3.1. Formaldehyde Reduction 136
6.3.2. Carbon Monoxide 140
6.4. Conclusions 144
Appendix I. Supplementary Information for Chapter 2. 146
Appendix II. Additional spectral data for experiments presented in Chapter 3 148
Appendix III. Decomposition of $H_2Fe_3(CO)_9P^tBu$ in a variety of surfactant combinations. 161
Appendix IV. Supplementary information for Chapter 4. 166
Appendix V. Supplementary information for the decompositions of $H_2Fe_3(CO)_9P^tBu$ with $Mn_2(CO)_{10}$ or $Mn(CO)_5Br$ and the decompositions of $HMn_2(CO)_8PPh_2$. 170
Appendix VI. Supplementary information for the gold coating of Fe_2P nanostructures. 172
Curriculum Vitae 174
References 176

List of Figures

Figure 1.1. Iron Phosphorus Clusters.[48,49] 6

Figure 2.1. X-Ray Powder Diffraction Pattern for the iron phosphide nanorods. Peaks correspond to PDF 51-0943 (Fe_2P). 13

Figure 2.2. Transmission electron microscopy (TEM) images of iron phosphide nanorods synthesized from 0.50 mmol precursor in different solvent ratios: (A) 7:1 TOA:OA, aspect ratio 11. (B) 6:2 TOA:OA, aspect ratio 5. All scale bars represent 100 nm. 14

Figure 2.3. Polycrystalline Selected Area Electron Diffraction (SAED) pattern of the nanorods with measured d-spacings compared to published values. More discrepancies are seen in the weaker reflections due to the fact that measurements taken from TEM data are not as precise as those from X-ray diffraction data. [a] JCPDS card file 33-670. [b] vvw: very very weak, vw: very weak, w: weak, m: medium, s: strong, vs: very strong. Data obtained by Irene Rusakova. 15

Figure 2.4. SEM image of bundles of Fe_2P nanorods synthesized from a 4:4 TOA:OA surfactant system. 15

Figure 2.5. HR-TEM image of a split rod. Black arrows indicate moiré fringes, while white arrows indicate the location of splitting. Image obtained by Irene Rusakova. 16

Figure 2.6. A schematic representation of the Fe_2P crystal structure (A) looking down the *c* axis and (B) perpendicular to the *c* axis.[39] Structure consists of tetrahedral (lavender) and pyramidal (green) iron sites. The atom coordinates are Fe(1): 0.255, 0, 0; Fe(2): 0.596, 0, 0.5; P(1): 0.33333, 0.66667, 0; P(2): 0, 0, 0.5. The Fe-P bonds are generally longer for the square pyramidal Fe(2) [four bonds of 2.485 and one of 2.371 Å], than to those to Fe(1) [two bonds of 2.222 and two of 2.287 Å]. 16

Figure 2.7. TEM image of a T-shaped bundle. 17

Figure 2.8. (A) BF TEM image of bundle showing a cross-shaped morphology. Black arrows indicate moiré fringes while white arrows indicate the twin boundaries. M: matrix bundle, T: twin bundle. Inset: Schematic figure of a penetration twin. (B-C) Experimental and simulated SAED patterns of cross-shaped bundle; black reflections in (C) arise from the matrix bundle of rods and white reflections arise from the twin bundle of rods. Images obtained by Irene Rusakova. 18

Figure 2.9. Central DF TEM images of a cross-shaped bundle using reflections from matrix (A) and twin (B). Both scalebars represent 20 nm. Images obtained by Irene Rusakova. 20

Figure 2.10. HR TEM image recorded from the area close to the center of the bundle showing planar defects (stacking faults) as marked by white arrows. Image obtained by Irene Rusakova..... 20

Figure 2.11. TEM images displaying the effect of the addition of alkanes. All scale bars represent 200 nm..... 21

Figure 2.12. SEM image of iron phosphide nanorods synthesized with the addition of 100 μL hexane. 21

Figure 2.13. (A) TEM image of a cross-shaped bundle from decomposition with 4 mL TOA, 4 mL OA, and 200 μL hexane. (B) TEM image of a T-shaped bundle obtained from a decomposition with 4 mL TOA, 4 mL OA, and 100 μL nonane. Similar shapes were seen in all of the decompositions with added alkanes. Scalebars represent 200 nm. 22

Figure 2.14. TEM images of the nanostructures synthesized with the addition of 100 μL of H_2O (A-C) and 100 μL of EtOH (D-F) in 4:4 TOA:OA..... 23

Figure 2.15. TEM images of the decomposition of $H_2Fe_3(CO)_9P^tBu$ in 2.5 mL TOA & 2.5 mL OA with trimethylacetic acid. 23

Figure 2.16. TEM image of a one-minute reaction, solvent system TOA:OA 4:4..... 26

Figure 2.17. ZFC/FC graph of iron phosphide nanorods at 1000 Oe. 28

Figure 2.18. Hysteresis loops of the iron phosphide nanorods with bundle-morphology (B). 28

Figure 3.1. TEM images from the variation of the rate of decomposition. 45

Figure 3.2. Nanoparticles resulting from the injection of $H_2Fe_3(CO)_9P^tBu$ into a hot surfactant system (TOA/OA)..... 46

Figure 3.3. TEM images of the decompositions of $H_2Fe_3(CO)_9P^tBu$ in ODE & OA. (A) 7:1 ODE:OA. (B) 6:2 ODE:OA..... 48

Figure 3.4. XRPD of the decomposition of $H_2Fe_3(CO)_9P^tBu$ in 7:1 ODE:OA 49

Figure 3.5. EDS spectrum of the split nanorods synthesized in ODE:OA (6:2)..... 50

Figure 3.6. XRPD of decomposition of $H_2Fe_3(CO)_9P^tBu$ in 6:2 ODE:OA. 50

Figure 3.7. TEM images of the nanorods synthesized from the decomposition of $H_2Fe_3(CO)_9P^tBu$ in DOE:OA (10:1)..... 51

Figure 3.8. (A) TEM image and (B) Polycrystalline selected area electron diffraction pattern of the nanorods formed via the injection of $H_2Fe_3(CO)_9P^tBu$ in DCB into DOE:OA (10:1)..... 52

Figure 3.9. TEM images from the decomposition of $H_2Fe_3(CO)_9P^tBu$ in OAm and OA. (A) 7:1 OAm:OA. (B) 4:4 OAm: OA. (C) 1:7 OAm:OA..... 53

Figure 3.10. XRPD of the decomposition of $H_2Fe_3(CO)_9P^tBu$ in 1:7 OAm:OA..... 54

Figure 3.11. BF TEM image of a particle synthesized in 7:1 OAm:OA, with line to indicate the direction of the crystal planes. Inset: Polycrystalline diffraction pattern of the particle. Images obtained by Irene Rusakova. 55

Figure 3.12. XRPD spectrum of the nanoparticles synthesized in 4:4 OAm:OA..... 56

Figure 3.13. Representation of the binding of oleic acid to the (A) (001) and (B) (100) faces of the Fe_2P crystal structure..... 58

Figure 3.14. TEM images of the various nanoparticles synthesized in (A) 5.7 g HDA (similar pKa to OAm) & 1 mL OA, (B) 7 mL HDOH and 1 mL OA, (C) 7 mL OOH and 1 mL OA, (D) 7 mL ODOH and 1 mL OA. 62

Figure 3.15. TEM images of the nanoparticles formed from the decomposition of $H_2Fe_3(CO)_9P^tBu$ in HDOH and OA (7:0.15 v:v)..... 68

Figure 3.16. XRPD of the decomposition of $H_2Fe_3(CO)_9P^tBu$ in 7:0.15 HDOH:OA.... 68

Figure 3.17. TEM images of the decomposition of $H_2Fe_3(CO)_9P^tBu$ in (A) TOA:OA and (B) ODE:OA (7:0.15 v:v). 69

Figure 3.18. TEM images of the nanoparticles synthesized via the decomposition of 0.24 mmol $H_2Fe_3(CO)_9P^tBu$ in (A) TOA/OA and (B) TDDA/OA, both with 7/1 volumetric ratios of trialkylamine to OA. 71

Figure 3.19. TEM images of the nanoparticles synthesized via the decomposition of 0.49 mmol $H_2Fe_3(CO)_9P^tBu$ in (A) TOA/OA and (B) TDDA/OA, both with 7/1 volumetric ratios of trialkylamine to OA. 71

Figure 3.20. TEM images of the decomposition of $H_2Fe_3(CO)_9PPh$ in 1:1 TOA:OA. .. 73

Figure 3.21. TEM images of the decomposition of $Fe_2(CO)_6(PH^tBu)_2$ in 2 mL TOA & 2 mL OA. 75

Figure 3.22. TEM images of the decomposition of $Fe_3(CO)_{10}P^tBu$ in 4 mL TOA & 4 mL OA..... 76

Figure 3.23. TEM images of the decomposition of $Fe_3(CO)_9(P^tBu)_2$ in 4 mL TOA & 4 mL OA. 77

Figure 3.24. XRPD of the decomposition of $Fe_3(CO)_9(P^tBu)_2$ in TOA & OA..... 77

Figure 3.25. TEM images of the decomposition of $Fe_4(CO)_{12}(P^tBu)_2$ in 2 mL TOA & 2 mL OA. 78

Figure 4.1. IR spectra from the decomposition of $H_2Fe_3(CO)_9P^tBu$ in TOA:OA (1:1). (A) IR of $H_2Fe_3(CO)_9P^tBu$ in hexane at room temperature. (B) IR of a solution of $H_2Fe_3(CO)_9P^tBu$ in THF with a few drops of TOA added. (C, D) IR of an aliquot of the decomposition reaction taken at 135 & 140 °C, respectively. 89

Figure 4.2. IR spectra of the decomposition of $H_2Fe_3(CO)_9P^tBu$ in ODE:OA (3:1) taken at (A) 160 °C, (B) 195 °C, and (C) 255 °C..... 90

Figure 4.3. IR spectra of the decomposition of $H_2Fe_3(CO)_9P^tBu$ in OAm:OA (1:1) taken at (A) 25 °C, (B) 140 °C, (C) 170 °C, (D) 200 °C, and (E) 250 °C. 91

Figure 4.4. IR spectra of the decomposition of $Fe_3(CO)_{10}P^tBu$ in TOA:OA (1:1) taken at (A) 25 °C, (B) 140 °C, (C) 180 °C, and (D) 235 °C. 92

Figure 4.5. IR spectra of the decomposition of $H_2Fe_3(CO)_9P^tBu$ in TOA/MeOA (7:1) taken at (A) 25 °C, (B) 145 °C, (C) 225 °C, and (D) 300 °C. 93

Figure 4.6. IR spectra of the decomposition of $Fe_3(CO)_{10}P^tBu$ in TOA/MeOA (7:1) taken at (A) 25 °C, (B) 120 °C, (C) 180 °C, and (D) 240 °C. 93

Figure 4.7. TEM images of the nanoparticles obtained from the decomposition of $H_2Fe_3(CO)_9P^tBu$ in TOA/MeOA (7:1). 94

Figure 4.8. TEM image of the nanoparticles obtained from the decomposition of $Fe_3(CO)_{10}P^tBu$ in TOA:MeOA (7:1). 94

Figure 4.9. IR spectra of the decomposition of $H_2Fe_3(CO)_9P^tBu$ in TOA/Na^+ oleate (8 mmol:0.5 mmol) taken at (A) 25 °C, (B) 150 °C, (C) 200 °C, and (D) 270 °C. 95

Figure 4.10. IR spectrum of the quenched decomposition. The sample was prepared by dissolving a few drops of the reaction solution in hexane. 96

Figure 4.11. TEM images of (A, B) Nanoparticles isolated from quenched decomposition and (C, D) nanoparticles isolated from a normal decomposition. Both decompositions were performed in a 1:1 (v:v) solution of TOA:OA. 97

Figure 4.12. TEM image of the particles synthesized from the decomposition of $H_2Fe_3(CO)_9P^tBu$ in 8 mL ODE. 98

Figure 4.13. TEM images of particles synthesized via the decomposition $H_2Fe_3(CO)_9P^tBu$ in 7 mL TOA. 98

Figure 4.14. XRPD of the annealed product from the decomposition of $H_2Fe_3(CO)_9P^tBu$ in 7 mL TOA. 99

Figure 4.15. TEM images of nanoparticles synthesized from the decomposition of $H_2Fe_3(CO)_9P^tBu$ in 7 mL HDOH 99

Figure 4.16. EDS spectrum of the nanoparticles synthesized in 7 mL HDOH 100

Figure 4.17. HR-TEM image of a nanoparticle synthesized in HDOH. 100

Figure 4.18. IR spectra from the decomposition of $H_2Fe_3(CO)_9P^tBu$ in HDOH taken at (A) 95 °C, (B) 150 °C, (C) 175 °C, and (D) 195 °C. 101

Figure 4.19. Whole pattern fitting of the XRPD pattern for the solid isolated from the bulk decomposition of $H_2Fe_3(CO)_9P^tBu$ under vacuum. The plot on top is the original data and the plot on the bottom is the derived pattern. 102

Figure 4.20. Whole pattern fitting of the XRPD of the solid obtained from the bulk decomposition of $H_2Fe_3(CO)_9P^tBu$ under a flow of Ar. The plot on top is the original data and the plot on the bottom is the derived pattern. 103

Figure 4.21. TEM images of the decomposition of $H_2Fe_3(CO)_9P^tBu$ in TOA:OA (4:4) with 42 μL of benzene. 106

Figure 5.1. TEM images of nanoparticles synthesized via the decomposition of $H_2Fe_3(CO)_9P^tBu$ and $Mn_2(CO)_{10}$ in TOA:OA (7:1). 115

Figure 5.2. XPS spectrum of the nanoparticles synthesized from $H_2Fe_3(CO)_9P^tBu$ and $Mn_2(CO)_{10}$ in TOA:OA (7:1) 115

Figure 5.3. TEM images of nanoparticles synthesized via the decomposition of $H_2Fe_3(CO)_9P^tBu$ and $Mn_2(CO)_{10}$ in TOA:OA (4:4). All scalebars correspond to 200 nm. 116

Figure 5.4. (A) XRPD and (B) EDS spectra of the nanoparticles synthesized from $H_2Fe_3(CO)_9P^tBu$ and $Mn_2(CO)_{10}$ in TOA:OA (4:4). 117

Figure 5.5. TEM images of nanoparticles synthesized via the decomposition of $H_2Fe_3(CO)_9P^tBu$ and $Mn_2(CO)_{10}$ (A) injected into a hot surfactant solution of DOE:OA (10:1) and (B) reagents combined at room temperature and heated. 119

Figure 5.6. EDS spectrum of the decomposition of $H_2Fe_3(CO)_9P^tBu$ and $Mn_2(CO)_{10}$ in DOE and OA (10:1) heated from room temperature. 119

Figure 5.7. TEM images of the self-assembly of the nanorods synthesized via the decomposition of $H_2Fe_3(CO)_9P^tBu$ and $Mn_2(CO)_{10}$ injected into a hot surfactant solution of DOE:OA (10:1). 120

Figure 5.8. TEM images of nanoparticles synthesized via the decomposition of $H_2Fe_3(CO)_9P^tBu$ and $Mn(CO)_5Br$ in TOA and OA (1:1). (A) split bundles, (B) center of one of the bundles, (C) cross-shaped particle with one of the arms partially broken..... 121

Figure 5.9. XRPD of the nanoparticles synthesized from $H_2Fe_3(CO)_9P^tBu$ and $Mn(CO)_5Br$ in TOA and OA (1:1). 122

Figure 5.10. EDS spectrum of the nanoparticles synthesized from $H_2Fe_3(CO)_9P^tBu$ and $Mn(CO)_5Br$ in TOA and OA (1:1). 122

Figure 5.11. TEM images of the nanoparticles synthesized from $H_2Fe_3(CO)_9P^tBu$ in 4 mL TOA, 4 mL OA, and 25 μL Br_2. (A) Fe_2P split bundle, (B) Fe_2P bundle that had broken in half. 123

Figure 5.12. TEM image of the nanoparticles synthesized from $H_2Fe_3(CO)_9P^tBu$ and $Mn(O_2CH)_2$ in TOA:OA (6:2). 125

Figure 5.13. (A) XRPD and (B) EDS spectra of the nanoparticles synthesized from $H_2Fe_3(CO)_9P^tBu$ and $Mn(O_2CH)_2$ in TOA OA (6:2). 126

Figure 5.14. (A) TEM image and (B) EDS spectrum of the nanoparticles isolated from the decomposition of $HMn_2(CO)_8PPh_2$ in DOE:OA:OAm (10:0.1:0.1) 127

Figure 6.1. TEM image of the Fe_2P nanorod after decoration with Au colloid (inset shows the entire nanorod). 135

Figure 6.2. TEM images of the Fe_2P nanoparticles (A-C) as synthesized, dispersed in hexane and (D-F) after being solubilized in water and decorated with Au nanoparticles. 137

Figure 6.3. TEM images of the Fe_2P nanoparticles plated with a gold shell via formaldehyde reduction, using (A-C) 50 μL, (D-F) 75 μL, and (G-I) 125 μL of decorated precursor. 138

Figure 6.4. Solution extinction spectra of the Fe_2P-Au core-shell particles synthesized using formaldehyde reduction (λ_{max} = 584 nm for 50 μL, 565 nm for 75 μL, 559 nm for 100 μL, and 540 nm for 125 μL of decorated precursor). Spectra offset for clarity..... 139

Figure 6.5. TEM images of the split Fe_2P nanorods and crosses. (A-B) Original nanoparticles dispersed in hexane and (C-D) Nanoparticles functionalized with GABA and decorated with small colloidal gold particles. All scalebars are 200 nm. 140

Figure 6.6. (A) Solution extinction spectra of the carbon monoxide reduction with various decorated precursor volumes (spectra offset for clarity). (B) TEM images of (i) Au-decorated Fe_2P nanostructure and the Fe_2P-Au core-shell nanostructures synthesized by the reduction of Au onto the surface with (ii) 100 μL, (iii) 75 μL, (iv) 50 μL, and (v) 25 μL of decorated precursor. All scalebars are 200 nm. 141

Figure 6.7. TEM image of a partially coated Fe_2P nanorod from the sample in which 100 μL of decorated precursor was used. 142

Figure 6.8. TEM images of rods, T-shapes, and crosses of unfunctionalized Fe_2P nanoparticles. All scalebars are 200 nm. 143

Figure 6.9. SEM images of rods, T-shapes, and crosses of the Fe_2P-Au core-shell structures for systems using (A-C) 25 μL and (D-F) 50 μL decorated precursor solutions (100,000X magnification). All scalebars are 200 nm. 144

Figure AII.1. EDS spectrum of the injection of $H_2Fe_3(CO)_9P^tBu$ into a hot surfactant system (TOA/OA). 148

Figure AII.2. EDS data collected for the decomposition of $H_2Fe_3(CO)_9P^tBu$ in 6:2 ODE:OA (split rods and spheres). The pink box represents the area of the sample analyzed. For the first spectrum, the weight percentage values obtained are close to that of Fe_2P (calculated values: 78.3% Fe, 21.7% P). The second spectrum values are close to FeP (calculated values: 64.3% Fe, 35.7% P). 149

Figure AII.3. Whole Pattern Fitting of the XRPD spectrum from the decomposition of $H_2Fe_3(CO)_9P^tBu$ in ODE:OA (6:2); the graph on top shows the original data with the derived pattern overlayed, while the bottom graph shows the derived pattern along with the PDF files of the phases present. Based on the EDS data presented in the previous figure, it appears that the split nanorods are Fe_2P and the spherical particles are FeP... 150

Figure AII.4. EDS spectrum of the decomposition of $H_2Fe_3(CO)_9P^tBu$ in 10:1 DOE:OA. 151

Figure AII.5. EDS spectrum of the decomposition of $H_2Fe_3(CO)_9P^tBu$ in 7:1 HDA:OA. 151

Figure AII.6. EDS spectrum of the decomposition of $H_2Fe_3(CO)_9P^tBu$ in 7:1 OOH:OA. 152

Figure AII.7. EDS spectrum of the decomposition of $H_2Fe_3(CO)_9P^tBu$ in 7:1 ODOH:OA. 152

Figure AII.8. EDS spectrum of the decomposition of $H_2Fe_3(CO)_9P^tBu$ in 7:1 HDOH:OA. 153

Figure AII.9. XPS data for the decomposition of $H_2Fe_3(CO)_9P^tBu$ in 7:1 HDA:OA.. 154

Figure AII.10. XPS data for the decomposition of $H_2Fe_3(CO)_9P^tBu$ in 7:1 HDOH:OA. 155

Figure AII.11. XPS data for the decomposition of $H_2Fe_3(CO)_9P^tBu$ in 7:1 OOH:OA. The indium peaks are a result of the sample being pressed onto In foil for analysis. 156

Figure AII.12. XPS data for the decomposition of $H_2Fe_3(CO)_9P^tBu$ in 7:1 ODOH:OA. 157

Figure AII.13. XPS data for the decomposition of $H_2Fe_3(CO)_9P^tBu$ in 7:1 OAm:OA. 158

Figure AII.14. EDS analysis of the particles synthesized from $Fe_3(CO)_{10}P^tBu$ in 4 mL TOA & 4 mL OA. The pink box represents the area of the grid on which the EDS analysis was conducted. The weight percentage analysis is close to that of Fe_2P (calculated values: 78.3% Fe, 21.7% P). 159

Figure AII.15. Representative EDS analysis of the decomposition of $Fe_4(CO)_{12}(P^tBu)_2$ in 2 mL TOA & 2 mL OA. The yellow box indicates the area of the sample analyzed by EDS. Weight percentage analysis is close to that of Fe_2P (calculated values: 78.3% Fe, 21.7% P)..... 160

Figure AIV.1. Summary of the cluster transformations seen for $H_2Fe_3(CO)_9P^tBu$ and $Fe_3(CO)_{10}P^tBu$ in the IR studies..... 166

Figure AIV.2. GC-MS data from the bulk decomposition of $H_2Fe_3(CO)_9P^tBu$. The top image shows the GC chromatogram. The MS chromatograms shown are for CO (RT = 1.901 min) and isobutylene (RT = 1.947 min). The small peaks in the GC chromatogram are due to the presence of hexane and methylcyclopentane. 167

Figure AIV.3. GC-MS data from the bulk decomposition of $H_2Fe_3(CO)_9PPh$. The top image shows the GC chromatogram. The MS chromatograms shown are for CO/CO_2 (RT = 1.907 min) and benzene (RT = 3.051 min). The small peaks in the GC chromatogram are due to the presence of hexane (and its isomers) and methylcyclopentane. 168

Figure AIV.4. GC-MS data from the bulk decomposition of $Fe_3(CO)_{10}PPh$. The top image shows the GC chromatogram. The MS chromatograms shown are for CO (RT = 1.911 min) and benzene (RT = 3.051 min). The additional peak in the GC chromatogram (RT ~ 2.2 min) is due to the presence of acetone. 169

Figure AV.1. Elemental mapping of the split nanorods synthesized from the decomposition of $H_2Fe_3(CO)_9P^tBu$ and $Mn_2(CO)_{10}$ in TOA and OA (4:4)..... 171

Figure AV.2. Elemental mapping of the split nanorods synthesized from the decomposition of $H_2Fe_3(CO)_9P^tBu$ and $Mn(CO)_5Br$ in TOA and OA (4:4). 171

Figure AVI.1. TEM images of Fe_2P-Au structures obtained using CO-reduction. The images shown represent the structures synthesized from 75 μL (A-C), 100 μL (D-F), and 125 μL (G-I) of gold-decorated precursor. Note that in figures D and G, it appears as though some of the particles do not have a complete shell; this is believed to account for the shift back to higher wavelengths of the extinction maximum for the sample synthesized from 100 μL of gold-decorated precursor (see Figure 6.6)..... 172

Figure AVI.2. Representative SEM image of the CO-reduced particles, from 50 μL of gold-decorated precursor. 173

List of Tables

Table 3.1. Experimental and Literature IR values for $Fe_3(CO)_{10}(\mu_3\text{-}P^tBu)$, $Fe_3(CO)_9(P^tBu)_2$, and $Fe(CO)_4P^tBuCl_2$. 41

Table 3.2. Alternate surfactants used for the decompositions 47

Table 3.3. Comparing the length and width of nanorods synthesized in different solvent systems (* precursor injected into the surfactant system in 4 mL DCB) 60

Table 3.4. Properties of the alternate surfactants (* pK_a values found in SciFinder). 61

Table 3.5. Binding energies (eV) of the nanoparticles synthesized in 7 mL HDA, HDOH, OOH, or ODOH with 1 mL OA determined using XPS. The percent area of each peak is indicated in parentheses. 64

Table 3.6. Binding energies (eV) for nanoparticles synthesized in OAm/OA (7/1) vs. HDOH/OA (7/1) determined using XPS. 66

Table 4.1. Literature IR values of the clusters present during the decompositions (w: weak, m: medium, s: strong, vs: very strong). 88

Table 5.1. Magnetic properties of some binary and ternary metal phosphides 108

Table AI.1. Summary of the decompositions of $H_2Fe_3(CO)_9P^tBu$. 146

Table AI.2. Decomposition results with different methods of stirring. 147

Table AVI.1. Summary of the sizing and solution extinction maxima for various sizes of Fe_2P-Au core-shell structures synthesized via CO-reduction. The Au decorated-Fe_2P particles had dimensions of $1051 \pm 62 \times 193 \pm 22$ nm (aspect ratio: 5.4, λ_{max} 365 nm). 173

List of Schemes

Scheme 3.1. Proposed decomposition pathway for $H_2Fe_3(CO)_9P^tBu$. 74

Scheme 3.2. Synthesis of alternate iron phosphorus compounds 74

Scheme 6.1. Functionalization of the Fe_2P nanostructures with GABA via ligand exchange. 132

Scheme 6.2. General procedure for the coating of Fe_2P nanoparticles with gold to form Fe_2P-Au nanostructures (not to scale) 135

Chapter 1. General Introduction

Recent advances in the synthesis of materials on the nanoscale have introduced a wide array of opportunities to improve existing technologies. The growing interest in the formation of nanomaterials stems from the fact that, when decreasing at least one of the dimensions of a particle to the nano regime, various properties can change, including magnetic, optical, and catalytic properties. One of the reasons that making things smaller has such an impact on a substance's properties is the large increase in the surface to volume ratio. Catalytic properties are greatly enhanced on the nanoscale as a result of increased surface area.[1] The increase in efficiency leads to a reduction in the amount of expensive metals used in catalysis. Shape has also been found to impact catalytic activity; El Sayed *et al.* reported that in platinum nanocrystals, catalytic activity increased with shapes having a large number of atoms at edges or corners.[2] It is also known that, for bulk platinum, high-index planes have a higher catalytic activity.[3] Therefore, by being able to control the shape of the nanocrystal, the reactivity and selectivity of the catalyst can be tailored.[4]

Optical properties of semiconductor nanoparticles are strongly related to size and shape.[5-7] This dependence has to do with quantum confinement, which occurs when the size of a semiconductor crystal becomes small enough that it approaches the size of the material's Bohr exciton radius. The size and composition of the crystal determines the peak emission frequency, so it is possible to tune the size of the bandgap by changing the size of the particle.

In addition to morphology altering a material's optical properties, changes in size, shape, and surface properties also introduce interesting changes in magnetism.[8-12] In a ferromagnetic material, strong magnetic properties are seen due to the presence of magnetic domains, in which all of the moments of the individual atoms are aligned with each other, separated by domain walls. As the size of the material is decreased and reaches a critical size, it is no longer energetically favorable for walls to form, and the particles become single domain. This change as size decreases leads to larger coercivity values.[13] If the particle is decreased to a small enough size, the particles become thermally unstable, so the material will only possess magnetic properties when in the presence of an external magnetic field. This behavior is called superparamagnetism, and nanoparticles possessing this property have found use in the biomedical field for magnetic resonance imaging (MRI) and drug delivery.[14,15]

The dependence of these various physical properties on the morphology of the nanoparticle allows for the tailoring of nanostructures to give optimal conditions for different applications. In order to reach full potential, the ability to synthesize nanocrystals of the desired phase, size, and shape needs to be optimized. While there have been major advances over the last few years regarding the synthesis of monodisperse nanocrystals as well as understanding the growth mechanisms of various materials, including metal chalcogenides and metal oxides,[16-18] none of these theories can be applied across all phases of materials. Much of the current research aims at optimizing such reaction parameters in order to synthesize pure nanomaterials of the desired shape, size, and composition.[19]

A variety of methods have been investigated for the synthesis of nanoparticles, including thermolysis, solvothermal or hydrothermal synthesis, and photolysis. In moving toward better control of nanoparticle syntheses, it has been found that for producing highly crystalline and monodisperse nanomaterials, synthesis in the presence of organic surfactants is advantageous in tailoring the size and shape of a variety of nanoparticles. By varying synthetic parameters such as the type of surfactant, temperature, rate of decomposition, etc., size and shape control of the product is possible.

Tuning the morphology of nanoparticles can be accomplished by adjusting the environment in which they are formed. The formation of nanoparticles is initiated by the nucleation of seed particles when there is a rapid increase of monomers in solution followed by the growth stage, in which precipitation of monomers onto the seed occurs. Shape-controlling parameters of the growth include time, temperature, and the type of surfactant molecules present. Because the crystallographic phase of the initially formed seed usually determines the shape of the particles formed, the most stable phase at the temperature of nucleation will likely result. For example, in a manganese sulfide system, when the $Mn(S_2CNEt_2)_2$ precursor is injected into a hot solution of hexadecylamine (>200 °C), nanocubes form because, at this temperature, the rock-salt structure is more stable. In contrast, when the reaction occurs at temperatures below 200 °C, the würtzite structure is more stable, and nanowires result.[20]

The morphology of nanoparticles is also strongly influenced by the kinds of surfactants present during the decomposition. Surfactants serve to stabilize the surface of the nanoparticles as they grow as well as to prevent agglomeration of the nanoparticles. The manner in which a specific surfactant binds to the surface of the particle will dictate

along which crystallographic axis the growth will occur. In comparing the binding of long chain alkylamines and carboxylic acids, such as oleyl amine and oleic acid, to nanoparticles, alkylamines are believed to bind to particle surfaces by non-covalent interactions less strongly than carboxylic acids with similar carbon-chain lengths.[21,22] The strength with which the surfactant binds to the crystal surface will influence the growth because a more weakly binding molecule will be able to reversibly coordinate to the particle's surface, so growth along the crystal face to which the surfactant binds will not be inhibited as greatly as with a molecule that binds more strongly to the surface of the particle. This difference in binding, in addition to the surfactant's binding selectivity, will strongly affect the shape of the nanoparticle.

When synthesizing a nanomaterial comprised of more than one element, many of the reported methods involve the use of separate precursors, each acting as a source of one of the desired elements.[6,23-25] While this has been a successful approach for nanoparticle synthesis, the incorporation of all elements into one molecule introduces the possibility for greater control over the decomposition product. Single-source precursors are advantageous in that certain phases of material can be targeted by designing the precursor to have a certain ratio of the desired elements. Additionally, with the use of separate precursors, the decomposition temperatures and solubilities of each precursor will vary; a single-source precursor will circumvent these issues. At higher temperatures, excess thermal energy is present in the system; therefore, growth will likely proceed to give the thermodynamically favored product. By choosing organometallic molecules that decompose at moderate temperatures, more control is possible over the crystallographic phase formed as well as parameters such as size and shape. A variety of different

nanomaterials have been synthesized via the decomposition of single-source molecular precursors. Metal diethylthiocarbamate precursors have been used as single-source precursors to synthesize CdS,[26] MnS,[20] PbS,[27,28] and ZnS.[29] These and various other semiconductor nanoparticles have been successfully synthesized using this approach.[30-33]

We are interested in studying the formation of transition metal pnictides from single-source precursors, specifically iron phosphide, manganese phosphide, and mixed metal phosphides. This class of materials is interesting because it exhibits magnetic, catalytic, magnetoresistant, and magnetocaloric properties.[34-37] Iron phosphides exist in a variety of phases, including FeP, Fe_2P, and Fe_3P. Both Fe_3P and Fe_2P are ferromagnetic, with Curie temperatures (T_c) of 716 and 217 K, respectively.[38,39] While there has been an interest in the magnetic properties of metal phosphides for decades, there has not been much exploration of these materials on the nanoscale. Traditionally, bulk iron phosphide materials have been synthesized by combining iron and phosphorus and heating to high temperatures.[40,41] The problem with such synthetic methods is the parallel formation of a variety of phases, which are often difficult to separate. The relative high temperatures at which these reactions are carried out also prohibit the formation of thin films and nanostructures. Use of a single-source molecular precursor will serve as a convenient pathway to metal phosphide nanomaterials.

Transition metal carbonyls have often been used as precursors to nanoparticles. Stable Fe, Ru, and Os nanoparticles have been synthesized by thermal or photolytic decomposition of $Fe_2(CO)_9$, $Ru_3(CO)_{12}$, and $Os_3(CO)_{12}$.[42] Another synthesis reported the formation of Cr, Mo, and W nanoparticles from metal carbonyl precursors in ionic liquids.[43] In addition to forming pure metal nanoparticles, mixed metal nanoparticles or

oxides can be also be synthesized via the decomposition of metal carbonyl precursors.[44-46]

Given that transition metal carbonyls have been used successfully as precursors to a variety of different nanoparticles, we have investigated the use of iron-phosphorus carbonyl clusters as single-source precursors to iron phosphide materials. There are a variety of such clusters that have been synthesized with different stoichiometric ratios of iron to phosphorus (Figure 1.1). We hypothesized that cluster complexes would function better than simpler complexes as single-source precursors because of the greater number of phosphorus-metal interactions which more closely mimic those found in the solid state materials. Indeed, metal clusters can be viewed as fragments of metal and/or metal alloy lattices. Furthermore, in the clusters, the Fe-P bonds are usually covalent, whereas in the substituted complexes, dative bonds are more common; therefore, the loss of the phosphorus fragment is more likely to occur during the decomposition of the simpler complexes, resulting in the synthesis of phosphorus-poor products. The synthetic methodology is based on the reaction of iron carbonyls and alkyl phosphines (RPH_2) or alkyl phosphine halides (RPX_2).[47-49] The decomposition of such clusters should provide an efficient means of synthesizing transition metal phosphides having the same stoichiometry as the parent cluster.

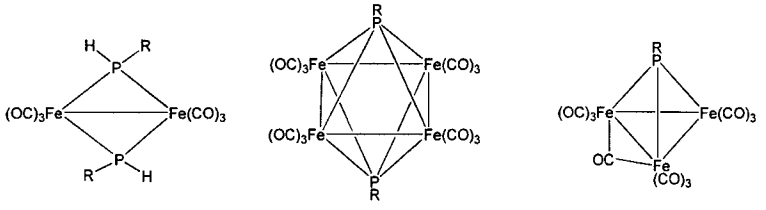

$Fe_2(CO)_6(PHR)_2$
R = Me, tBu, Ph, p-Tol
Fe:P = 1:1

$Fe_4(CO)_{12}(PR)_2$
R = Me, tBu, Ph, p-Tol
Fe:P = 2:1

$Fe_3(CO)_{10}PR$
R = Me, Et, iPr, nBu, tBu, cyhex, Ph
Fe:P = 3:1

Figure 1.1. Iron Phosphorus Clusters.[48,49]

Investigations into the decomposition of $H_2Fe_3(CO)_9P^tBu$ in a solvent system of trioctylamine and oleic acid along with magnetic data of the obtained nanomaterials will be presented in Chapter 2. Further investigation of the role of reaction temperature, surfactants, and various precursors on the resulting products will be presented in Chapter 3. Chapter 4 will present the mechanistic studies of the decomposition reactions. Expanding to mixed metal (iron and manganese) phosphides has also been studied via the combination of an iron-phosphorus cluster and a manganese-containing compound. These experiments will be discussed in Chapter 5.

In addition to the synthesis of these materials on the nanoscale, functionalization of the nanostructures for potential future applications is in progress. The first approach taken was the coating of various iron phosphide nanoparticles with a gold shell. The magnetic properties of the metal phosphides combined with the optical properties of the gold shell could offer an interesting hybrid material. This data will be presented in Chapter 6.

Chapter 2. Synthesis of a variety of Fe_2P nanostructures via the decomposition of $H_2Fe_3(CO)_9P^tBu$

2.1. Introduction

A variety of methods for producing nanoscale iron phosphides have been reported. The reduction of iron phosphate nanoparticles in a H_2/Ar atmosphere resulted in the formation of a mixture of FeP and Fe_2P nanoparticles.[34,50] The phase produced was dependent upon the temperature to which the particles were heated; the FeP phase was evident at 700 °C and Fe_2P was present at 1100 °C. Another more common approach is the use of separate sources of iron and phosphorus. Iron phosphide (FeP) nanowires and nanorods were synthesized by the injection of a solution of iron pentacarbonyl in trioctylphosphine (TOP) into a mixture of trioctylphosphine oxide (TOPO) and TOP, where TOP served as the phosphorus source.[51] Similar methods have been reported in which some variant of an iron carbonyl was used as the iron source.[51-53] Although these methods have produced pure phases of iron phosphide nanomaterials, there was no control over which phase was obtained.

In contrast, the use of single-source molecular precursors could presumably offer a method in which the desired phase can be targeted. Single-source molecular precursors may allow for the control of as well as isolation of pure products.[54] Only one previous attempt to synthesize iron phosphide nanomaterials via a single-source molecular precursor has been reported; the decomposition of $Fe(CO)_4[PPh_2CH_2CH_2Si(OMe)_3]$ in a silica xerogel matrix resulted in the formation of Fe_2P nanoclusters.[55]

In this chapter, the decomposition of the organometallic cluster, $H_2Fe_3(CO)_9P^tBu$, as a potential single-source precursor to the Fe_3P phase in a solvent system of trioctylamine and oleic acid of varying ratios will be discussed. Additional experiments involving the introduction of small amounts of solvents (i.e. hexane, ethanol, and water) and how such variations impact the morphology of the isolated nanostructures will be discussed. Magnetic measurements taken of a variety of different morphologies of these iron phosphide nanoparticles will also be presented. The majority of the work presented in this chapter has been published.[56]

2.2. Experimental Procedure

Reactions were carried out using standard Schlenk techniques. Tri-*n*-octylamine (TOA; 98%), oleic acid (OA; 90%), ethanol, toluene, tetrahydrofuran, and hexane were obtained from Sigma-Aldrich. TOA and OA were dried separately before use by heating to ~110 °C under vacuum. All other solvents were distilled using standard procedures.[57] $Fe_3(CO)_{12}$, t-butyl dichlorophosphine ($^tBuPCl_2$), and lithium aluminum hydride ($LiAlH_4$) were obtained from Strem and used as received. Tert-butyl phosphine ($^tBuPH_2$) was synthesized via the reduction of $^tBuPCl_2$ with $LiAlH_4$. Heating was performed using a Barnstead Electrothermal heat controller with a Glas-Col heating mantle.

2.2.1. Characterization.

Fourier Transform-Infrared (FTIR) spectra were collected with a Thermo-Nicolet 670 FT-IR using a 0.1 mm CaF_2 cell. Scanning Electron Microscopy was performed using a FEI XL-30 Environmental Scanning Electron Microscope (ESEM). Transmission electron microscopy (TEM) experiments were performed by depositing a

drop of a suspension diluted in hexane on a carbon-coated copper grid. The solvent was evaporated and the sample was analyzed using JEOL 2000FX and JEOL 2010 microscopes that were equipped with energy-dispersive spectrometers and operated at 200 kV and 100 kV, respectively. Conventional and high-resolution TEM imaging, selected area electron diffraction (SAED) and energy-dispersive spectroscopy (EDS) methods have been used for analysis of the iron phosphide nanoparticles. X-ray diffraction (XRD) data were obtained with a powder diffractometer (Rigaku D/Max-2100PC) using unfiltered Cu Kα radiation (λ = 1.5406 Å) at 40 kV and 40 mA. The contribution from $K\alpha 2$ radiation was removed using the Rachinger algorithm. Goniometer alignment was verified by daily analysis of a Rigaku-supplied SiO_2 reference standard. Elemental analyses were obtained from Galbraith Analytical Laboratories. Superconducting quantum interference device (SQUID) magnetization measurements were performed on a Super Quantum magnetometer (MPMS 5.5, equipped with a Squid detector). The temperature was varied between 2 and 300 K according to a classical zero-field cooling/field cooling (ZFC/FC) procedure in the presence of a very weak applied magnetic field (1000 Oe), and the hysteresis cycles were obtained at different temperatures in a magnetic field varying from +50 to -50 kOe.

2.2.2. Synthesis of $H_2Fe_3(CO)_9P^tBu$.

The synthesis is based on a literature procedure.[47] In a 500-mL Schlenk flask, 15.7 g (31 mmol) $Fe_3(CO)_{12}$ was weighed out. In order to remove the methanol present in the $Fe_3(CO)_{12}$ as a stabilizer, ~50 mL of toluene was added to the flask, the mixture was stirred for about 10 minutes, and then the flask was placed under vacuum until the solid was dry. The $Fe_3(CO)_{12}$ was then dissolved in ~250 mL toluene, resulting in a dark

green solution. To this dark green solution, a solution of $^{t}BuPH_2$ in THF (~75 mL) was transferred via cannula; the solution became red-purple. A reflux condenser was attached to the flask and the flask was placed in an oil bath. The oil bath temperature was stabilized at ~110 °C and the reaction was refluxed for 12 hours. The reaction was cooled to room temperature and filtered over ~10 g dry silica on a Schlenk frit; the filtrate was deep red. The toluene was removed under vacuum and the remaining red oily residue was extracted into hexanes. Multiple extractions were performed until the filtrate was no longer red. The product was crystallized by cooling the flask to -20 °C. Dark red crystals (the crystals look black, but form a deep red solution) were collected by filtration over a Schlenk frit. In order to obtain as much product as possible, the filtrate was concentrated and placed in the freezer. This was repeated until no more crystals were formed. Yield: 20% (3.19 g, 6.25 mmol). Analysis of the dark brown solution remaining after most of the $H_2Fe_3(CO)_9P^{t}Bu$ had been crystallized out by thin layer chromatography (TLC), using hexane as the solvent, and IR analysis of the spots indicated a combination of $Fe_3(CO)_{10}P^{t}Bu$ (black spot) and $Fe_2(CO)_6(PH^{t}Bu)_2$ (red-orange spot).

2.2.3. Synthesis of Iron Phosphide Nanofibers (1).

Iron phosphide nanofibers were synthesized by decomposing 0.25 g (0.50 mmol) $H_2Fe_3(CO)_9P^{t}Bu$ in the presence of TOA (7 mL) and OA (1 mL). This deep red solution was heated to 315 °C with a standard heating mantle and magnetic stirring, at which time the solution turned black. The exact temperature at which the solution turned black varied, depending on the ratios of surfactant, from 315 to 330 °C. The mixture was stirred for an additional 20 minutes at that temperature. After cooling to room

temperature, the nanoparticles were precipitated with ethanol. The supernatant was removed, and the remaining black solid was washed several times with hexane.

2.2.4. Synthesis of Nanofiber "Bundles" (2).

Keeping all conditions as in (1), but varying the ratio of TOA to OA (6 mL:2 mL, 4 mL:4 mL, etc.) resulted in "bundles" of nanofibers.

2.2.5. Synthesis of Dumbbell-Shaped Nanofiber "Bundles" (3).

Using the same conditions as in (1), but adding small amounts of hexane, other alkanes (i.e. nonane or tridecane), ethanol, or water before heating the solution, dumbbell-shaped bundles of nanofibers were formed. An experiment in which 0.10 g trimethylacetic acid was introduced before decomposition of the starting material was also carried out.

2.3. Results & Discussion

The cluster $H_2Fe_3(CO)_9P^tBu$ was examined as a single-source precursor targeted to the Fe_3P phase. The formation of iron phosphide nanoparticles was accomplished by the decomposition of the cluster in the presence of a surfactant system of trioctylamine (TOA) and oleic acid (OA). Surprisingly, X-Ray Powder Diffraction (XRPD) analysis of the product indicated formation of the Fe_2P phase (Figure 2.1), as did elemental analysis (observed (calculated) weight percent for Fe_2P): Fe 71.7 (78.3), P 20.1 (21.7); Galbraith Analytical Laboratories).

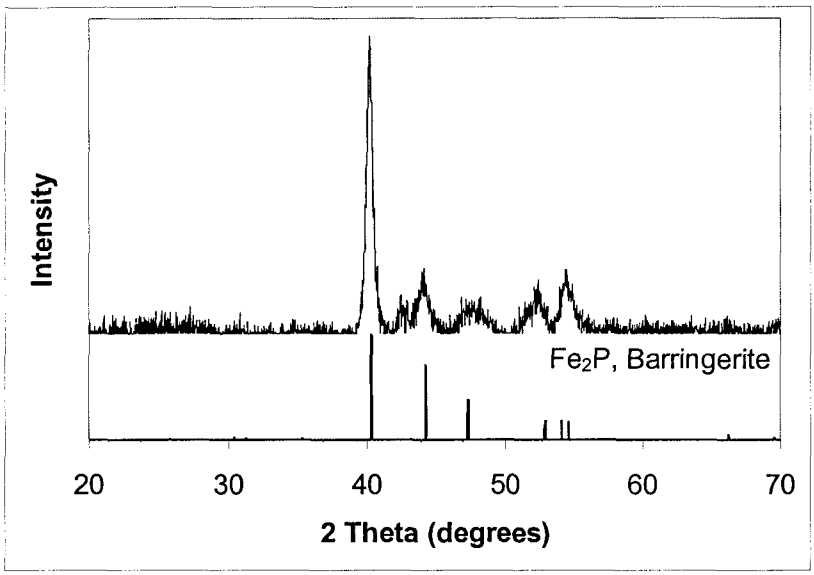

Figure 2.1. X-Ray Powder Diffraction Pattern for the iron phosphide nanorods. Peaks correspond to PDF 51-0943 (Fe_2P).

Upon investigation of the decomposition mechanism, however, it was discovered that the precursor transformed in the solvent system before decomposition to the iron phosphide material took place. The precursor is highly acidic,[58] and in the presence of TOA, it was first deprotonated as evidenced by FTIR. Further thermal rearrangement of the cluster after deprotonation resulted in the formation of $Fe_4(CO)_{12}(P^tBu)_2$. A more detailed discussion of this mechanistic study as well as the IR data is presented in Chapter 4.

By varying the concentrations of TOA and OA, different nanoparticle shapes were observed (Figure 2.2). Using a ratio of TOA:OA 7:1 (v:v), individual iron phosphide rods having an aspect ratio of ~ 11 were obtained (Figure 2.2A). When the concentration of OA was increased (TOA:OA = 6:2 or 4:4), a more complex system of split nanocrystals was obtained (Figure 2.2B depicts those synthesized from a 6:2 ratio). Both the 6:2 and 4:4 TOA:OA surfactant systems produced similar bundles, but the 4:4

system resulted in a more monodisperse product. The bundles had an average size of 415 ± 28 nm × 70 ± 9 nm and an average aspect ratio of 6, whereas the bundles synthesized in the 6:2 solvent system had an average size of 403 ± 65 nm × 90 ± 17 nm and an average aspect ratio of 5.

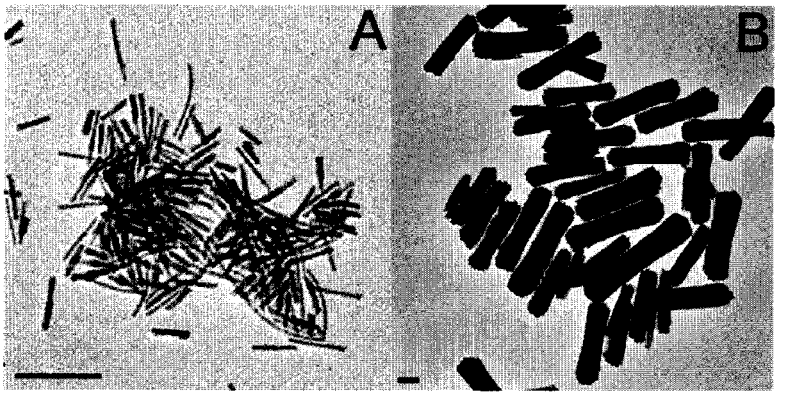

Figure 2.2. Transmission electron microscopy (TEM) images of iron phosphide nanorods synthesized from 0.50 mmol precursor in different solvent ratios: (A) 7:1 TOA:OA, aspect ratio 11. (B) 6:2 TOA:OA, aspect ratio 5. All scale bars represent 100 nm.

The polycrystalline selected area electron diffraction (SAED) pattern (Figure 2.3) recorded from the bundles confirmed that the material is single phase Fe_2P (hexagonal, $P\bar{6}2m$, a = 5.877Å, c = 3.437 Å). Single crystal SAED patterns and high resolution (HR) TEM images indicated growth of the rods along the c-axis. Electron diffraction spectroscopy (EDS) confirmed that all bundles were composed of iron and phosphorus; no other elements were observed. Scanning electron microscopy (SEM) analysis provided a 3D view of the bundles (Figure 2.4).

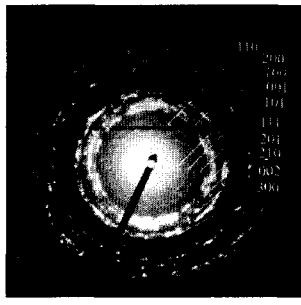

hkl	Measured d-spacing (Å)	Intensity	Fe_2P d-spacing (Å)[a]
(110)	4.98	vw[b]	5.09
(001)	3.46	vw	3.44
(110)	3.01	vvw	2.94
(101)	2.85	vw	2.85
(200)	2.55	w	2.55
(111)	2.26	vs	2.23
(201)	2.07	s	2.05
(210)	1.93	m	1.92
(002)	1.75	m	1.72
(300)	1.69	m	1.70

Figure 2.3. Polycrystalline Selected Area Electron Diffraction (SAED) pattern of the nanorods with measured d-spacings compared to published values. More discrepancies are seen in the weaker reflections due to the fact that measurements taken from TEM data are not as precise as those from X-ray diffraction data. [a] JCPDS card file 33-670. [b] vvw: very very weak, vw: very weak, w: weak, m: medium, s: strong, vs: very strong. Data obtained by Irene Rusakova.

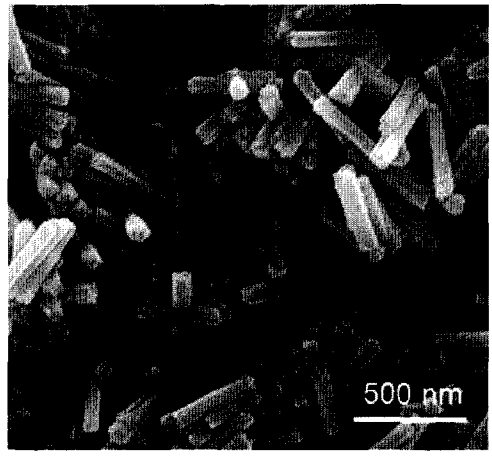

Figure 2.4. SEM image of bundles of Fe_2P nanorods synthesized from a 4:4 TOA:OA surfactant system.

Upon increasing the proportion of oleic acid with respect to trioctylamine, the rods acquire a bundle-like morphology. Initially from the TEM images, the rods appeared to be closely packed assemblies; however, upon further examination, it was found that splitting was occurring along the c-axis (Figure 2.5). Similar growth initiated by crystal splitting has been recently observed by our group for lead sulfide (PbS) nanorods as well as by Tang and Alivisatos in the Bi_2S_3 system.[59,60] Unlike the Bi_2S_3 system, the crystal structure of Fe_2P (Figure 2.6) does not possess one-dimensional chain

structures nor two-dimensional layers in the direction of growth that would provide obvious splitting vectors for the growing crystal. The asymmetry of this space group, however, promotes fast growth of the *C* face, and a high density of crystal defects was observed in proximity to the splitting, which unfortunately made it difficult to obtain high quality HR TEM micrographs at these areas. Overlapping of individual rods also made recording HR TEM images in these areas problematic. As a result of small angular deviation and overlapping of individual rods after splitting, rotational moiré fringes could be observed.

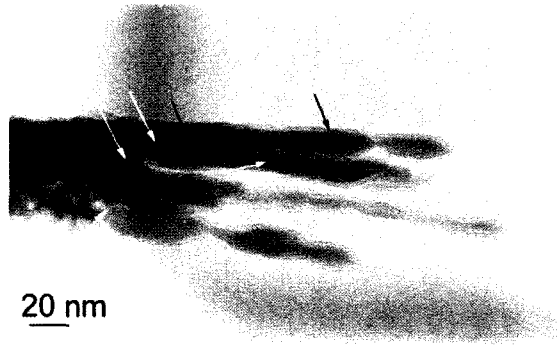

Figure 2.5. HR-TEM image of a split rod. Black arrows indicate moiré fringes, while white arrows indicate the location of splitting. Image obtained by Irene Rusakova.

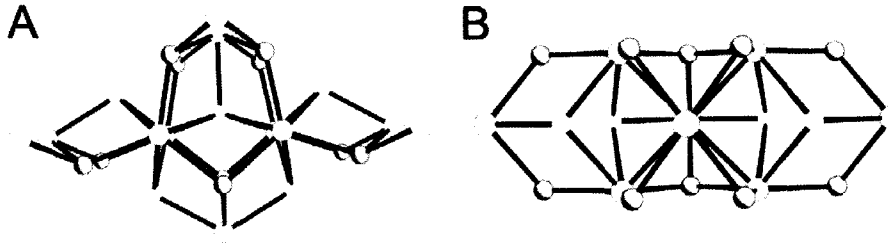

Figure 2.6. A schematic representation of the Fe_2P crystal structure (A) looking down the *c* axis and (B) perpendicular to the *c* axis.[39] Structure consists of tetrahedral (lavender) and pyramidal (green) iron sites. The atom coordinates are Fe(1): 0.255, 0, 0; Fe(2): 0.596, 0, 0.5; P(1): 0.33333, 0.66667, 0; P(2): 0, 0, 0.5. The Fe-P bonds are generally longer for the square pyramidal Fe(2) [four bonds of 2.485 and one of 2.371 Å], than to those to Fe(1) [two bonds of 2.222 and two of 2.287 Å].

While the simple bundles dominated in all of the variations studied, cross-shaped and T-shaped (Figure 2.7) bundles were also observed. From the initial TEM and SEM images showing cross-shaped nanoparticles, it was unclear whether they arose from random overlap of the rod-shaped crystals or from an interrupted growth process. In order to shed light on the growth mechanism we investigated their microstructure using TEM diffraction coupled with bright (BF) and dark field (DF) imaging. It is clear from the BF image of one of the cross-shaped bundles (Figure 2.8A) that the structure had grown from the same seed crystal or – more likely – formed as the result of a twinning mechanism leading to so-called penetration twins.

Figure 2.7. TEM image of a T-shaped bundle.

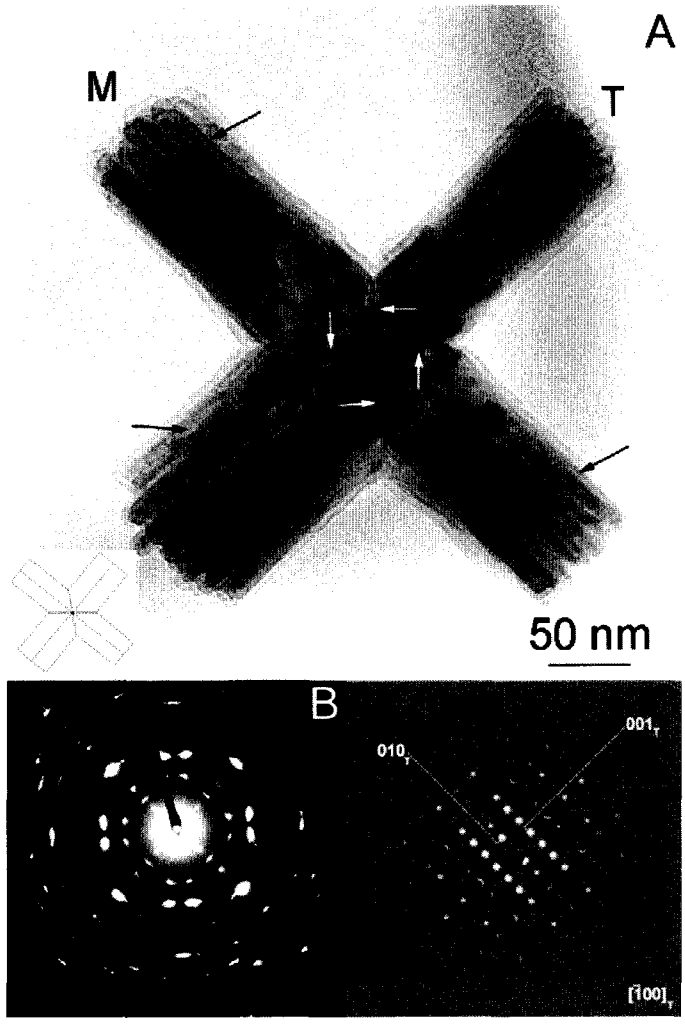

Figure 2.8. (A) BF TEM image of bundle showing a cross-shaped morphology. Black arrows indicate moiré fringes while white arrows indicate the twin boundaries. M: matrix bundle, T: twin bundle. Inset: Schematic figure of a penetration twin. (B-C) Experimental and simulated SAED patterns of cross-shaped bundle; black reflections in (C) arise from the matrix bundle of rods and white reflections arise from the twin bundle of rods. Images obtained by Irene Rusakova.

The X-shaped junction seen using TEM studies are indeed similar to features observed in penetration twins typical for various minerals, including staurolite (for schematic representation, see Figure 2.8A inset).[61] The formation of growth twins results from an interruption in the crystal lattice during growth. When crystals join to form a twin during nucleation, they should develop to become equal in size, which is observed in

this system. In support of this intergrowth mechanism is the observation that the crosses are only observed with arms at ~90° angles, which supports the contention that the arm orientation is controlled by the crystal structure.

Further support of the twinning mechanism is provided by the SAED pattern (Figure 2.8B), which arises from the twinning of the crystal. The matrix bundle has a [100] zone axis orientation whereas the twin bundle has a $[\bar{1}00]$ zone axis orientation. The twinning plane is (032) and the twinning law is a fourfold rotation (tetrad) around [100]. Splitting and azimuthal deviations of reflections in Figure 2.8B are caused by small angle deviations of individual rods inside a bundle. The rotational moiré fringes that we observed in BF TEM images originate from such deviations as well as from overlapping of individual rods inside a bundle. The thickness fringes observed result from overlapping of the split crystals near the ends of the bundles. The DF TEM images (Figure 2.9) further confirm the twinning mechanism of the growth of the cross-shaped bundles; the X-shaped junction is also observed in these images. HR TEM images reveal the presence of other planar defects (stacking faults) in the microstructure of bundles, which contribute to splitting of the rods (Figure 2.10). The presence of stacking faults explains the observation of streaks in the SAED pattern (Figure 2.8B).

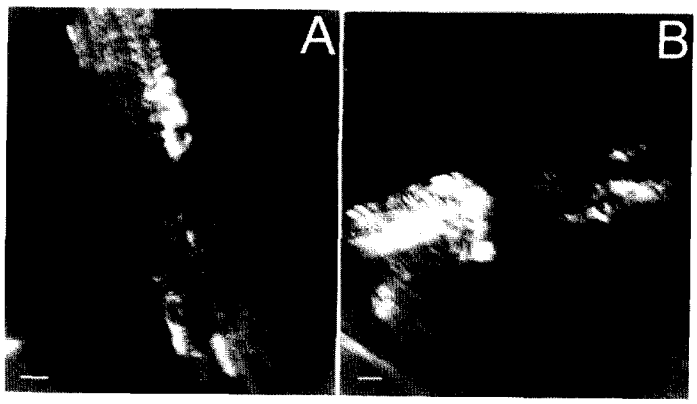

Figure 2.9. Central DF TEM images of a cross-shaped bundle using reflections from matrix (A) and twin (B). Both scalebars represent 20 nm. Images obtained by Irene Rusakova.

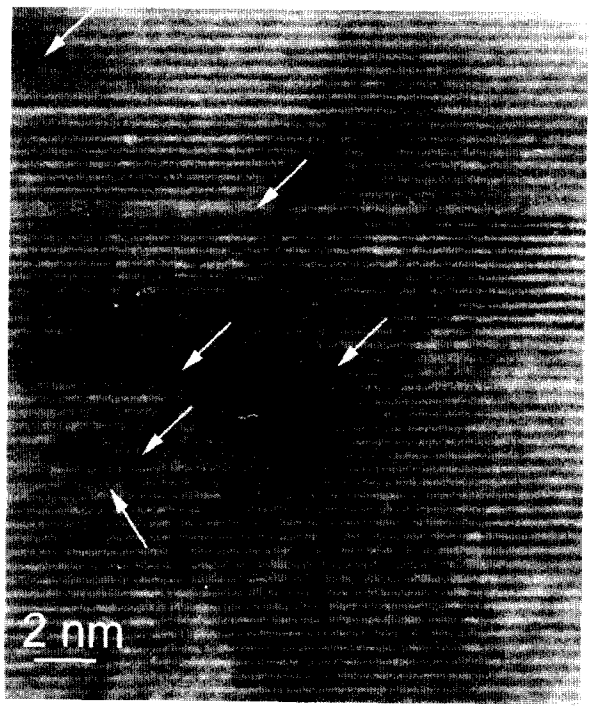

Figure 2.10. HR TEM image recorded from the area close to the center of the bundle showing planar defects (stacking faults) as marked by white arrows. Image obtained by Irene Rusakova.

Additional changes in the morphologies obtained were seen upon addition of controlled amounts of alkanes, ethanol, water, or trimethylacetic acid to the decomposition. When alkanes, such as hexane, nonane, and tridecane were added, an

even more complex crystal-splitting was observed, having a haystack (Figure 2.11A), dumbbell (Figure 2.11B), or spherulitic morphology (Figure 2.11C). The identity of the alkane was not found to be important. SEM images were also obtained of these materials (Figure 2.12).

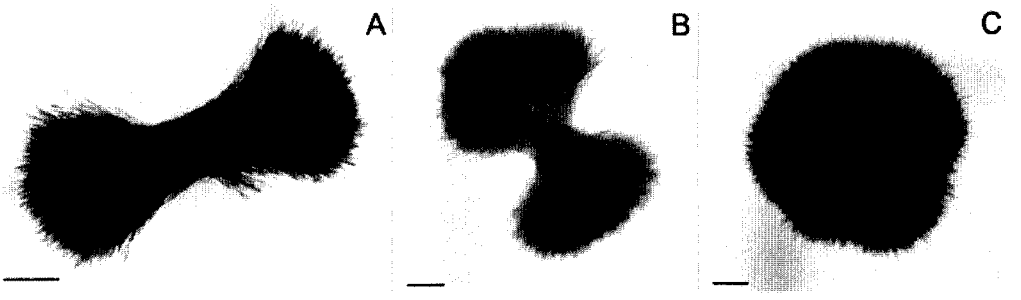

Figure 2.11. TEM images displaying the effect of the addition of alkanes. All scale bars represent 200 nm.

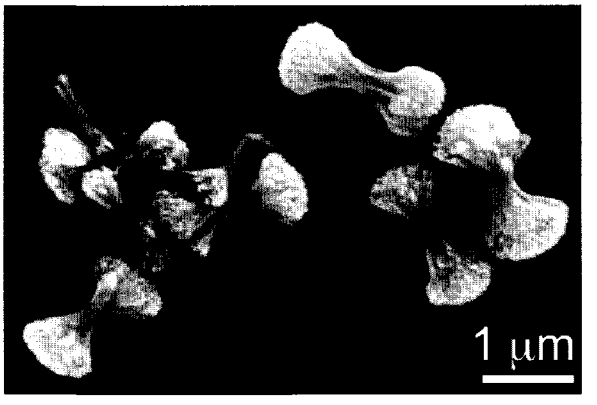

Figure 2.12. SEM image of iron phosphide nanorods synthesized with the addition of 100 μL hexane.

As was seen for the bundles discussed previously, cross-shaped and T-shaped bundles (Figure 2.13) were also seen in these experiments. A table of the resulting nanostructures with the addition of various alkanes can be found in Appendix I. Other

reactions were carried out in which the method of stirring was varied (magnetic or mechanical stirring); these results can be seen in Appendix I.

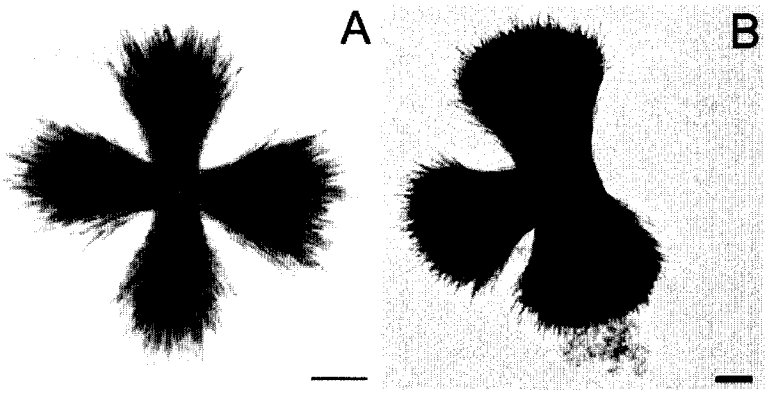

Figure 2.13. (A) TEM image of a cross-shaped bundle from decomposition with 4 mL TOA, 4 mL OA, and 200 μL hexane. (B) TEM image of a T-shaped bundle obtained from a decomposition with 4 mL TOA, 4 mL OA, and 100 μL nonane. Similar shapes were seen in all of the decompositions with added alkanes. Scalebars represent 200 nm.

For the decompositions with added water or ethanol, similar morphologies were seen (Figure 2.14). However, when water was added, the individual fibers of the bundles had rougher surfaces. The addition of ethanol also presented an interesting feature in that some of the branched rods appeared to have been "chopped" in half (Figure 2.14F). Similar features were seen in some of the functionalization experiments discussed in Chapter 6 that were carried out in ethanol. Figure 2.15 displays the results of decomposing $H_2Fe_3(CO)_9P^tBu$ with a small amount of trimethylacetic acid added to the reaction.

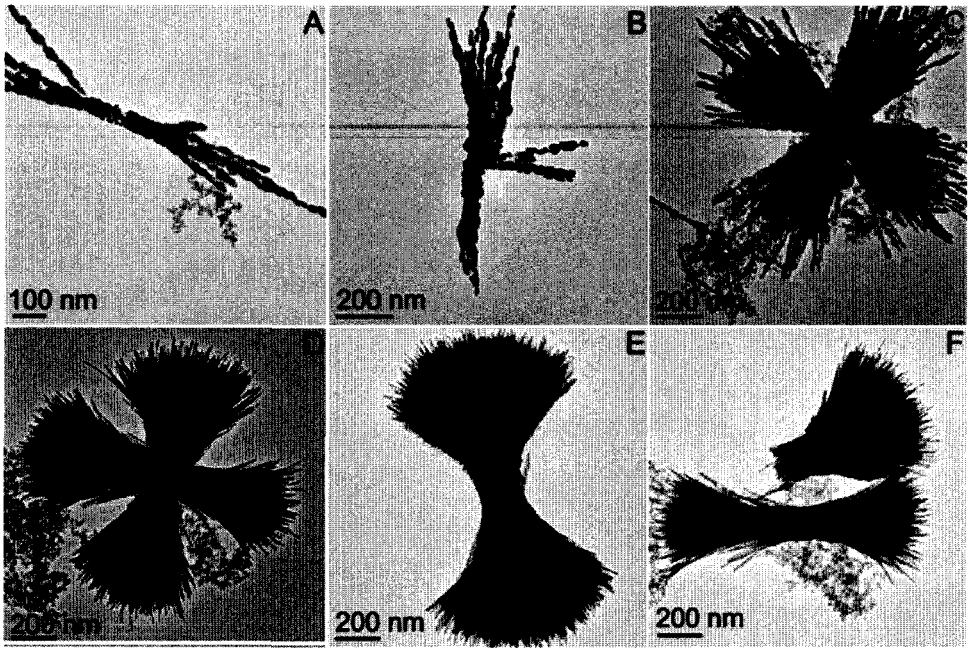

Figure 2.14. TEM images of the nanostructures synthesized with the addition of 100 μL of H_2O (A-C) and 100 μL of EtOH (D-F) in 4:4 TOA:OA.

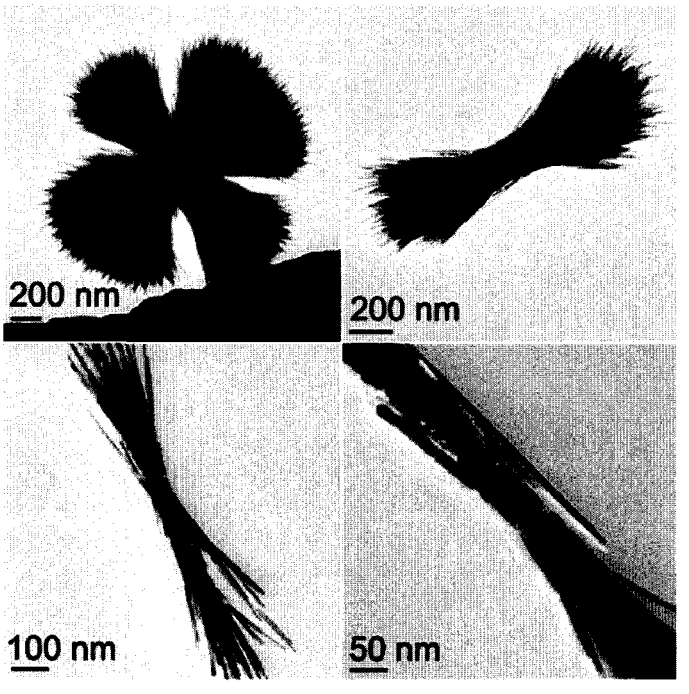

Figure 2.15. TEM images of the decomposition of $H_2Fe_3(CO)_9P^tBu$ in 2.5 mL TOA & 2.5 mL OA with trimethylacetic acid.

All decompositions produced Fe_2P nanorods. It has been well documented that the surfactants employed in the synthesis of nanoparticles influence the shape and size of the resulting nanomaterials.[62] Others have also reported the synthesis of metal phosphide nanorods.[51-53,63] In one of those systems, tri-*n*-octylphosphine and oleylamine were used as surfactants. The formation of nanorods was explained by the cooperative effect of the surfactants along with the intrinsically anisotropic crystal structure of the phosphides.[63] As mentioned previously, Fe_2P has a hexagonal crystal structure ($P\bar{6}2m$ space group, Figure 2.6), which is known for anisotropic growth. The structure has a unique [001] axis, and growth occurs along this direction.

Crystal formation takes place first by nucleation of a small aggregate followed by growth via binding of additional molecules to the aggregate. Successful growth requires that the approaching molecule binds to the aggregate in a specific orientation. Binding has been shown to be more effective when the molecule binds at defects on the crystal surface; defects provide steps and ledges which allow for strong binding of the molecule.[64] One example of such a defect is a screw dislocation. If a screw dislocation is formed at the center of a crystal face, the crystal face can grow perpetually along this direction because growth sites are continuously being formed.[65] The presence of a screw dislocation is likely in the iron phosphide system, as growth has been found to occur along the [001] axis.

Crystal splitting in the Fe_2P system appears to occur from the high concentration of defects produced due to the high rate of growth in the *c* direction. While similar structures have been shown to arise from crystal splitting in Bi_2S_3[60,66,67] and Sb_2S_3,[68,69] for

Fe_2P, obvious one-dimensional or layer-like arrangements of the atoms that would give rise to cleavage planes are not obvious in any crystallographic direction.

As far as the effect of surfactants on the growth and splitting, we found that increasing the concentration of oleic acid appears to cause the rods to split. From the system in which trioctylamine and oleic acid are in a 7:1 ratio, single iron phosphide nanorods are synthesized. However, upon increasing the concentration of oleic acid, splitting of the rods occurs. Additionally, when alkanes were added in microliter amounts to the reaction, a more complex dumbbell-shaped splitting was observed.

For the Tang and Alivisatos synthesis[60] of Bi_2S_3, the various nanostructures were synthesized by the reaction of elemental sulfur and a bismuth carboxylate in 1-octadecene. The control of shape in that system was achieved via variations in the injection temperature of sulfur. In contrast, for Fe_2P, the temperature was not varied; instead, variation of the surfactants or addition of small amounts of alkanes caused the formation of more complex nanostructures. New surface area forms every time the crystal splits, so the introduction of molecules that stabilize the growing surfaces would favor crystal splitting. Increasing the amount of oleic acid, a good stabilizing surfactant, also appeared to promote crystal splitting. Because oleic acid is a strongly coordinating surfactant, increasing the concentration of oleic acid would likely decrease the nanoparticle nucleation rate, thereby increasing the growth rate. Sunagawa reported that split growth is seen often in systems having high growth rates.[61] Nucleation and growth occurs rapidly in the iron phosphide system, as can be seen in a TEM image taken from a one-minute reaction (reaction time after the solution turned black, Figure 2.16).

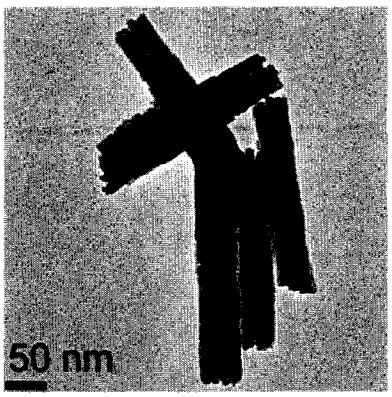

Figure 2.16. TEM image of a one-minute reaction, solvent system TOA:OA 4:4.

Many of the shapes seen in our synthesis as well as in the recently reported work with bismuth sulfide resemble those seen in spherulites and other forms of minerals, which are also believed to form via a split growth mechanism.[61] While the precise formation mechanism of spherulites via crystal splitting is not well understood, there has been speculation regarding the possible causes.[70-72] There are two classes of spherulites formed by two distinctly different overall growth processes. In the first, growth occurs radially from a common nucleation site. The second growth process begins with a single fiber that branches as growth continues, forming a sheaf and eventually evolving into the spherulite. Based on these classifications, it appears as though the iron phosphide system follows a similar growth process as that leading to the second class of spherulites. The evolution from rod-shaped and split crystals to dumbbell-shaped bundles and spherulites occurred with the incremental addition of microliter amounts of alkanes to the system before decomposition of the precursor. Keith and Padden[70] reported the presence of low molecular weight components, which may be considered impurities, to be common in spherulite-forming solutions. The presence of the alkanes in small concentrations seems to have a significant impact on the growth kinetics. We may speculate that the alkanes

interrupt the crystallization process, leading to a bifurcation of the growth process and consequently enhanced the splitting of the rods. As stated previously, oleic acid serves as a surface-coordinating surfactant, stabilizing the forming nanoparticle surface. The stabilization provided by oleic acid results in slow nucleation and fast growth. It is possible that the lower molecular weight alkanes used, in which the organometallic precursor is more soluble, aids oleic acid in stabilizing the cluster in solution, further delaying the nucleation, thus resulting in an even greater rate of growth.

Information regarding the temperature-dependent magnetic behavior of the nanorods as the temperature was varied is seen in the Zero-Field-Cooling (ZFC) and Field-Cooling (FC) graphs. Figure 2.17 presents the ZFC/FC of three of the different iron phosphide morphologies synthesized. Interestingly, the blocking temperature (T_B) was seen to increase from a T_B centered around 124 K for well dispersed nanorods (Figure 2.17**A**) to a T_B of 180 K for rods that had a bundle-like morphology (simple splitting, Figure 2.17**B**), although there was a broader distribution of blocking temperatures, probably due to the distribution of the magnetic size as a result of the dipolar coupling within the rods. A further increase in T_B was observed in the more complex dumbbell-shaped system (Figure 2.17**C**) where the blocking temperature reaches 205 K. This increase in blocking temperature with increased interparticle interaction was not unexpected, as it has been reported that with increasing strength of dipolar interactions, the mean T_B value increases.[73-75]

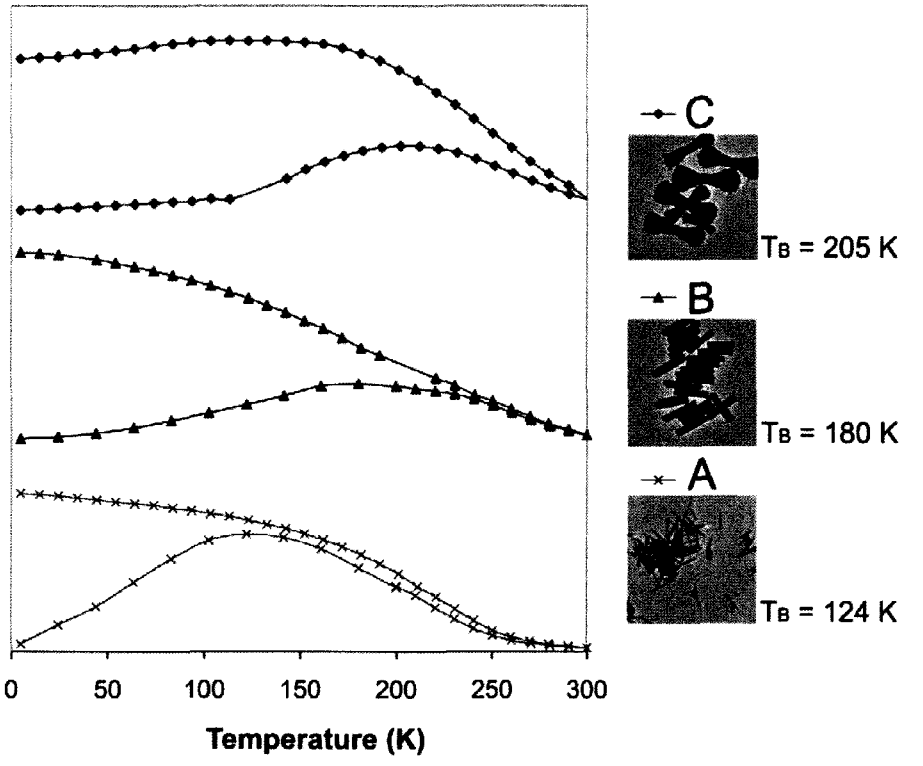

Figure 2.17. ZFC/FC graph of iron phosphide nanorods at 1000 Oe.

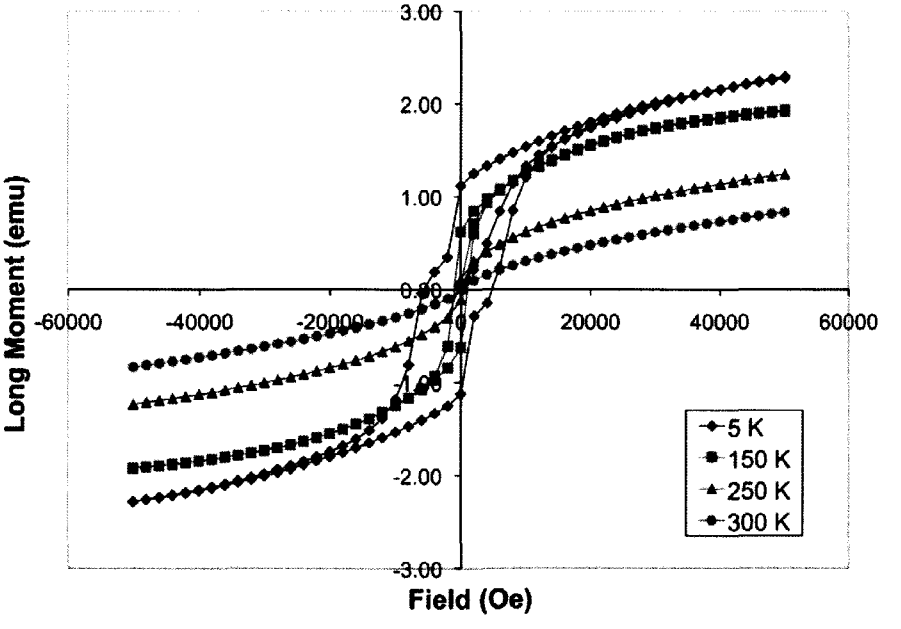

Figure 2.18. Hysteresis loops of the iron phosphide nanorods with bundle-morphology (B).

The hysteresis loops indicate the presence of a coercive field at 5 K (Figure 2.18). A very small hysteresis remains at 250 K, above the Curie temperature. This suggests that a small amount of impurity is most likely present in the product. The decomposition occurs via the formation of the $Fe_4(CO)_{12}(P^tBu)_2$ cluster (the decomposition mechanism is discussed in more detail in Chapter 4); therefore, it is likely that $Fe(CO)_5$ is produced as a byproduct. The thermal decomposition of $Fe(CO)_5$ has been reported to produce both iron and iron oxide nanoparticles.[46,76-79] The presence of these nanoparticles could explain the observed magnetic properties. However, the magnetic moment calculated from the saturation magnetization (M_s) at 5 K was 2.28 μ_B, which is similar in magnitude to the most recently reported magnetic moment of single-crystalline Fe_2P (2.81 μ_B; determined by neutron diffraction).[40] It is important to note that the magnetic measurements on Fe_2P have been found to be very sensitive to impurities and deviations from an ideal stoichiometry. Values reported for the magnetic moment, using a variety of methods for determination as well as a variety of temperatures, have ranged from 2-3 μ_B.[38,80-82] Another reason proposed for the wide range of reported magnetic moments has to do with the large magnetic anisotropy of Fe_2P, resulting in a slow approach to saturation in measurements made using polycrystalline samples.[83]

2.4. Conclusions

We have successfully used a soluble single-source molecular precursor to synthesize iron phosphide nanomaterials. A variety of different morphologies, the result of crystal splitting, were seen as a result of changing synthetic parameters (i.e. ratio of oleic acid to trioctylamine and addition of small amounts of alkanes, ethanol, water, or trimethylacetic acid). Additional cross-shaped structures were also observed and

attributed to the twinning of two individual bundles during growth as the result of an interrupted growth process.

Chapter 3. Effects of variations in precursor, surfactant system, and other reaction parameters on the synthesis of iron phosphide nanomaterials

3.1. Introduction

The decomposition of $H_2Fe_3(CO)_9P^tBu$ in a TOA & OA solvent system resulted in a variety of different morphologies all of the same phase, Fe_2P. In an attempt to target an alternate phase, Fe_3P in particular, a variety of parameters were tested. The previous decompositions did not result in the Fe_3P phase as expected, due to the rearrangement of the cluster in solution before decomposing. Two different approaches were taken to circumvent the cluster rearrangement of the $H_2Fe_3(CO)_9P^tBu$ cluster before decomposition: varying the rate of decomposition and incorporating different surfactants into the system. Additional attempts for obtaining alternate phases involved the decomposition of other iron phosphorus carbonyl clusters.

The rate or temperature at which the precursor decomposes has been found to play a role in the outcome of nanoparticle syntheses. For example, Yin *et al.* reported the synthesis of more uniform, monodisperse iron oxide nanocrystals at higher heating rates due to the shorter nucleation window under these reaction conditions.[84] In conditions with slower heating rates, the rate of nucleation decreases, likely resulting in uneven growth and a broader size distribution. With regard to the phase of nanomaterial synthesized, temperature can also play a role. For example, face-centered cubic or hexagonal close-packed nickel nanoparticles could be obtained from the decomposition of nickel acetate in hexadecylamine, depending on the reaction temperature.[85]

Surfactants are known to impact the shape of nanomaterials via dynamic solvation of the faces of the growing nanocrystal.[86] Therefore, a better understanding of the interface between the organic surfactants and the inorganic core is imperative if more advanced materials are to be formulated. Anisotropic nanomaterials are higher energy structures; therefore, their growth is likely determined by kinetics rather than thermodynamics. The choice of surfactant is important, because if it selectively binds to a particular crystallographic face, that face will be stabilized relative to the other crystal surfaces during growth, promoting growth along faces not stabilized by the surfactant. The interaction of organic species with crystal faces is not completely understood and is, therefore, not yet predictable. However, by studying a variety of different systems and gaining insight into how the surfactants influence each system, a broader understanding of the mechanisms at work may be elucidated.

The influence of a variety of different surfactants was studied in the iron phosphide system in order to determine whether changes in the functional groups present in the decomposition solution impacted the reaction pathway and, hence, the resulting nanoparticle morphology or phase. Another approach taken in aiming for alternate iron phosphide phases was the decomposition of other iron phosphorus compounds, including $Fe(CO)_4P^tBuCl_2$, $Fe_3(CO)_9(P^tBu)_2$, $Fe_2(CO)_6(PH^tBu)_2$, $Fe_4(CO)_{11}P^tBu_2$, and $Fe_3(CO)_{10}P^tBu$. We were interested in determining whether varying the arrangement and ratio of iron and phosphorus atoms in the starting material would impact the phase of nanomaterial obtained.

3.2. Experimental Procedure

Dioctylether (DOE, 99%), 1-hexadecanol (HDOH, 99%), 1-octadecene (ODE, 90%), oleylamine (OAm, 70%), hexadecylamine (HDA, 90%), oleyl alcohol (OOH, 85%), octadecanol (ODOH, 99%), tridodecylamine (TDDA, 85%), and mesitylene (98%) were purchased from Sigma-Aldrich and used as received. 1,2-dichlorobenzene (99%) was purchased from Acros Organics and used as received. Iron pentacarbonyl ($Fe(CO)_5$, 99.5%) and phenylphosphine ($PhPH_2$) were purchased from Strem and used as received, handled under an inert atmosphere.

All decompositions were carried out in a 25-mL, 3-neck roundbottom flask, equipped with a reflux condenser and N_2 adapter hooked up to an oil bubbler for release of any pressure built up over the course of the reaction. A Glas-Col Series O heating mantle was used with a Barnstead Electrothermal, Cat. No. MC242X1 power controller. After cooling of the reactions, ethanol was added in order to precipitate the nanoparticles. Unless otherwise indicated, the precipitate was then washed with ethanol followed by hexane, aided by sonication, and centrifuged. Washing was performed until the supernatant was clear.

JEOL JEM-2100F TEM equipped with an energy-dispersive spectrometer operated at 200 kV was used to obtain HR-TEM images as well as EDS spectra. Oxford INCA software was used to collect and analyze the EDS data. For weight percentages determined using EDS, a few areas of the TEM grid were analyzed to get an average Fe and P composition. X-ray Photoelectron Spectroscopy (XPS) analyses were performed on a Phi Quantera XPS spectrometer. Samples were prepared by pressing a small amount of the solid to be analyzed onto a piece of indium foil.

3.2.1. Heating Rate Experiments.

Fast: $H_2Fe_3(CO)_9P^tBu$ (0.10 g, 0.20 mmol) + 2 mL TOA + 2 mL OA

The heating mantle was turned up to the maximum setting (#10) before inserting the flask. When the temperature of the mantle reached ~250 °C, the solvents and the precursor were added to a 3-neck flask (trying to minimize the time between combining reagents and starting the decomposition in an attempt to prevent any solvent-precursor reactions). When the temperature reached ~300 °C, the flask was inserted into the heating mantle. The solution changed from deep red to brown to clear orange to amber to black (345 °C). The time from the insertion of the flask into the heating mantle to the time when the solution turned black was ~7.5 minutes.

Intermediate: $H_2Fe_3(CO)_9P^tBu$ (0.10 g, 0.20 mmol) + 2 mL TOA + 2 mL OA

The precursor and solvents were combined in a 3-neck flask and placed in the heating mantle. The power was then turned on to the maximum setting. As the solution was heated, the color progressed from deep red to red-orange to orange to yellow-gray to black (350 °C). The solution turned black in this reaction after approximately 20 minutes of heating.

Slow: $H_2Fe_3(CO)_9P^tBu$ (0.10 g, 0.20 mmol) + 2 mL TOA + 2 mL OA

After combining the precursor and solvents in the 3-neck flask, the flask was placed in the heating mantle, and the power was turned on to the medium setting (#5). The temperature was gradually increased, and the same color progression was seen as with the previous decomposition (Intermediate). The length of time for the solution to turn black was ~26 minutes.

Injection of precursor: In a scintillation vial, $H_2Fe_3(CO)_9P^tBu$ (0.20 g, 0.39 mmol) was combined with 1 mL TOA and 1 mL OA. In a 3-neck flask, 3 mL OA and 3 mL TOA were combined and the surfactant solution was heated. When the temperature reached ~330 °C, ~0.3 mL of the precursor solution was injected via syringe through a rubber septum. The solution immediately turned orange. Addition of the precursor in ~0.1 mL increments was continued until all of the solution had been added (the solution was too viscous to efficiently inject it all at once). The addition took ~3 minutes. As the solution was heated, it changed from orange to amber to black (at 340 °C, ~10 minutes from first injection). The temperature was held at 340 °C for 15 minutes.

3.2.2. Varying solvent/surfactant system

ODE/OA (7:1; 6:2): 0.25 g (0.50 mmol) $H_2Fe_3(CO)_9P^tBu$ was combined with 7 mL ODE and 1 mL OA, forming a deep red solution. As the temperature reached ~200 °C, the solution became foamy. Around 245 °C, the solution was dark brown with orange foam. By 260 °C, the solution was a clear dark brown. When the reaction reached 300 °C, the solution was black, and a metallic mirror appeared on the walls of the flask. The reaction was held at 300 °C for 10 minutes. The decomposition in 6 mL ODE and 2 mL OA proceeded similarly.

OAm/OA (4:4; 7:1; 1:7; 2:6): 0.25 g (0.50 mmol) $H_2Fe_3(CO)_9P^tBu$ was combined with 4 mL OAm and 4 mL OA, forming a reddish-brown solution. As the solution was heated, it became brown and slightly foamy, with a yellow solution on the walls and on the condenser (240 °C). The reaction proceeded to change to a clear orange-red color (270 °C) then to dark brown (300 °C) and finally to black (305 °C). The reaction was held at

~320 °C for 20 minutes. The decomposition proceeded similarly for all other variations of solvent ratios.

HDOH/OA: 0.25 g (0.50 mmol) $H_2Fe_3(CO)_9P^tBu$ was combined with 7 mL (5.73 g) HDOH and 0.15 mL (0.50 mmol) OA. The flask was slowly warmed in order to melt the HDOH. When the temperature reached ~100 °C and most of the HDOH had melted, the flask was placed under vacuum to remove any moisture. After 20 minutes, the flask was filled with Ar and opened to the bubbler. The solution was very dark red-black in color. As the temperature was increased, the solution became brown (260 °C) and then black with a yellow solution refluxing on the walls of the flask (290 °C). The solution began to get foamy at ~300 °C, and the yellow color was no longer evident at 320 °C. Stirring was continued at 320 °C for an additional 5 minutes. When the reaction had cooled, ethanol was added to precipitate the particles, and a black solid was isolated after centrifugation and washing with hexane. It was difficult to centrifuge the particles from hexane due to their small size, so TEM grids were prepared of the hexane wash as well as of the black solid redispersed in hexane.

DOE/OA (7:1; 10:1): 0.25 g (0.50 mmol) $H_2Fe_3(CO)_9P^tBu$ was dissolved in 7 mL DOE and 1 mL OA. As the reaction was heated, the solution became foamy and a cloudiness developed above the solution. At 245 °C, the reaction had become dark brown with an orange-brown foam. The solution became dark brown-black at 310 °C, and was held at this temperature for approximately 10 minutes. The reaction in 10 mL DOE and 1 mL

OA followed a similar pattern in color changes, but appeared to turn black (as opposed to brown-black).

DOE/OA, injection: The surfactants, 10 mL of DOE and 1 mL of OA, were combined in a 3-neck flask and the solution was heated. When the temperature reached 180 °C, a solution of 0.25 g (0.50 mmol) $H_2Fe_3(CO)_9P^tBu$ dissolved in 4 mL of 1,2-dichlorobenzene was injected into the flask via syringe. The temperature dropped to ~170 °C after injection, but was quickly ramped up again. When the reaction reached 210 °C, the solution was dark brown and very foamy. The solution appeared black at around 240 °C; heating was continued for an additional 30 minutes.

DOE/OA/OAm: 0.25 g (0.50 mmol) $H_2Fe_3(CO)_9P^tBu$ was dissolved in 10 mL DOE, 0.1 mL OA, and 0.1 mL OAm, forming a deep red solution. The reaction was heated and when the temperature reached 215 °C, the solution had become dark brown. At 330 °C, the reaction changed to black; the solution was held at this temperature for 30 minutes.

3.2.3. Varying the Functional Groups of the Surfactants

For the four decompositions of $H_2Fe_3(CO)_9P^tBu$ described below (in HDA, OOH, HDOH, ODOH), the washing procedure for isolating the nanoparticles varied from the general procedure. After the initial precipitation of particles using EtOH, the particles were redispersed in hexane. However, the particles did not precipitate out of solution when centrifuged, likely due to the small size of the particles, so more EtOH was added

in order to reprecipitate the particles. This cycle was repeated for each of the decompositions several times, until the washes were clear.

HDA/OA: In a 3-neck flask, 5.7 g (7 mL) HDA and 1 mL OA were combined and heated in order to melt the HDA. At ~80 °C, all of the HDA had melted. Under a flow of argon, $H_2Fe_3(CO)_9P^tBu$ (0.50 mmol; 0.25 g) was added to the flask. The red solution was heated, turning brownish red at 235 °C, dark brown at 255 °C and black at 300 °C. After the solution turned black, it was maintained at this temperature for 15 minutes. The flask was removed from the heating mantle and, while the solution was still above the melting point of HDA, ~3 mL of the decomposition solution was added to 10 mL EtOH in a centrifuge tube. After centrifugation of the solution, the washings were performed as described above.

OOH/OA: In a 3-neck flask, 0.50 mmol (0.25 g) $H_2Fe_3(CO)_9P^tBu$ was dissolved in 7 mL OOH and 1 mL OA. The precursor did not initially appear to be as soluble in this system as in the others, but appeared to be dissolved completely at 100 °C. The solution became foamy and brown at 200 °C, dark brown at 220 °C, and black at 290 °C. After the solution turned black, heating was continued for 20 minutes, remaining between 300 and 320 °C during that time period. The precipitation and washing of the particles was carried out as described above. The isolated solid was not a stable suspension in hexane (it precipitated out quickly).

HDOH/OA: In a 3-neck flask, 0.50 mmol (0.25 g) $H_2Fe_3(CO)_9P^tBu$ was combined with 5.73 g (7 mL) HDOH and 1 mL OA. The mixture was heated, and when the temperature reached 40 °C, the flask was placed under vacuum in order to remove any moisture that may have been present. After 30 minutes (temperature was 115 °C), the flask was filled with Ar; the solution was dark red-black. The solution was heated and became cloudy at 190 °C, brown at 260 °C, and foamy and black with a yellow solution on the walls at 325 °C. The solution was heated for an additional 10 minutes after turning black. Washing and precipitation were performed as described above.

ODOH/OA: In a 3-neck flask, 5.7 g (7 mL) ODOH and 1 mL OA were combined. The flask was warmed in order to melt the ODOH. When the ODOH had melted (80 °C), 0.50 mmol (0.25 g) $H_2Fe_3(CO)_9P^tBu$ was added to the flask. As the solution was heated, it became brown-red and very foamy (180 °C), dark brown with orange foam at 205 °C and black at 275 °C. After an additional 20 minutes of heating, the reaction was turned off. The washing of this decomposition was difficult due to the ODOH being only sparingly soluble in EtOH.

3.2.4. Varying Trialkylamines

Two sets of decompositions were carried out, one using 0.12 g (0.25 mmol) and the other using 0.25 g (0.50 mmol) $H_2Fe_3(CO)_9P^tBu$. Each decomposition used 8 mL of solvent (7 mL of the trialkylamine and 1 mL oleic acid). The color progression from deep red to black for each of the decompositions are noted:

0.25 mmol $H_2Fe_3(CO)_9P^tBu$. When TOA/OA were used, the solution became foamy and dark brown at 280 °C, red-orange with orange foam at 295 °C, brown-orange with yellow foam at 325 °C and finally black at 340 °C. When tridodecylamine (TDDA) and OA were used, the solution became clear orange at 285 °C, brownish-orange at 320 °C, and black at 330 °C.

0.50 mmol $H_2Fe_3(CO)_9P^tBu$. When TOA/OA were used, the solution became dark brown with orange foam at 290 °C, changing to black at 310 °C. The solution never became orange during this decomposition. When TDDA/OA were used, the solution became dark brown at 260 °C, clear dark orange at 290 °C, and black at ~330 °C.

3.2.5. Synthesis of iron-phosphorus clusters.

$Fe(CO)_4P^tBuCl_2$, $Fe_3(CO)_9(P^tBu)_2$, & $Fe_3(CO)_{10}P^tBu$[48]:

$Na_2Fe(CO)_4 \cdot {}^3/_2$ dioxane (1.8 g, 5.2 mmol) was weighed into a three-neck roundbottom flask in the glovebox. The beige solid was dissolved in ~ 50 mL dry THF; to this solution, 0.70 mL $Fe(CO)_5$ (1.0 g, 5.2 mmol) was added via syringe over ~5 minutes. The solution changed from a brown-tan color to deep orange, and was then cooled to ~ 0 °C in an ice bath. When the solution had cooled, a solution of $^tBuPCl_2$ (0.83 g, 5.2 mmol) in THF was added dropwise via a pressure-equalizing dropping funnel. The solution became brick red, then darkened to brown, and finally to a very dark brown/almost black. The addition was completed after 15 minutes. The flask was removed from the ice bath, the solvent was removed under vacuum, and then the product was extracted into hexane.

TLC of the extract, using hexane as the eluting solvent, resulted in two spots. The spots were scraped off and the IR was taken in hexane. The first corresponded to $Fe_3(CO)_9(P^tBu)_2$, and the second to $Fe_3(CO)_{10}P^tBu$. Column chromatography (Silica, hexane): the product was loaded onto 8 g of silica gel (70-230 mesh powder) that had been dried in a Fisher Scientific Isotemp oven at 120 °C overnight. The total column length was ~23 cm. Three fractions were collected and characterized by IR (Table 3.1): 1 = $Fe(CO)_4P^tBuCl_2$, yellow; 2 = $Fe_3(CO)_9(P^tBu)_2$, dark red-orange; 3 = $Fe_3(CO)_{10}P^tBu$, yellowish-brown.

$Fe_3(CO)_{10}(\mu_3\text{-}P^tBu)$		**$Fe_3(CO)_9(P^tBu)_2$**		**$Fe(CO)_4P^tBuCl_2$**	
Literature[48] pentane	Experimental hexane	Literature[48] pentane	Experimental hexane	Literature[48] pentane	Experimental hexane
2084 w	2083 w	2035 vs	2034 vs	2077 m	2077 s
2042 s	2042 s	2016 vs	2016 vs	2068 s	2068 s
2025 vs	2025 vs	1994 s	1994 vs	2002 s	2002 vs
2016 m	2016 s	1986 w	1986 m, sh	1975 vs	1975 vs
1998 w	1998 w	1979 vw	1978 m, sh	1962 vs	1962 vs
1977 w	1977 w			1929 vw	1928 w
1965 w	1964 w				
1875 vw	1876 w				

Table 3.1. Experimental and Literature IR values for $Fe_3(CO)_{10}(\mu_3\text{-}P^tBu)$, $Fe_3(CO)_9(P^tBu)_2$, and $Fe(CO)_4P^tBuCl_2$.

<u>$Fe_2(CO)_6(PH^tBu)_2$</u>: The compound $Fe_2(CO)_6(PH^tBu)_2$ was obtained as a byproduct in the synthesis of $H_2Fe_3(CO)_9P^tBu$ described in Chapter 2. When a majority of the $H_2Fe_3(CO)_9P^tBu$ had been extracted, the remaining solution was chromatographed on a silica column using hexane as the eluting solvent.

<u>$H_2Fe_3(CO)_9PPh$</u>[47]: $Fe_3(CO)_{12}$ (9.01 g, 17.9 mmol) was weighed into a 3-neck roundbottom flask in the glovebox. Dry toluene (~30 mL) was added to the flask; the

toluene was then removed under vacuum to remove the MeOH present in the $Fe_3(CO)_{12}$ as a stabilizer. After the $Fe_3(CO)_{12}$ was dried, it was redissolved in ~300 mL dry toluene, then 2.0 g (18 mmol) $PhPH_2$ was added to the dark green solution via syringe. The flask was then placed in an oil bath and heated to reflux. The reaction was refluxed overnight, during which time the solution became dark brown-black. After cooling the solution to room temperature, it was filtered over dry silica, and the toluene was removed under reduced pressure. The product was then extracted into hexane, filtered, and the hexane removed under vacuum from the supernatant. The dark brown crystalline residue was transferred into a sublimation apparatus for further purification.

$Fe_4(CO)_{11/12}(P^tBu)_2$: This cluster was isolated as a product of the decomposition of $H_2Fe_3(CO)_9P^tBu$ at ~140 °C (the decomposition mechanism is discussed in Chapter 4). In a Schlenk flask, $H_2Fe_3(CO)_9P^tBu$ (0.68 mmol) was dissolved in mesitylene with 6 mL of TOA. The solution was heated to 170 °C and held at this temperature for 1.5 hours. The solution was concentrated under vacuum and then the solution was chromatographed, using hexane as the eluting solvent. A brown-orange fraction was isolated and determined to be a mixture of the $Fe_4(CO)_{11}(P^tBu)_2$ and $Fe_4(CO)_{12}(P^tBu)_2$ clusters. The hexane solution was concentrated and placed in the freezer for crystallization; the isolated solid, which was a mixture of the two compounds, was used for the decomposition.

3.2.6. Decomposition of Various Precursors

The majority of these decompositions were performed on a smaller scale in order to obtain qualitative results.

$H_2Fe_3(CO)_9PPh$: 0.26 g (0.49 mmol) $H_2Fe_3(CO)_9PPh$ was dissolved in 4 mL TOA and 4 mL OA, forming a red-brown solution. As the solution was heated, it changed from dark brown (175 °C) to clear orange (280 °C) to yellow (310 °C) and finally to black (340 °C). The temperature was held between 330 and 350 °C for 15 minutes.

$Fe_3(CO)_{10}P^tBu$: 0.10 g (0.19 mmol) $Fe_3(CO)_{10}P^tBu$ was dissolved in 2 mL TOA and 2 mL OA in a 3-neck flask, forming a brown solution. The cluster appeared to be more soluble than $H_2Fe_3(CO)_9P^tBu$ in this solvent system. As the flask was heated, the color changed from brown to reddish-brown to dark brown (with orange foam) to red-orange to amber and finally to black (330 °C). The reaction was held between 320 and 330 °C for 15 minutes after the solution turned black. The workup of the reaction proceeded as previously described.

$Fe_4(CO)_{11/12}(P^tBu)_2$: The isolated solid was dissolved in 2 mL TOA and 2 mL OA. As the solution was heated, the color changed from orange to yellow (235 °C) to gray (320 °C). The solution never became any darker (reaction held above 300 °C for 20 minutes); the workup proceeded as usual and a small amount of black solid was isolated.

$Fe_3(CO)_9(P^tBu)_2$: 0.10 g (0.17 mmol) $Fe_3(CO)_9(P^tBu)_2$ was dissolved in 4 mL TOA and 4 mL OA, forming a red-orange solution. Heating the solution resulted in changes in

color from dark orange (230 °C) to yellow (340 °C) and finally to black (345 °C). After the solution turned black, the temperature was held at 345 °C for 15 minutes before removing the flask from the heating mantle.

$Fe_2(CO)_6(PH^tBu)_2$: This cluster was obtained as a side product from the reaction of $[HFe_3(CO)_{11}][Et_3NH]$ with $^tBuPCl_2$ and NEt_3 in THF.[87] It was isolated and purified using column chromatography. The compound (0.031 g, 0.068 mmol) was dissolved in 2 mL TOA and 2 mL OA. Before heating, the solution was orange-yellow. As the solution was heated, it changed from orange to yellow-orange to yellow to clear and colorless (300 °C). After 20 minutes above 300 °C no darkening of the solution was noted (maximum temperature reached was 360 °C). At that point the heat was turned off and the work-up was carried out as usual.

3.3. Results & Discussion

3.3.1. Varying Heating Rates

In an attempt to vary the rate at which the decomposition occurred, the solutions were heated at various rates. The decompositions were carried out in TOA:OA (1:1) at three different speeds: fast, intermediate, and slow. The rate was identified by the length of time it took for the solution to turn black (indicating that nanoparticles had formed). In the quickest decomposition, this change took place after 6.5 minutes, and in the slowest reaction, 26 minutes. Further detail regarding these experiments can be found in the Experimental Section (see above). As can be seen from the TEM images (Figure

3.1), the rate of the reaction did not have an impact on the particle phase; similar morphologies were obtained regardless of the rate of decomposition.

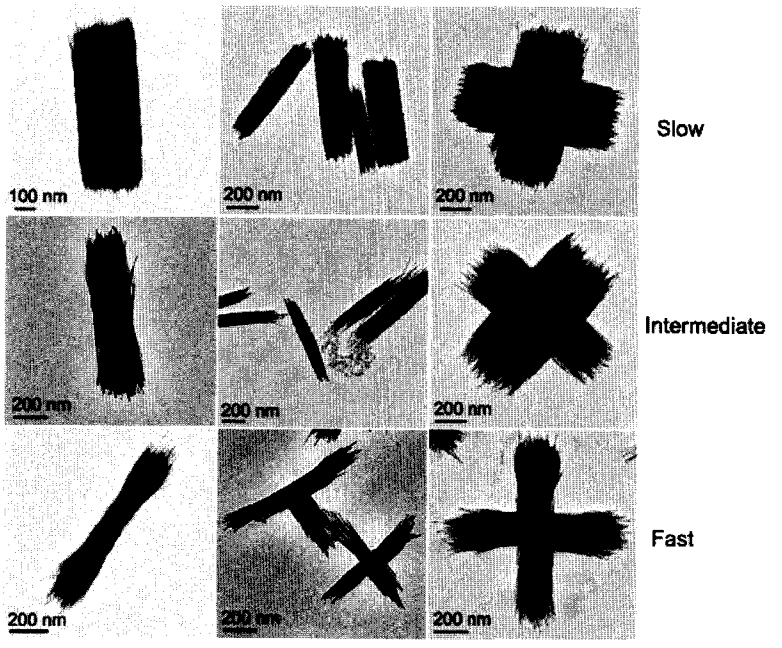

Figure 3.1. TEM images from the variation of the rate of decomposition.

In addition to the experiments in which the heating rate of the decomposition was varied, a qualitative test was performed in order to determine what effect injection of the precursor into a hot surfactant system would have. For this study, the precursor was dissolved in 2 mL of solvent (1 mL TOA and 1 mL OA) and injected into a pre-heated surfactant solution. The progression of color after the injection occurred in the same manner as the other decompositions, suggesting that the rearrangement of the precursor was still taking place. The synthesized particles are shown in Figure 3.2.

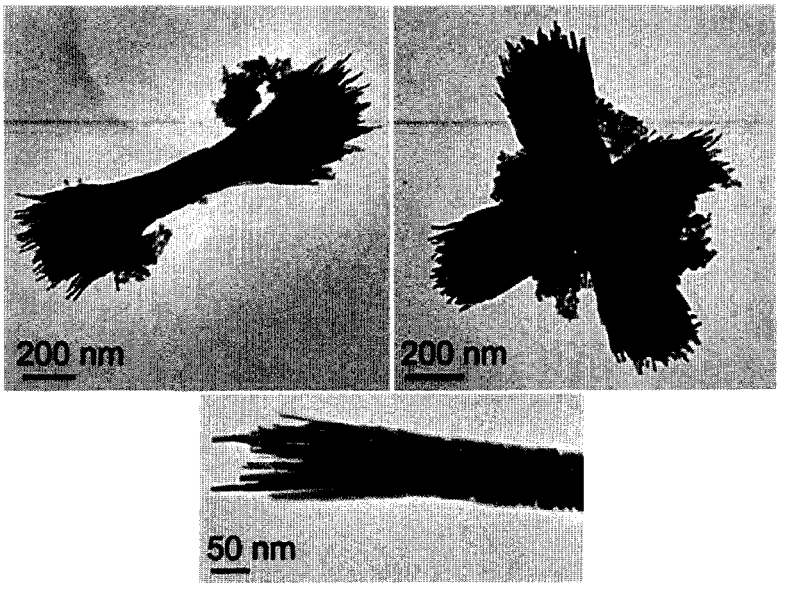

Figure 3.2. Nanoparticles resulting from the injection of $H_2Fe_3(CO)_9P^tBu$ into a hot surfactant system (TOA/OA).

There was insufficient sample to perform XRPD analysis, but EDS analysis (see Appendix II, Figure AII.1 for spectrum) of the particles gave weight percentages close to that of Fe_2P (experimental: 73.6% Fe, 26.4% P; calculated for Fe_2P: 78.3% Fe, 21.7% P). Additionally, as the morphologies of the nanoparticles formed were comparable to those of previous decompositions, it is likely that the Fe_2P phase was formed. It was evident from the results of these reactions that the rate of decomposition in this system does not circumvent the rearrangement of the starting material and, therefore, the phase or morphology of the nanoparticles remained unchanged.

3.3.2. Changing the Solvent System

In order to further investigate the decomposition of $H_2Fe_3(CO)_9P^tBu$, decompositions were performed in a variety of different solvent systems to determine whether changing the solvent allowed for the formation of Fe_3P. Various surfactants were used to determine whether changing the functional groups (as well as the boiling

points) would affect the outcome of the decomposition. Table 3.2 lists the various surfactants used.

Surfactant	Structure	Boiling Point
trioctylamine (TOA)	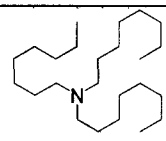	365 °C
oleic acid (OA)	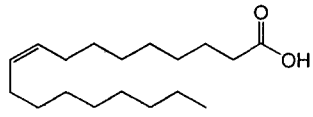	360 °C
oleyl amine (OAm)	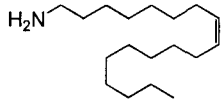	350 °C
octadecene (ODE)	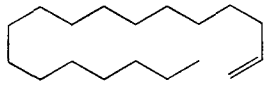	315 °C
dioctyl ether (DOE)	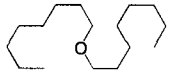	286 °C
hexadecylamine (HDA)	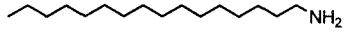	330 °C
hexadecanol (HDOH)	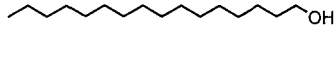	344 °C
oleyl alcohol (OOH)	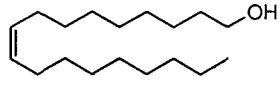	207 °C (13 mmHg)
methyl oleate (MeOA)	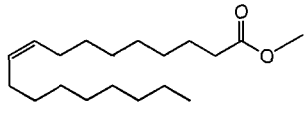	218 °C (20 mmHg)
octadecanol (ODOH)	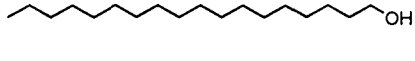	336 °C

Table 3.2. Alternate surfactants used for the decompositions.

In the case of octadecene (ODE) and OA, a similar trend to the TOA/OA system was seen. When ODE/OA were used in a 7:1 (v:v) ratio, individual nanorods were obtained (Figure 3.3A). Upon increasing the concentration of oleic acid, bundled/split rods formed (Figure 3.3B). X-ray powder diffraction confirmed the formation of the Fe_2P phase for the individual rods (Figure 3.4).

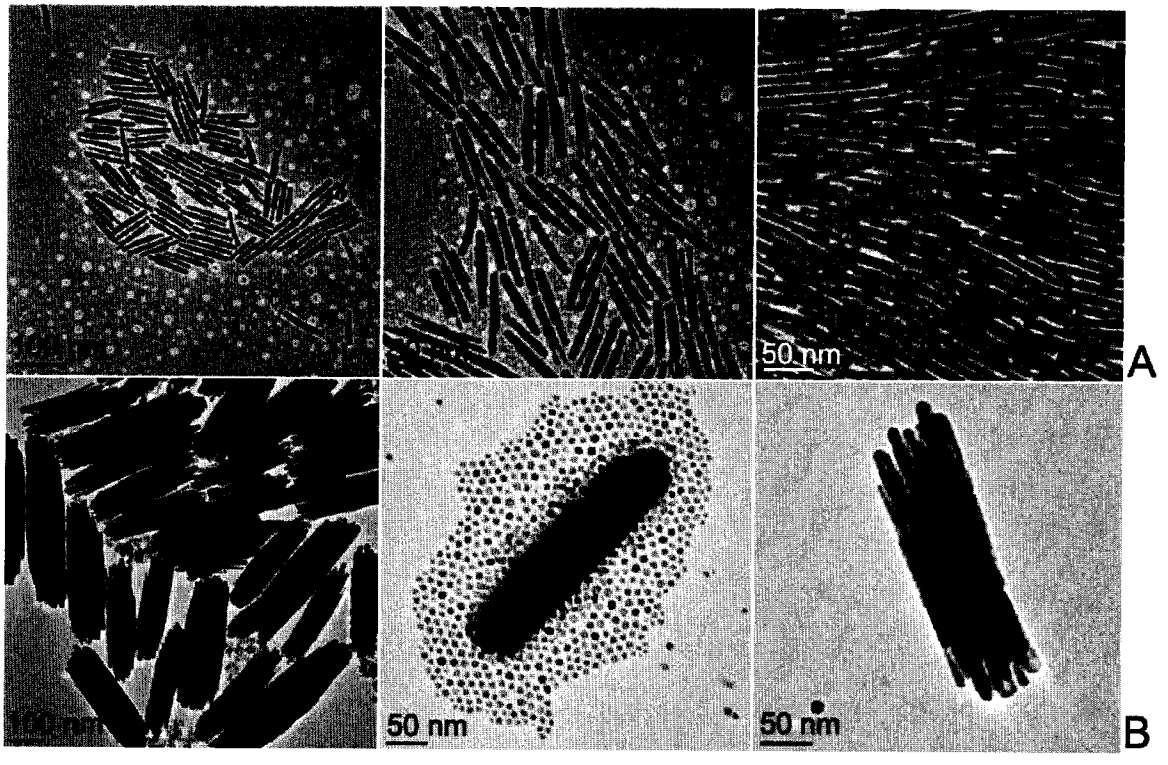

Figure 3.3. TEM images of the decompositions of $H_2Fe_3(CO)_9P^tBu$ in ODE & OA. (A) 7:1 ODE:OA. (B) 6:2 ODE:OA.

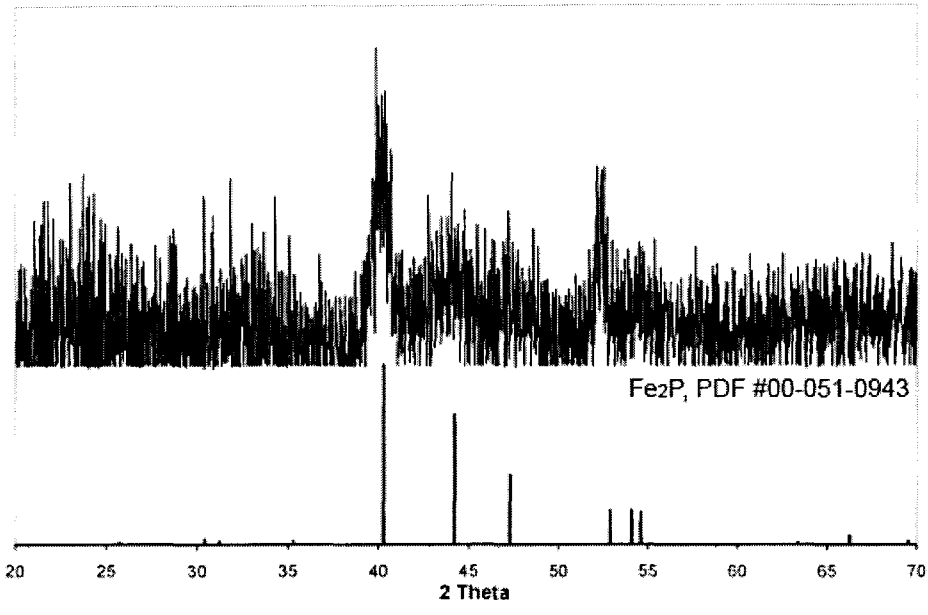

Figure 3.4. XRPD of the decomposition of $H_2Fe_3(CO)_9P^tBu$ in 7:1 ODE:OA

As can be seen in Figure 3.3B, small spherical particles were isolated in addition to the split rods. In order to determine whether the rods and small particles were the same phase, energy dispersive X-ray spectroscopy (EDS) was performed. Analysis of the split rods by EDS (Figure 3.5; additional data included in Appendix II, Figure AII.2) indicated the Fe_2P phase (weight percentages – experimental: 76.4% Fe, 23.6% P; calculated for Fe_2P: 78.3% Fe, 21.7% P).

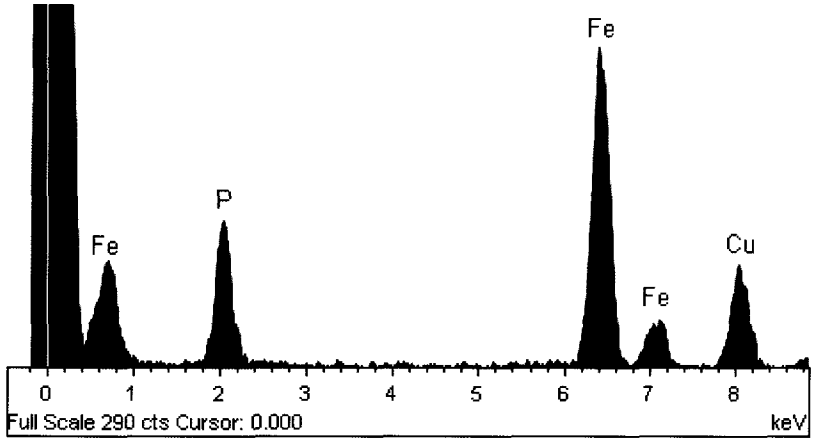

Figure 3.5. EDS spectrum of the split nanorods synthesized in ODE:OA (6:2).

The spherical particles were found to have a composition close to FeP, as detected by EDS (wt %); Fe 61.03, P 38.97 (theoretical values: Fe 64.3, P 35.7). Additional phase data was obtained using XRPD, and it indicated the presence of Fe_2P with FeP as a minor phase (Figure 3.6). Whole pattern fitting of the data gave 79% Fe_2P and 21% FeP (Appendix II, Figure AII.3).

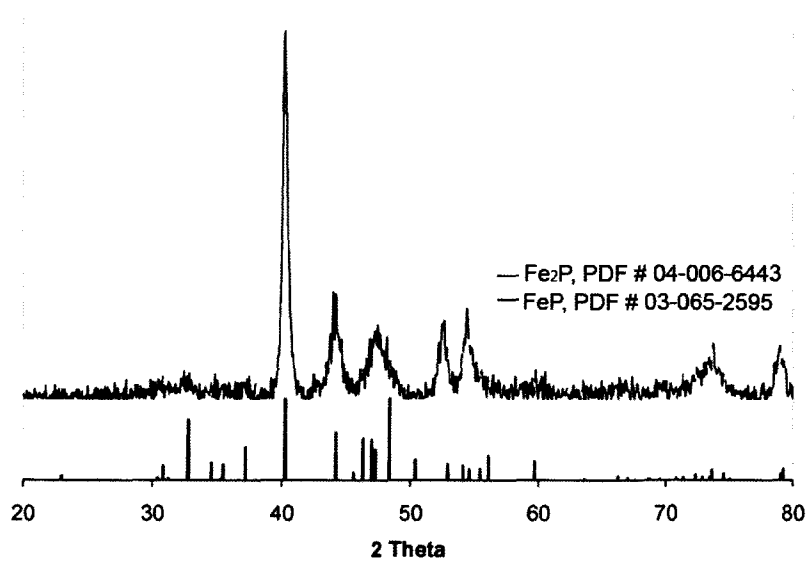

Figure 3.6. XRPD of decomposition of $H_2Fe_3(CO)_9P^tBu$ in 6:2 ODE:OA.

Exchanging ODE for dioctylether (DOE) resulted in the formation of nanorods when 10 mL of DOE was used in combination with 1 mL OA (Figure 3.7). EDS analysis of the particles indicated weight percentages close to those of Fe_2P (experimental: 77.3 Fe, 22.7 P; calculated: 78.3 Fe, 21.7 P; see Appendix II, Figure AII.4 for EDS spectrum). For comparison, a similar decomposition using 10 mL ODE and 1 mL OA was carried out; nanorods also resulted in this system (see Appendix III for TEM images).

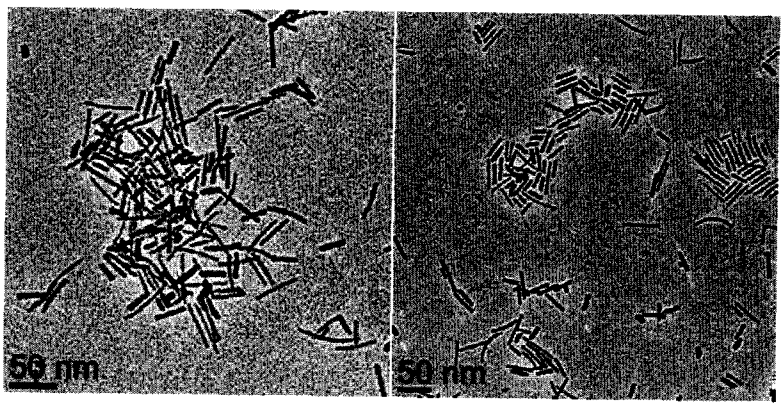

Figure 3.7. TEM images of the nanorods synthesized from the decomposition of $H_2Fe_3(CO)_9P^tBu$ in DOE:OA (10:1).

Woo *et al.* reported the synthesis of iron oxide (Fe_2O_3) nanoparticles via the injection of $Fe(CO)_5$ into a 100 °C solution of DOE and OA followed by heating to reflux.[88] A variety of other groups have reported the successful synthesis of nanoparticles from the injection of a precursor into a hot surfactant system. We were interested in seeing how the application of such a decomposition technique to the iron phosphide system would impact the morphology and phase of the nanoparticles. However, as the precursor $H_2Fe_3(CO)_9P^tBu$ is a solid, it was dissolved in ~4 mL of 1,2-dichlorobenzene (DCB, bp 180 °C) to facilitate the introduction of the precursor at elevated temperatures. DCB has been used in a similar capacity for the synthesis of $CoPt_3$ particles.[89] The injection of the precursor dissolved in DCB into a system of DOE

and OA at 180 °C resulted in smaller nanorods with a higher monodispersity (Figure 3.8A; 24 ± 5.0 × 5.3 ± 1.5 nm) as compared to those synthesized by combining the precursor, DOE, and OA at room temperature (Figure 3.7).

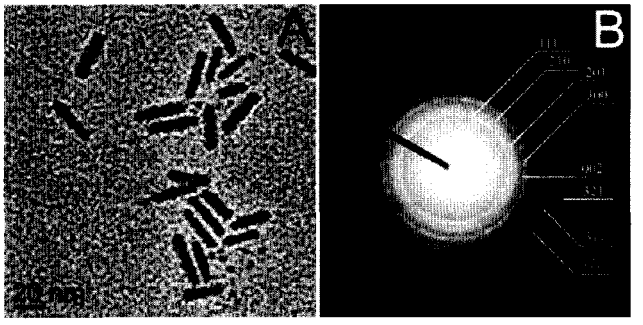

Figure 3.8. (A) TEM image and (B) Polycrystalline selected area electron diffraction pattern of the nanorods formed via the injection of $H_2Fe_3(CO)_9P^tBu$ in DCB into DOE:OA (10:1).

Inductively coupled plasma – atomic emission spectroscopy (ICP-AES) analysis of this sample indicated the formation of Fe_3P (76% Fe, 24% P). TEM EDS analysis suggested the presence of Fe_3P as well. However, a polycrystalline selected area electron diffraction pattern obtained of the rods indicated Fe_2P (Figure 3.8B). Nanoparticles of both of these phases are likely to be present but the Fe_2P particles may reveal better crystallinity compared to the particles of Fe_3P. The presence of small Fe particles could also account for this discrepancy.

Another solvent system which has produced interesting results is a mixture of oleyl amine (OAm) and OA. This system turned out to be markedly different than the TOA/OA and ODE/OA systems. Beginning with a 7:1 ratio of OAm:OA, popcorn-shaped particles formed, which appeared to be an agglomeration of smaller particles (Figure 3.9A). Increasing the amount of OA to 50% (OAm:OA 4:4) did not result in any dramatic changes in morphology (Figure 3.9B). However, when a decomposition was

performed in which the amount of OA was greater than that of OAm (OAm:OA 1:7), split nanorods were formed (Figure 3.9C). XRPD analysis of the split nanorods formed from the 1:7 OAm:OA solvent system revealed the formation of the Fe_2P phase (Figure 3.10).

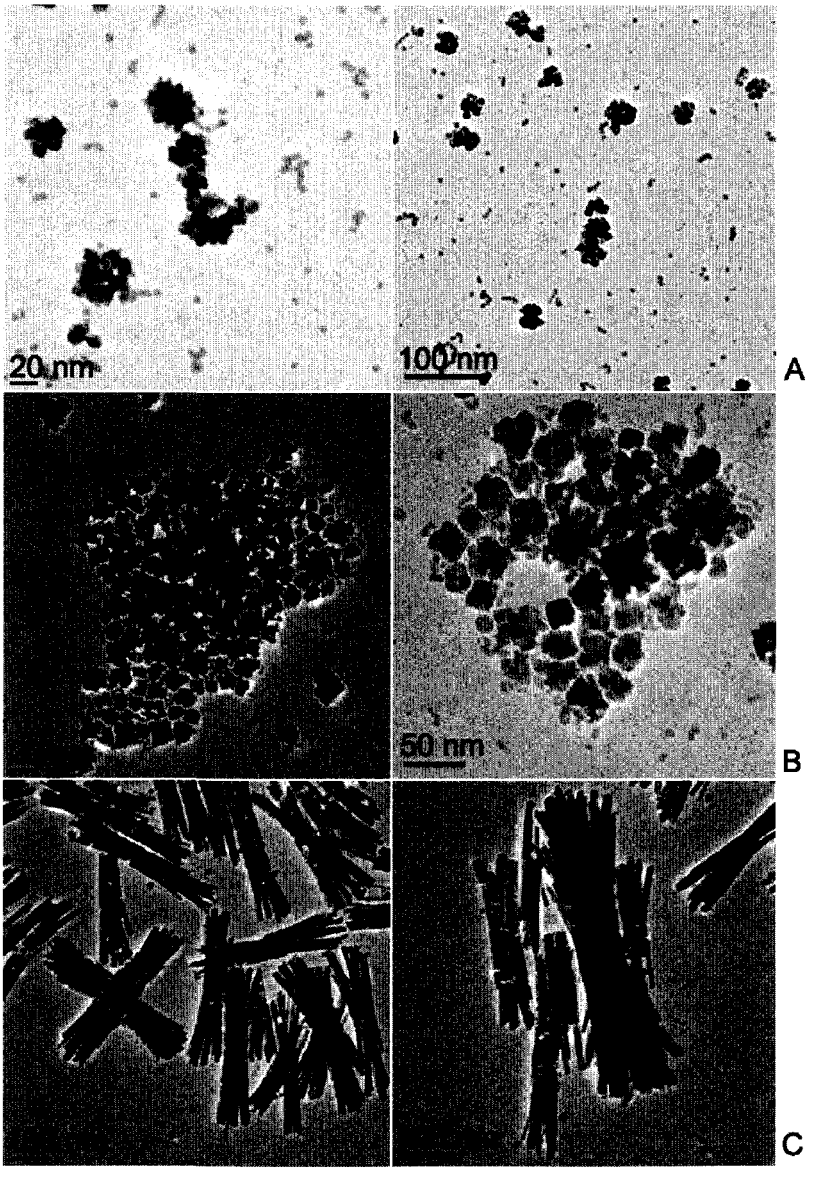

Figure 3.9. TEM images from the decomposition of $H_2Fe_3(CO)_9P^tBu$ in OAm and OA. (A) 7:1 OAm:OA. (B) 4:4 OAm: OA. (C) 1:7 OAm:OA.

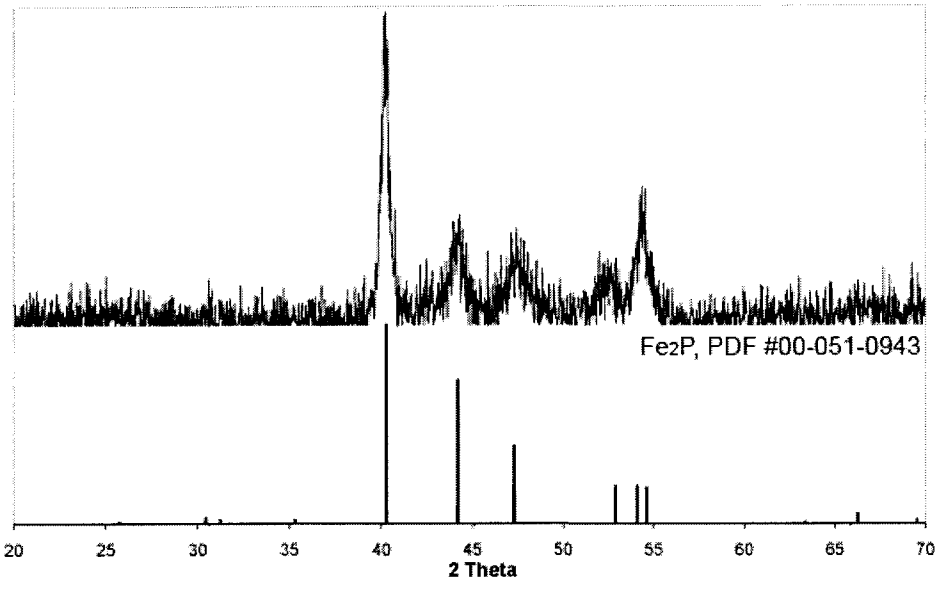

Figure 3.10. XRPD of the decomposition of $H_2Fe_3(CO)_9P^tBu$ in 1:7 OAm:OA.

XRPD analysis of the samples synthesized in the presence of an excess of OAm was inconclusive, likely due to the small size of the particles. Further analysis of the particles synthesized in the 7:1 OAm:OA system by BF TEM verified that they were crystalline; crystal planes are apparent in the BF TEM image (Figure 3.11). Analysis of the popcorn-shaped particles synthesized in OAm:OA (7:1) by EDS indicated that no phosphorus was present.

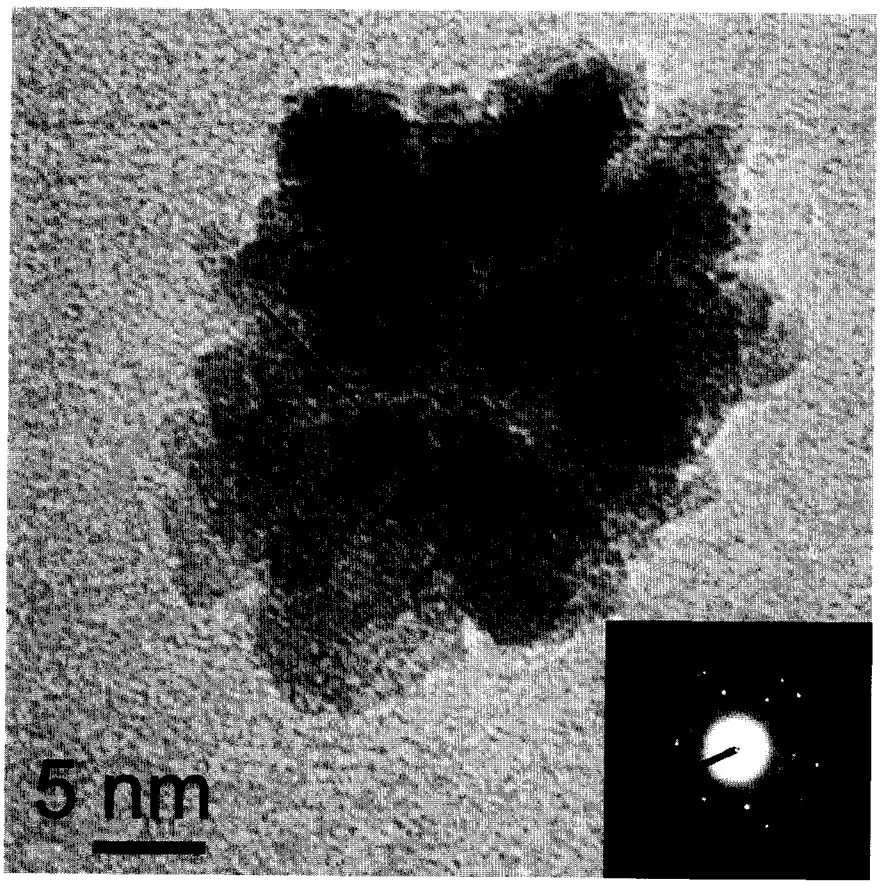

Figure 3.11. BF TEM image of a particle synthesized in 7:1 OAm:OA, with line to indicate the direction of the crystal planes. Inset: Polycrystalline diffraction pattern of the particle. Images obtained by Irene Rusakova.

Analysis of the particles synthesized with equal amounts of OAm and OA by XRPD revealed the presence of magnetite (Fe_3O_4) and $Fe_{0.942}O$ (Figure 3.12). A similar morphology has been seen for cobalt oxide (CoO) nanoflowers, for which it was observed that the primary particles had dimensions of 5×10 nm, whereas the whole nanoflower was ~71 nm in diameter.[90] The selected area electron diffraction pattern of a single nanoflower demonstrated single crystalline behavior. It is believed that the larger crystalline domains are formed by the orientational alignment and recrystallization of the smaller primary nanoparticles.

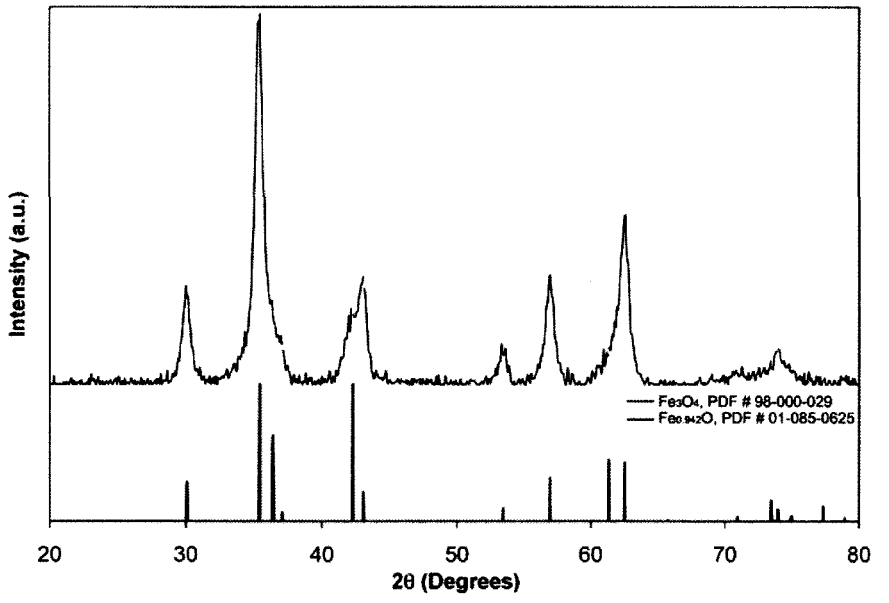

Figure 3.12. XRPD spectrum of the nanoparticles synthesized in 4:4 OAm:OA.

Interestingly, in a related system, MnP nanorods were formed when a Mn-TOP complex (formed by the combination of $Mn_2(CO)_{10}$ and TOP at 70 °C) was injected into a solution of TOPO.[63] However, when injected into a solution of DOE and OAm, spherical MnO nanoparticles formed, similar in morphology to the popcorn seen in the iron phosphide system (Figure 3.11).

The important role of oleic acid in the growth of nanoparticles has been attributed in some cases to the higher oxophilicity of some metals toward oleic acid as compared to oleyl amine. This argument has been presented in the synthesis of In_2O_3, CeO_2, Ln_2O_3, and FeCo nanoparticles.[91-93] The tendency of OA to form stronger bonds with atoms on the surface of nanoparticles is also believed to result in more chemically stable nanoparticles as opposed to those synthesized in OAm.[93] In a europium sulfide (EuS) synthesis, the anisotropic growth was attributed to the significant increase in the strength

of binding of OA to the surface of the growing nanoparticles.[94] Alkyl amines are believed to bind via non-covalent interactions, and therefore the interaction with the particle surface is not as strong as that of carboxylic acids with the same carbon-chain length. In a study of iron oxide (FeO) nanoparticles, varying the ratio of OAm and OA resulted in different shapes. In excess OAm, spherical particles formed, attributed to the fact that OAm is a weaker ligand that exhibits non-selective adsorption, giving rise to uniform growth in all directions. More faceted growth was seen in the presence of excess OA due to its more selective binding.[95] Similar results, highlighting the tendency for OA to play a more significant role in the shaping of nanoparticles, was seen for cobalt nanoparticles.[96] With increasing amounts of OAm, the aspect ratio and size of the particles decreased.

The propensity for the formation of Fe_2P nanorods when using OA as a surfactant indicates that OA binds preferentially to certain faces of the nucleated nanoparticles. Fe_2P has a hexagonal crystal structure ($P\bar{6}2m$); growth of the nanorods occurs along the *c*-axis.[56] It was discovered in a system of $CoFe_2O_4$ nanoparticles, using IR analysis, that a bridging bidentate interaction took place between the carboxylate ligand and the iron and cobalt atoms of the nanoparticle surface.[97] Keeping this binding mode in mind, it would appear that OA would bind more effectively to the (100) faces of the crystal, thereby promoting growth along the *c*-direction (Figure 3.13). In comparing the (001) and (100) faces of the structure, the Fe-Fe distances are similar (2.59 and 2.64 Å), but the Fe atoms on the (001) face form triangles while on the (100) face a zig-zag pattern is observed (Figure 3.13). We hypothesize that there is less effective binding of oleic acid to (001) faces because only 2 out of the 3 Fe atoms in the triangular arrangement can interact in

the binding of oleic acid (Figure 3.13A). On the (100) face, the binding of OA can involve all of the Fe atoms (Figure 3.13B). The role of the various solvents and how they influence the binding of OA to the nanoparticles will be used to rationalize the outcome of the decompositions of $H_2Fe_3(CO)_9P^tBu$.

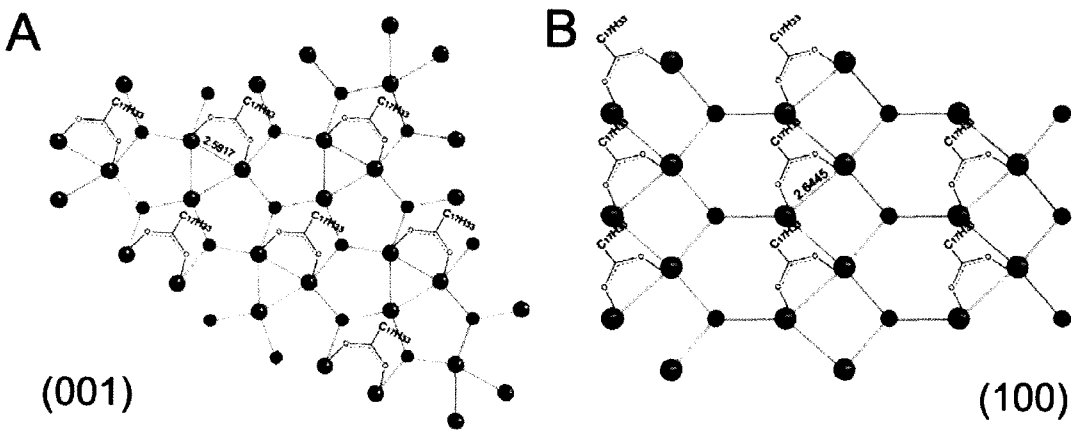

Figure 3.13. Representation of the binding of oleic acid to the (A) (001) and (B) (100) faces of the Fe_2P crystal structure.

For the synthesis of nanoparticles in a surfactant system containing 7 mL of TOA, ODE or DOE with 1 mL OA, Fe_2P nanorods formed. However, when OAm/OA (7/1) was used, a "popcorn" shape was obtained. Analysis of particles with a similar morphology synthesized in equal amounts of OAm and OA by XRPD revealed the formation of iron oxide (Figure 3.12).

The influence of the surfactants used on the formation of nanoparticles is dependent on the coordinating ability of the functional groups. ODE is commonly used as a non-coordinating solvent in nanoparticle synthesis.[98-100] DOE and TOA are also considered to be weak or non-coordinating surfactants. Therefore, for each of these solvents, nanorods were formed because the co-surfactants used did not interfere with the mechanism of OA. However, when OAm and OA were used together, the formation of

Fe_2P nanorods was disrupted. The same surfactant system was used in the synthesis of uranium dioxide nanocrystals, and it was discovered that N-(*cis*-9-octadecenyl)oleamide (OOA) formed as a result of the condensation reaction of OA and OAm.[99] IR analysis of the UO_2 nanocrystals indicated the presence of OA on the nanocrystal surface; there was no OOA present, suggesting that it does not function as a coordinating surfactant. Given this reaction between the surfactants, in the iron phosphide system, when an excess of OAm was present, all of the OA would have reacted to form the amide. Similarly, when the surfactants were present in approximately equivalent amounts (4 mL OAm:4 mL OA = 12.2 mmol OAm: 12.6 mmol OA), virtually all of the OA present would be converted to the amide. Similar morphologies were seen for both of these cases, and the formation of an iron oxide phase was confirmed for the reaction using equal amounts of surfactants. Because OA was not present to stabilize the nanoparticles when they nucleated, this likely resulted in the loss of phosphorus, and the formation of the iron oxide phase. When the amount of OA in the system was greater than that of OAm, Fe_2P nanorods were formed, supporting the argument that OA is needed for anisotropic growth of Fe_2P nanomaterials.

Changes in the relative amounts of surfactants when using TOA, ODE, or DOE did not cause any changes in morphology, i.e. nanorods formed in all cases. The similar results obtained for each of these solvents indicate that as weak- or non-coordinating solvents, they do not interfere with the role of oleic acid. A similar argument was made in the synthesis of semiconductor nanocrystals, in which ODE and TOA were believed to be non-coordinating or weakly coordinating, whereas OAm, a primary amine, could be a potential ligand for binding to metal (via nitrogen) and chalcogen (via weak hydrogen

bonding) sites.[101] These variations in reactivity were used for the selective formation of the hexagonal or cubic phase of CdSeS.

The nanorods synthesized varied in length and width depending on the surfactants used; the dimensions of each of the systems are displayed in Table 3.3. Progressing from ODE to TOA to DOE resulted in a decrease in both length and width. The most monodisperse rods resulted when the precursor was injected into a preheated solvent system of DOE and OA.

Reaction	Length (nm)	Width (nm)
294 ODE:OA (7:1)	84 ± 7.1	11 ± 1.2
340 ODE:OA (10:1)	70 ± 17	9.9 ± 1.6
276 TOA:OA (7:1)	37 ± 13	6.1 ± 1.3
341 DOE:OA (10:1)	35 ± 10	4.7 ± 1.3
358 DOE:OA (10:1)*	24 ± 5.0	5.3 ± 1.5

Table 3.3. Comparing the length and width of nanorods synthesized in different solvent systems (* precursor injected into the surfactant system in 4 mL DCB).

In contrast to the 7:1 ODE:OA system forming individual nanorods, when the ratio was increased to 6:2, split nanorods formed. The same trend was seen in the system of TOA and OA; this observation was attributed to a combination of the fast growth of the nanorods and the ability of OA to stabilize the surface of the Fe_2P nanorods.[56] The splitting of nanorods was favored in the systems where OA was present in higher concentrations because the additional OA was able to stabilize the surface of the rods as they split.

3.3.2.1. Varying Functional Groups

We were interested in studying other surfactants having similar functional groups and determining how the morphology of the resulting nanoparticles varied. A series of surfactants were studied, in which the chain lengths and presence of unsaturated bonds were varied (Table 3.4). Oleic acid was used as the co-surfactant in each of the decompositions.

	Surfactant	C-Chain Length	Functional Group	pK_a * (at T=25 °C)
	OA	C_{18}	-COOH C=C bond	4.78 ± 0.10
Amines	TOA	C_8 (x3)	3° amine	10.08 ± 0.50
	OAm	C_{18}	1° amine C=C bond	10.66 ± 0.10
	HDA	C_{16}	1° amine	10.67 ± 0.10
Alcohols	HDOH	C_{16}	1° alcohol	15.19 ± 0.10
	OOH	C_{18}	1° alcohol C=C bond	15.19 ± 0.10
	ODOH	C_{18}	1° alcohol	15.19 ± 0.10

Table 3.4. Properties of the alternate surfactants (* pK_a values found in SciFinder).

The results of the decomposition of $H_2Fe_3(CO)_9P^tBu$ in TOA/OA and OAm/OA have already been presented. Based on the finding that using TOA in combination with OA (in a 7 to 1 ratio, by volume) resulted in Fe_2P nanorods whereas using OAm instead of TOA resulted in popcorn-shaped iron oxide nanoparticles, closer examination of the physical properties and how slight changes in surfactants affect the nanoparticle morphology was investigated. In comparing TOA and OAm, TOA is a tertiary amine

whereas OAm is a primary amine, resulting in a slight difference in pK_a values. Another difference is the presence of a C-C double bond in OAm.

In order to determine whether the double bond was influencing the nanoparticle formation, hexadecylamine (HDA) was used. Given that the pK_a values for OAm and HDA are similar (Table 3.4), one could determine whether the double bond or the slightly longer chain length influenced the resulting morphology. Neither popcorn-shaped particles nor nanorods formed (as seen for the 7/1 TOA system), but small amorphous looking particles were isolated instead (Figure 3.14A). This suggested that both the alkene and carbon chain length influenced the formation of the nanoparticles. Keeping the carbon chain length the same, the solvent was changed from an amine (HDA) to an alcohol, hexadecanol (HDOH). With this change came an increase in the pK_a (Table 3.4). The particles were small and appeared to have a more defined structure than those isolated from the HDA/OA system (Figure 3.14B).

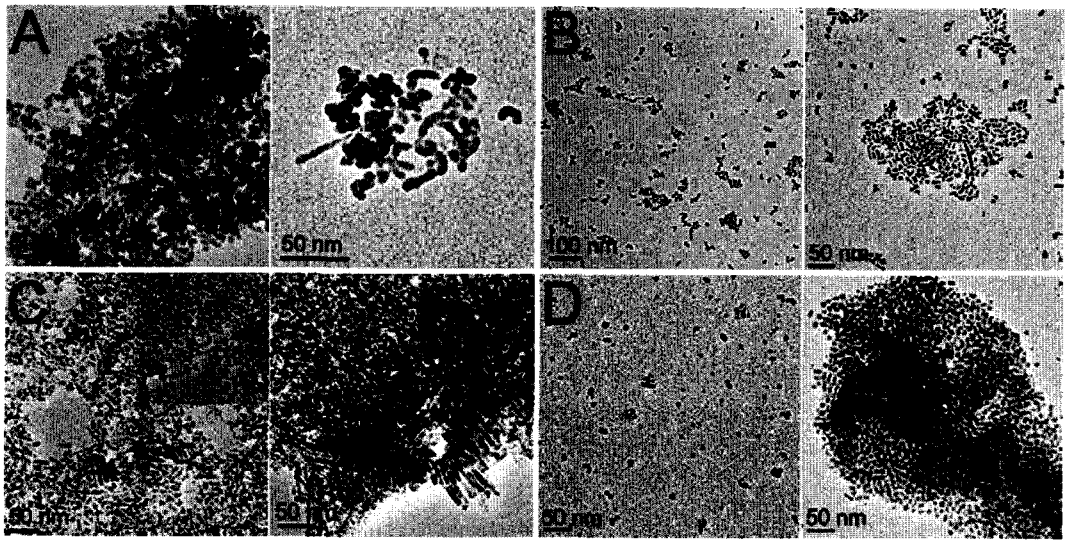

Figure 3.14. TEM images of the various nanoparticles synthesized in (A) 5.7 g HDA (similar pKa to OAm) & 1 mL OA, (B) 7 mL HDOH and 1 mL OA, (C) 7 mL OOH and 1 mL OA, (D) 7 mL ODOH and 1 mL OA.

Performing a similar progression, although retaining the C_{18} chain length as compared to OAm, oleyl alcohol (OOH) and octadecanol (ODOH) were used. Transition from the primary amine to the alcohol did not result in any drastic changes in morphology. In the OOH/OA system, decomposition of the precursor resulted in a mixture of small particles and nanorods, though the small particles comprised the majority of the isolated nanoparticles (Figure 3.14C). ODOH in combination with OA produced very small spherical particles (Figure 3.14D).

EDS measurements indicated that both iron and phosphorus were present in the nanoparticles synthesized in HDA, HDOH, and ODOH. No phosphorus peak was visible for the particles synthesized in OOH. Attempts to obtain quantitative analysis from the EDS data were inconsistent, and in some of the samples, a Si peak was present which presented interference for the peak area measurements (see Appendix II Figures Figure AII.5 - Figure AII.8 for EDS spectra). ICP analysis was performed on the nanoparticles isolated from the decompositions in HDA/OA and HDOH/OA, giving atomic percentages (Fe,P) of (82, 18) and (96, 4), suggesting that neither Fe_2P nor Fe_3P were formed. XPS spectra were also collected for each of the samples to obtain information about the composition of the nanoparticles.

The XPS data presented in Table 3.5 suggests that there is a significant amount of Fe^{2+} and Fe^{3+} present in the samples analyzed.[102] Reported XPS data for metal phosphides have shown both the metal and the phosphorus to have binding energies close to that of the neutral species.[103] The P 2p binding energy for elemental phosphorus is 129.9 eV and the Fe $2p_{3/2}$ binding energy for elemental iron is 707.0 eV; if the nanoparticles analyzed are in fact iron phosphide, binding energy peaks would be

expected to fall close to these values.[102] All of the nanoparticles had a peak at this position, but it was not the major peak. For the P $2p_{3/2}$ region, there was a peak present at ~129.6 eV, but the major peak was observed at ~133 eV, the value indicative of P^{5+}.[102] The XPS spectra for each of the samples can be found in Appendix II, Figures Figure AII.9 to Figure AII.12. Binding energy values obtained using XPS can serve to determine whether an iron phosphide is present, but the differences in energies for the various iron phosphides are too close to allow for conclusive phase determination (Fe $2p_{3/2}$ = 706.9, 706.8, and 706.9 eV and P 2p = 129.34, 129.31, and 129.43 eV for FeP, Fe_2P, and Fe_3P, respectively).[103]

		HDA/OA	HDOH/OA	OOH/OA	ODOH/OA
Fe $2p_{3/2}$	Fe^0	706.86 (3.3)	707.04 (5.0)	707.31 (3.3)	707.05 (5.2)
	Fe^{2+}	710.24 (74.0)	710.45 (74.9)	710.79 (88.8)	710.67 (69.3)
	Fe^{3+}	712.66 (22.7)	712.77 (20.1)	713.59 (7.9)	712.77 (25.5)
P 2p	P^0	129.62 (18.5)	129.64 (18.4)	129.42 (6.5)	129.70 (8.6)
	P^{5+}	133.27 (81.5)	133.25 (81.6)	132.74 (93.5)	132.80 (91.4)
C 1s	C-C		284.44 (60.5)		
	C-C		285.03 (36.4)		
	COO^-		288.12 (3.1)		

Table 3.5. Binding energies (eV) of the nanoparticles synthesized in 7 mL HDA, HDOH, OOH, or ODOH with 1 mL OA determined using XPS. The percent area of each peak is indicated in parentheses.

In a study of cobalt nanoparticles (~15 nm) synthesized with OA as the surfactant, an XPS study of the C 1s, O 1s, and Co 2p peaks was used to determine the interaction of the surfactant with the nanoparticles.[104] The C 1s region exhibited two peaks, 284.8 and 288.2 eV, corresponding to an aliphatic carbon chain (-C-C-) and a carboxylate ($-COO^-$), respectively. There was no peak corresponding to free carboxylic acid, indicating that all of the OA present was bound to the surface of the particles. For the Co 2p region of the

spectrum, there were two sets of peaks, corresponding to the Co-O bond in the carboxylate and the metallic Co atoms underneath the chemisorbed carboxylate.

Comparing the data presented by Wu *et al.* to that of the nanoparticles synthesized in HDOH/OA, there are similarities in the C 1s peak positions, indicating the same C-C and COO^- functionalities. The metal peaks are similar in that both metal-oxygen and metallic binding energies are present, however, in the case of the iron phosphide nanoparticles, the peak corresponding to Fe-O is the major peak. This difference could be attributed to the size of the nanoparticles. The Co particles are on the order of 15 nm, whereas the iron phosphide particles are smaller (~5-10 nm). As nanoparticles get smaller, the surface area increases, so one would expect to see a change in the relative ratio of the metal versus the metal-oxide binding energy peaks because there will be more surfactant-coated nanoparticle as opposed to the metal atoms at the core of the nanoparticle (the metal oxide peak will become more predominant as the size of the nanoparticles decrease).

In order to verify this theory, XPS data was collected for the Fe_2P nanoparticles synthesized in 1:7 OAm/OA (Figure 3.9C, ~375 × 57 nm; see Appendix II Figure AII.13 for XPS spectra). The binding energies for these split nanorods are indicated in Table 3.6 along with those for the nanoparticles synthesized in HDOH/OA.

Peak	OAm/OA	HDOH/OA
Fe $2p_{3/2}$	**706.64 (22.7)** **707.71 (2.5)** 710.53 (74.8)	**707.04 (5.0)** 710.45 (74.9) 712.77 (20.1)
P 2p	**128.73 (9.7)** **129.45 (41.3)** 132.96 (49.0)	**129.64 (18.4)** 133.25 (81.6)

Table 3.6. Binding energies (eV) for nanoparticles synthesized in OAm/OA (7/1) vs. HDOH/OA (7/1) determined using XPS. Bolded values indicate the peak positions corresponding to oxidation states indicative of iron phosphide. Value in parentheses indicates the % area.

There is an increase in the % area for the Fe $2p_{3/2}$ peaks corresponding to Fe^0, from 5% for the nanoparticles synthesized in HDOH/OA to 25.2% for the split nanorods synthesized in OAm/OA. Similarly, for the P 2p peak, there is an increase in the % area from 18.4% to 51.0% when going from the HDOH/OA to the OAm/OA system. This increase supports the proposed idea that as the particles get smaller and, correspondingly, the amount of surfactant per surface area of the particle increases, the size of the peak corresponding to the Fe-O (Fe^{III}) or P-O (P^V) increases.

Further investigation will need to be carried out in order to gain a better understanding of how changes in the solvent impact morphology. It is known in this system that varying the ratios of surfactants can have a substantial influence on the shapes obtained, though the precise reasoning behind these changes has not been determined conclusively. A more in depth study into whether the changes seen in the series of solvents discussed here impact the nanoparticles isolated could offer further insight into such questions as whether the presence or absence of an alkene or using an amine instead of an alcohol changes what is produced.

3.3.2.2. Changing the ratio of precursor to surfactant.

Another parameter studied was the ratio of the precursor to the surfactant. Andelman *et al.* reported the synthesis of zinc oxide nanostructures from zinc acetate decomposed in TOA, HDOH, or ODE using OA as the capping agent (1:1 ratio of precursor:capping agent).[105] Depending on the solvent used, nanorods (TOA), nanotriangles (HDOH), or spherical nanoparticles (ODE) resulted. The reasoning behind the formation of different shapes was the different coordination abilities of the solvents. TOA was stated as being a relatively strong coordinating solvent that can function as a ligand, ODE is believed to be a non-coordinating solvent, and HDOH is a moderately coordinating solvent that can function as a relatively weak ligand.

An examination of how varying the solvent while keeping the ratio of the precursor to the surfactant (or capping agent) equal affected the morphology of the nanoparticles was carried out in the iron phosphide system. A series of decompositions of 0.50 mmol $H_2Fe_3(CO)_9P^tBu$ were carried out in 7 mL TOA, HDOH, or ODE with 0.50 mmol OA. Interestingly, when HDOH was used as the solvent, rectangular particles were formed with dimensions on the order of 12×8 nm (Figure 3.15). XRPD analysis of the sample indicated that the Fe_2P phase had been formed (Figure 3.16).

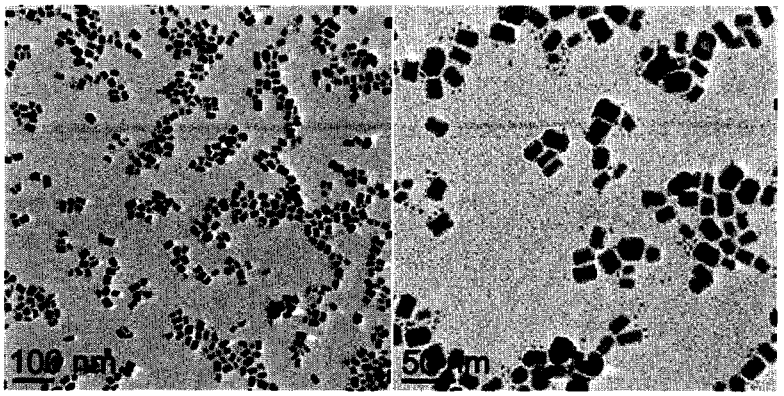

Figure 3.15. TEM images of the nanoparticles formed from the decomposition of $H_2Fe_3(CO)_9P^tBu$ in HDOH and OA (7:0.15 v:v).

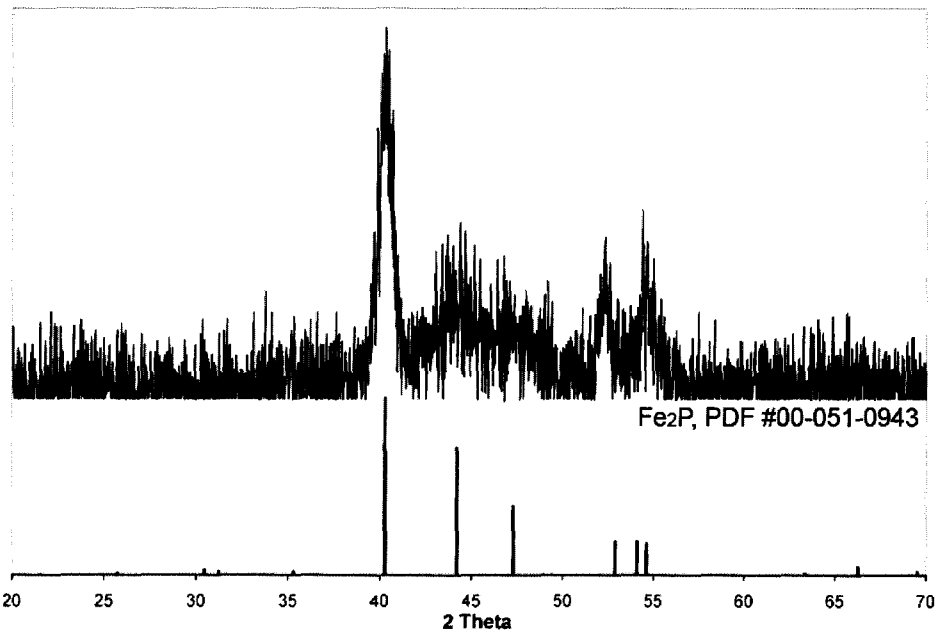

Figure 3.16. XRPD of the decomposition of $H_2Fe_3(CO)_9P^tBu$ in 7:0.15 HDOH:OA.

The reactions using TOA or ODE as the solvent both gave small particles (Figure 3.17). It is evident for these surfactant systems that a higher concentration of oleic acid is necessary for the formation of shaped nanoparticles, as nanorods were observed for both when a 7:1 ratio (TOA or ODE:OA) was used.

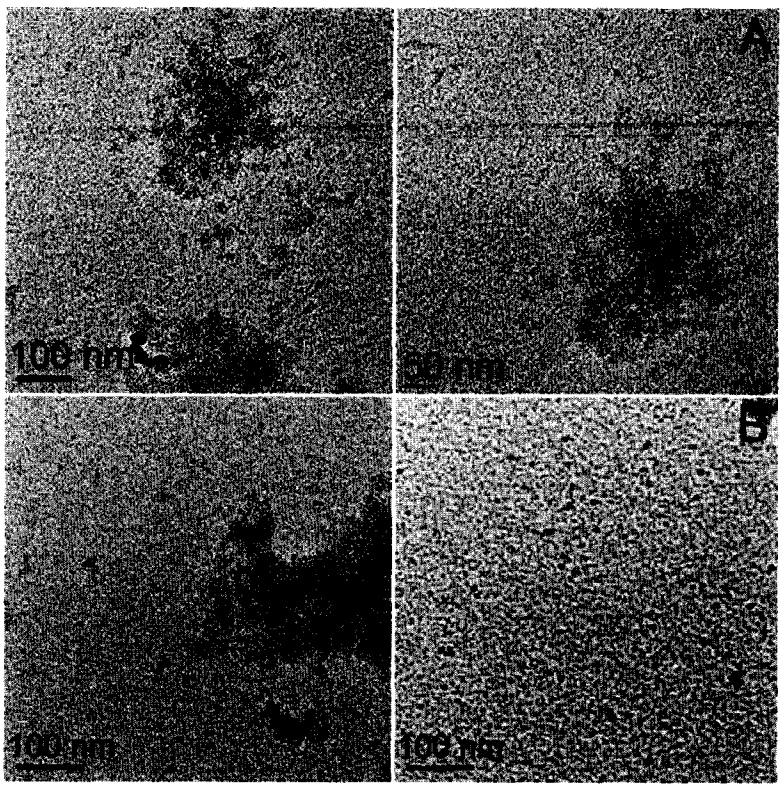

Figure 3.17. TEM images of the decomposition of $H_2Fe_3(CO)_9P^tBu$ in (A) TOA:OA and (B) ODE:OA (7:0.15 v:v).

3.3.2.3. Varying the Trialkylamine

Changes in morphology were seen in a system using oleic acid as the surfactant when changing the co-solvent from trioctylamine to long chain primary amines or alcohols. TOA contains 24 C atoms ($3xC_8$ chains), whereas the other solvents used contained a single chain of either 16 or 18 C atoms. The configuration of the hydrophobic tails of these solvents presumably impacts the formation of nanoparticles.

In a system of ZnO (space group $P6_3mc$) nanorods, synthesized using zinc acetate dihydrate as the precursor, oleic acid as the surfactant, and a trialkylamine as the solvent (trihexyl-, trioctyl-, or tridodecylamine), the chain length was reported to impact the dimensions of the nanorods.[106] The diameter of the nanorods when using trihexylamine

or TOA was 203 nm, whereas with tridodecylamine (TDDA), rods with diameters in the range of 50-80 nm were synthesized. It was suggested that the tertiary amine functioned as a strong coordinating solvent that, in addition to oleic acid, acts as a ligand to stabilize and quench growth in the radial direction. Due to increased steric hindrance and bulkiness of the carbon chains on going from C_6 or C_8 to C_{12}, the ability of the amine to quench the radial growth decreased.

Variation of the trialkylamine from TOA to TDDA was studied for the decomposition of $H_2Fe_3(CO)_9P^tBu$ to investigate what impact the change in bulkiness of the solvent would have on the resulting nanoparticle morphology. Experiments were conducted using 0.24 mmol or 0.49 mmol of the precursor in a solution of 7 mL trialkylamine and 1 mL OA (Figure 3.18 & Figure 3.19Figures 36 & 37). EDS analysis performed on the nanoparticles synthesized in TDDA/OA (shown in Figure 3.18B) indicated weight percentages close to that of Fe_2P (experimental: 79.8 Fe, 20.2 P; calculated: 78.3 Fe, 21.7 P).

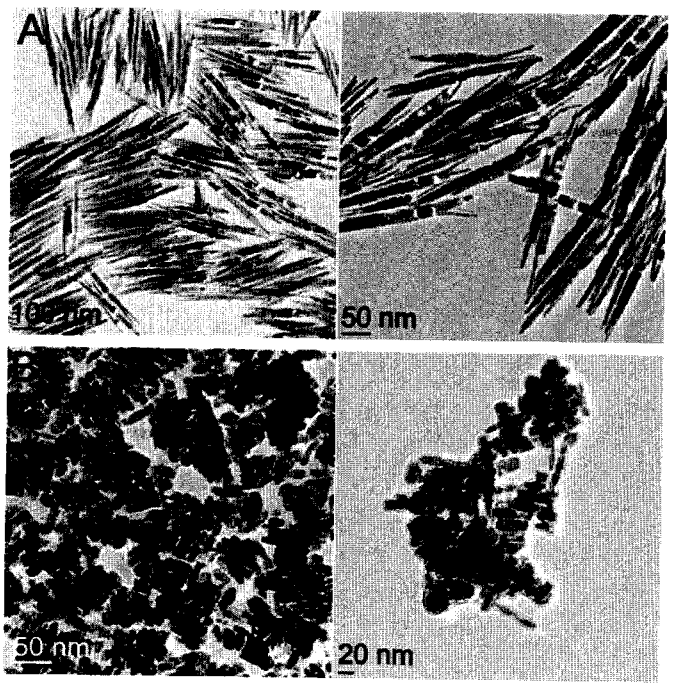

Figure 3.18. TEM images of the nanoparticles synthesized via the decomposition of 0.24 mmol $H_2Fe_3(CO)_9P^tBu$ in (A) TOA/OA and (B) TDDA/OA, both with 7/1 volumetric ratios of trialkylamine to OA.

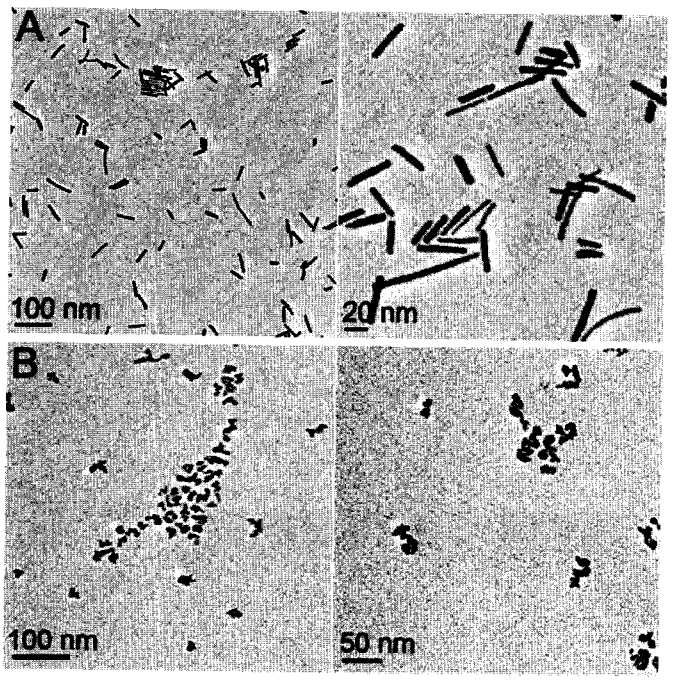

Figure 3.19. TEM images of the nanoparticles synthesized via the decomposition of 0.49 mmol $H_2Fe_3(CO)_9P^tBu$ in (A) TOA/OA and (B) TDDA/OA, both with 7/1 volumetric ratios of trialkylamine to OA.

The change in trialkylamine in the iron phosphide system had a dramatic effect on the resulting nanoparticle morphology, although not with the same trend seen by Andelman *et al.* Changing from trioctylamine (C8) to tridodecylamine (C12) resulted in a transition from nanorods to small clustered particles. We would not expect, as was stated by Andelman *et al.*, for tertiary amines to function as strong coordinating ligands due to their bulkiness. The change in morphology seen in the iron phosphide system is likely a result of the increased bulk present in the co-surfactant, which would interfere with the ability of oleic acid to stabilize the nucleating nanoparticles, preventing the growth of nanorods.

In addition to the change in chain length causing steric hindrance in the system, such alterations can also result in changes in the decomposition temperature of the precursor. This has been reported for a couple of systems, one of which was the synthesis of iron oxide (Fe_2O_3) nanocrystals.[84] Iron pentacarbonyl was used as the precursor, and it was found that for a solution of TOA in combination with either oleic acid (C18), lauric acid (C12), or octanoic acid (C8), the decomposition temperature increased as the chain length of the surfactant increased. This observation was attributed to the higher dipole moments present in the shorter carboxylic acid surfactants, which resulted in an increase in the surfactant's effectiveness to "catalyze" the decomposition.

The concentration of the precursor cluster also had an effect on the size of the nanoparticles. In a system of FePt nanoparticles synthesized in OAm and OA, the effect of changes in the molar ratio of the surfactant to the precursor was studied.[107,108] As the surfactant concentration increased, the nanoparticles increased in size. This is believed to be a result of the change in the number of nuclei formed during the initial stages of

particle formation. When more surfactant is present, stable complexes of the individual metal atoms of the precursor are formed in solution. Therefore, the nucleation process is suppressed, resulting in the formation of larger particles. A similar trend was seen in the iron phosphide system; when $H_2Fe_3(CO)_9P^tBu$ was decomposed in TDDA/OA (7/1 v/v), the decomposition with 0.24 mmol precursor resulted in larger particles than when 0.49 mmol precursor was used.

3.3.3. Changing the Precursor

Another parameter that was varied is the R-group on the $H_2Fe_3(CO)_9PR$ precursor. A majority of the reactions were performed where R = *t*-Bu. The other R-group examined was Ph. In this decomposition, a 1:1 TOA:OA solvent system was used. TEM images of the product can be seen in Figure 3.20.

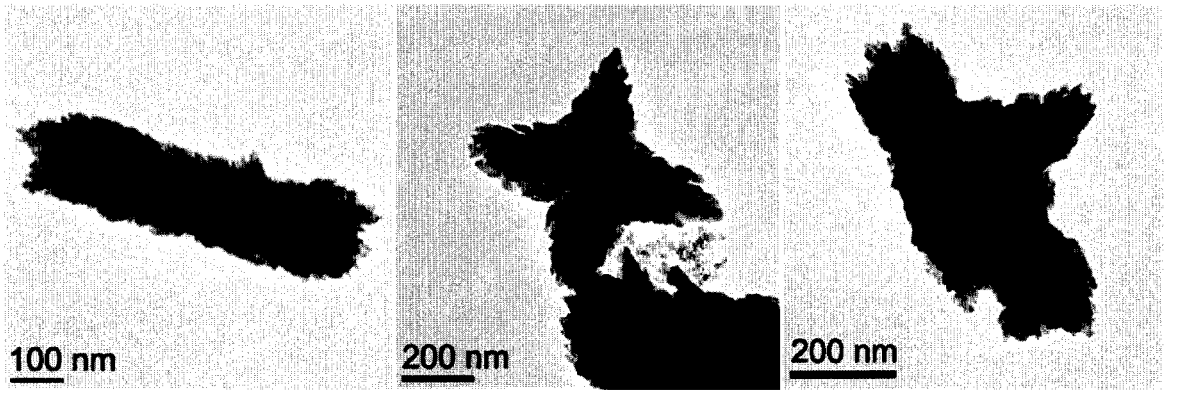

Figure 3.20. TEM images of the decomposition of $H_2Fe_3(CO)_9PPh$ in 1:1 TOA:OA.

It is apparent from the TEM images that the decomposition does not proceed as cleanly in this system, most likely resulting from the decomposition pathway. It is believed that the cluster having a *t*-Bu group will likely decompose via the release of isobutylene, which is a better leaving group (Scheme 3.1). The phenyl derivative does

not possess as clean an elimination pathway for the side products generated during decomposition. Further studies into the decomposition of the cluster, presented in Chapter 4, revealed that the elimination of isobutylene does in fact occur when $H_2Fe_3(CO)_9P^tBu$ is decomposed without the presence of a solvent.

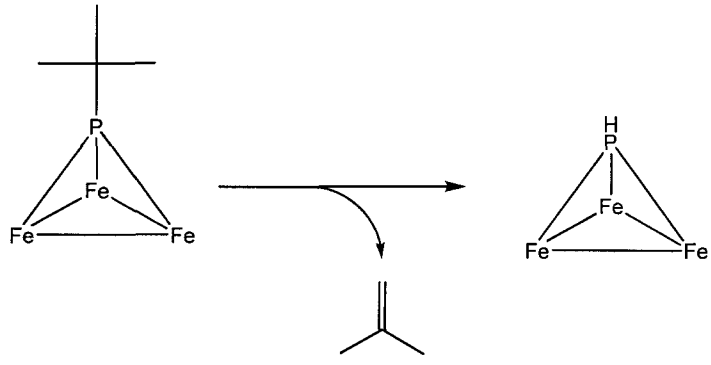

Scheme 3.1. Proposed decomposition pathway for $H_2Fe_3(CO)_9P^tBu$.

The decomposition of other iron- and phosphorus- containing carbonyl clusters, $Fe_3(CO)_{10}P^tBu$, $Fe_3(CO)_9(P^tBu)_2$, $Fe_4(CO)_{12}(P^tBu)_2$, and $Fe_2(CO)_6(PH^tBu)_2$, has also been investigated. Three of these clusters were synthesized using the same reaction, shown in Scheme 3.2. The decompositions were performed in a 1:1 TOA:OA surfactant system, all resulting in similar morphologies. For most of the decompositions, there was insufficient material for conclusive XRPD data to be obtained.

$$Na_2Fe(CO)_4 \cdot {}^3/_2 \text{ dioxane} + Fe(CO)_5 \xrightarrow{THF} Na_2Fe_2(CO)_8 + CO$$

$$Na_2Fe_2(CO)_8 + {}^tBuPCl_2 \xrightarrow{THF} Fe(CO)_4P^tBuCl_2 + Fe_3(CO)_9(P^tBu)_2 + Fe_3(CO)_{10}P^tBu$$

Scheme 3.2. Synthesis of alternate iron phosphorus compounds.

When $Fe_2(CO)_6(PH^tBu)_2$ was decomposed, the particles in Figure 3.21 were isolated. No elemental analysis was performed on these nanostructures, though the morphology suggested that the phase was Fe_2P.

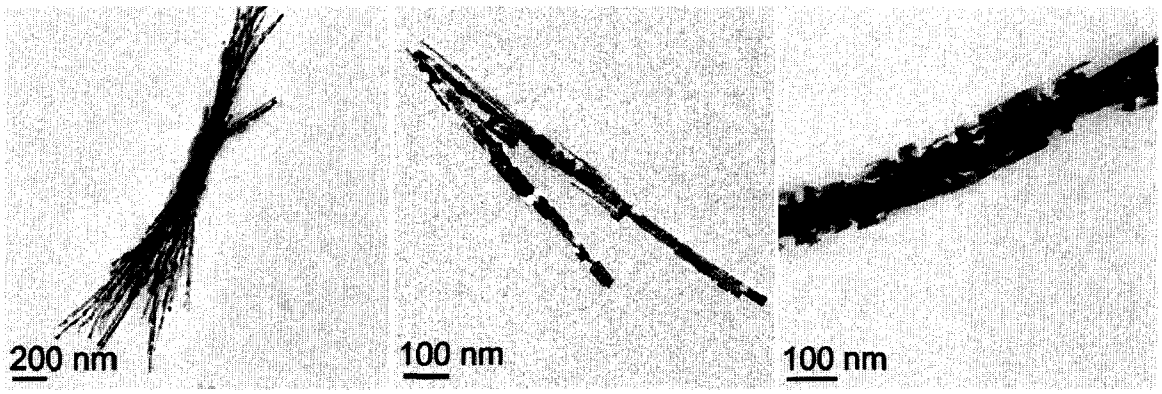

Figure 3.21. TEM images of the decomposition of $Fe_2(CO)_6(PH^tBu)_2$ in 2 mL TOA & 2 mL OA.

The decomposition of $Fe_3(CO)_{10}P^tBu$ resulted in nanoparticles having split rod and cross-shaped morphologies like those seen when $H_2Fe_3(CO)_9P^tBu$ was decomposed in the same solvent system (Figure 3.22).

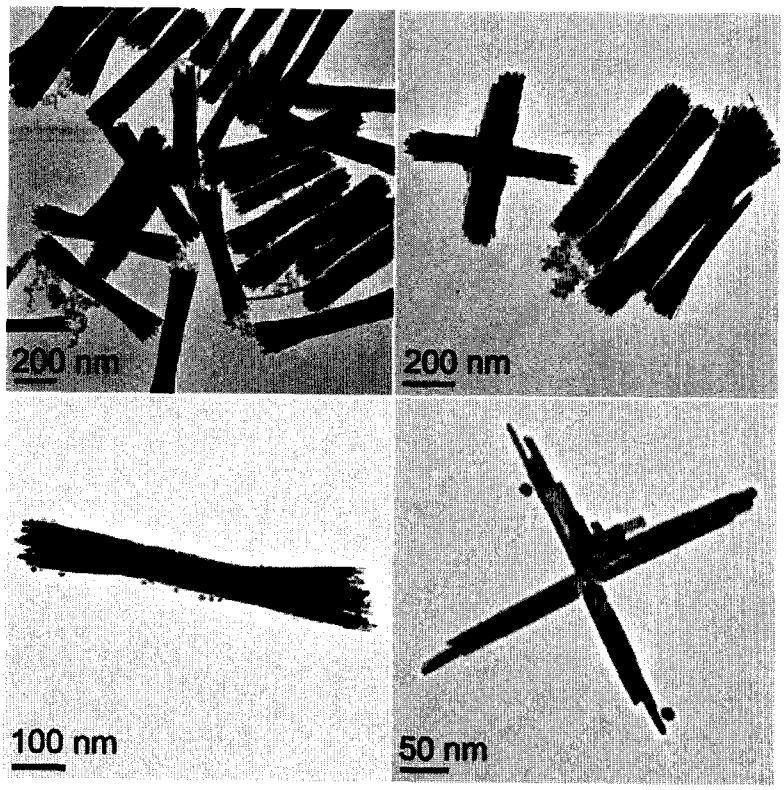

Figure 3.22. TEM images of the decomposition of $Fe_3(CO)_{10}P^tBu$ in 4 mL TOA & 4 mL OA.

EDS analysis of these particles gave a composition of 78.6 wt% Fe and 21.4 wt% P, close to the theoretical values for Fe_2P (78.3% Fe, 21.7% P; for a representative data set, see Appendix II Figure AII.14).

Decomposition of the $Fe_3(CO)_9(P^tBu)_2$ cluster resulted in the split rods and crosses seen in Figure 3.23. Confirmation of the formation of the Fe_2P phase was achieved via XRPD (Figure 3.24).

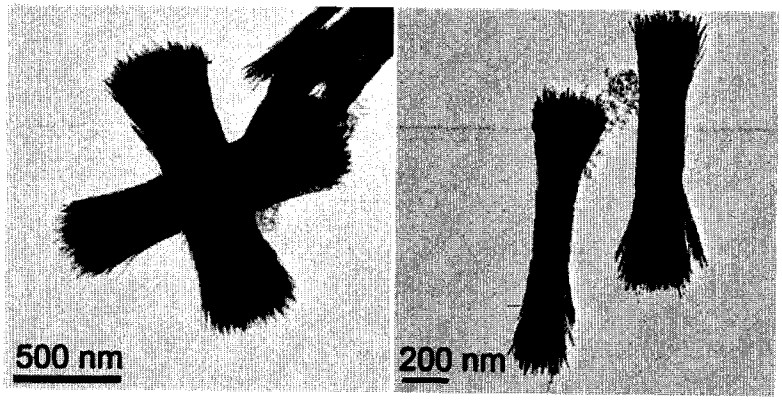

Figure 3.23. TEM images of the decomposition of $Fe_3(CO)_9(P^tBu)_2$ in 4 mL TOA & 4 mL OA.

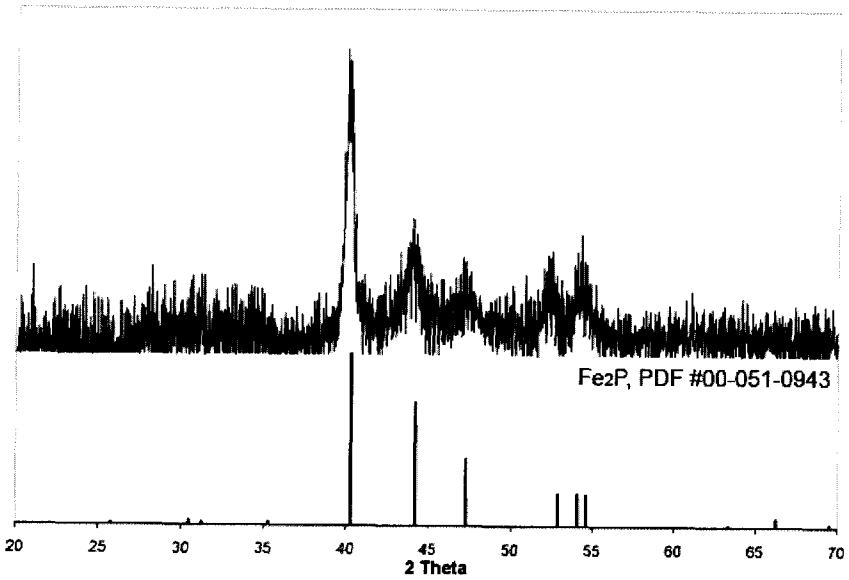

Figure 3.24. XRPD of the decomposition of $Fe_3(CO)_9(P^tBu)_2$ in TOA & OA.

When $Fe_4(CO)_{12}(P^tBu)_2$ was decomposed, rods or split rods were obtained (Figure 3.25), and determined to be the Fe_2P phase using EDS, giving weight percent values for Fe and P of 76.8% Fe and 23.2% P, which are close to the calculated values for Fe_2P (see Appendix II Figure AII.15 for a representative EDS spectrum).

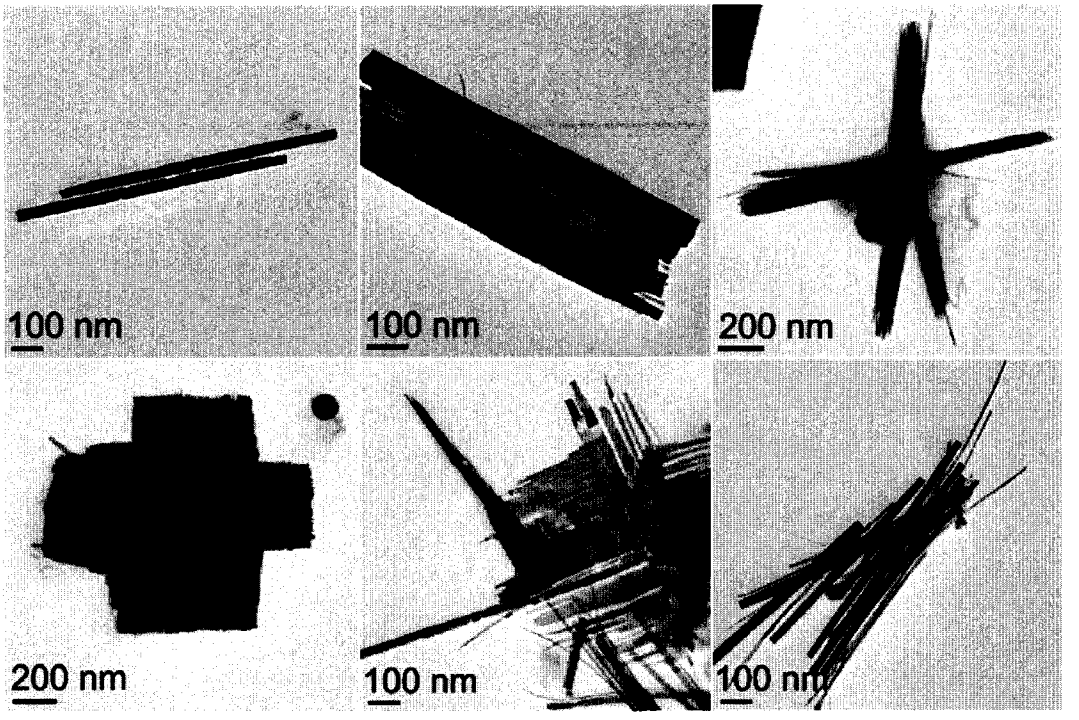

Figure 3.25. TEM images of the decomposition of $Fe_4(CO)_{12}(P^tBu)_2$ in 2 mL TOA & 2 mL OA.

Altering the cluster used as the precursor for decomposition in a solvent system of TOA and OA did not have any effect on the phase of nanoparticles obtained. It was observed that each of the decompositions proceeded with a similar progression in colors, so it is likely that there are rearrangements of the clusters taking place during the decomposition process, and the cluster present in solution just prior to the precipitation of nanoparticles is the same for each reaction, regardless of the starting cluster. Further analysis of the cluster rearrangements and how the solvent interacts with the cluster to induce these changes will be presented in Chapter 4.

3.4. Conclusions

A variety of approaches toward the isolation of different morphologies of Fe_2P nanomaterials, as well as to produce the Fe_3P phase instead of Fe_2P, were attempted. Altering the rate of the reaction was proven not to be effective for the synthesis of the alternate iron phosphide phase. A variety of different solvents were used in combination with oleic acid in an attempt to isolate different morphologies via the decomposition of a single source precursor, $H_2Fe_3(CO)_9P^tBu$. Most of the decompositions resulted in nanorods, the most monodisperse nanorods being synthesized by the injection of the precursor into a pre-heated surfactant solution of DOE and OA. We attribute the propensity of these systems to form nanorods to the more efficient binding of OA to the [001] face of the nucleated Fe_2P nanocrystals. Interference of the binding of OA to the nanocrystals, either by a solvent that exhibited non-selective binding and competed with OA (in this case, OAm) or through steric hindrance (seen with TDDA), prevented the formation of nanorods.

The results obtained by decomposing a variety of different starting materials in a TOA/OA solvent system indicated that the identity of the starting cluster did not affect the phase of nanomaterial obtained. A table summarizing all of the decompositions of $H_2Fe_3(CO)_9P^tBu$ performed can be found in Appendix III.

In order to determine whether alternate synthetic approaches would be successful in isolating an alternate phase of iron phosphide, the decomposition of $Fe_3(CO)_{10}P^tBu$ in addition to that of $H_2Fe_3(CO)_9P^tBu$ in a variety of solvents has been monitored by IR in order to gain a better understanding of the decomposition pathway. The results of these studies are presented in Chapter 4.

Chapter 4. Investigation of the mechanism of decomposition for the formation of iron phosphide nanoparticles

4.1. Introduction

Mechanistic studies into the transformation from molecular precursors to nanoparticles are useful because they can provide insight into the potential for control over various aspects of molecular decompositions, including the phase and shape of nanoparticles synthesized. Surfactants are known to stabilize nanoparticles as they are nucleated as well as to influence the growth and, therefore, the shape of the materials isolated. However, when it comes to the role of the surfactants prior to the nucleation of nanoparticles, very little is known.[109,110]

As shown in Chapters 2 and 3, the decompositions of a variety of iron phosphorus carbonyl compounds in different surfactant systems all resulted in the formation of Fe_2P nanoparticles. A couple of different approaches were taken in order to gain better insight into how the compounds decompose to form nanomaterials, including monitoring the solutions by IR spectroscopy as the decompositions were carried out and GC-MS analysis of the volatile products released when the clusters were decomposed as solids.

A recently reported mechanistic study of nanoparticle formation from a molecular precursor involved the synthesis of cobalt nanoparticles from an acetylene-bridged dicobalt octacarbonyl.[110] By following the IR spectra as the precursor was heated in a variety of surfactants, it was found that the surfactant system influenced the reaction pathway before nucleation of the nanoparticles as well as effecting the crystal structure and magnetic properties of the isolated nanoparticles.

IR spectroscopy is a useful method for the detection of metal carbonyl compounds. Metal carbonyl clusters in solution often exhibit different colors depending on their composition; the decomposition reactions were always accompanied by changes in color before decomposition took place, which suggested that the decompositions of the iron phosphide clusters involved the formation of various clusters, by thermal rearrangement or through reaction of the starting cluster with the solvents used. IR studies were performed for a variety of systems, including the decomposition of $H_2Fe_3(CO)_9P^tBu$ in a 1:1 (v:v) solution of TOA:OA, a 3:1 solution of ODE:OA, and a 1:1 solution of OAm:OA. In addition to the studies monitoring how the molecular precursors decompose in solution, results of the solid state decomposition of the clusters under vacuum as well as under a flow of argon will also be presented.

4.2. Experimental Procedure

The reaction setup was similar to those for the decompositions of the clusters, but on a smaller scale. Methyl oleate (MeOA; technical grade, 75% purity) was purchased from Alfa Aesar and used as received. Sodium oleate (Na^+ oleate; 99%) was purchased from Sigma-Aldrich and used as received.

Characterization

Gas Chromatography-Mass Spectrometry (GC-MS). GC-MS analysis was performed on an Agilent 6890N GC instrument interfaced to an Agilent 5973N MSD system with a Restek Rtx-35ms column (30 m x 0.25 mm x 0.1 μm). The inlet temperature was set to 30 °C, and the oven temperature was held at 30 °C for 1 minute then ramped at 5 °C/minute to 100 °C.

4.2.1. Monitoring IR spectra of decompositions

$H_2Fe_3(CO)_9P^tBu$ in TOA & OA (**1**): As verification of the composition of the starting cluster, an IR spectrum was taken in which the precursor was dissolved in hexane. Also, in order to determine the effect that the TOA had on the precursor, a few drops of TOA were added to a solution of the precursor in THF, and an IR was taken. 50 mg (0.10 mmol) of $H_2Fe_3(CO)_9P^tBu$ was combined in a 3-neck roundbottom flask with 3 mL of TOA and 3 mL OA. The solution was gradually heated, and IR spectra were collected at 100 °C, 125 °C, 135 °C, and 140 °C (a small amount of solution was removed via pipette and diluted in a hexane solution). Upon heating, the solution changed from a deep red to a brownish color and finally to brown-orange. The background solution for the IR spectra was composed of hexane with 2 drops each of TOA & OA.

$H_2Fe_3(CO)_9P^tBu$ in ODE & OA (**2**): The reaction was setup as in **1**. 54 mg (0.10 mmol) of $H_2Fe_3(CO)_9P^tBu$ was dissolved in 3 mL ODE and 1 mL OA. The solution was stirred for 15 minutes, at which time an IR was taken. The solution was heated, taking an IR spectrum approximately every 5 minutes. The solution became slightly foamy at 160 °C. The reaction changed from to red to brown-red to orange-brown (190 °C) to orange (195 °C) to orange-yellow (255 °C), at which time the heat was turned off. The background solution contained hexane, 9 drops of ODE, and 3 drops of OA.

$H_2Fe_3(CO)_9P^tBu$ in OAm & OA (**3**): The reaction was setup as in **1**. 56 mg (0.11 mmol) of $H_2Fe_3(CO)_9P^tBu$ was dissolved in 2 mL OAm and 2 mL OA (not completely soluble at room temperature). The solution was gradually heated, taking IR spectra every 5

minutes. The solution remained red until ~190 °C, at which time it changed to brownish red. From this point, the color progressed from brown-yellow (197 °C) to yellow (200 °C) to orange-yellow (210 °C) to yellow-brown (220 °C) to dark brown and foamy (225 °C) to black (250 °C). The IR spectrum collected at 270 °C did not have any carbonyl peaks. The heat was turned off, and the reaction was worked up to determine whether any nanoparticles were present (precipitated with ethanol and washed with hexane).

$Fe_3(CO)_{10}P^tBu$ in TOA & OA (**4**): The reaction was setup as in **1**. 55 mg (0.09 mmol) of $Fe_3(CO)_{10}P^tBu$ was dissolved in 2 mL TOA and 2 mL OA; the solution was dark brown-black. An IR spectrum was collected every 5 minutes. The solution changed from brown-black to red-orange (105 °C) to dark brown (200 °C) to orange (208 °C) to yellow (235 °C). Heating was discontinued when the temperature had reached 285 °C; the solution was very pale yellow.

$H_2Fe_3(CO)_9P^tBu$ in TOA and MeOA (**5**): The reaction was setup as in **1**. 56 mg (0.11 mmol) of $H_2Fe_3(CO)_9P^tBu$ was dissolved in 3.5 mL TOA and 0.5 mL MeOA. As the solution was gradually heated, aliquots of the solution were removed for IR analysis every ~3 minutes. The solution began as a deep red color, changed to brown (200 °C), and then to black (270 °C). The maximum temperature reached was 340 °C. When the reaction had cooled, another IR was taken.

$Fe_3(CO)_{10}P^tBu$ in TOA & MeOA (**6**): The reaction was setup as in **1**. 7 mg (0.01 mmol) of $Fe_3(CO)_{10}P^tBu$ was dissolved in 3.5 mL TOA and 0.5 mL MeOA. The solution was

dark brown at room temperature. An IR of the reaction mixture was taken every 3-5 minutes. The solution changed to brown-yellow at 210 °C and to brown-black at 265 °C, at which time the heating was discontinued.

$H_2Fe_3(CO)_9P^tBu$ in TOA and Na^+ oleate (**7**): The reaction was setup as in **1**. TOA (3.5 mL) and Na^+ oleate (0.15 g) were combined in a 3-neck flask; the Na oleate did not completely dissolve at room temperature. To the flask, 54 mg (0.11 mmol) $H_2Fe_3(CO)_9P^tBu$ was added. As the solution was heated, IR spectra were taken about every five minutes. The solution became deeper red in color, and as it reached ~100 °C, a greasy red-black solid appeared on the walls. Further heating resulted in the progression from a red solution to a dark brown solution with orange foam (~210 °C). The solution was heated to a maximum of 270 °C, at which time the heat was turned off.

$H_2Fe_3(CO)_9P^tBu$ in HDOH (**8**): The reaction was setup as in **1**. HDOH (2.86 g, 3.5 mL) was added to the flask; began heating under vacuum in order to remove any moisture. When the temperature reached 95 °C, the reaction was placed under a flow of Ar and $H_2Fe_3(CO)_9P^tBu$ (56 mg, 0.11 mmol) was added, resulting in a red solution. The solution was further heated, taking an IR spectrum at every ~25 °C interval. The color of the solution progressed from red to brown-orange (190 °C) to yellow-orange to dark brown (250 °C) and finally to black (300 °C). Heating was discontinued ~20 minutes after the temperature had reached 300 °C. When the solution had cooled, another IR was taken; no carbonyl bands were present.

4.2.2. Quenching of the decomposition

0.12 g (0.24 mmol) $H_2Fe_3(CO)_9P^tBu$ was dissolved in 2 mL TOA and 2 mL OA. The reaction was setup as in **1**. As the solution was heated, the reaction changed color as seen previously, from red to red-orange to orange to yellow. When the reaction was pale yellow (~310 °C), the heating mantle and stirplate were removed and the flask was lowered into dry ice; no visible change in the reaction was observed. When the reaction had cooled, the flask was transferred to a water bath to thaw the solution. The solution was pale yellow with a brownish residue at the bottom of the flask. An IR of the solution was taken (a couple of drops of the solution were dissolved in hexane). During manipulation, the solution became more orange-brown, indicating that it may be air-sensitive. The workup was carried out as usual, beginning with precipitation (using EtOH). After centrifuging the solution, there was an orange supernatant and gelatinous orange precipitate. Hexane was added to the precipitate and the centrifuge tube was sonicated; after all of the precipitate had dissolved, the solution was centrifuged, leaving a yellow solution with a small amount of black precipitate. A TEM grid was prepared of the black precipitate redispersed in hexane.

4.2.3. Decompositions in a single solvent

$H_2Fe_3(CO)_9P^tBu$ in ODE: 0.25 g (0.50 mmol) $H_2Fe_3(CO)_9P^tBu$ was dissolved in 8 mL ODE in a 3-neck flask. As the reaction was heated the solution became deep red and around 280 °C, the solution had darkened to black with a mirror on the walls of the flask. Orange foam appeared on the solution when the temperature reached 300 °C. The temperature was held at ~310 °C for 15 minutes, at which time the heat was turned off. When the reaction had cooled, EtOH was added to precipitate the particles, followed by

washing with hexanes. The particles did not form a stable suspension in hexane, and appeared to be very magnetic (moved freely when a magnet was moved along the outside of the centrifuge tube).

$H_2Fe_3(CO)_9P^tBu$ in TOA: 0.25 g (0.50 mmol) $H_2Fe_3(CO)_9P^tBu$ was dissolved in 7 mL TOA in a 3-neck flask. The solution darkened as the temperature increased. At 150 °C, the solution was foamy and there was an oily red substance on the walls of the flask. The solution appeared black at ~230 °C. When the temperature reached 300 °C, the temperature was held for an hour, and then the heat was turned off. The nanoparticles were precipitated with EtOH, followed by washings with EtOH and hexanes.

$H_2Fe_3(CO)_9P^tBu$ in HDOH: 0.25 g (0.50 mmol) $H_2Fe_3(CO)_9P^tBu$ was combined with 5.73 g (7 mL) HDOH in a 3-neck flask. The flask was heated, and by 145 °C, most of the HDOH had melted, resulting in a dark red solution. The solution became foamy around 200 °C, dark brown at 290 °C, and appeared black at 320 °C. The temperature was held at ~320 °C for an hour. After the solution had cooled, EtOH was added to the flask. Aliquots of the reaction were centrifuged, adding fresh EtOH when all of the solution had been transferred to the centrifuge tube. Sonication and centrifugation cycles were repeated until the EtOH wash looked clear.

4.2.4. Bulk Decompositions

Under flow of Argon: A Schlenk flask was attached to an oil bubbler with a steady flow of Ar. To the flask, 0.22 g (0.43 mmol) $H_2Fe_3(CO)_9P^tBu$ was added. Using a heating mantle, the flask was heated. When the temperature reached ~250 °C, there was some

sublimed product on the walls and a dark solid at the bottom of the flask. Heating was continued at >300 °C for an hour. At this time, the flask was cooled; the walls of the flask were black and silver at the bottom, gray in the middle, and red at the top. The walls were scraped using a spatula (the black/silver solid appeared to be magnetic as it was interacting with the stirplate) and heating was resumed for ~10 hours at ~340 °C. When the flask had cooled, the solid was removed from the flask and analyzed using XRPD.

Under Static Vacuum: 0.10 g (0.20 mmol) $H_2Fe_3(CO)_9P^tBu$ was dissolved in a small amount of hexanes in a Schlenk flask. The solvent was removed under vacuum, leaving a film of the precursor on the walls. The flask was then placed on the High Vac line, and pumped down to $\sim 10^{-7}$ Torr. After the flask was pumped down, it was lowered into a pre-heated mantle (270 °C); the flask became filled with a cloudy black substance. Some of the precursor sublimed onto the upper part of the flask, so the flask was rotated in order to ensure decomposition of most of the cluster. A mirror also formed on the bottom of the flask. The temperature was raised to ~330 °C and held at this temperature for 90 minutes, at which time the heat was turned off. When the flask had cooled, hexane was added to wash away any remaining starting material. The solution was centrifuged, leaving a pale pink supernatant. The glittery black solid was dried and analyzed by XRPD. The same procedure was followed for $H_2Fe_3(CO)_9PPh$, but the decomposition did not look the same; a brown smoke was evolved, but no mirror was formed, and the solid did not appear to sublime as readily onto the upper walls of the flask.

Sample preparation for GC-MS analysis: The same procedure described above, for the decomposition of $H_2Fe_3(CO)_9P^tBu$ under static vacuum, was followed. Using a 10 μL syringe, ~5 μL of the headspace was injected into the GC-MS for analysis.

4.3. Results & Discussion

4.3.1. IR studies of the decompositions.

As demonstrated in Chapter 3, the decomposition of a variety of different iron-phosphorus clusters resulted in the same phase of nanomaterial. Because the decompositions proceeded with a similar change in color, a variety of decomposition conditions were monitored using IR spectroscopy with the intention of gaining a better understanding of the mechanism of decomposition. Table 4.1 lists the literature values for the various clusters detected by the mechanistic studies. The clusters will be referred to in the IR spectra and discussion using the abbreviation and the symbol shown in Table 4.1.

$H_2Fe_3(CO)_9P^tBu$ [47] (H_2Fe_3P, ▼) **hexane**	**$HFe_3(CO)_9P^tBu^-$** [111] (HFe_3P, ●) **THF**	**$Fe_4(CO)_{12}(P^tBu)_2$** [112] (Fe_4P_2, ■) **cyclohexane**	**$Fe_2(CO)_6(PH^tBu)_2$** [49] (Fe_2P_2, ♦) **cyclohexane**	**$Fe_3(CO)_{10}P^tBu$** [48] (Fe_3P, ∇) **pentane**
2081 m	2039 m	2033 vs	2058 m	2084 w
2058 s	1995 vs	2020 s	2019 vs	2042 s
2032 vs	1966 s	1993 s	1983 s	2025 vs
2008 s	1953 s	1979 m	1975 s	2016 m
1985 m	1934 m		1966 sh	1998 w
1973 w	1901 w			1977 w
				1965 w
				1875 vw

Table 4.1. Literature IR values of the clusters present during the decompositions (w: weak, m: medium, s: strong, vs: very strong).

The first decomposition monitored was that of $H_2Fe_3(CO)_9P^tBu$ in 3 mL TOA and 3 mL OA (Figure 4.1). As mentioned in Chapter 2, the precursor is deprotonated in the

presence of TOA. An IR spectrum supporting this can be seen in Figure 4.1B. As the solution was heated further, changes in the IR band positions continued. At 135 °C, the IR spectra suggested a mixture of HFe_3P and Fe_4P_2. By 140 °C, further rearrangement had taken place, giving a mixture of Fe_4P_2 and Fe_2P_2.

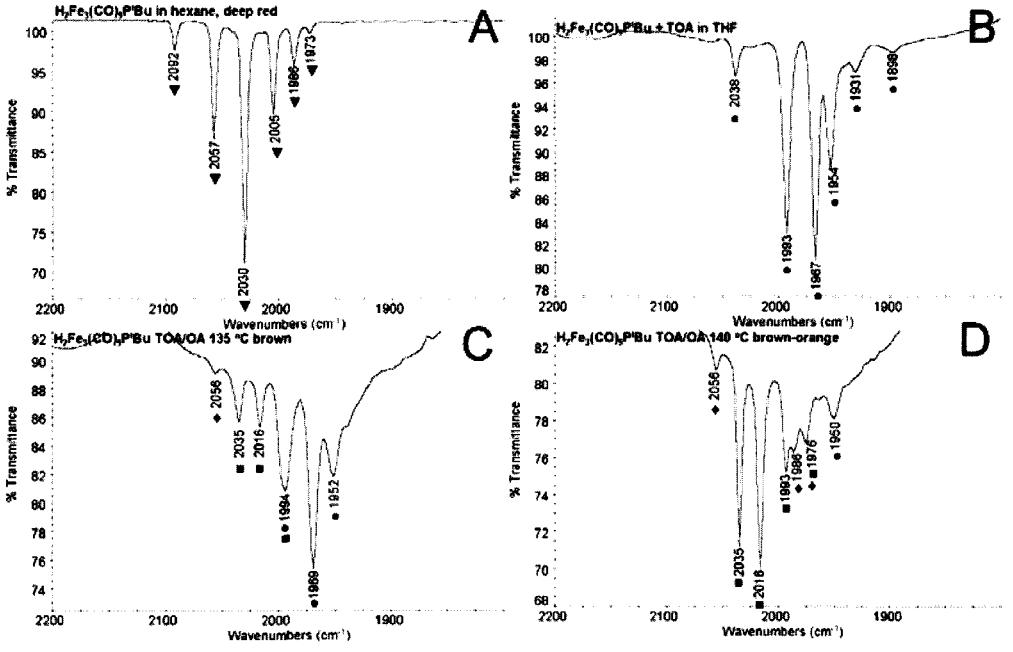

Figure 4.1. IR spectra from the decomposition of $H_2Fe_3(CO)_9P^tBu$ in TOA:OA (1:1). (A) IR of $H_2Fe_3(CO)_9P^tBu$ in hexane at room temperature. (B) IR of a solution of $H_2Fe_3(CO)_9P^tBu$ in THF with a few drops of TOA added. (C, D) IR of an aliquot of the decomposition reaction taken at 135 & 140 °C, respectively.

Having seen in the TOA and OA system that the rearrangement appeared to have been initiated by the deprotonation of $H_2Fe_3(CO)_9P^tBu$ by TOA, the surfactant system was changed, substituting a hydrocarbon (ODE) for the amine-containing solvent (TOA). As presented in Chapter 3, the ODE:OA surfactant system gave nanoparticles with similar morphologies to those seen in the TOA:OA system. The IR spectra for this system are presented in Figure 4.2.

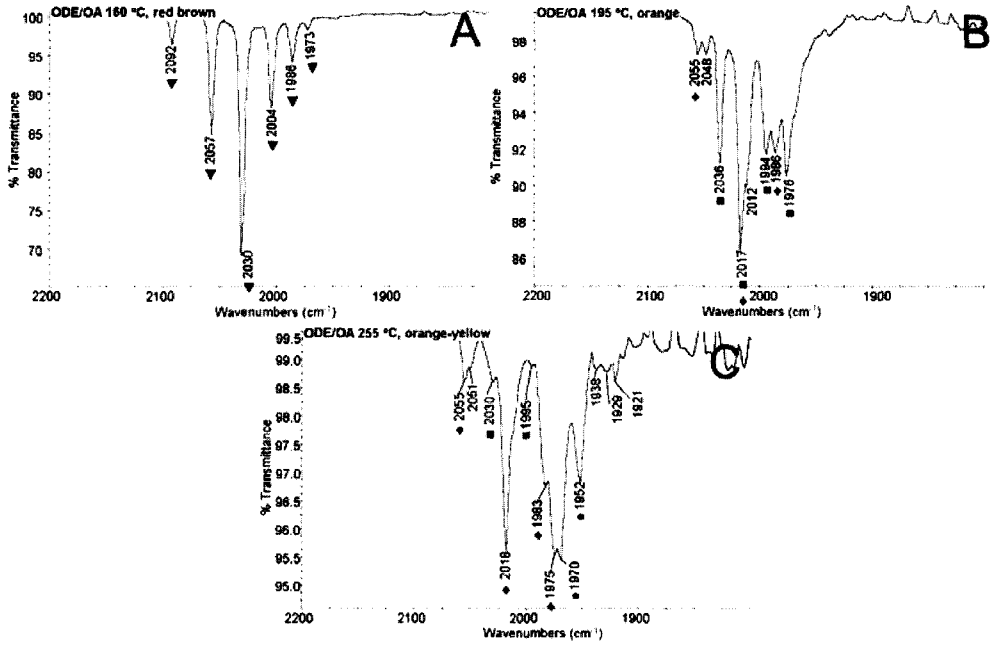

Figure 4.2. IR spectra of the decomposition of $H_2Fe_3(CO)_9P^tBu$ in ODE:OA (3:1) taken at (A) 160 °C, (B) 195 °C, and (C) 255 °C.

As seen in Figure 4.2A, CO bands corresponding to H_2Fe_3P were present up to 160 °C. When the reaction reached 195 °C, there was a mixture of Fe_4P_2 and Fe_2P_2. At 255 °C, the strongest peaks corresponded to Fe_2P_2 with additional peaks that indicated the presence of the Fe_4P_2 and HFe_3P clusters. These results suggested that the presence of the amine was not the determining factor in the rearrangement of the starting cluster.

Another variation used was the substitution of the tertiary amine (TOA) with a primary amine (OAm). When the decomposition of H_2Fe_3P in OAm and OA was followed using IR, a similar rearrangement took place, the first step being the deprotonation of the cluster to give HFe_3P and then rearrangement to the Fe_2P_2 cluster. The progression can be seen in Figure 4.3. Interestingly, when the reaction solution became black at ~250 °C, peaks corresponding to the Fe_2P_2 cluster were still evident (Figure 4.3E).

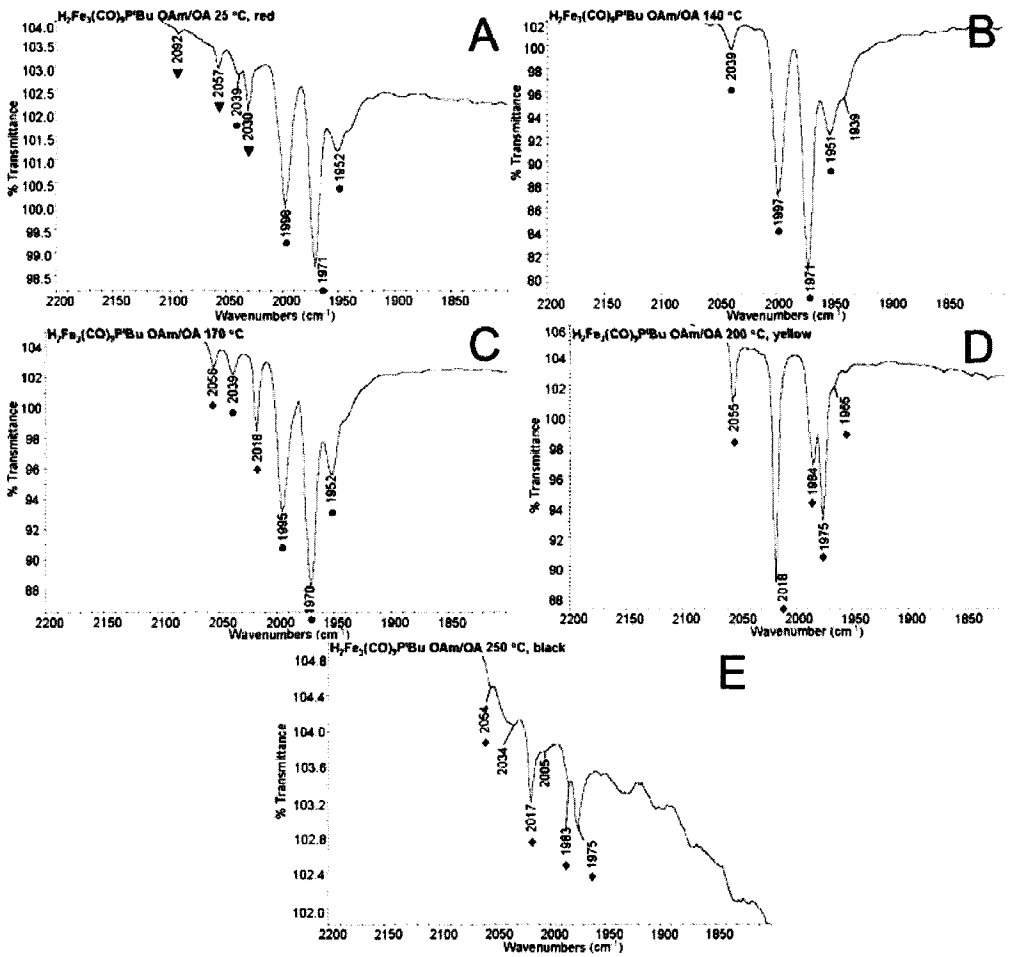

Figure 4.3. IR spectra of the decomposition of $H_2Fe_3(CO)_9P^tBu$ in OAm:OA (1:1) taken at (A) 25 °C, (B) 140 °C, (C) 170 °C, (D) 200 °C, and (E) 250 °C.

Further attempts to try circumventing the cluster rearrangement before decomposition involved the use of $Fe_3(CO)_{10}P^tBu$ instead of $H_2Fe_3(CO)_9P^tBu$. Because monitoring of the rearrangement of H_2Fe_3P before decomposition usually showed deprotonation of the cluster during the early stages of the reaction, the use of a cluster without any acidic protons present was chosen in order to see how this would affect the course of the reaction. The Fe_3P cluster was decomposed in TOA and OA (1:1); an IR taken at 140 °C indicated the presence of the HFe_3P cluster (Figure 4.4B), suggesting that the cluster was acquiring a proton from the solution, most likely from OA. From this

stage, the rearrangement proceeded in a similar fashion to the previously presented decompositions, the last cluster seen in solution being Fe_2P_2 (Figure 4.4D).

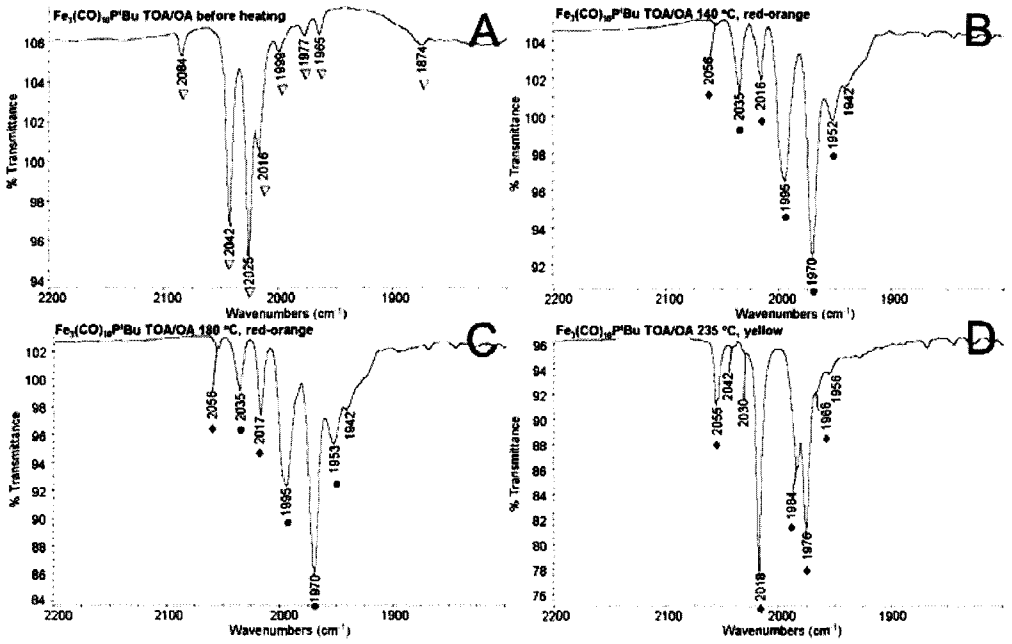

Figure 4.4. IR spectra of the decomposition of $Fe_3(CO)_{10}P^tBu$ in TOA:OA (1:1) taken at (A) 25 °C, (B) 140 °C, (C) 180 °C, and (D) 235 °C.

In order to determine whether the proton was coming from oleic acid, another decomposition was carried out, using methyl oleate (MeOA) instead of oleic acid (the acidic proton was replaced with a methyl group). The changes in IR spectra for the reaction of both H_2Fe_3P and Fe_3P in TOA:MeOA (7:1) were monitored (Figure 4.5 and Figure 4.6, respectively).

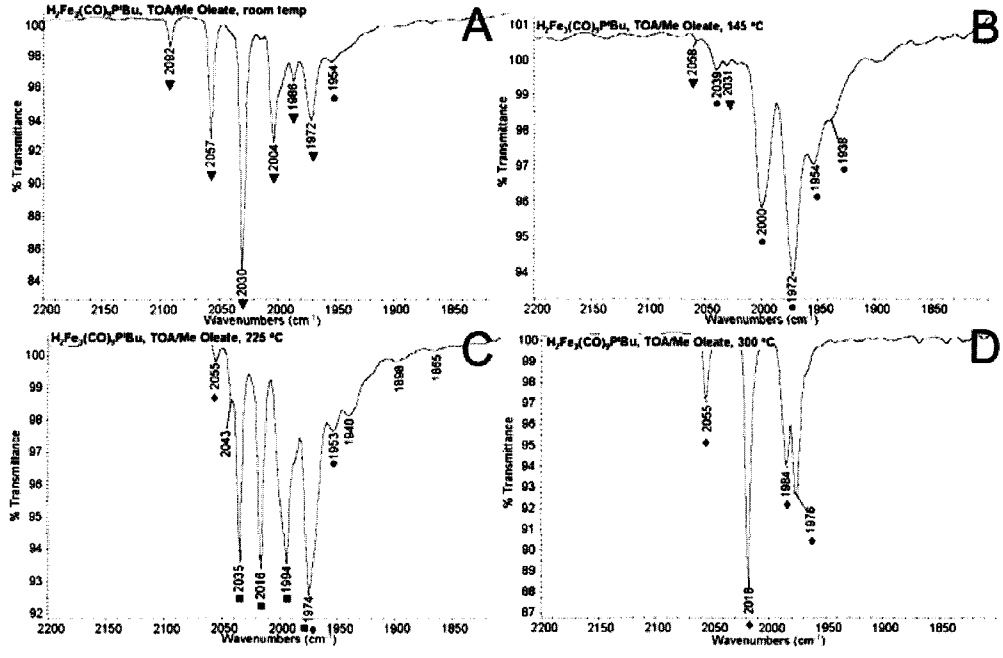

Figure 4.5. IR spectra of the decomposition of $H_2Fe_3(CO)_9P^tBu$ in TOA/MeOA (7:1) taken at (A) 25 °C, (B) 145 °C, (C) 225 °C, and (D) 300 °C.

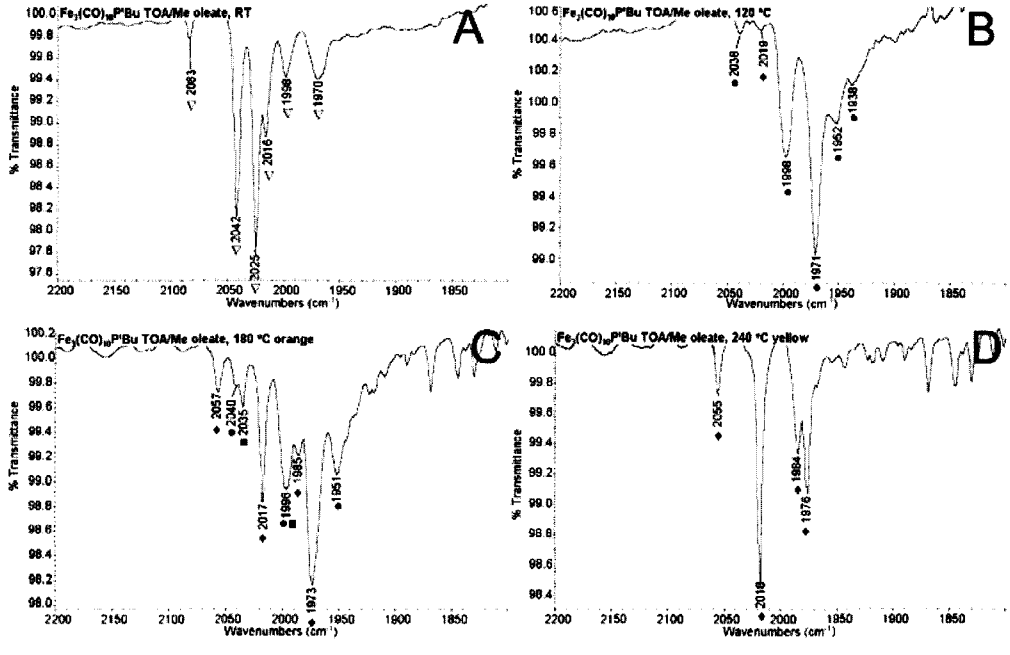

Figure 4.6. IR spectra of the decomposition of $Fe_3(CO)_{10}P^tBu$ in TOA/MeOA (7:1) taken at (A) 25 °C, (B) 120 °C, (C) 180 °C, and (D) 240 °C.

For each of the reactions monitored in TOA/MeOA, the solutions became dark brown between 210 and 270 °C. When the solution had cooled, EtOH was added in order to precipitate any nanoparticles that had formed. TEM images of the isolated particles from the decomposition of $H_2Fe_3(CO)_9P^tBu$ and $Fe_3(CO)_{10}P^tBu$ can be seen in Figure 4.7 and Figure 4.8. Both of the decompositions resulted in the formation of small spherical particles, further confirming the role of oleic acid in the formation of rod-like structures.

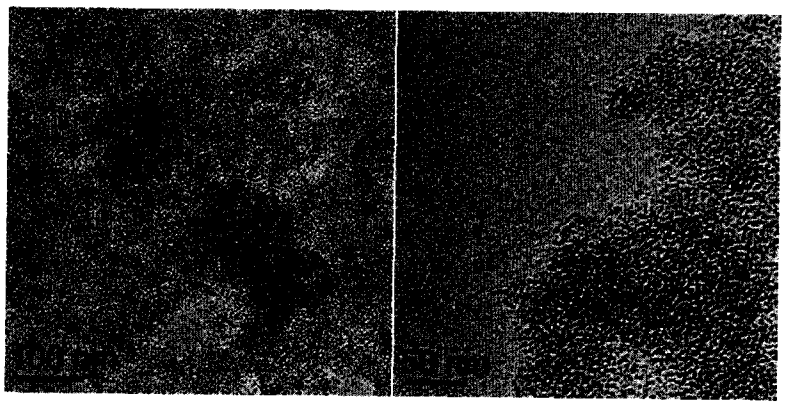

Figure 4.7. TEM images of the nanoparticles obtained from the decomposition of $H_2Fe_3(CO)_9P^tBu$ in TOA/MeOA (7:1).

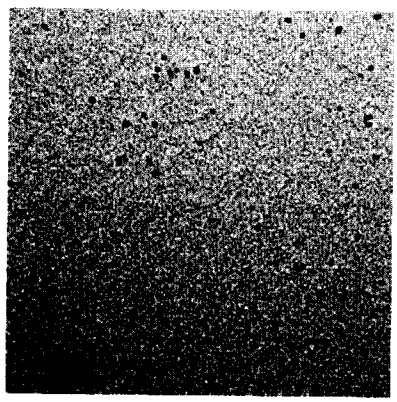

Figure 4.8. TEM image of the nanoparticles obtained from the decomposition of $Fe_3(CO)_{10}P^tBu$ in TOA:MeOA (7:1).

The rearrangement appeared to follow the same pathway, regardless of the starting cluster, through HFe_3P to Fe_4P_2 and finally to Fe_2P_2. However, it is difficult to

rule out the presence of oleic acid in the system using TOA and MeOA because the surfactants are difficult to purify. The MeOA used was only 75% pure, so it is likely that OA was one of the impurities present.

An alternate approach, using sodium oleate, available in 99% purity from Aldrich, was carried out. The decomposition of H_2Fe_3P in TOA and sodium oleate resulted in the same progression of cluster rearrangements seen previously (Figure 4.9). A summary of the transformations seen via IR for each of the solvent systems can be seen in Appendix IV.

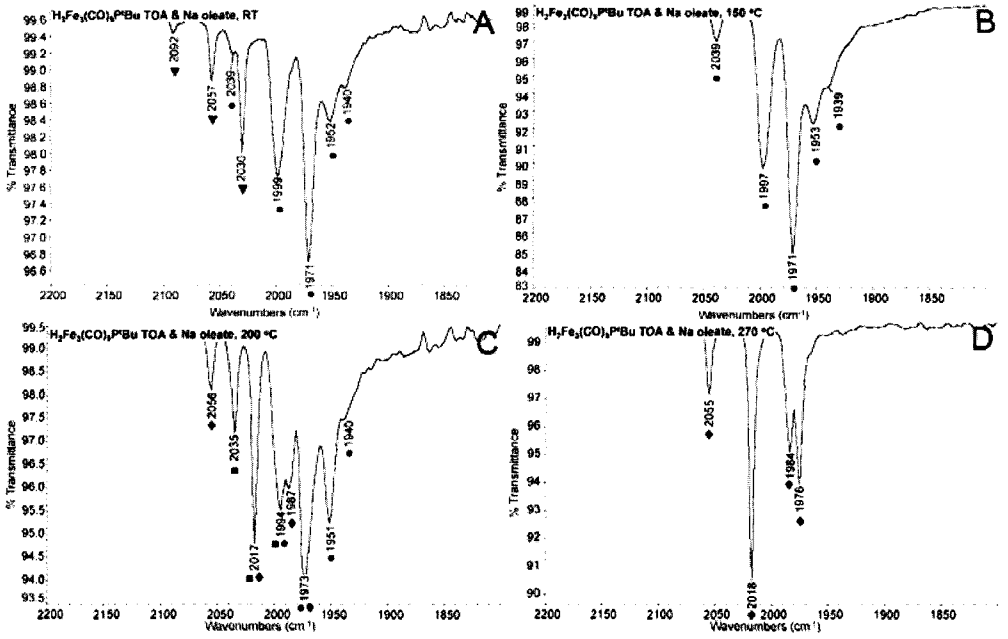

Figure 4.9. IR spectra of the decomposition of $H_2Fe_3(CO)_9P^tBu$ in TOA/Na^+ oleate (8 mmol:0.5 mmol) taken at (A) 25 °C, (B) 150 °C, (C) 200 °C, and (D) 270 °C.

The presence of impurities or moisture in the surfactants is a potential cause for the rearrangements in the clusters. Another possibility is that the Fe_2P_2 cluster is more thermodynamically stable at elevated temperatures than the other iron phosphorus clusters formed in earlier stages of the decomposition reaction.

4.3.2. Quenching of the decomposition.

The change in color during the decompositions usually ended in a pale yellow color prior to the solution becoming black, indicating the formation and growth of nanoparticles. In order to discover whether any nanoparticles were present at this point in the reaction when the transition to a gray- or black-colored solution had not yet occurred, the reaction of H_2Fe_3P in TOA and OA (1:1, v:v) was quenched when the solution became yellow; the maximum temperature reached was ~310 °C. After the reaction had cooled, an IR was taken and the workup of the reaction was carried out as usual to determine if any nanoparticles were present. As can be seen in Figure 4.10, a broad peak was still present at this point of the reaction, with peaks corresponding to both the Fe_4P_2 and Fe_2P_2 clusters.

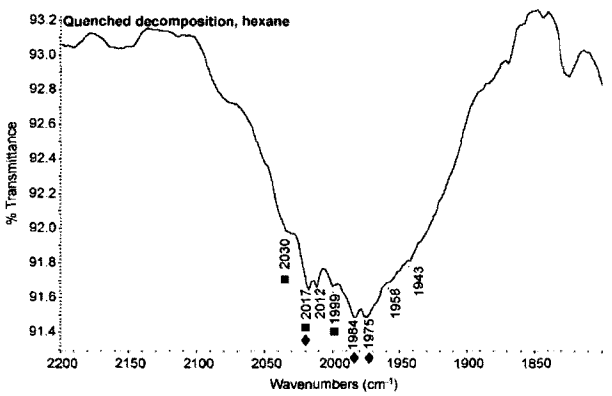

Figure 4.10. IR spectrum of the quenched decomposition. The sample was prepared by dissolving a few drops of the reaction solution in hexane.

A small amount of black solid was isolated from the workup of the reaction; analysis of the solid by TEM indicated that there were nanoparticles present having a similar morphology (Figure 4.11 A & B) to those seen in the reactions run until the solution became black (Figure 4.11 C & D). The dimensions of the particles from the quenched reaction were ~250 × 120 nm. Seen together with nanoparticles synthesized in

a similar surfactant system but with a longer growth time, the quenched particles appear to be shorter and wider.

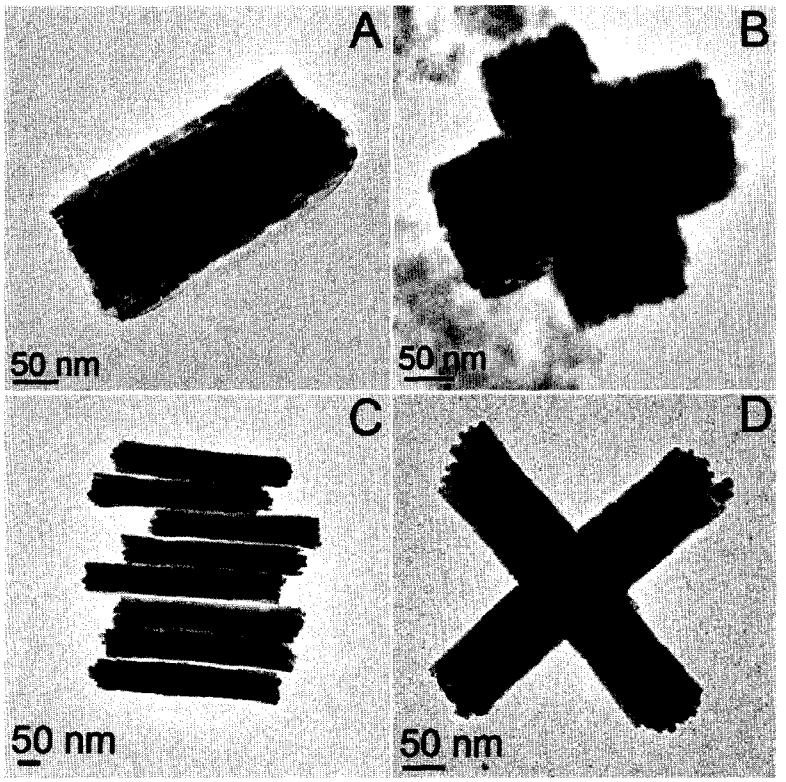

Figure 4.11. TEM images of (A, B) Nanoparticles isolated from quenched decomposition and (C, D) nanoparticles isolated from a normal decomposition. Both decompositions were performed in a 1:1 (v:v) solution of TOA:OA.

4.3.3. Decompositions in a single solvent.

Given that oleic acid appeared to be playing a role in the cluster rearrangement, a variety of alternate decompositions were performed in order to try to circumvent the influence of OA. $H_2Fe_3(CO)_9P^tBu$ was decomposed in 8 mL of ODE or 7 mL of either TOA or HDOH without the presence of an additional surfactant.

As mentioned in the experimental section, the particles synthesized in ODE alone did not form a stable suspension in hexane. The particles were analyzed by TEM, indicating only clumps of particles without a well-defined morphology (Figure 4.12).

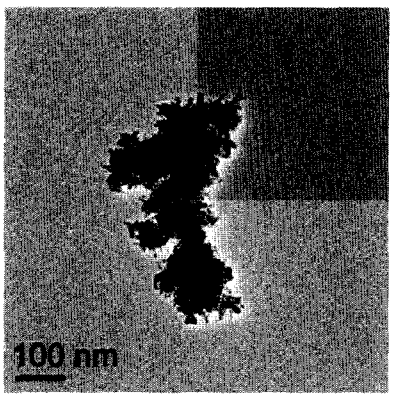

Figure 4.12. TEM image of the particles synthesized from the decomposition of $H_2Fe_3(CO)_9P^tBu$ in 8 mL ODE.

The particles obtained from the decomposition in 7 mL TOA appeared to form a more stable solution in hexane; however, the TEM images showed particles that were not very monodisperse (Figure 4.13). Analysis of the isolated solid by XRPD did not show any diffraction, so the solid was annealed under argon at temperatures >300 °C for ~8 hours. XRPD of the annealed solid revealed the presence of Fe_3O_4 (Figure 4.14).

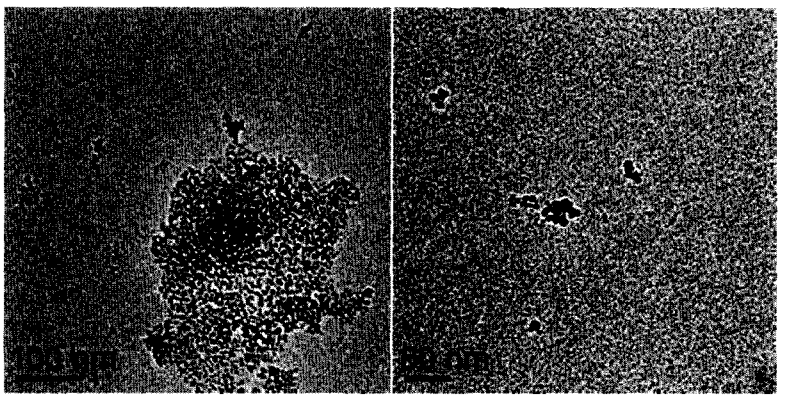

Figure 4.13. TEM images of particles synthesized via the decomposition $H_2Fe_3(CO)_9P^tBu$ in 7 mL TOA.

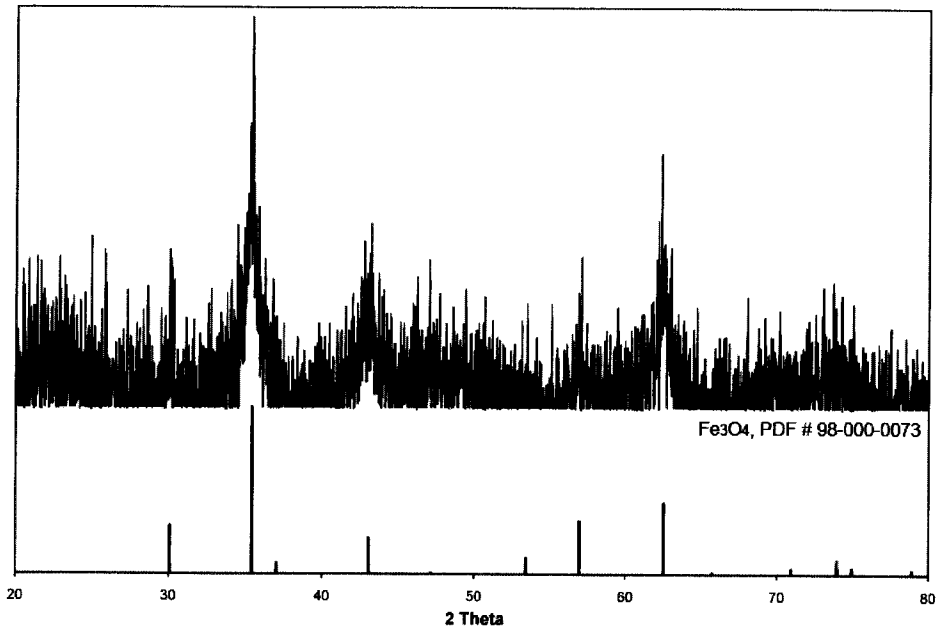

Figure 4.14. XRPD of the annealed product from the decomposition of $H_2Fe_3(CO)_9P^tBu$ in 7 mL TOA.

The decomposition of $H_2Fe_3(CO)_9P^tBu$ in HDOH resulted in the formation of spherical nanoparticles of two different sizes, the larger particles being ~10 nm and the smaller particles ~ 5 nm in diameter (Figure 4.15). Quantitative data from EDS analysis (Figure 4.16) indicated values close to those for Fe_3P; the experimentally obtained values were 87 wt% Fe and 13 wt% P, whereas the theoretical values for Fe_3P are 84 wt% Fe and 16 wt% P.

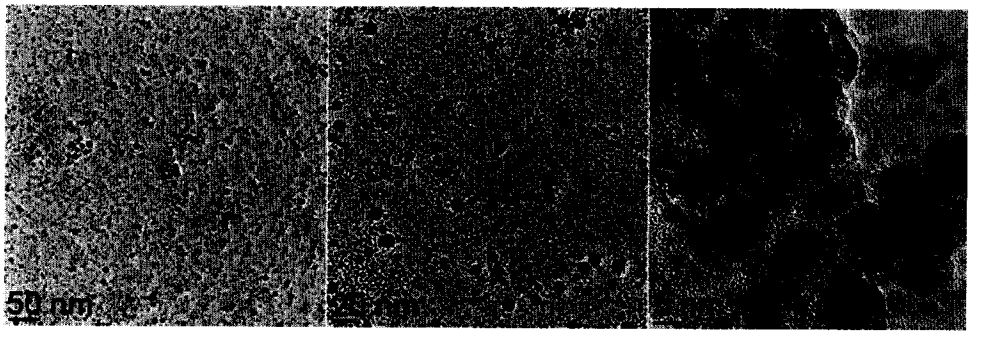

Figure 4.15. TEM images of nanoparticles synthesized from the decomposition of $H_2Fe_3(CO)_9P^tBu$ in 7 mL HDOH.

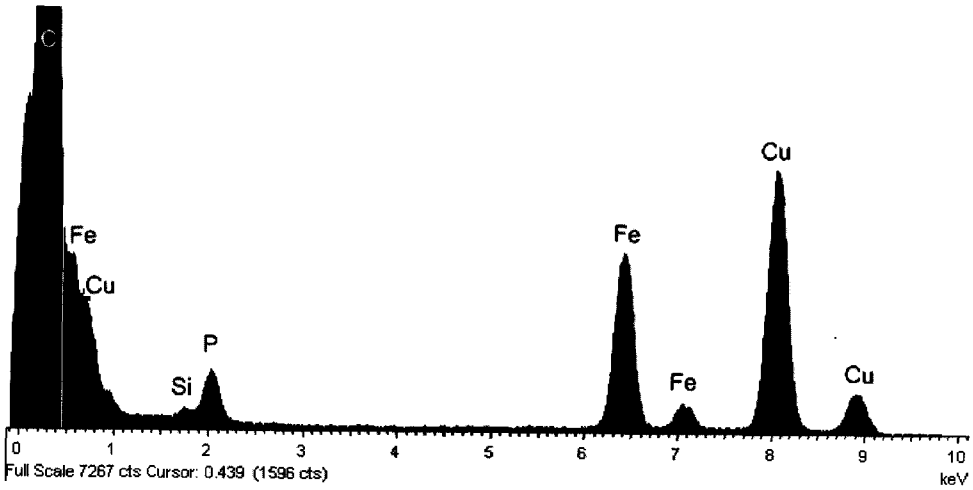

Figure 4.16. EDS spectrum of the nanoparticles synthesized in 7 mL HDOH.

HR-TEM analysis of the nanoparticles indicated that they were crystalline as atomic planes are visible (Figure 4.17). Further analyses of the nanoparticles are being carried out in order to determine what phase is present.

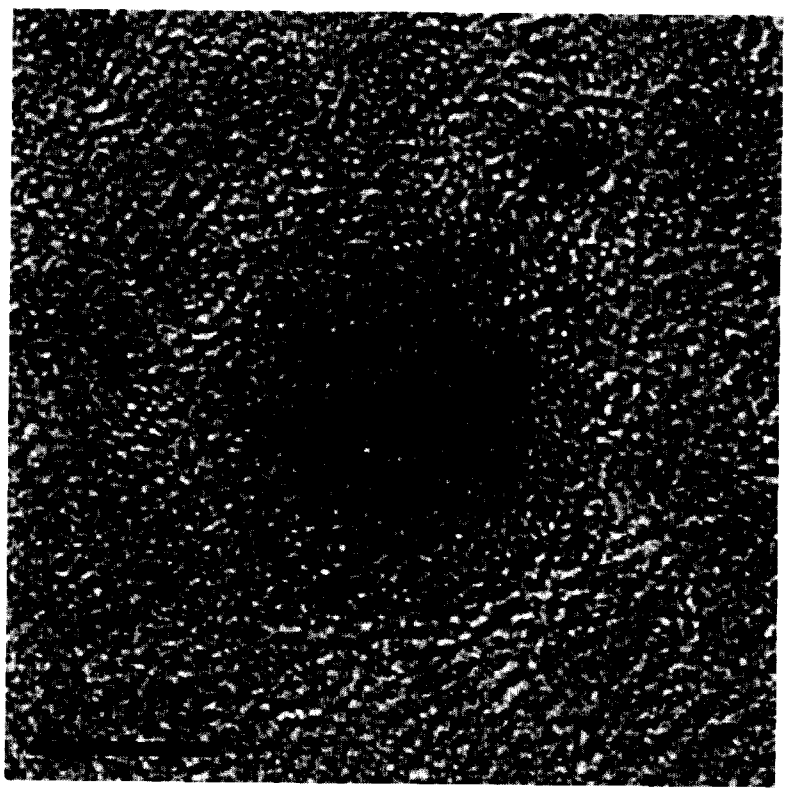

Figure 4.17. HR-TEM image of a nanoparticle synthesized in HDOH.

An IR study of the decomposition in HDOH indicated that there was still rearrangement of the cluster taking place (Figure 4.18). IR analysis showed that the Fe_2P_2 cluster was being formed prior to decomposition, as was seen in all of the previous IR studies.

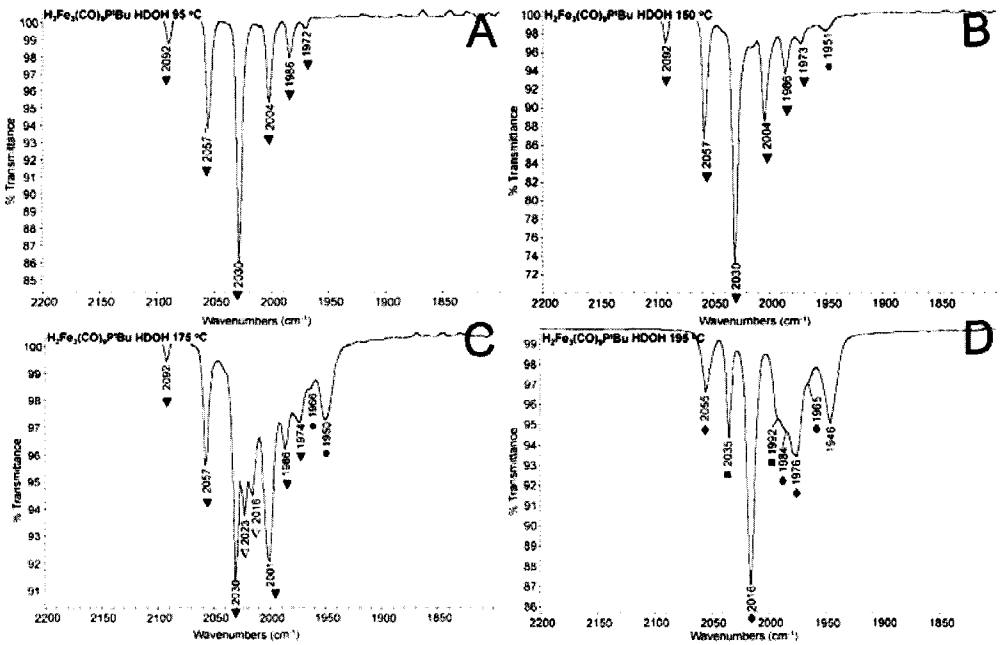

Figure 4.18. IR spectra from the decomposition of $H_2Fe_3(CO)_9P^tBu$ in HDOH taken at (A) 95 °C, (B) 150 °C, (C) 175 °C, and (D) 195 °C.

However, the starting cluster remained in solution up to higher temperatures than was seen in the other systems studied by IR; it appears as though the rearrangement from the H_2Fe_3P to the Fe_2P_2 cluster takes place between 175 and 195 °C.

4.3.4. Bulk Decompositions

Having performed a variety of solution decompositions, the majority of which resulted in the formation of Fe_2P nanoparticles, $H_2Fe_3(CO)_9P^tBu$ was decomposed in a Schlenk flask under static vacuum as well as under a flow of argon. These experiments,

conducted in solvent-free conditions, were performed in order to determine whether the Fe_3P phase could be isolated in the absence of surfactants.

The decomposition of $H_2Fe_3(CO)_9P^tBu$ under vacuum was performed by placing the precursor into a Schlenk flask, and pumping the flask down to ~10^{-7} Torr. The flask was then placed into a pre-heated mantle and heated for 90 minutes at 300-330 °C. XRPD analysis of the obtained black solid indicated a mixture of Fe_3P, Fe_2P, and Fe_3O_4; whole pattern fitting of the data gave 63.3% Fe_3P, 20.3% Fe_2P, and 16.4% Fe_3O_4 (Figure 4.19). Formation of Fe_3O_4 under high vacuum suggested that oxygen was derived from the carbonyl molecules during decomposition.

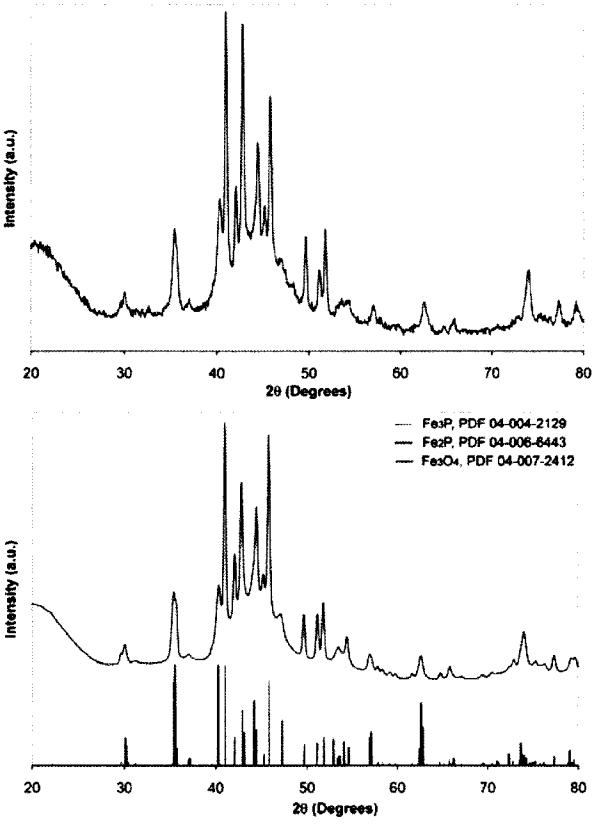

Figure 4.19. Whole pattern fitting of the XRPD pattern for the solid isolated from the bulk decomposition of $H_2Fe_3(CO)_9P^tBu$ under vacuum. The plot on top is the original data and the plot on the bottom is the derived pattern.

The decomposition was also performed under a flow of argon in order to remove any carbon monoxide generated from the flask as it was formed in order to prevent the formation of iron oxide. While some of the precursor sublimed out of the reaction flask during the decomposition, XRPD analysis and subsequent whole pattern fitting of the obtained spectrum (Figure 4.20) indicated that the mixture was 84.0% Fe_3P, 13.3% Fe_2P, and 2.7% Fe. This analysis suggests that the Fe_3O_4 was indeed formed in the decomposition performed under vacuum via abstraction of oxygen from the carbon monoxide molecules released from the precursor.

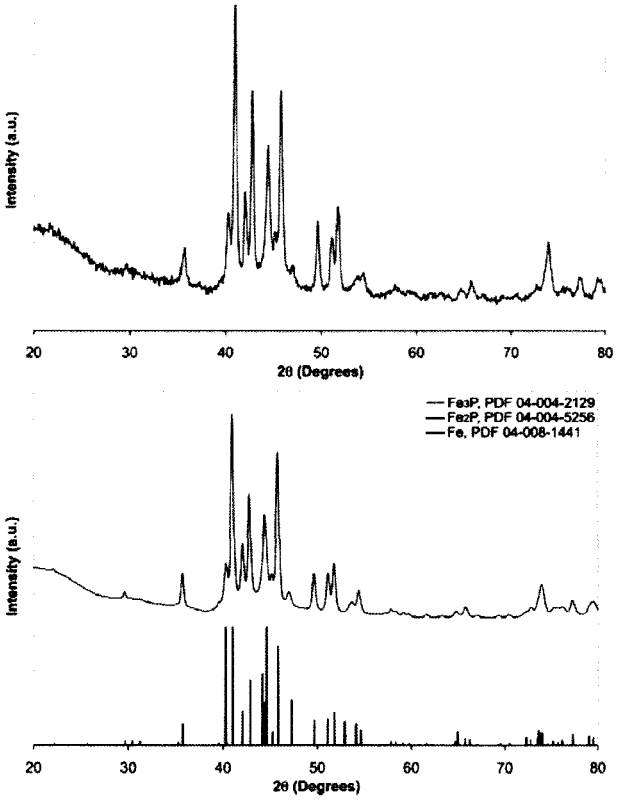

Figure 4.20. Whole pattern fitting of the XRPD of the solid obtained from the bulk decomposition of $H_2Fe_3(CO)_9P^tBu$ under a flow of Ar. The plot on top is the original data and the plot on the bottom is the derived pattern.

It is important to note that this is the lowest reported temperature for the formation of the Fe_3P phase; the maximum temperature reached in the bulk decompositions was ~330-340 °C. Previous reports of the synthesis of Fe_3P, either the formation of bulk Fe_3P by reducing iron powder by hydrogen with a stoichiometric amount of red phosphorus at 1000 °C or the formation of Fe_3P composite nanorods by the reductive annealing of iron phosphate at 650-800 °C, have both exceeded the temperature used in our experiments.[41,113]

As was originally presented in Chapter 3, the decomposition of $H_2Fe_3(CO)_9P^tBu$ is believed to occur with the elimination of isobutylene (C_4H_9) as a side product. In order to verify this, a sample of the headspace was taken from the flask in which the cluster was decomposed under vacuum via microsyringe and analyzed using GC-MS. Peaks for carbon monoxide, isobutylene, hexane, and methylcyclopentane were observed. The hexane and methyl cyclopentane, an isomer of hexane, is likely present due to the crystallization of the cluster in hexanes (the hexanes used was purchased from EMD Chemicals and contains hexane isomers and methylcylopentane).

A similar experiment was run using the $H_2Fe_3(CO)_9PPh$ cluster. GC-MS analysis revealed the presence of benzene. Decomposition of this cluster in a solvent system of TOA and OA resulted in nanostructures with a rougher surface than those seen in the decomposition of $H_2Fe_3(CO)_9P^tBu$ under the same conditions (TEM images of this reaction are shown in Chapter 3). In order to determine whether the additional H-atom originated from the cluster or from the residual solvent present in the flask to give Ph-H in the bulk decomposition, an additional GC-MS experiment was performed on $Fe_3(CO)_{10}PPh$ (one of the side products isolated via column chromatography from the

synthesis of $H_2Fe_3(CO)_9PPh$). This analysis also showed benzene, suggesting that the transformation from Ph → Ph-H resulted from the presence of residual solvent. The GC-MS spectra can be seen in Appendix IV.

Having a better understanding of the decomposition mechanisms from the GC-MS analysis, it appears as though the decomposition of the ^{t}Bu cluster occurs more cleanly due to the generation of isobutylene as a side product, as it is much more volatile than benzene (isobutylene bp = -6.9 °C, benzene bp = 80 °C). Benzene is more likely to remain in solution as the nanoparticles are forming, which has an impact on the nanoparticle growth. The effect of the addition of lower molecular weight solvents was demonstrated in Chapter 2 via the addition of alkanes to the decomposition of $H_2Fe_3(CO)_9P^tBu$ (more branching and splaying of the ends of the nanorods were seen when alkanes were added to the decomposition). The decomposition of $H_2Fe_3(CO)_9PPh$ resulted in split nanorods with rougher edges than those synthesized from $H_2Fe_3(CO)_9P^tBu$ in the same surfactant system.

The decomposition of $H_2Fe_3(CO)_9P^tBu$ in TOA:OA (1:1, v:v) was run in the presence of 42 μL benzene to determine whether the benzene added to the system would result in nanoparticles with a similar morphology to those seen in the decomposition of $H_2Fe_3(CO)_9PPh$. The isolated nanoparticles (Figure 4.21) did not have the same rough edges seen when $H_2Fe_3(CO)_9PPh$ was decomposed in the same solvent system, rather they looked very similar to the split nanorods seen when $H_2Fe_3(CO)_9P^tBu$ was decomposed in only TOA and OA. This suggests that the decomposition in the surfactant is not occurring as cleanly as the bulk decomposition, with the generation of benzene. A

benzene radical is likely being generated *in situ* via homolytic cleavage, interfering with the growth of the nanoparticles.

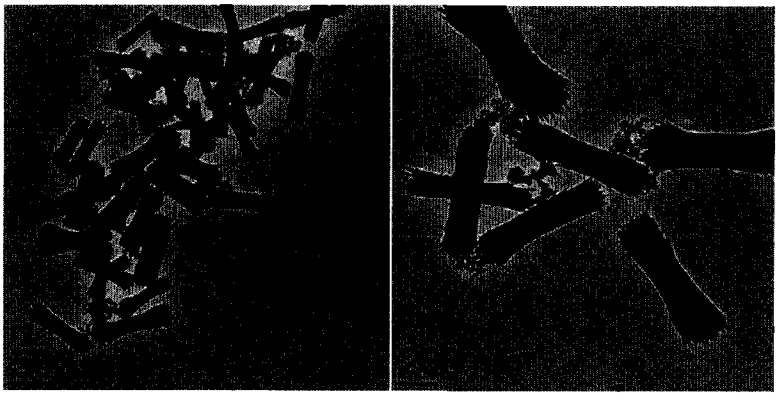

Figure 4.21. TEM images of the decomposition of $H_2Fe_3(CO)_9P^tBu$ in TOA:OA (4:4) with 42 μL of benzene.

4.4. Conclusions

A combination of analytical techniques were used to understand the decomposition mechanism of the iron-phosphorus clusters. IR studies indicated that regardless of the starting cluster or the solvents present, just prior to the nucleation of nanoparticles, $Fe_2(CO)_6(PHR)_2$ was present. From these studies, it became apparent that the surfactants were influencing the rearrangements taking place in addition to directing the growth of the nanoparticles after nucleation. As the decompositions in solvents all resulted in Fe_2P particles due to the influence of the surfactants, bulk decompositions were carried out. These reactions resulted in the formation of Fe_3P as the major product, along with Fe_2P and Fe_3O_4. Further analysis of the bulk decompositions by GC-MS revealed the release of isobutylene and benzene during the decomposition of $H_2Fe_3(CO)_9P^tBu$ and $H_2Fe_3(CO)_9PPh$, respectively. These results, in combination with the decomposition studies in TOA:OA solvent systems of the same clusters, indicated

that the R-group influences the morphology of the nanoparticles. Having a better understanding of the mechanism of decomposition, the most promising avenue for using the $H_2Fe_3(CO)_9PR$ or $Fe_3(CO)_{10}PR$ clusters as a source of Fe_3P materials is likely through the optimization of the bulk decomposition technique.

Chapter 5. Synthesis of iron-manganese phosphide nanomaterials

5.1. Introduction

In addition to binary metal phosphides synthesized in previous chapters (Fe_2P and Fe_3P), investigations into incorporating manganese into the iron phosphide system have been carried out. There are a variety of different ternary and quaternary metal phosphides that have been reported in the literature. The magnetic properties of mixed metal phosphides with iron and either manganese, cobalt, or nickel have been studied ($(Fe_{1-x}Mn_x)_2P$,[114,115] $(Fe_{1-x}Co_x)_2P$,[116] $(Fe_{1-x}Ni_x)_2P$ [117,118]). Table 5.1 gives an overview of the magnetic properties of the binary phases, in which only one transition metal is present, as well as the effect of incorporating a second transition metal into the crystal structure on the magnetic properties.

Phase	Crystal Structure	Magnetic Properties	Ref
Fe_2P	Hexagonal, $P\bar{6}2m$	Ferromagnetic $T_C = 217$ K	39
Mn_2P	Hexagonal, $P\bar{6}2m$	Antiferromagnetic $T_N = 140$ K	115
FeMnP	Orthorhombic, *Pnma*	Antiferromagnetic $T_N = 340$ K	119
Co_2P	Orthorhombic, *Pnma*	Paramagnetic	120
$(Fe_{0.70}Co_{0.30})_2P$	Orthorhombic, *Pnma*	Ferromagnetic Tc = 450 K	121
Ni_2P	Hexagonal, $P\bar{6}2m$	Paramagnetic	122
$(Fe_{0.93}Ni_{0.07})_2P$	Hexagonal, $P\bar{6}2m$	Ferromagnetic $T_C = 295$ K	123

Table 5.1. Magnetic properties of some binary and ternary metal phosphides.

It is apparent that small amounts of Co and Ni substituted for Fe in the Fe_2P structure cause a significant increase in the Curie temperature (from $T_C = 217$ K for Fe_2P to $T_C = 450$ K and 295 K for the Co and Ni-doped structures, respectively). The $(Fe_{1-}$

$_xMn_x)_2P$ system is orthorhombic when $x \geq 0.31$.[81] Mossbauer studies of the doping with Mn versus Co or Ni into the Fe_2P structure indicated that Mn substitutes for iron atoms in the pyramidal-sites, whereas Co and Ni preferentially substitute the iron in the tetrahedral sites.

While there has been a significant amount of research into the magnetic properties of the bulk ternary metal phosphides, very little has been reported about these materials on the nanoscale. $(Fe_xNi_{1-x})_2P$ nanorods were recently reported to have been synthesized using $Fe(CO)_5$, nickel acetylacetonate, and TOP.[124] Magnetic measurements were found to be very sensitive to the Ni concentration; the blocking temperature (T_B) was 76 K for the pure Fe_2P rods and 27 K for $(Fe_{0.90}Ni_{0.10})_2P$. Hysteresis measurements indicated that the hysteresis loop became smaller as the concentration of Ni was increased.

Jourdain *et al.* have used FeCoP (55, 14, 31 atomic % Fe, Co, and P, respectively) and FeNiP (45, 28, 27 atomic % Fe, Ni, and P, respectively) nanoparticles to induce the sequentially catalyzed growth of carbon nanotubes that contain periodically spaced metal phosphide nanoparticles.[125,126] The metal phosphide nanoparticles in these experiments were generated from the evaporation of the desired metal onto an anodic alumina membrane, which contains a small percentage of P due to oxidation of the membrane with phosphoric acid. As the system was heated, P diffused into the metal layer to form metal phosphide nanoparticles. The ellipsoidal nanoparticles had lengths from 25-100 nm and widths from 10-60 nm.

The initial experiments to isolate bimetallic (iron and manganese) phosphide nanoparticles have involved the combination of $H_2Fe_3(CO)_9P^tBu$ with a manganese source, either $Mn_2(CO)_{10}$ or $Mn(CO)_5Br$, to see whether Mn becomes incorporated into

the resulting nanostructures. Additional decompositions of $HMn_2(CO)_8PPh_2$ were also performed in order to determine whether it could serve as a single source precursor to manganese phosphide.

5.2. Experimental Procedure

Manganese carbonyl was purchased from Strem and used as received. Bromine (Br_2) was purchased from Aldrich and used as received. $Mn(CO)_5Br$ was synthesized according to a literature procedure using CH_2Cl_2 as the solvent.[127] $HMn_2(CO)_8PPh_2$ was prepared from $Mn_2(CO)_{10}$ and Ph_2PH in decalin following a literature procedure.[128] Manganese (II) formate ($Mn^{II}(O_2CH)_2 \cdot nH_2O$, $n \cong 2$) was purchased from Aldrich and dried at 110 °C under reduced pressure (~10^{-2} torr) for a few hours and kept under an inert atmosphere until used. All decompositions were carried out as described in Chapter 3.

5.2.1. Decompositions of $H_2Fe_3(CO)_9P^tBu + Mn_2(CO)_{10}$

$H_2Fe_3(CO)_9P^tBu + Mn_2(CO)_{10}$ in TOA & OA (7:1): 0.25 g (0.50 mmol) $H_2Fe_3(CO)_9P^tBu$ and 0.20 g (0.51 mmol) $Mn_2(CO)_{10}$ were combined in a 3-neck roundbottom flask with 7 mL TOA and 1 mL OA. The reaction was heated, and when the temperature reached 80 °C, a yellow film formed on the walls of the flask (due to the sublimation of $Mn_2(CO)_{10}$) and the solution was a cherry red color. As the temperature reached 125 °C, the solution became foamy. The reaction progressed from red to brown to black (~270 °C). When the solution became black, the reaction temperature was held at ~320 °C for 20 minutes.

$H_2Fe_3(CO)_9P^tBu + Mn_2(CO)_{10}$ in TOA & OA (4:4): 0.25 g (0.50 mmol) $H_2Fe_3(CO)_9P^tBu$ and 0.20 g (0.51 mmol) $Mn_2(CO)_{10}$ were combined in a 3-neck roundbottom flask with 4 mL TOA and 4 mL OA. The initial stages of the reaction proceeded the same as the decomposition in 7:1 TOA:OA. When the temperature reached 320 °C, the solution changed from dark brown to clear red-orange, then to yellow (345 °C), and gradually darkened to black (350 °C). The transition from the red-orange to the black solution took about 25 minutes. After the solution became black, the temperature was held steady for an additional 20 minutes.

$H_2Fe_3(CO)_9P^tBu + Mn_2(CO)_{10}$ injected into DOE and OA (10:1): 0.13 g (0.25 mmol) $H_2Fe_3(CO)_9P^tBu$ and 0.10 g (0.26 mmol) $Mn_2(CO)_{10}$ were dissolved in 2 mL DCB in a scintillation vial. The other solvents (10 mL DOE and 1 mL OA) were combined in a 3-neck flask and heated to 150 °C. At this temperature, the precursor solution was injected via syringe into the flask. The scintillation vial was then rinsed with an additional 2 mL DCB and this solution was injected into the reaction flask ~30 seconds after the first injection. As the heat was increased, the solution changed from brown-red (165 °C) to dark brown (300 °C) to black (310 °C). The temperature was further increased to 330-350 °C and held for ~1 hour. An additional reaction was carried out using the exact same conditions, except that only one injection was made.

$H_2Fe_3(CO)_9P^tBu + Mn_2(CO)_{10}$ in DOE and OA (10:1): 0.14 g (0.27 mmol) $H_2Fe_3(CO)_9P^tBu$ and 0.11 g (0.28 mmol) $Mn_2(CO)_{10}$ were combined with 10 mL DOE and 1 mL OA in a 3-neck roundbottom flask. The solution changed from red to dark

brown-orange (310 °C) to dark brown (330 °C) to black (355 °C). The temperature was held at ~350 °C for an hour after the solution became black.

$Mn_2(CO)_{10}$ injected into DOE and OA (10:1): 0.20 g (0.51 mmol) $Mn_2(CO)_{10}$ was dissolved in 2 mL DCB in a scintillation vial. The other solvents (10 mL DOE and 1 mL OA) were combined in a 3-neck flask and heated to 160 °C. At this time, the $Mn_2(CO)_{10}$ solution was injected into the flask, forming a golden yellow solution. The reaction was heated, and the solution became orange-yellow at 260 °C, then clear at 300 °C. When no additional change in the solution's appearance had taken place after an additional 2 hours of heating at ~300 °C, the heat was discontinued.

5.2.2. Decompositions of $H_2Fe_3(CO)_9P^tBu$ + $Mn(CO)_5Br$

$H_2Fe_3(CO)_9P^tBu$ + $Mn(CO)_5Br$ in TOA & OA (4:4): 0.25 g (0.50 mmol) $H_2Fe_3(CO)_9P^tBu$ and 0.41 g (1.5 mmol) $Mn(CO)_5Br$ were combined in a 3-neck roundbottom flask with 4 mL TOA and 4 mL OA. The bright red solution was heated, becoming foamy at 180 °C. The color of the solution progressed as follows: reddish-brown (250 °C), clear bright red-orange (290 °C), yellow (330 °C), clear gray (335 °C), and black (350 °C). It took ~45 minutes for the color to develop from gray to black. The solution was heated for an additional 20 minutes at ~350 °C after changing to black.

$H_2Fe_3(CO)_9P^tBu$ + $Mn(CO)_5Br$ in TOA & OA (4:4): The decomposition was the same as the previously described reaction, but using only 0.12 g (0.23 mmol) $H_2Fe_3(CO)_9P^tBu$ and 0.19 g (0.68 mmol) $Mn(CO)_5Br$. The reaction followed a similar progression in

color, ultimately changing to a clear black color (not an opaque solution) after the solution was above 300 °C for 15 minutes. The solution was held at ~335 °C for 20 minutes after changing to black.

$H_2Fe_3(CO)_9P^tBu$ + Br_2 in TOA & OA (4:4): 0.25 g (0.5 mmol) $H_2Fe_3(CO)_9P^tBu$ was combined in a 3-neck roundbottom flask with 4 mL TOA and 4 mL OA. To this solution, 25 μL Br_2 was added via micropipettor. The deep red solution was heated, becoming brown-orange (240 °C) then clear bright orange (255 °C) before becoming gray (310 °C). The temperature was held above 300 °C for 20 minutes.

5.2.3. Decomposition of $H_2Fe_3(CO)_9P^tBu$ & manganese formate

$H_2Fe_3(CO)_9P^tBu$ + $Mn(O_2CH)_2$ in TOA & OA (6:2): 0.25 g (0.50 mmol) $H_2Fe_3(CO)_9P^tBu$ and 0.13 g (0.86 mmol) $Mn(O_2CH)_2$ was combined in a 3-neck roundbottom flask with 6 mL TOA and 2 mL OA, forming a dark red solution. As the solution was heated, the color changed to dark brown (240 °C), clear red-orange (260 °C), brown-black (305 °C), and black (315 °C). After changing to black, the solution was maintained at 310-340 °C for 20 minutes.

5.2.4. Decompositions of $HMn_2(CO)_8PPh_2$

$HMn_2(CO)_8PPh_2$ in TOA & OA (4:4): 0.26 g (0.50 mmol) $HMn_2(CO)_8PPh_2$ was combined with 4 mL TOA and 4 mL OA, forming a bright yellow solution (the compound was not fully soluble in the surfactant mixture at room temperature). As the reaction was heated, the color changed to bright orange (150 °C), then duller orange with

a yellow foam (205 °C), red-orange with pale yellow foam (280 °C), clear pale yellow (300 °C), and finally to a clear colorless solution (300 °C). The reaction was heated up to 360 °C and held for 40 minutes, but there was no further change in color. After cooling the solution, ethanol was added but no precipitate was isolated, indicating that no nanoparticles had formed.

$HMn_2(CO)_8PPh_2$ DOE, OA, & OAm: 0.25 g (0.48 mmol) $HMn_2(CO)_8PPh_2$ was dissolved in 2.8 mL DCB in a scintillation vial. The surfactants (10 mL DOE, 0.1 mL OA, and 0.1 mL OAm) were combined a 3-neck roundbottom flask and heated to ~120 °C; at this time the yellow precursor solution was injected into the surfactant solution. The solution gradually changed from yellow to orange (230 °C) to dark red orange (280 °C). After heating at ~330 °C for 4 hours, the solution was still orange, so the heating was discontinued and the reaction was worked up as usual. A small amount of brown solid was obtained and analyzed by TEM.

5.3. Results & Discussion

5.3.1. $H_2Fe_3(CO)_9P^tBu + Mn_2(CO)_{10}$

As a first approach to isolating mixed metal phosphides, $H_2Fe_3(CO)_9P^tBu$ was decomposed with $Mn_2(CO)_{10}$ in a surfactant system of TOA and OA. When a 7:1 ratio (TOA:OA, v:v) was used, small spherical particles formed (Figure 5.1). The TEM images show two different sizes of particles; one is ~10 nm in diameter and the other ~5 nm. No phase confirmation was obtained for these particles, although XPS analysis verified the presence of Fe, Mn, and P (Figure 5.2).

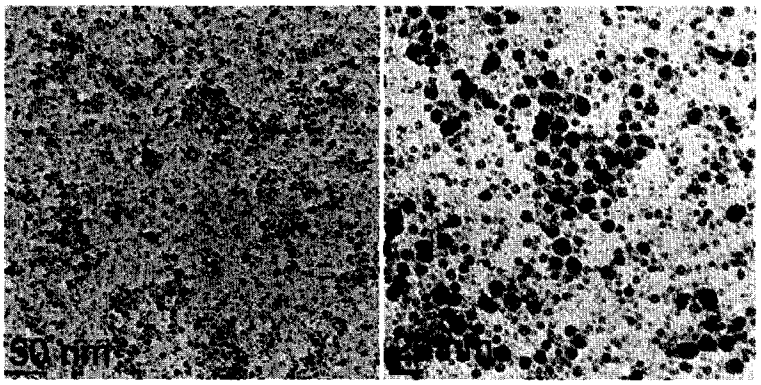

Figure 5.1. TEM images of nanoparticles synthesized via the decomposition of $H_2Fe_3(CO)_9P^tBu$ and $Mn_2(CO)_{10}$ in TOA:OA (7:1).

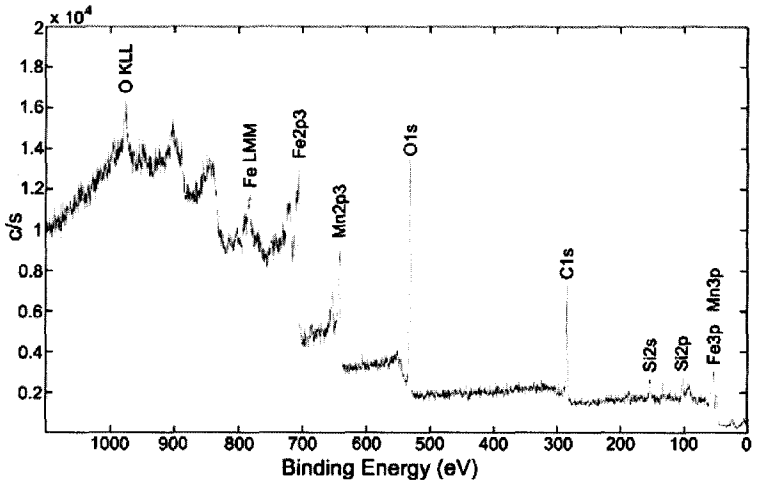

Figure 5.2. XPS spectrum of the nanoparticles synthesized from $H_2Fe_3(CO)_9P^tBu$ and $Mn_2(CO)_{10}$ in TOA:OA (7:1).

When the concentration of OA was increased (4:4 TOA:OA), branched rods were isolated similar to those seen in the iron phosphide system (Figure 5.4). Both XRPD and EDS analysis was performed on the particles (Figure 5.4). The XRPD gave broad peaks; this in addition to the negligible changes in 2θ values upon increases in the Mn concentration made it difficult to get any definitive phase identification with this data (Figure 5.4A includes the PDF files for a few different $Mn_xFe_{1-x}P$ phases to indicate this). EDS analysis of the particles verified the presence of Mn, but it only appeared to be

present in a small amount (Figure 5.4B, weight %: Fe 77.6, Mn 6.1, P 16.3); elemental mapping of these split nanorods can be seen in Figure AV.1. ICP analysis was also performed on these particles (atomic %: Fe 61.4, Mn 4.8, and P 33.7); the obtained values corresponded to $Fe_{1.82}Mn_{0.14}P$.

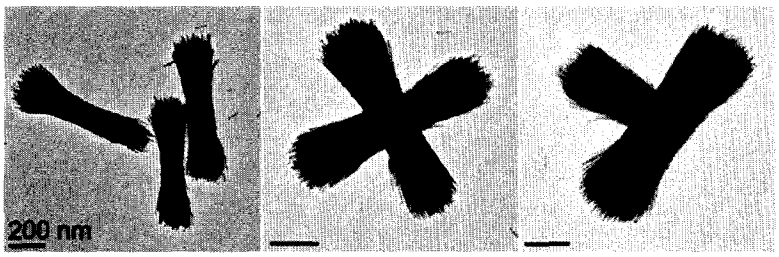

Figure 5.3. TEM images of nanoparticles synthesized via the decomposition of $H_2Fe_3(CO)_9P^tBu$ and $Mn_2(CO)_{10}$ in TOA:OA (4:4). All scalebars correspond to 200 nm.

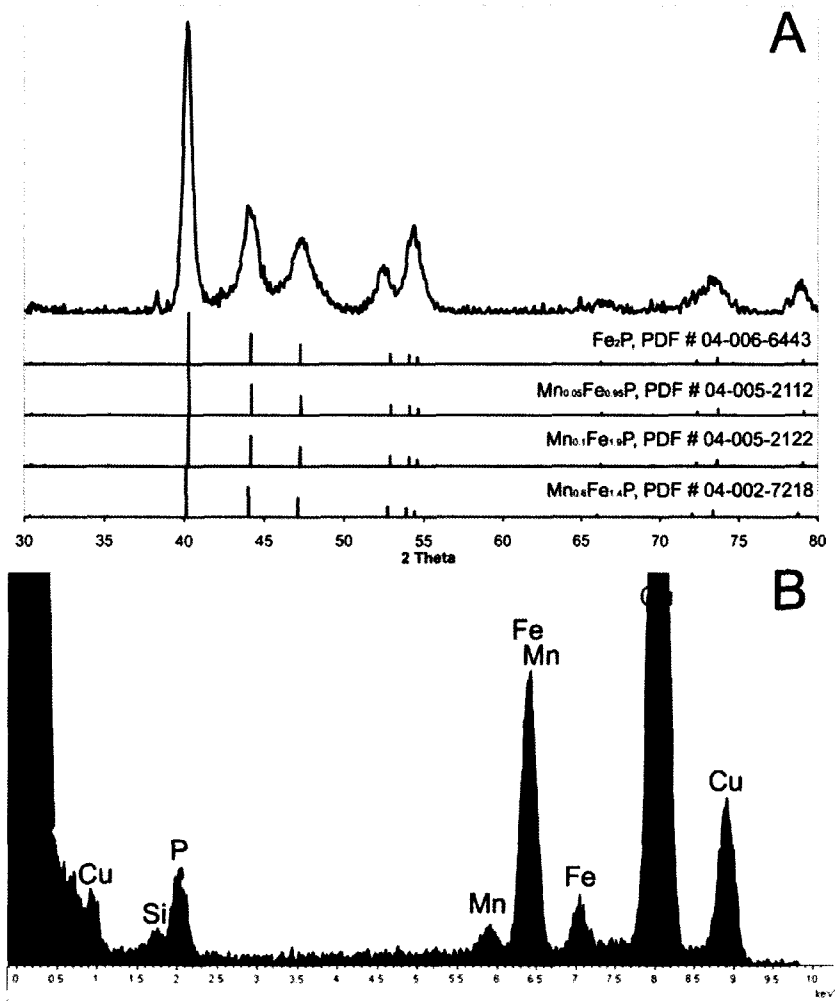

Figure 5.4. (A) XRPD and (B) EDS spectra of the nanoparticles synthesized from $H_2Fe_3(CO)_9P^tBu$ and $Mn_2(CO)_{10}$ in TOA:OA (4:4).

The injection of $H_2Fe_3(CO)_9P^tBu$ and $Mn_2(CO)_{10}$ dissolved in 1,2-dichlorobenzene (DCB) into a preheated solution of dioctylether (DOE) and OA (10:1) resulted in the formation of nanorods with lengths of ~20 nm (Figure 5.5A). There were two injections for this reaction; one was of the majority of the precursors and the second was performed as a rinse in order to ensure that all of the precursor had been added. A second similar decomposition was performed using a single injection to ensure that the double injection did not affect the morphology of the isolated nanoparticles; this reaction

resulted in nanoparticles of the same morphology (see Appendix V for TEM images). The reaction presented in Chapter 3 in which only $H_2Fe_3(CO)_9P^tBu$ was decomposed under the same conditions resulted in nanorods having similar dimensions as those seen in Figure 5.5A.

In order to gain an understanding of the influence of the injection on the outcome of the decomposition, another reaction was carried out in which $H_2Fe_3(CO)_9P^tBu$ and $Mn_2(CO)_{10}$ were combined with DOE and OA (10:1) at room temperature and heated. The resulting nanoparticles (Figure 5.5B) were not as monodisperse as those synthesized via injection of the precursors. EDS analysis of these particles gave the following weight percentages: 76.2% Fe, 3.5% Mn, and 20.4% P (see Figure 5.6 for EDS spectrum). The results of these experiments suggest that injecting the precursors into a pre-heated surfactant system is advantageous for obtaining monodisperse nanoparticles.

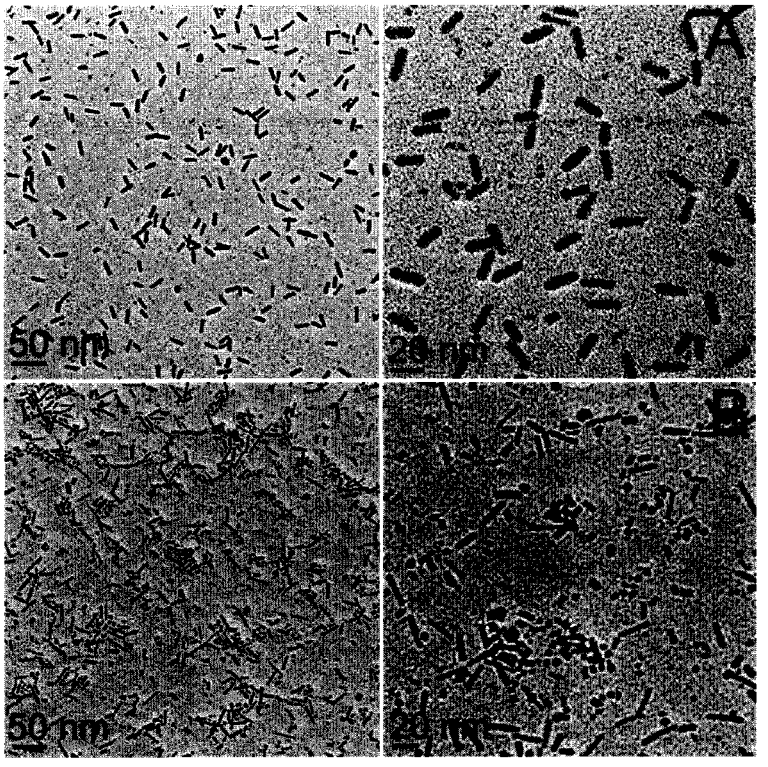

Figure 5.5. TEM images of nanoparticles synthesized via the decomposition of $H_2Fe_3(CO)_9P^tBu$ and $Mn_2(CO)_{10}$ (A) injected into a hot surfactant solution of DOE:OA (10:1) and (B) reagents combined at room temperature and heated.

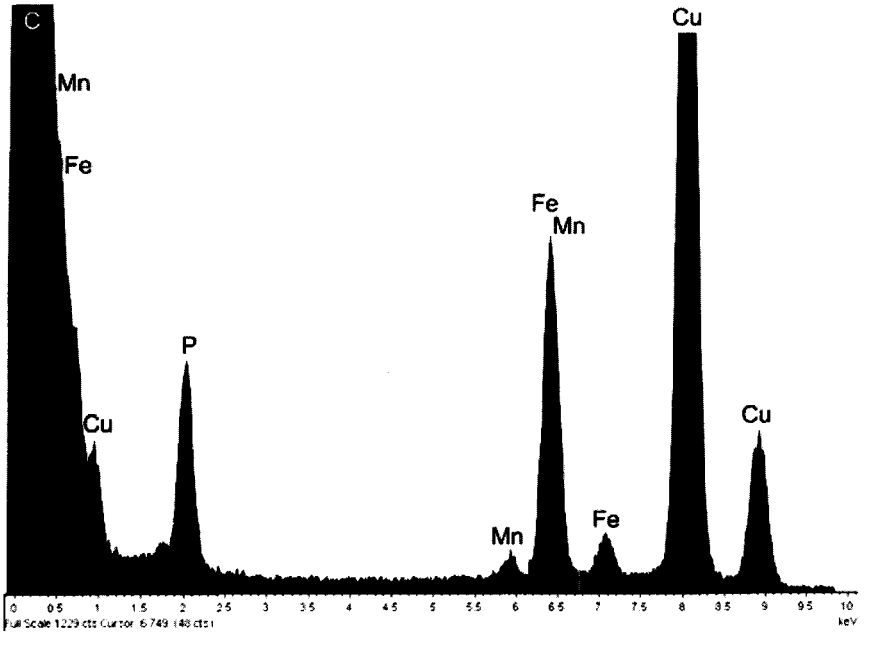

Figure 5.6. EDS spectrum of the decomposition of $H_2Fe_3(CO)_9P^tBu$ and $Mn_2(CO)_{10}$ in DOE and OA (10:1) heated from room temperature.

The nanorods appeared to self-assemble on their ends in a hexagonal close-packed manner when the TEM grid was prepared using EtOH as the solvent (Figure 5.7). EDS analysis of these particles gave weight percentages of 77.2 Fe, 6.4 Mn, and 16.4 P.

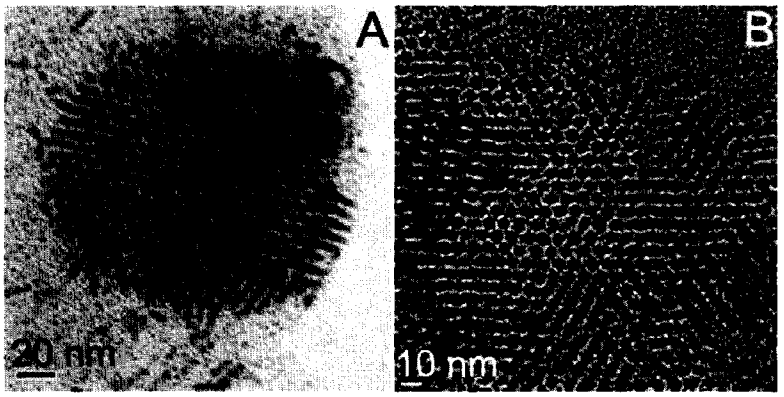

Figure 5.7. TEM images of the self-assembly of the nanorods synthesized via the decomposition of $H_2Fe_3(CO)_9P^tBu$ and $Mn_2(CO)_{10}$ injected into a hot surfactant solution of DOE:OA (10:1).

From the initial experiments performed, it appears that the decomposition of $H_2Fe_3(CO)_9P^tBu$ and $Mn_2(CO)_{10}$ does not present an efficient pathway to the formation of the FeMnP phase.

5.3.2. $H_2Fe_3(CO)_9P^tBu + Mn(CO)_5Br$

In another attempt to synthesize a mixed metal phosphide, $H_2Fe_3(CO)_9P^tBu$ was combined with $Mn(CO)_5Br$ in TOA and OA (1:1) and decomposed. The nanoparticles synthesized have different morphologies than those seen in the same surfactant system when $H_2Fe_3(CO)_9P^tBu$ alone was decomposed (Figure 5.8). In this system, there are nanocrystals that appear to have split in a similar manner, but the bundles are more triangular in shape.

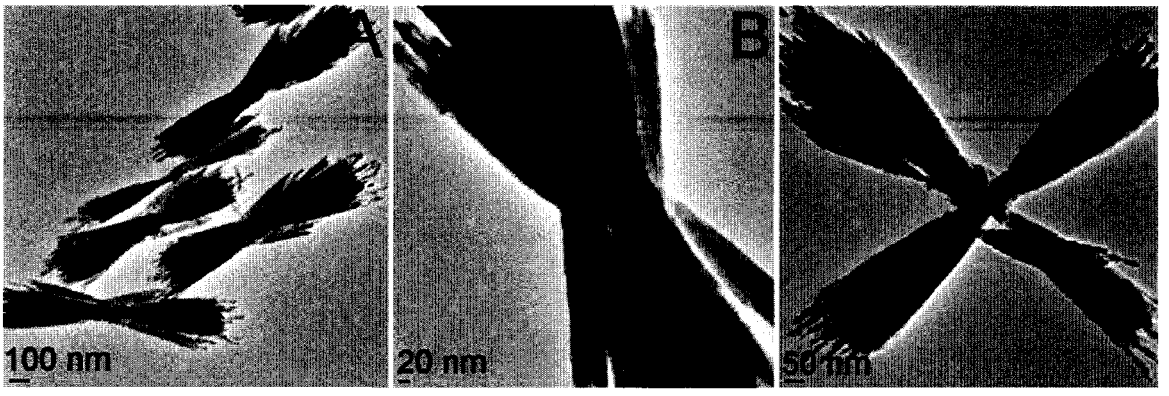

Figure 5.8. TEM images of nanoparticles synthesized via the decomposition of $H_2Fe_3(CO)_9P^tBu$ and $Mn(CO)_5Br$ in TOA and OA (1:1). (A) split bundles, (B) center of one of the bundles, (C) cross-shaped particle with one of the arms partially broken.

XRPD was performed on these particles (Figure 5.9). As was seen with the system using $Mn_2(CO)_{10}$ as the manganese source, XRPD analysis does not serve as an efficient method to determine the elemental composition of the nanoparticles, especially if the system studied results in a phase in which manganese is only incorporated in a small percentage. It does, however, verify the formation of a hexagonal phase, as the patterns displayed under the spectrum demonstrate (Fe_3P is tetragonal while FeP and FeMnP are orthorhombic). Interestingly, both Fe_2P and Mn_2P are hexagonal, but for $(Fe_{1-x}Mn_x)_2P$, when $0.31 \leq x \leq 0.62$, the structure exhibits orthorhombic symmetry.[81] EDS analysis confirmed the presence of manganese; the obtained weight percentages were 78.6 Fe, 7.2 Mn, and 14.2 P (Figure 5.10). Mapping of the elements was also performed, the results of which can be seen in Figure AV.2.

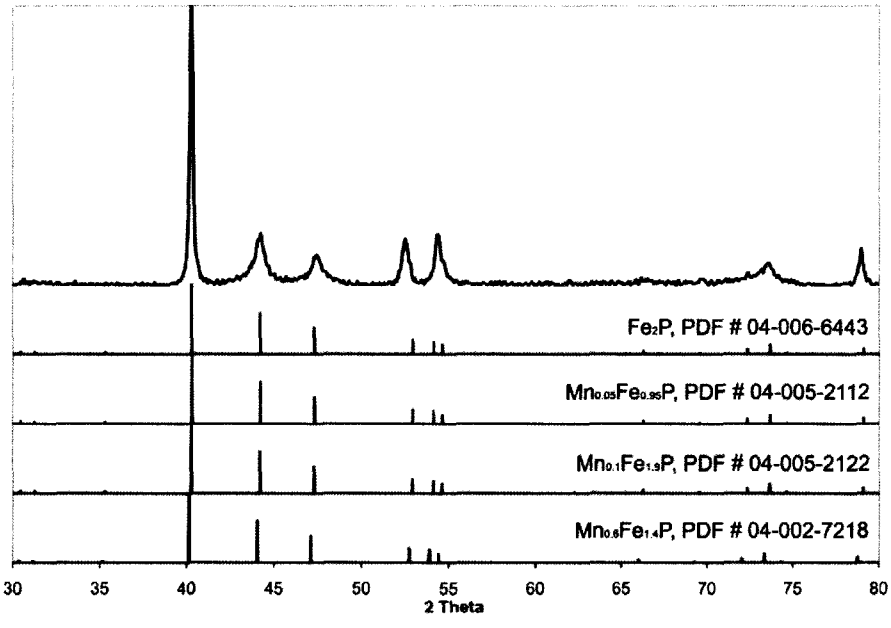

Figure 5.9. XRPD of the nanoparticles synthesized from $H_2Fe_3(CO)_9P^tBu$ and $Mn(CO)_5Br$ in TOA and OA (1:1).

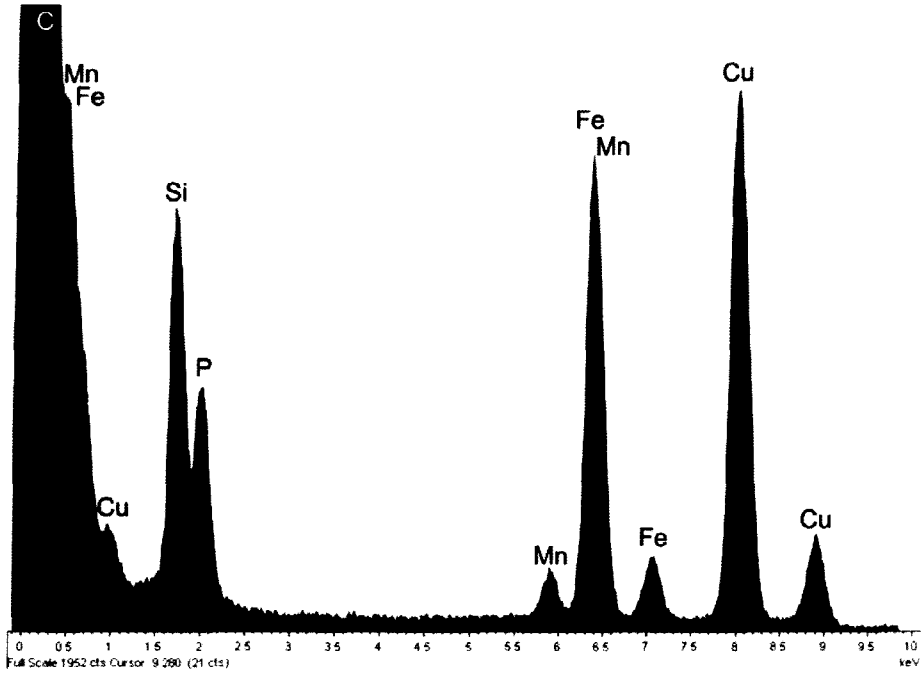

Figure 5.10. EDS spectrum of the nanoparticles synthesized from $H_2Fe_3(CO)_9P^tBu$ and $Mn(CO)_5Br$ in TOA and OA (1:1).

Because $Mn(CO)_5Br$ was synthesized from $Mn_2(CO)_{10}$ and Br_2, there was a possibility that the product used contained some residual Br_2. In order to determine whether the presence of Br_2 in the decomposition solution would affect the nanoparticle morphology, a decomposition was performed of $H_2Fe_3(CO)_9P^tBu$ in TOA and OA (4:4 v:v) with 25 μL Br_2. The isolated nanoparticles are shown in Figure 5.11.

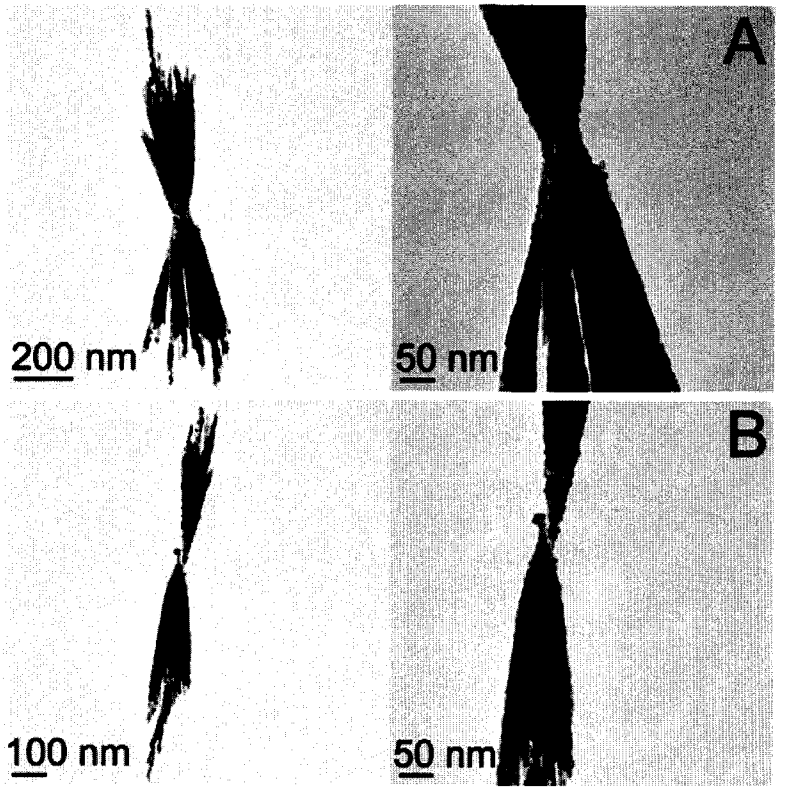

Figure 5.11. TEM images of the nanoparticles synthesized from $H_2Fe_3(CO)_9P^tBu$ in 4 mL TOA, 4 mL OA, and 25 μL Br_2. (A) Fe_2P split bundle, (B) Fe_2P bundle that had broken in half.

The nanoparticles demonstrated a similar morphology to that seen in the decomposition of $H_2Fe_3(CO)_9P^tBu$ and $Mn(CO)_5Br$ in the same surfactant system (Figure 5.8). The similarities seen in these two systems suggest that bromine is playing a role in the shaping of the particles, forming a more triangular-shaped sheaf, causing them to be more fragile at the center and even causing sheaves to break in half in some cases. These

nanoparticles also appear to be less dense than the Fe_2P nanoparticles synthesized in TOA and OA in the absence of Br_2.

There has been some investigation into the role of halide ions in the synthesis of gold nanoparticles.[129] Various morphologies were seen by varying the halide ion present. The presence of KBr in concentrations above 1 mM in the gold system reported by Ha *et al.* resulted in the formation of rods and plates, while concentrations below 1 mM resulted in spherical and rice-shaped nanoparticles. These changes in morphology were attributed to the binding strength of the halide. All of the halide ions, with the exception of F^-, adsorbed onto low-indexed gold surfaces. The degree to which the ions specifically adsorb to a certain crystal surface will influence the shape of nanoparticles formed.[130] In order to fully understand the role of bromine in the iron phosphide system, further experiments will need to be performed with bromine as well as with other halides.

5.3.3. $H_2Fe_3(CO)_9P^tBu + Mn(O_2CH)_2$

Our lab has reported the synthesis of manganese oxide (MnO) nanoparticles in a system of TOA and OA, using manganese (II) formate, $Mn(O_2CH)_2$, as the precursor.[131] Because Mn formate had been used successfully for the formation of nanoparticles in the same surfactant system used in the iron phosphide system, it was used as an alternate source of Mn. The decomposition of $H_2Fe_3(CO)_9P^tBu$ and $Mn(O_2CH)_2$ was carried out in 6 mL TOA and 2 mL OA; the isolated nanoparticles are shown in Figure 5.12.

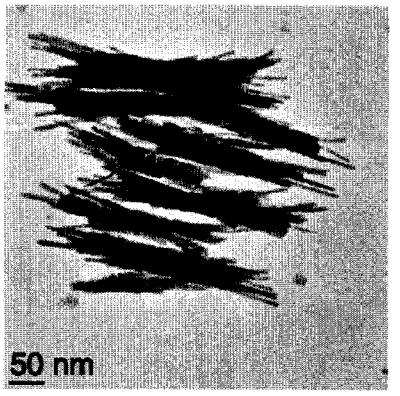

Figure 5.12. TEM image of the nanoparticles synthesized from $H_2Fe_3(CO)_9P^tBu$ and $Mn(O_2CH)_2$ in TOA:OA (6:2).

XRPD and EDS analysis was performed on the nanoparticles (Figure 5.13). The XRPD indicated the formation of a hexagonal phase and the EDS confirmed the presence of Fe, Mn, and P (weight %: 79.3 Fe, 5.7 Mn, 15.0 P).

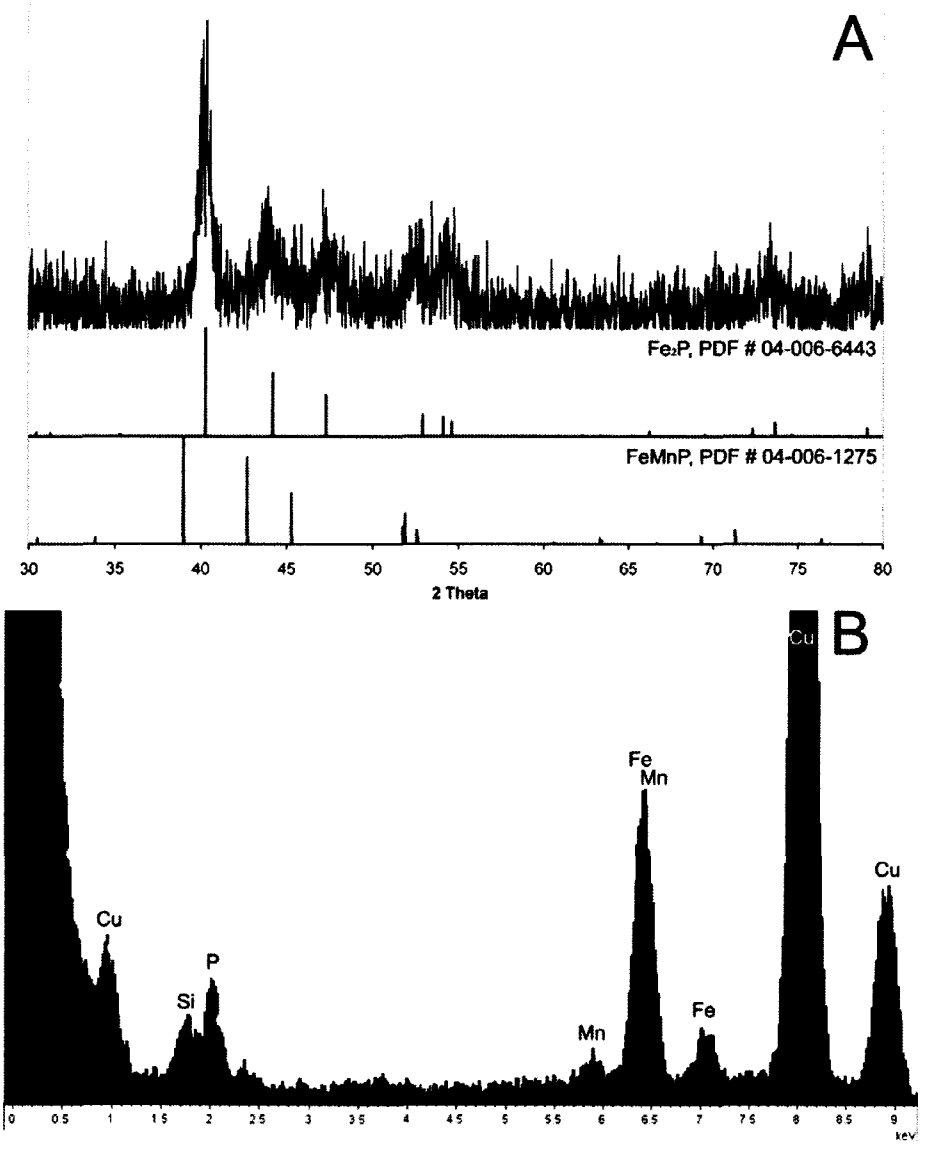

Figure 5.13. (A) XRPD and (B) EDS spectra of the nanoparticles synthesized from $H_2Fe_3(CO)_9P^tBu$ and $Mn(O_2CH)_2$ in TOA OA (6:2).

As was the case with the addition of $Mn_2(CO)_{10}$ or $Mn(CO)_5Br$ as a source of manganese into the decomposition system, the introduction of manganese formate produced a phase containing only a small percentage of manganese. These findings suggest that the use of a single source precursor may present a better route towards the formation of the FeMnP phase.

5.3.4. Decompositions of $HMn_2(CO)_8PPh_2$

The manganese and phosphorus-containing compound, $HMn_2(CO)_8PPh_2$, was decomposed in DOE using OA and OAm as surfactants to determine whether it would serve as an efficient precursor to manganese phosphide materials. The decompositions were carried out using two approaches; heating the precursor from room temperature or injecting the precursor dissolved in DCB into a pre-heated surfactant solution.

When the manganese-phosphorus compound was heated to reflux from room temperature, the solution changed from bright yellow to clear, never darkening further (the reaction was held at reflux for about one hour). No precipitate was isolated after treating the solution with ethanol, indicating that no nanoparticles had formed. In an attempt to determine whether the absence of nanoparticles for the reaction was the result of the disassociation of the compound before it decomposed, another reaction was performed in which the precursor was dissolved in DCB and injected into the surfactant solution at 120 °C. A similar progression was observed for this decomposition, and the reaction was held at reflux for several hours. After treatment with ethanol, a small amount of solid was obtained and analyzed by TEM and EDS (Figure 5.14).

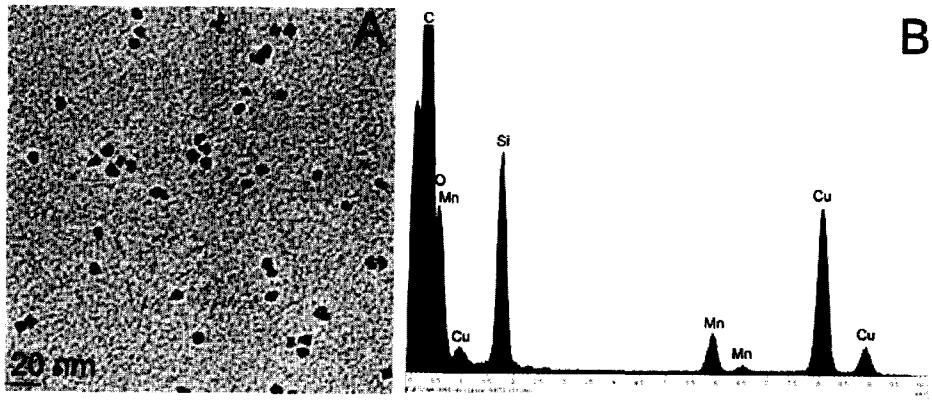

Figure 5.14. (A) TEM image and (B) EDS spectrum of the nanoparticles isolated from the decomposition of $HMn_2(CO)_8PPh_2$ in DOE:OA:OAm (10:0.1:0.1).

The TEM images indicated the formation of small spherical nanoparticles (only a few nanometers in diameter). EDS analysis indicated the presence of manganese, but no phosphorus was detected. An oxygen peak was observed in addition to manganese, suggesting that perhaps a manganese oxide had formed. No further analysis was performed on these particles.

Initial studies into the decomposition of $HMn_2(CO)_8PPh_2$ did not result in the formation of manganese phosphide nanomaterials. Variations of the R group to smaller groups (i.e. H, Me, Et, ^{t}Bu) may result in more successful precursors, as the Ph derivative of the $H_2Fe_3(CO)_9PR$ cluster did not prove to be as efficient a precursor as the ^{t}Bu derivative to Fe_2P nanomaterials.

5.4. Conclusions

Initial reactions combining the iron-phosphorus cluster, $H_2Fe_3(CO)_9P^tBu$, with a manganese-containing compound, $Mn_2(CO)_{10}$, $Mn(CO)_5Br$, or $Mn(O_2CH)_2$, proved unsuccessful in synthesizing the FeMnP phase. Each of the approaches resulted in the formation of a Mn-doped phase of iron phosphide. Further studies in which the solvent system is varied or changing the way in which the precursors are introduced into the system may prove more successful in producing more manganese-rich phases.

Current work in our lab by Adam Colson using a single source precursor, $FeMn(CO)_8PH_2$, for the isolation of FeMnP nanoparticles has yielded better decomposition results. Initial studies using this precursor resulted in the phase $Fe_{1.3}Mn_{0.7}P$, suggesting that this is a more promising approach toward the isolation of the FeMnP phase.

Chapter 6. Gold coated iron phosphide core-shell nanostructures

6.1. Introduction

Much insight has been gained into the control of the size and shape of nanoparticles over the past few years, which in turn allows for their rational design by tuning of their various properties. For example, magnetic nanoparticles have been investigated for use in catalysis, data storage, and biomedical applications.[132-137] Focus has now turned to combining nanoparticles having different properties to make multifunctional materials.[138] In catalysis, recent studies have involved the coupling of catalysts with magnetic nanoparticles for easy recovery of the catalyst.[139,140] Other systems have combined magnetic nanoparticles with fluorescent semiconductor quantum dots to obtain multifunctional nanoparticle systems.[141]

When incorporating magnetic nanoparticles into systems intended for biological applications, careful consideration must be taken to ensure the biocompatibility of the system. Magnetic nanoparticles are often synthesized in organic media and capped with long chain organic surfactants. Therefore, surface functionalization of these particles must be performed to make them biocompatible, one example being the use of starch-coated superparamagnetic iron oxide nanoparticles for *in vitro* thermal ablation of cancer cells.[142] A variety of successful approaches for the functionalization and incorporation of magnetic nanoparticles into biological systems have been reported.[143-145]

The combination of gold with magnetic nanoparticles in a core-shell structure presents an interesting bifunctional system. Gold is well-known for its biocompatibility and plasmonic properties, making it an optimal choice for the surface-coating of a variety

of nanoparticles to produce a non-toxic, water soluble material that can be optically tracked within the body. The gold surface, being relatively chemically inert, resists oxidation and provides protection for the core nanoparticle. Additionally, owing to its high electron density, gold can be visualized easily by microscopy.

There have been a few instances in which gold was used to coat spherical iron oxide nanoparticles.[146,147] Recently, our lab has reported the use of faceted or tetracubic iron oxide nanoparticles as cores coated with a gold shell layer.[148] In this work, it was shown that substitution of the core with a nonspherical morphology results in differences in the optical properties of these materials due to the reduction of symmetry introduced by variations in core geometry. When the spherical symmetry of the core was broken, new plasmon modes and larger shifts appeared in the spectrum, due to the mixing of plasmons of different multipolar symmetry. Other anisotropic core-Au shell morphologies have also been reported, including rice-shaped Fe_2O_3-Au[149] and Au-FeOOH nanomaterials.[150] Elongated structures are particularly interesting because they exhibit two plasmon resonances, transverse and longitudinal. The longitudinal plasmon is polarization dependent and its position is highly sensitive to the aspect ratio of the particles.[151,152]

The synthesis and characterization of iron phosphide (Fe_2P) nanostructures, including split bundles, t-shapes, and crosses with a gold shell layer are explored in this chapter. The anisotropic morphology of these structures is optically interesting because coupling between the plasmons will differ depending on the number and orthogonality of the nanoparticle arms. Two separate reducing agents were investigated for the reduction of gold onto the Fe_2P nanoparticle surface, formaldehyde and carbon monoxide. Both of

these approaches will be presented, along with the corresponding experimentally observed solution extinction spectra for varying degrees of shell thickness.

6.2. Experimental

Gold(III) chloride hydrate, γ-aminobutanoic acid (GABA), and tetrakis(hydroxymethyl)phosphonium chloride (THPC, 80% solution in water), were obtained from Aldrich. Formaldehyde (37% solution in water/ethanol) and potassium carbonate were purchased from Fisher Scientific. Carbon monoxide was obtained from Matheson TriGas. Milli-Q water was obtained from a Millipore Total Q system. Ultraviolet-Visible (UV-Vis) absorption studies were performed on a Varian Cary 5000 UV-Vis-NIR Spectrophotometer.

Core-shell nanostructure formation

The iron phosphide nanoparticles were coated with gold using a procedure based on that described by Oldenburg *et al.* for coating silica NPs.[153,154] The method was modified because the 3-aminopropyltrimethoxysilane (APTMS) used by Oldenburg *et al.* was not applicable to the iron phosphide system, as the $-Si(OMe)_3$ end of the molecule would not bind to the iron phosphide nanoparticles due to the absence of any oxygen atoms at the surface. Therefore, γ-aminobutanoic acid (GABA) was used instead, with the carboxylic acid functionality for binding to the surface of the Fe_2P nanoparticles and the amine group for the attachment of small (~1 to 2 nm) colloidal gold nanoparticles (Scheme 6.1). This ligand exchange step also served to make the particles water soluble by replacing the hydrophobic oleic acid surfactant. The gold colloid was prepared

according to Duff *et al.*,[155] and the colloidal solution was aged for at least two weeks before use.

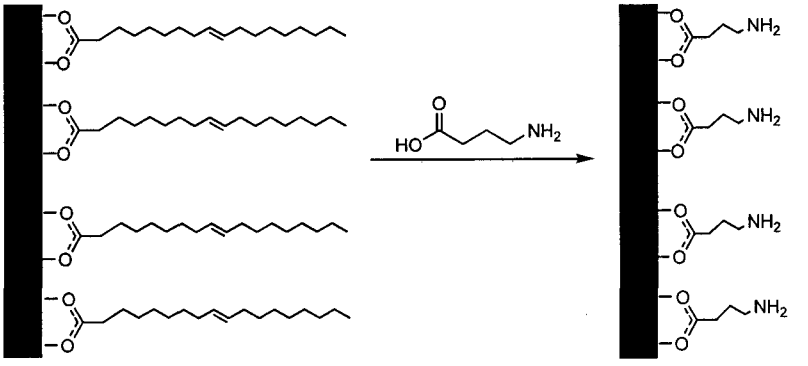

Scheme 6.1. Functionalization of the Fe_2P nanostructures with GABA via ligand exchange.

Functionalization with GABA was accomplished by dissolving 0.10 g (1 mmol) of GABA in ~1 mL of deionized water in a scintillation vial. To this, a concentrated solution of iron phosphide nanoparticles in hexane (~5 mL) was added dropwise with vigorous stirring. The solution was stirred overnight. When the stirring was terminated, the less dense hexane layer was clear and the aqueous layer was dark gray, indicating that the surfactant exchange had been successful, resulting in water soluble iron phosphide nanoparticles. A series of washes with water, involving the centrifugation of the sample followed by the removal of the supernatant and redispersion of the particles in water, were performed to remove any excess GABA present.

Decorated precursor nanoparticles were prepared by combining 40 mL of the colloidal gold solution with a concentrated solution of the GABA-functionalized iron phosphide nanoparticles in ethanol (~ 1 mL) and 4 mL of 1 M NaCl in a 50 mL centrifuge tube. The tube was shaken, then sonicated briefly and placed in a refrigerator overnight. The solution was centrifuged (the optimum setting was 3000 rcf for 20-30

minutes), leaving a small pellet at the bottom or side of the tube. The supernatant was removed, and the precipitated solid was washed a couple of times with H_2O to remove any free colloidal gold. The aqueous suspension of gold-decorated nanoparticles was purple in color.

Varying amounts of the Au-decorated precursor nanoparticles in H_2O were added to an aqueous potassium carbonate-gold (III) chloride hydrate ($K_2CO_3/HAuCl_4$) solution. The plating solution was made using 400 mL Milli-Q H_2O, 0.1 g K_2CO_3, and 6 mL of an aqueous 1% $HAuCl_4$ solution. The colloidal gold on the surface of the Fe_2P nanostructures functioned as nucleation sites for the reduction of Au^{3+} to Au^o using either formaldehyde or carbon monoxide. In the case of formaldehyde, 20 μL of formaldehyde was added to the decorated precursor/plating solution (50, 75, 100, or 125 μL of decorated precursor solution combined with 3 mL of plating solution) and the vial was shaken in order to initialize the reaction and ensure that the reduction was homogeneous throughout the solution. After extinction spectra were acquired, the solutions were centrifuged and washed with Milli-Q H_2O in order to stop the reaction and remove any residual formaldehyde. When CO was used as the reducing agent, 6 mL of the plating solution was combined with varying amounts of decorated precursor solution (25, 50, 75, 100, and 125 μL) in a vial and the solution was bubbled with CO for ~1 minute. As the solution was bubbled, the color changed to varying shades of pale gray to pink, depending on the thickness of the gold shell formed. The products were characterized using UV-Vis spectroscopy and TEM.

6.3. Results & Discussion

The first step toward the formation of Fe_2P-Au core-shell structures was the functionalization of the Fe_2P nanoparticles to promote water solubility and introduce a linker for the attachment of small gold colloid. There are a variety of publications in which ligand exchange was used to transfer nanoparticles from organic to aqueous solutions.[156-160] In the case of silica-Au nanoshells, aminopropyltriethoxysilane (APTES) was used to functionalize the silica cores before the deposition of gold. [153,154]

Previous reports for the synthesis of iron oxide nanoparticles with a gold shell used a ligand exchange reaction with an amino silane (such as APTES) to displace the long-chain surfactants, resulting in hydrophilic nanoparticles.[149,161,162] This approach was attempted in the iron phosphide system, but was unsuccessful, likely because the functionalization with APTMS is thought to occur through the free hydroxide terminal groups on the surface of the nanoparticles that would bind easily to the silane moiety. As this kind of functionality is not present on the Fe_2P nanoparticles, a different approach was taken to the solubilization. Decoration of the core nanoparticles with colloidal gold is known to take place via the covalent bonding of gold nanoparticles to the lone pair of terminal $-NH_2$ groups,[162,163] as was seen in the functionalization of the aminosilane-coated iron oxide nanoparticles. The capping agent chosen was γ-aminobutyric acid (GABA) because it is a short-chain molecule with both amine and carboxylic acid functionalities. It was believed that the carboxylic acid would bind to the surface of the iron phosphide particles, displacing the oleic acid present in the original system, leaving the amine functionality available for binding to the colloidal gold nanoparticles. Figure 6.1 shows an example of the Au-decorated Fe_2P nanorods.

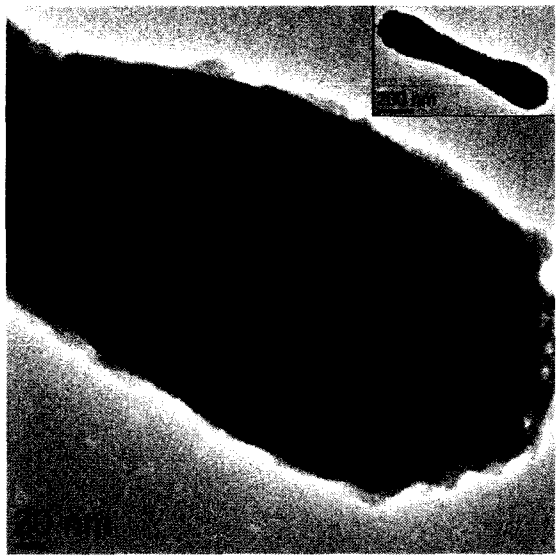

Figure 6.1. TEM image of the Fe_2P nanorod after decoration with Au colloid (inset shows the entire nanorod).

Once the Au-decorated precursor nanoparticles were obtained, electroless gold plating was accomplished using an aqueous solution of $HAuCl_4$, which was reduced onto the nanoparticles using formaldehyde or carbon monoxide, forming a layer of gold around the Fe_2P nanoparticles. The thickness of the gold shell is related to the amount of precursor solution added and the concentration of Au^{3+} in the solution. The general procedure for the formation of Au-coated Fe_2P nanoparticles is depicted in Scheme 6.2.

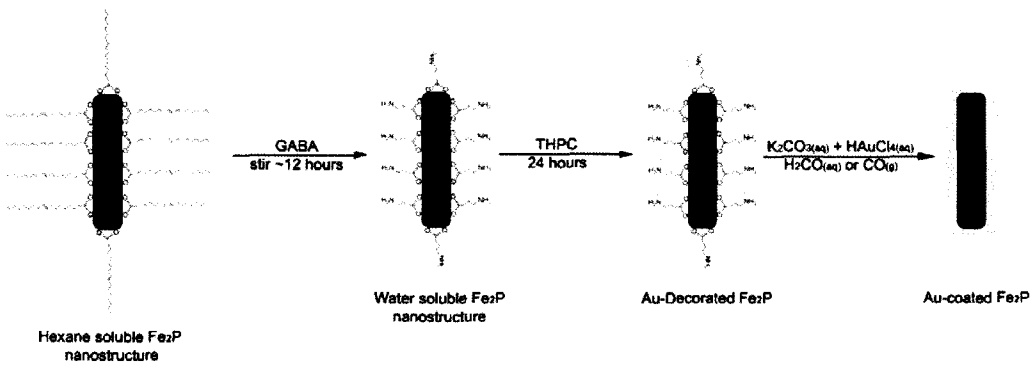

Scheme 6.2. General procedure for the coating of Fe_2P nanoparticles with gold to form Fe_2P-Au nanostructures (not to scale).

Formaldehyde has traditionally been used as the reducing agent in the synthesis of silica-Au nanoshells. However, a recent publication by Brinson *et al.* reported the use of carbon monoxide gas as the reducing agent to produce high quality, thin gold shell layers.[161] The results of both the formaldehyde and carbon monoxide reductions will be presented.

6.3.1. Formaldehyde Reduction

Nanoparticles synthesized from $H_2Fe_3(CO)_9P^tBu$ in a 1:1 system of TOA:OA were used for the experiments using formaldehyde as the reducing agent. Figure 6.2 depicts the nanoparticles before and after the treatment with GABA and decorating with gold colloid. In the water solubilization step, some of the sheaves were split in half, as can be seen in Figure 6.2F. A similar morphology was seen when $H_2Fe_3(CO)_9P^tBu$ was decomposed in a TOA:OA system with the addition of 100 μL of ethanol (Figure 2.14F). Aside from this, the morphology of the Fe_2P nanostructures remained the same after functionalization with GABA.

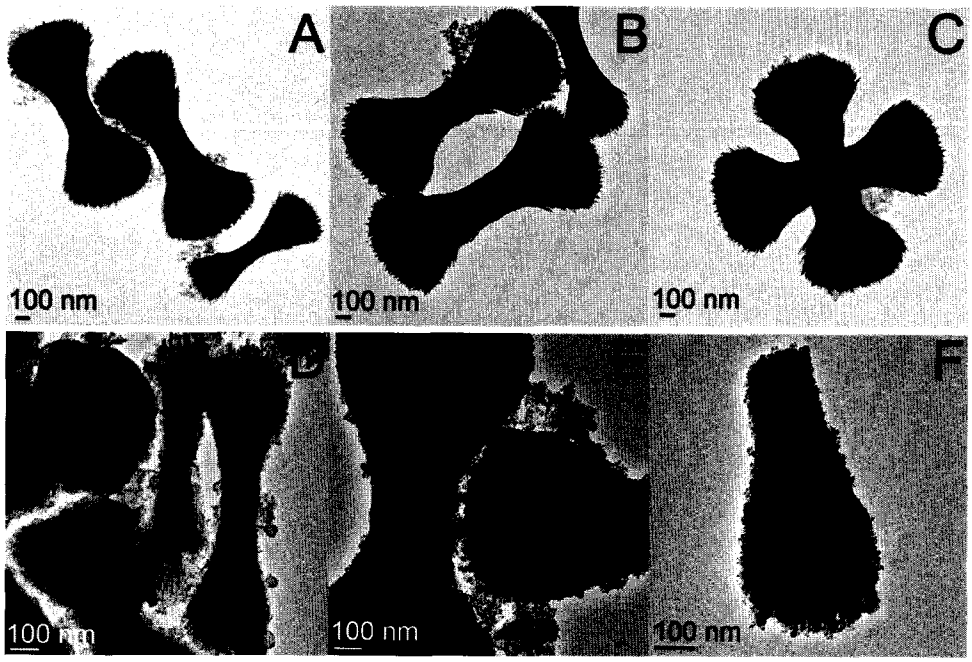

Figure 6.2. TEM images of the Fe_2P nanoparticles (A-C) as synthesized, dispersed in hexane and (D-F) after being solubilized in water and decorated with Au nanoparticles.

After decorating the precursor with gold colloid, the particles were combined in various amounts (50, 75, 100, 125, and 150 μL) with an aqueous gold plating solution ($HAuCl_4$ and K_2CO_3). Formaldehyde (20 μL) was then introduced to initiate the reduction of gold. Depending on the concentration of precursor particles present, the shell thickness varied, as can be seen in Figure 6.3. In the cases where less precursor was added, the gold shell was thicker and excess gold colloid was observed in the TEM images (as seen in Figure 6.3A-C).

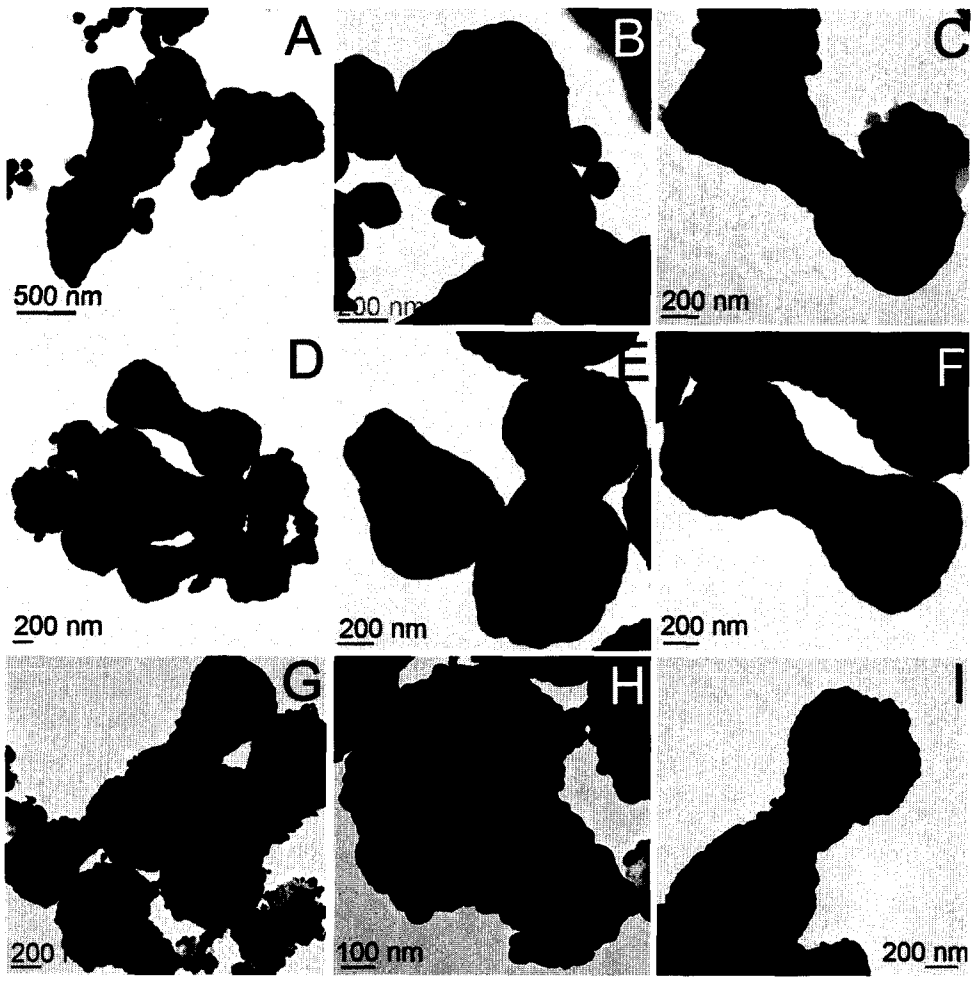

Figure 6.3. TEM images of the Fe_2P nanoparticles plated with a gold shell via formaldehyde reduction, using (A-C) 50 μL, (D-F) 75 μL, and (G-I) 125 μL of decorated precursor.

As the amount of decorated precursor was increased and combined with a constant amount of plating solution, thinner gold shells were formed around the Fe_2P structures. Extinction measurements were taken of the Au-Fe_2P core-shell structures in order to determine their plasmonic properties as a function of shell thickness (Figure 6.4). A redshift in the plasmon absorption peak was observed as the shell thickness increased.

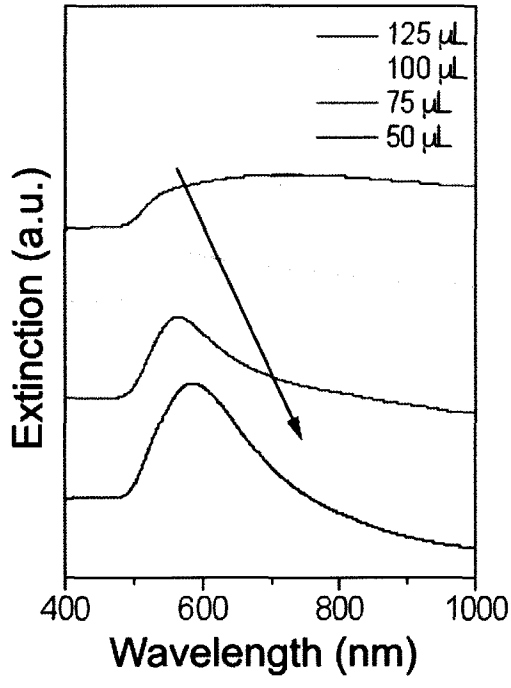

Figure 6.4. Solution extinction spectra of the Fe_2P-Au core-shell particles synthesized using formaldehyde reduction (λ_{max} = 584 nm for 50 μL, 565 nm for 75 μL, 559 nm for 100 μL, and 540 nm for 125 μL of decorated precursor). Spectra offset for clarity.

It is known that the plasmon resonant response of core-shell nanostructures will be dependent upon the core and shell dimensions, as well as the dielectric properties of the core, shell, and embedding medium.[164] In silica-gold core-shell nanostructures, a blueshift is observed as the thickness of the gold shell is increased.[154,165] Conversely, when iron oxide (Fe_3O_4 or FeO) cores with gold shells were studied, a redshift was observed upon increasing thickness of the gold shell.[147,148] This change in the optical behavior from silica to iron oxide nanoshells has been explained in terms of plasmon hybridization.[148,166,167] The redshift in the plasmon resonance as a function of increasing shell thickness is attributed to the high permittivity of the core iron oxide material (as compared to silica, which has a low permittivity).

6.3.2. Carbon Monoxide

Nanoparticles synthesized from $H_2Fe_3(CO)_9P^tBu$ in 2 mL TOA and 6 mL OA were used for the experiments using carbon monoxide as the reducing agent. Figure 6.5 depicts the Fe_2P nanoparticles before water solubilization with GABA (Figure 6.5A-B) and after decorating with gold colloid (Figure 6.5C-D).

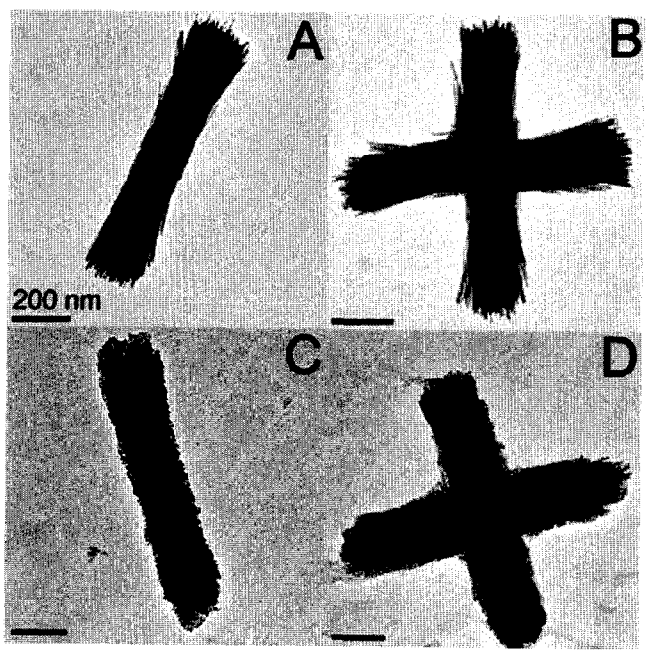

Figure 6.5. TEM images of the split Fe_2P nanorods and crosses. (A-B) Original nanoparticles dispersed in hexane and (C-D) Nanoparticles functionalized with GABA and decorated with small colloidal gold particles. All scalebars are 200 nm.

As was the case with the formaldehyde system, different volumes of decorated precursor were combined with a constant volume of plating solution. These solutions were then bubbled with carbon monoxide for 60 seconds. A representative SEM image for the 50 μL decorated precursor system and TEM images for the 75, 100, and 125 μL decorated precursor systems can be found in Appendix VI (Figure AVI.1 and Figure AVI.2). Extinction measurements were performed on the Fe_2P-Au solutions (Figure 6.6).

A more thorough presentation of the dimensions of the particles along with aspect ratio and shell thickness information can be found in Appendix VI.

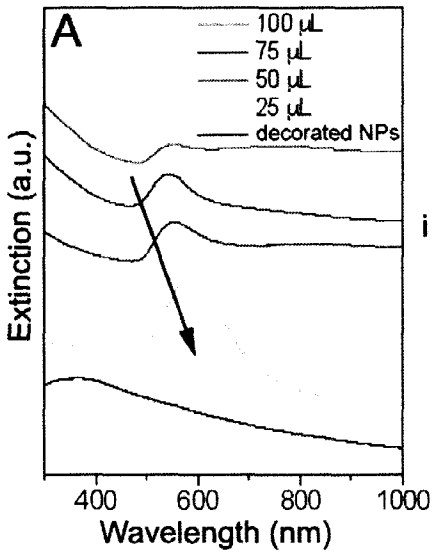

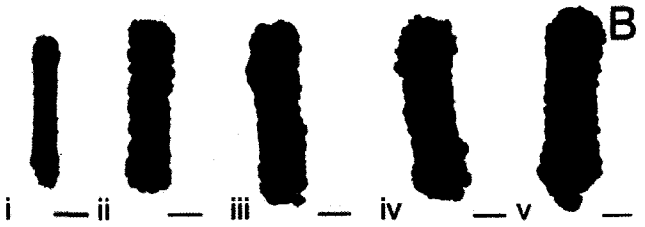

Volume of Decorated Precursor	Width (nm)	λ_{max} (nm)
Decorated Fe_2P (i)	193 ± 22	365
100 µL (ii)	246 ± 27	555
75 µL (iii)	279 ± 38	542
50 µL (iv)	317 ± 53	555
25 µL (v)	323 ± 42	588

Figure 6.6. (A) Solution extinction spectra of the carbon monoxide reduction with various decorated precursor volumes (spectra offset for clarity). (B) TEM images of (i) Au-decorated Fe_2P nanostructure and the Fe_2P-Au core-shell nanostructures synthesized by the reduction of Au onto the surface with (ii) 100 µL, (iii) 75 µL, (iv) 50 µL, and (v) 25 µL of decorated precursor. All scalebars are 200 nm.

As was seen for the formaldehyde reduced Fe_2P-Au particles, the extinction maximum increased as the shell thickness increased. The absorption for the sample made using 100 µL of decorated precursor redshifted back to higher wavelength, likely due to the fact that some of the Fe_2P nanostructures in this sample were not completely coated with a continuous gold layer (Figure 6.7).

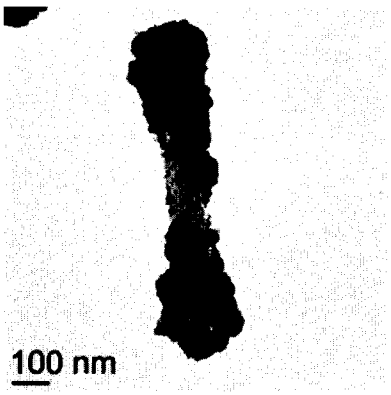

Figure 6.7. TEM image of a partially coated Fe_2P nanorod from the sample in which 100 μL of decorated precursor was used.

Gold nanorods are known to exhibit two surface plasmon modes, longitudinal and transverse, the longitudinal mode occurring at higher wavelengths than the transverse mode. It is expected that the anisotropic Au-Fe_2P structures should exhibit both transverse and longitudinal modes; the values reported here are believed to be of the higher energy transverse modes. Frequency of the longitudinal plasmon mode is known to depend sensitively on variations in aspect ratio[152,168,169] and polarization[152] and can occur into the near infrared (IR).[170,171] Mirkin *et al.* studied the extinction spectra in D_2O of gold rods of various lengths (96, 641, 735, and 1175 nm), all having diameters of ~85 nm.[170] For rods with lengths of 96 nm, the aspect ratio was close to 1, causing the transverse and longitudinal modes to overlap, resulting in one broad peak at ~600 nm. As the aspect ratio was increased, the longitudinal mode shifted to higher wavelengths, with a maximum value of 1410 nm (for the 1175 nm long rods, aspect ratio ~14). There have also been reports of the longitudinal band occurring in the mid IR region for Au, Ni, and Pd nanorods with aspect ratios greater than 25.[172]

Attempts to identify the longitudinal mode for the Au-Fe_2P structures were unsuccessful due to experimental limitations. However, work is currently underway in

collaboration with the Halas and Hafner groups to perform polarization-dependent dark field single particle microscopy.[173] These measurements will provide more accurate information regarding how the shape of the particle influences the plasmon peaks, as the data presented here were collected as ensemble measurements in water, and there are a variety of shapes and orientations present, as seen in Figure 6.8 and Figure 6.9.

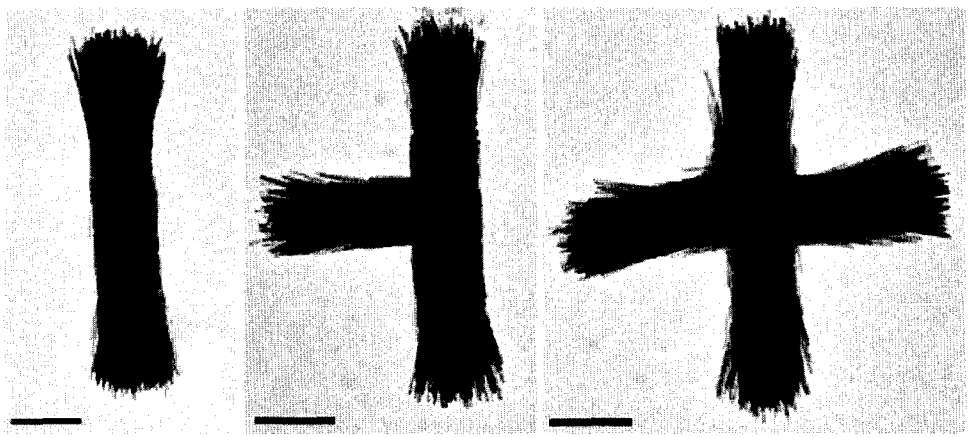

Figure 6.8. TEM images of rods, T-shapes, and crosses of unfunctionalized Fe_2P nanoparticles. All scalebars are 200 nm.

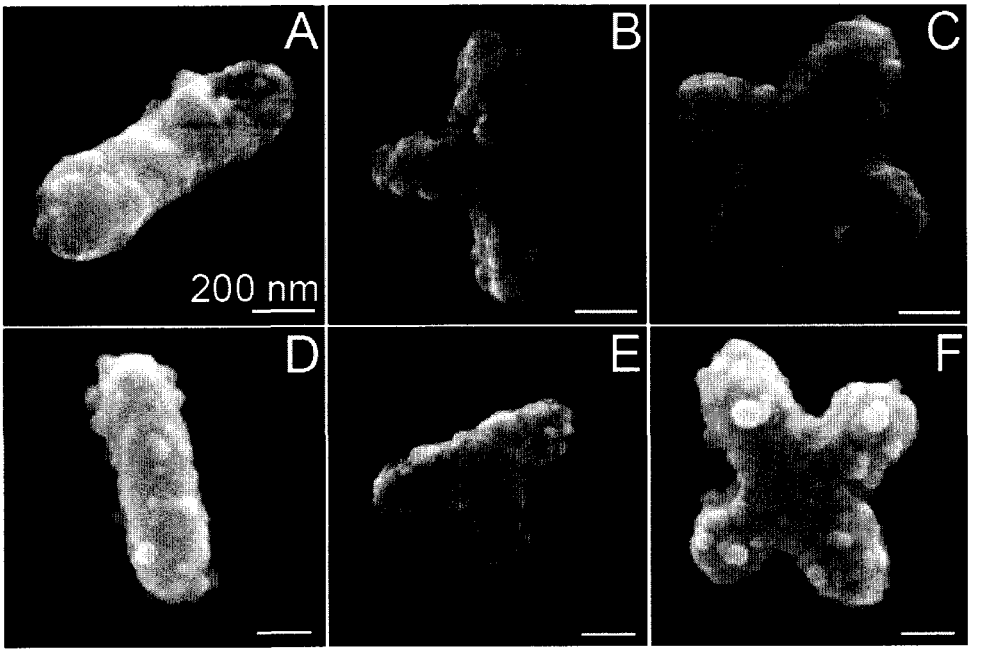

Figure 6.9. SEM images of rods, T-shapes, and crosses of the Fe_2P-Au core-shell structures for systems using (A-C) 25 μL and (D-F) 50 μL decorated precursor solutions (100,000X magnification). All scalebars are 200 nm.

6.4. Conclusions

Fe_2P split rods, T-shapes, and crosses were all successfully made water soluble through ligand exchange to replace the hydrophobic oleic acid present on the surface following their synthesis with the smaller GABA ligand. Water solubilization of these structures allowed for them to be coated with a gold shell, the amine group of the GABA serving to bind the colloidal gold particles. The reduction of gold onto the surface of the Fe_2P nanostructures resulted in thinner shell layers without the synthesis of excess gold colloid when the reduction was performed using carbon monoxide as opposed to formaldehyde. Their optical properties were studied, and a redshift in the extinction maximum was seen as the shell thickness increased. This plasmon peak shift, as opposed to the trends seen in silica-Au core-shell structures as shell thickness increases, is

attributed to the high permittivity of the Fe_2P core. The same trend has been reported in the coating of iron oxide (Fe_xO-Fe_3O_4) nanoparticles.[148]

Further studies into how changes in the shape of the Fe_2P core affect the optical properties of these core-shell nanostructures will be performed by single particle spectroscopy. Additionally, using the various other morphologies of the Fe_2P phase presented in previous chapters, there are a multitude of different shaped core-shell structures that could be synthesized and studied in the future.

Appendix I. Supplementary Information for Chapter 2.

Table AI.1. Summary of the decompositions of $H_2Fe_3(CO)_9P^tBu$. All decompositions were performed using the same batch of precursor.

Precursor (mmol)	TOA:OA (mL)	Other solvent, amount (μL)	
0.39	6:2	0	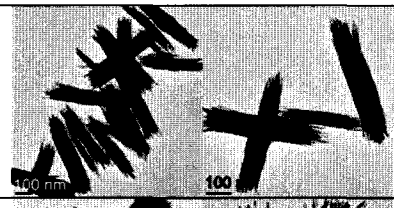
0.48	4:4	hexane, 200	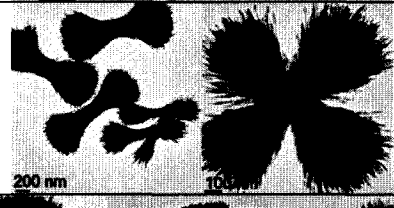
0.49	4:4	hexane, 400	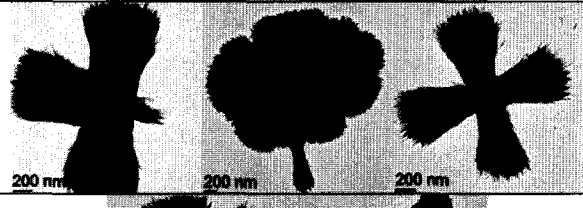
0.49	4:4	hexane, 100	
0.48	4:4	n-tridecane, 200	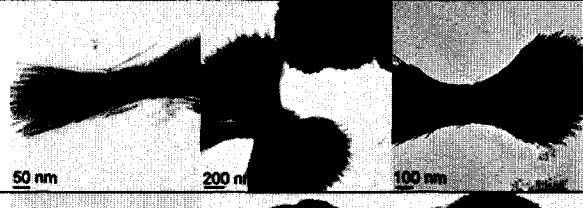
0.49	4:4	nonane, 200	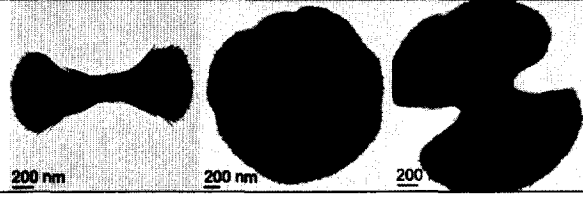

Table AI.2. Decomposition results with different methods of stirring.

Precursor (mmol)	Solvent	Stirring Conditions	TEM
0.49	6 mL TOA 2 mL OA	No stirring, on hotplate	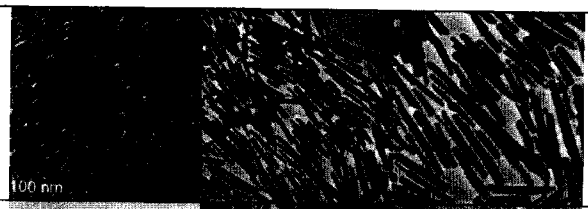
0.53	6 mL TOA 2 mL OA	Stirbar in flask, flask on jack	
0.55	4 mL TOA 4 mL OA	mechanical	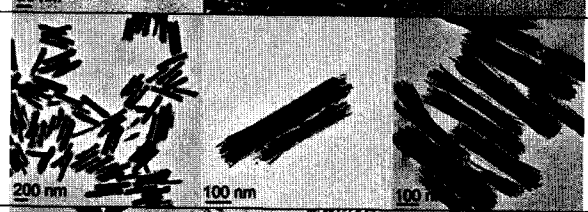
0.19	2 mL TOA 2 mL OA 100 µL hexane	No stirbar, on stirplate	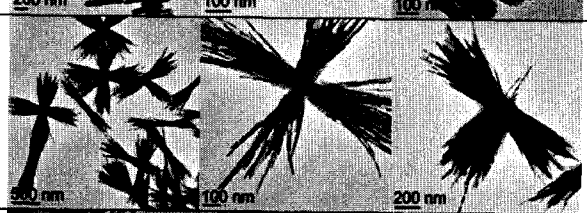
0.19	2 mL TOA 2 mL OA	No stirbar, on stirplate	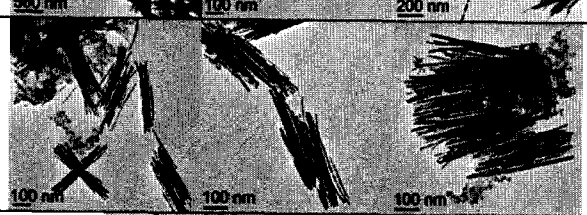
0.24	3 mL TOA 1 mL OA	No stirbar, on jack	

Appendix II. Additional spectral data for experiments presented in Chapter 3.

Note: For all EDS spectra shown in this appendix, the Cu peaks observed result from the TEM grid on which the samples were prepared. Also, for the spectra of smaller particles, Si peaks were observed, likely due to contamination from grease.

Figure AII.1. EDS spectrum of the injection of $H_2Fe_3(CO)_9P^tBu$ into a hot surfactant system (TOA/OA).

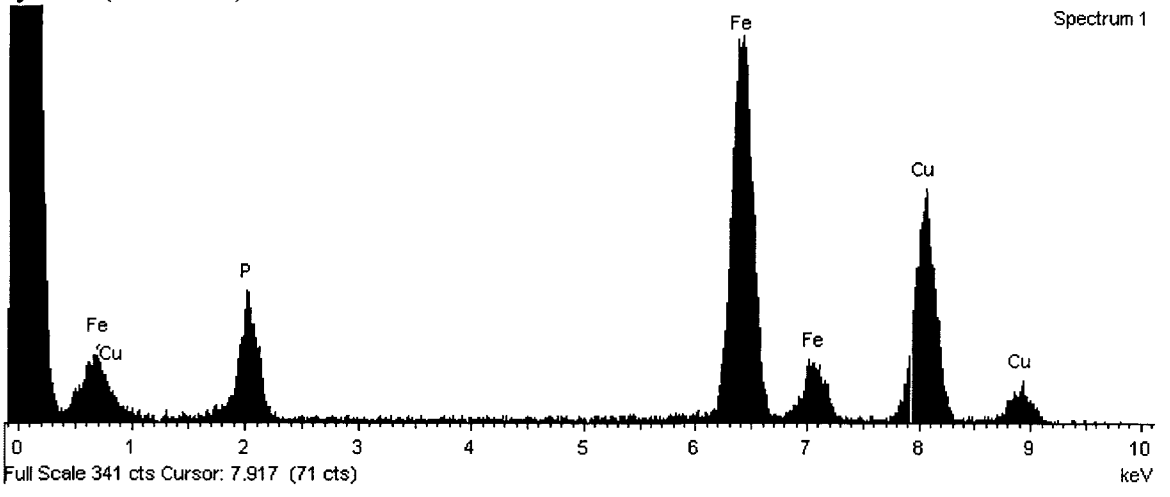

Figure AII.2. EDS data collected for the decomposition of $H_2Fe_3(CO)_9P^tBu$ in 6:2 ODE:OA (split rods and spheres). The pink box represents the area of the sample analyzed. For the first spectrum, the weight percentage values obtained are close to that of Fe_2P (calculated values: 78.3% Fe, 21.7% P). The second spectrum values are close to FeP (calculated values: 64.3% Fe, 35.7% P).

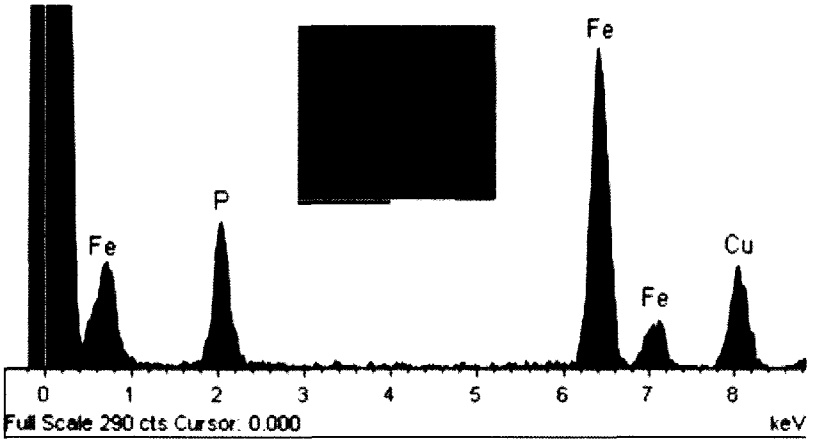

Element	Peak Area	Area Sigma	**Weight%**	Weight% Sigma	Atomic%
P K	1117	62	**23.64**	1.14	35.82
Fe K	3210	93	**76.36**	1.14	64.18

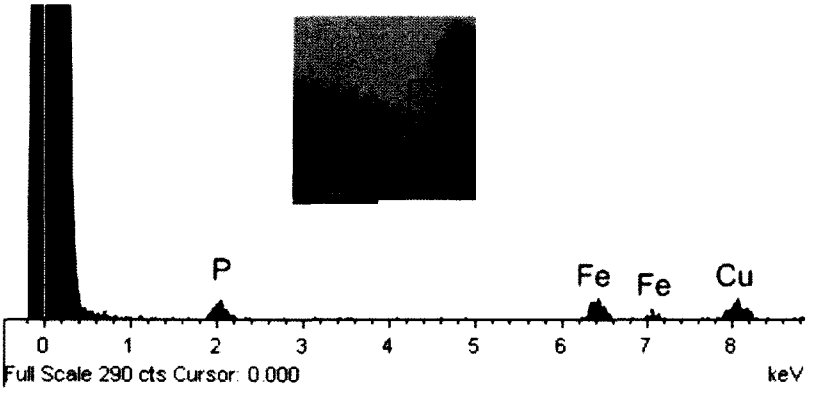

Element	Peak Area	Area Sigma	**Weight%**	Weight% Sigma	Atomic%
P K	135	22	**38.97**	4.96	53.52
Fe K	186	25	**61.03**	4.96	46.48

Figure AII.3. Whole Pattern Fitting of the XRPD spectrum from the decomposition of $H_2Fe_3(CO)_9P^tBu$ in ODE:OA (6:2); the graph on top shows the original data with the derived pattern overlayed, while the bottom graph shows the derived pattern along with the PDF files of the phases present. Based on the EDS data presented in the previous figure, it appears that the split nanorods are Fe_2P and the spherical particles are FeP.

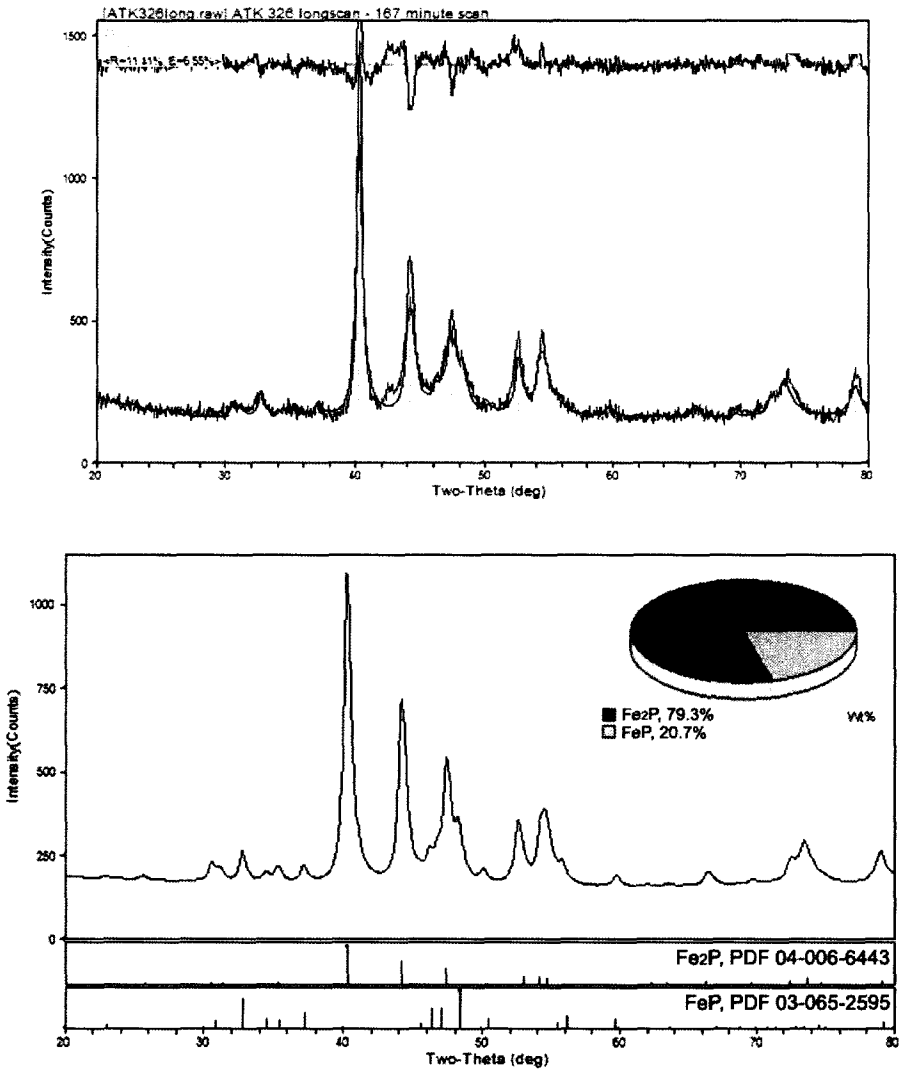

Figure AII.4. EDS spectrum of the decomposition of $H_2Fe_3(CO)_9P^tBu$ in 10:1 DOE:OA.

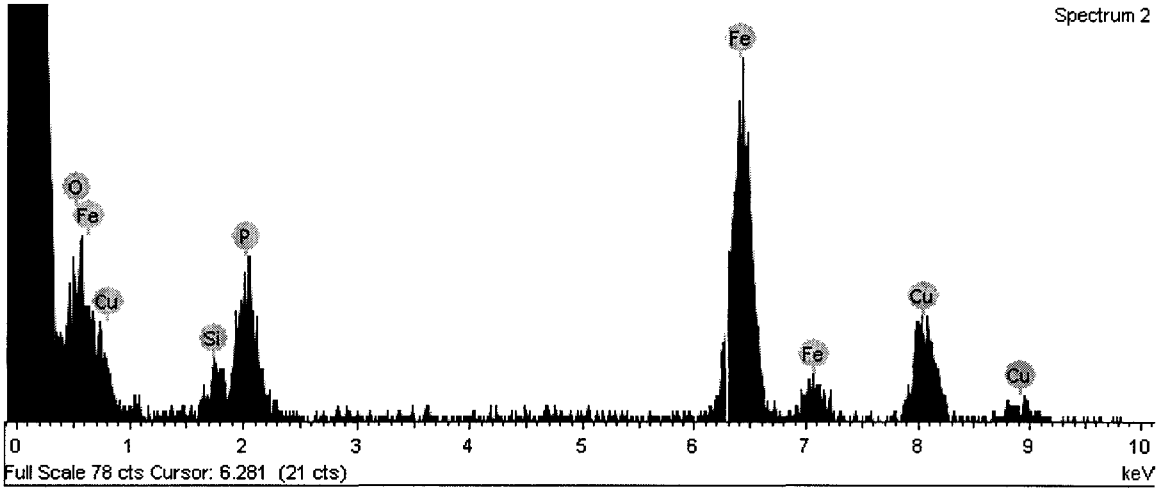

Figure AII.5. EDS spectrum of the decomposition of $H_2Fe_3(CO)_9P^tBu$ in 7:1 HDA:OA.

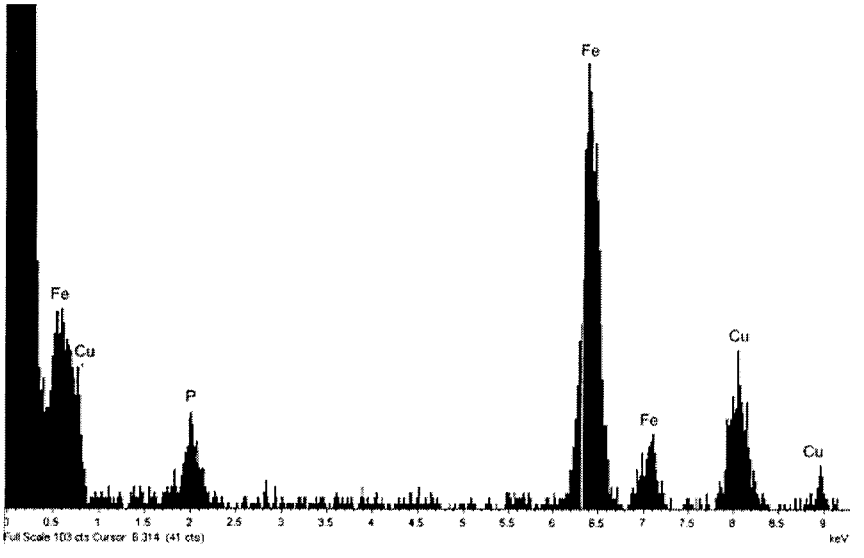

Figure AII.6. EDS spectrum of the decomposition of $H_2Fe_3(CO)_9P^tBu$ in 7:1 OOH:OA.

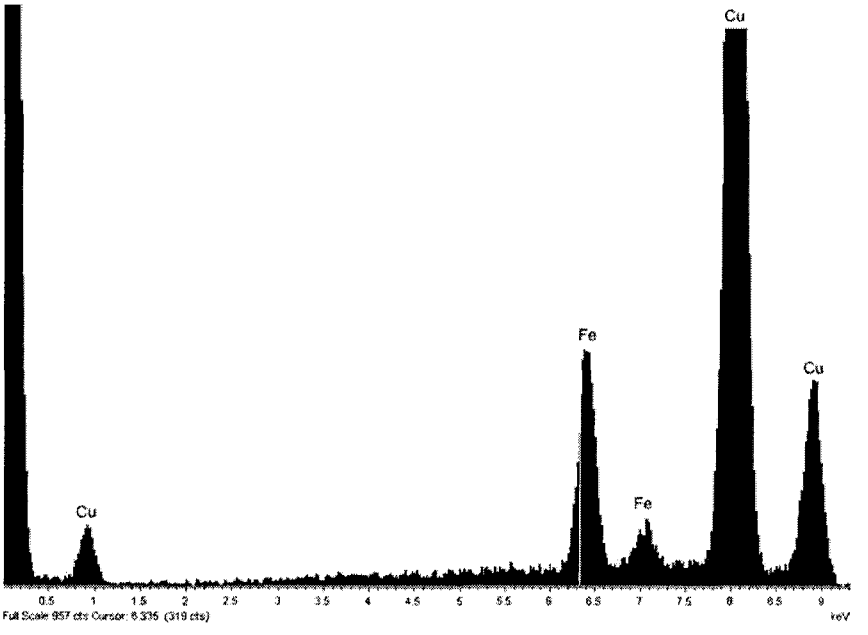

Figure AII.7. EDS spectrum of the decomposition of $H_2Fe_3(CO)_9P^tBu$ in 7:1 ODOH:OA.

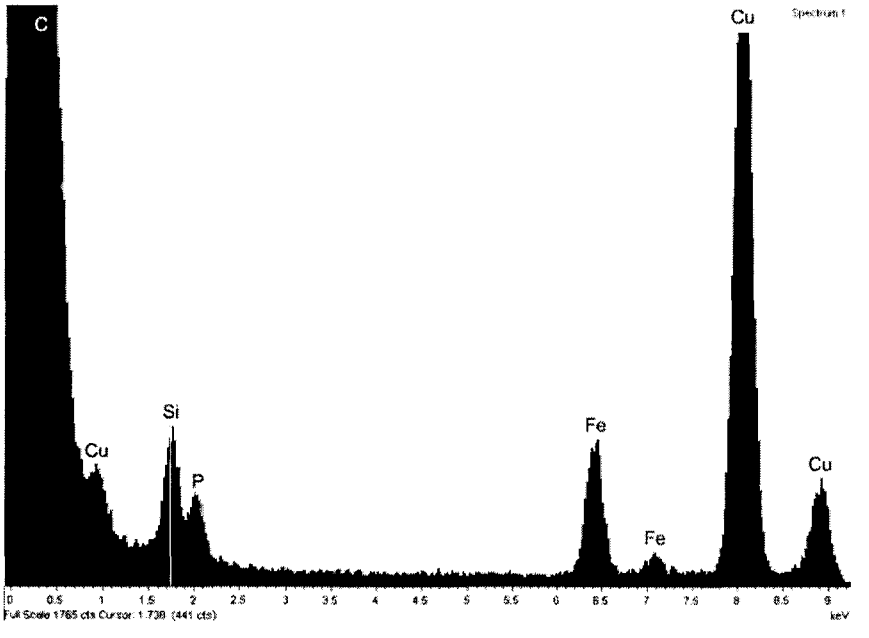

Figure AII.8. EDS spectrum of the decomposition of $H_2Fe_3(CO)_9P^tBu$ in 7:1 HDOH:OA.

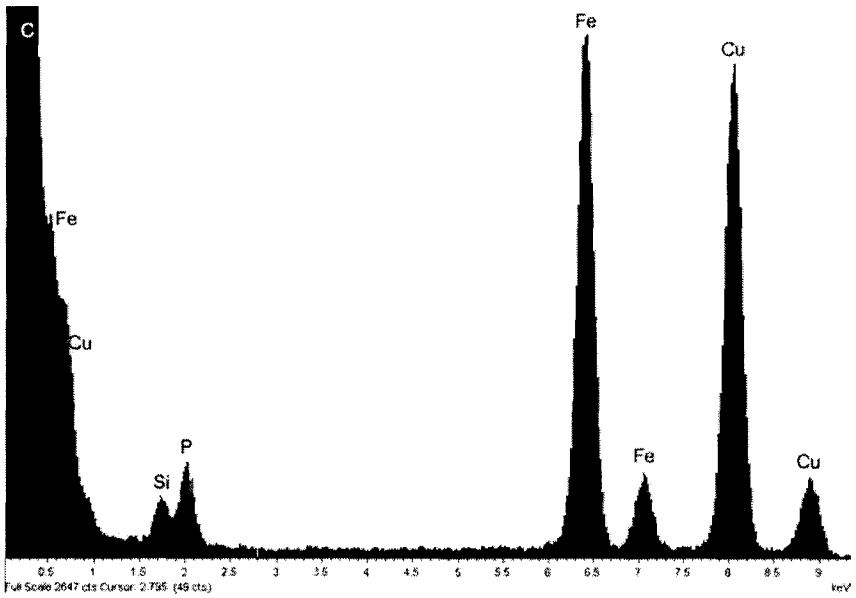

Figure AII.9. XPS data for the decomposition of $H_2Fe_3(CO)_9P^tBu$ in 7:1 HDA:OA.

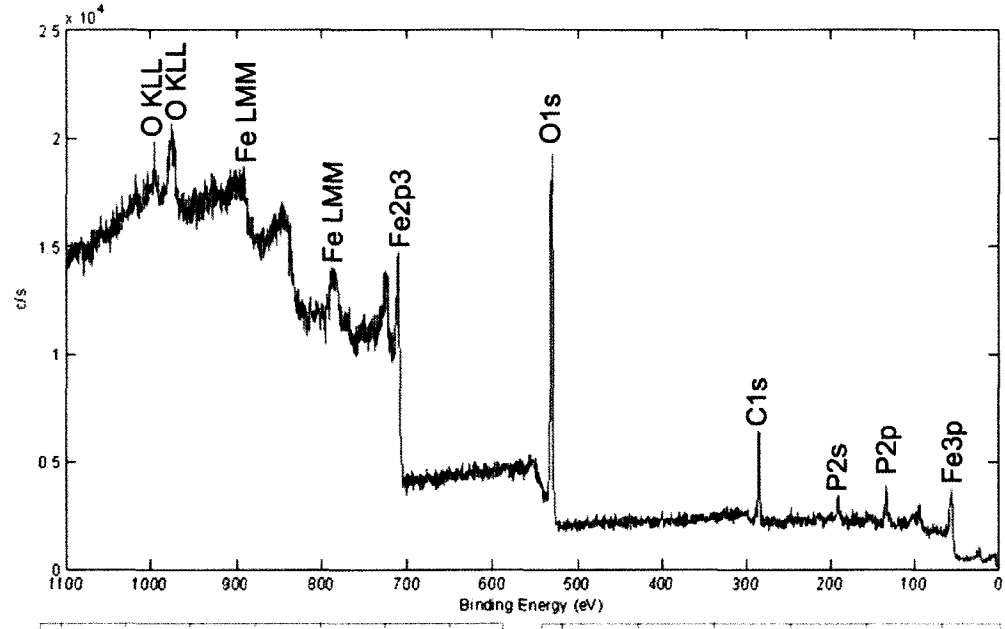

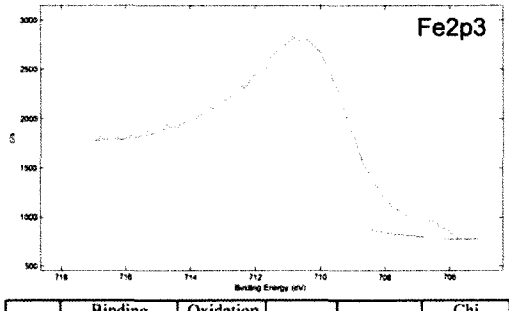

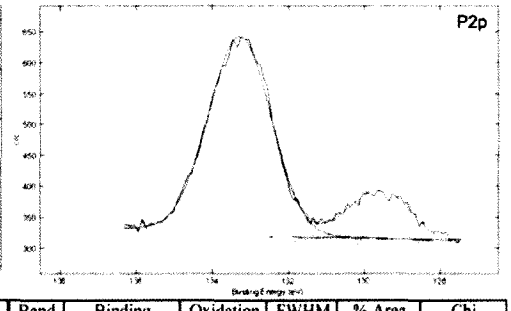

Band	Binding Energy (eV)	Oxidation State	FWHM	% Area	Chi Squared
1	706.86	0	1.30	3.30	1.60
2	710.24	+2	2.93	73.98	
3	712.66	+3	3.41	22.72	

Band	Binding Energy (eV)	Oxidation State	FWHM	% Area	Chi Squared
1	129.62	0	1.88	18.85	1.03
2	133.27	+5	1.91	81.85	

Figure AII.10. XPS data for the decomposition of $H_2Fe_3(CO)_9P^tBu$ in 7:1 HDOH:OA.

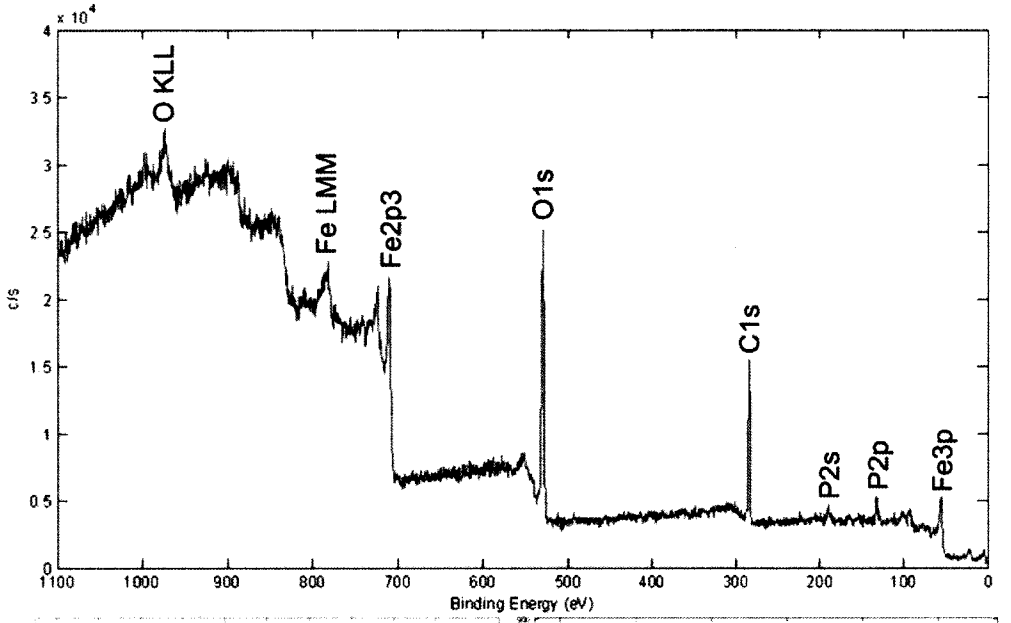

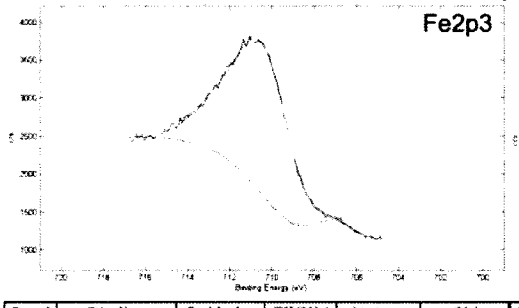

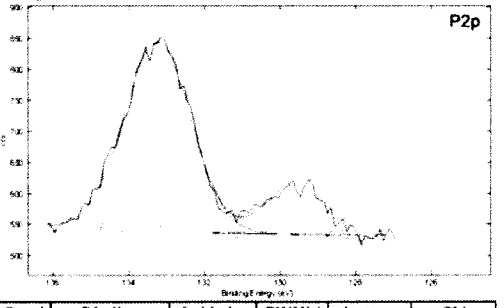

Band	Binding Energy (eV)	Oxidation State	FWHM	% Area	Chi Squared
1	707.04	0	1.81	5.00	1.44
2	710.45	+2	2.81	74.91	
3	712.77	+3	2.79	20.09	

Band	Binding Energy (eV)	Oxidation State	FWHM	% Area	Chi Squared
1	129.64	0	1.74	18.37	1.26
2	133.25	+5	2.06	81.63	

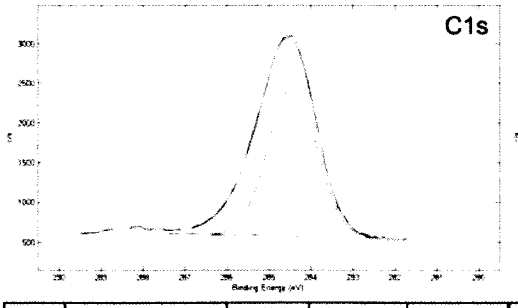

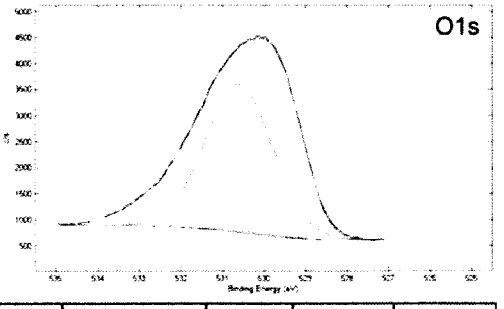

Band	Binding Energy (eV)	FWHM	% Area	Chi Squared
1	284.44 (C-C)	1.36	60.48	1.27
2	285.03 (C-C)	1.83	36.42	
3	288.12 (COO^-)	1.66	3.10	

Band	Binding Energy (eV)	FWHM	% Area	Chi Squared
1	529.54	1.33	27.05	1.32
2	530.61	1.91	52.93	
3	531.94	2.34	20.02	

Figure AII.11. XPS data for the decomposition of $H_2Fe_3(CO)_9P^tBu$ in 7:1 OOH:OA. The indium peaks are a result of the sample being pressed onto In foil for analysis.

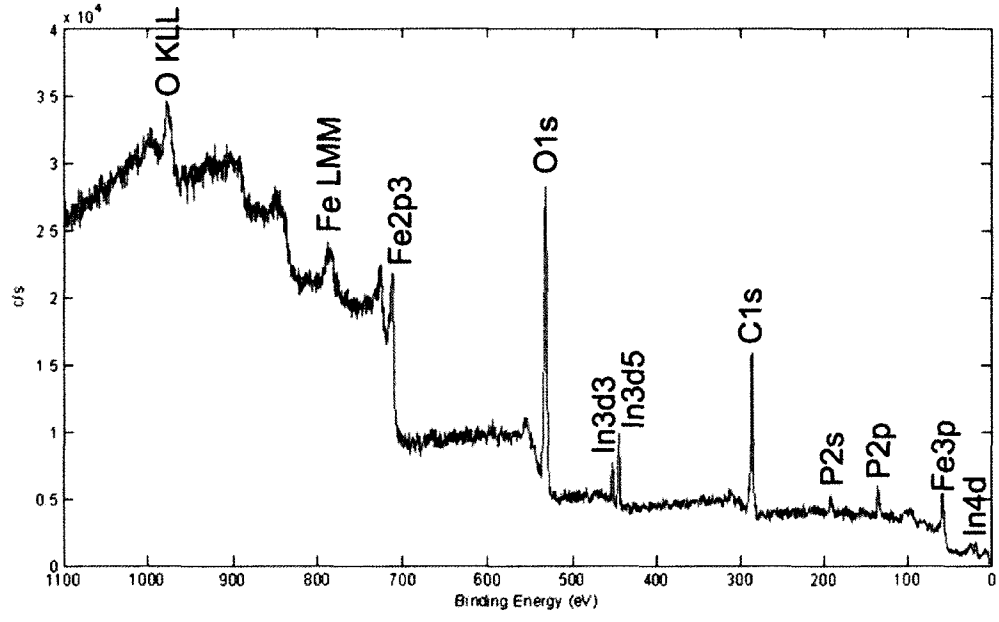

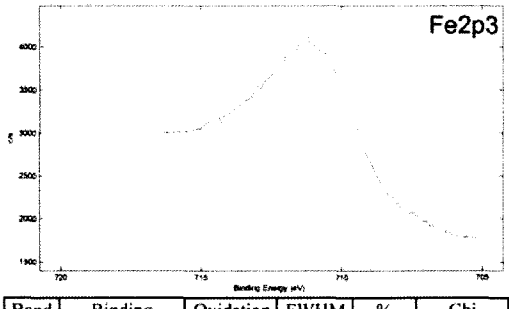

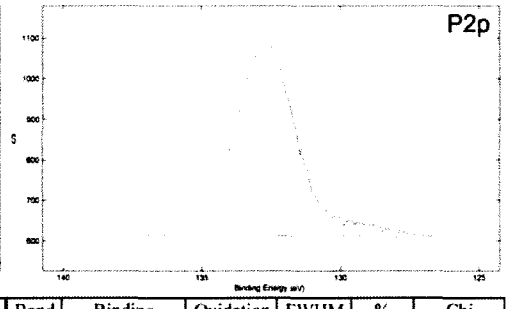

Band	Binding Energy (eV)	Oxidation State	FWHM	% Area	Chi Squared
1	707.31	0	1.68	3.33	1.13
2	710.79	+2	3.31	88.81	
3	713.59	+3	2.39	7.86	

Band	Binding Energy (eV)	Oxidation State	FWHM	% Area	Chi Squared
1	129.42	0	2.45	6.54	1.00
2	132.74	+5	2.35	93.46	

Figure AII.12. XPS data for the decomposition of $H_2Fe_3(CO)_9P^tBu$ in 7:1 ODOH:OA.

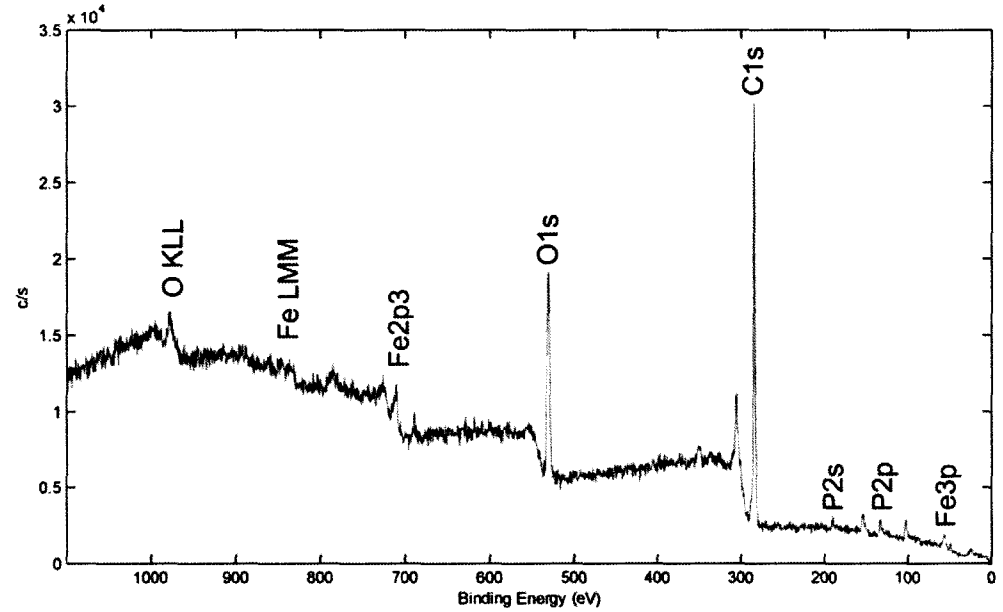

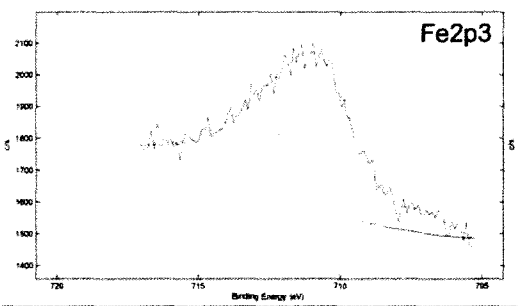

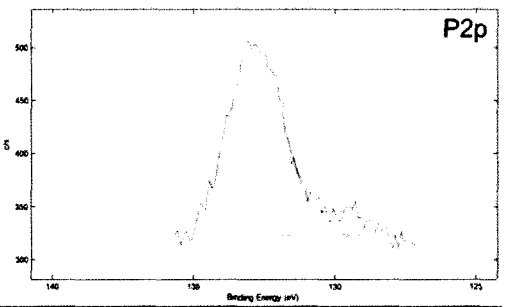

Band	Binding Energy (eV)	Oxidation State	FWHM	% Area	Chi Squared
1	707.05	0	1.65	5.15	1.34
2	710.67	+2	2.95	69.31	
3	712.77	+3	3.22	25.54	

Band	Binding Energy (eV)	Oxidation State	FWHM	% Area	Chi Squared
1	129.70	0	1.80	8.60	1.27
2	132.80	+5	2.26	91.40	

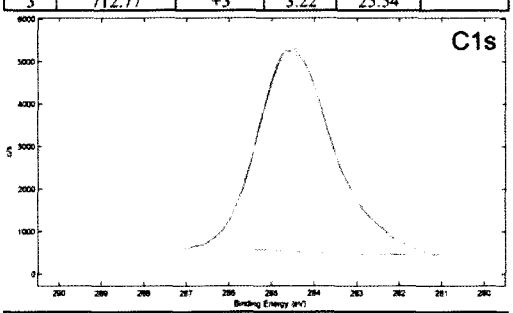

Band	Binding Energy (eV)	FWHM	% Area	Chi Squared
1	283.07	1.82	15.20	2.05
2	284.55	1.72	84.8	

Figure AII.13. XPS data for the decomposition of $H_2Fe_3(CO)_9P^tBu$ in 7:1 OAm:OA.

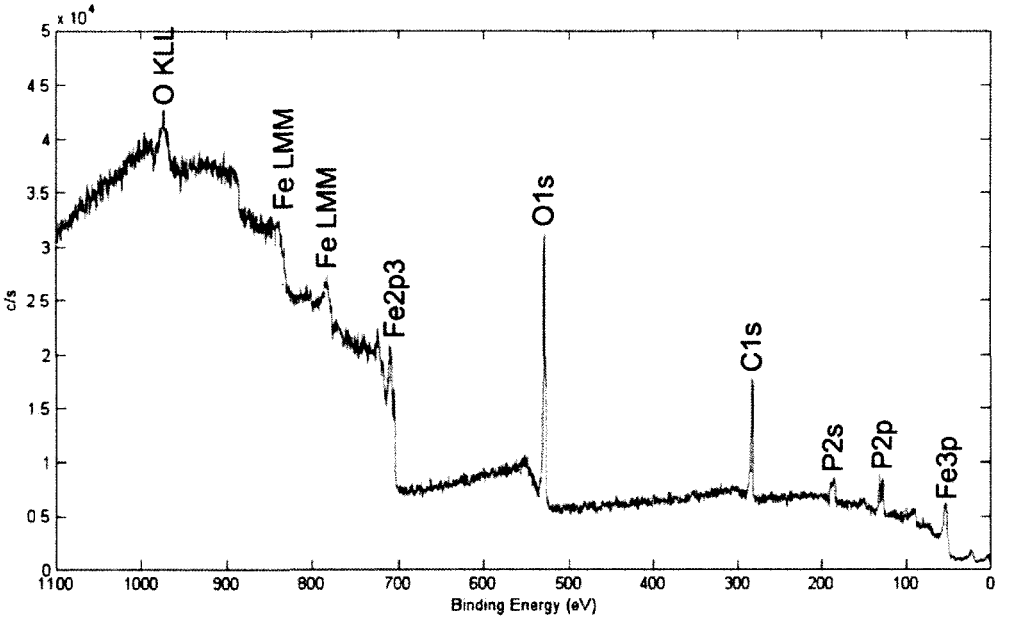

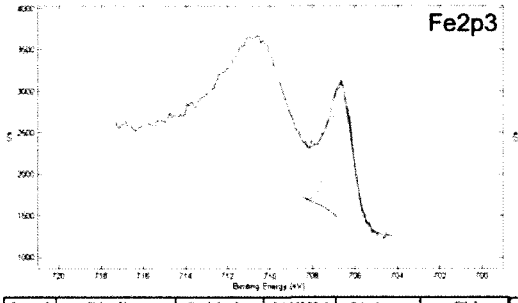

Band	Binding Energy (eV)	Oxidation State	FWHM	% Area	Chi Squared
1	706.64	0	1.22	22.73	2.36
2	707.71	0	0.79	2.48	
3	710.53	+3	3.72	74.79	

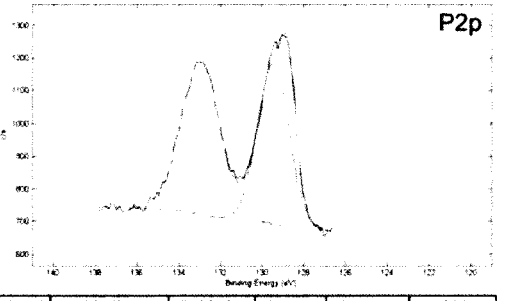

Band	Binding Energy (eV)	Oxidation State	FWHM	% Area	Chi Squared
1	128.73	0	0.83	9.65	1.32
2	129.45	0	1.76	41.34	
3	132.96	+5	2.22	49.01	

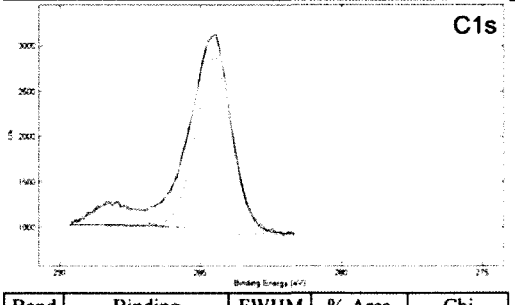

Band	Binding Energy (eV)	FWHM	% Area	Chi Squared
1	284.52 (C-C)	1.42	68.87	1.23
2	285.43 (C-C)	2.07	22.72	
3	288.15 (-COO⁻)	1.54	8.41	

Figure AII.14. EDS analysis of the particles synthesized from $Fe_3(CO)_{10}P^tBu$ in 4 mL TOA & 4 mL OA. The pink box represents the area of the grid on which the EDS analysis was conducted. The weight percentage analysis is close to that of Fe_2P (calculated values: 78.3% Fe, 21.7% P).

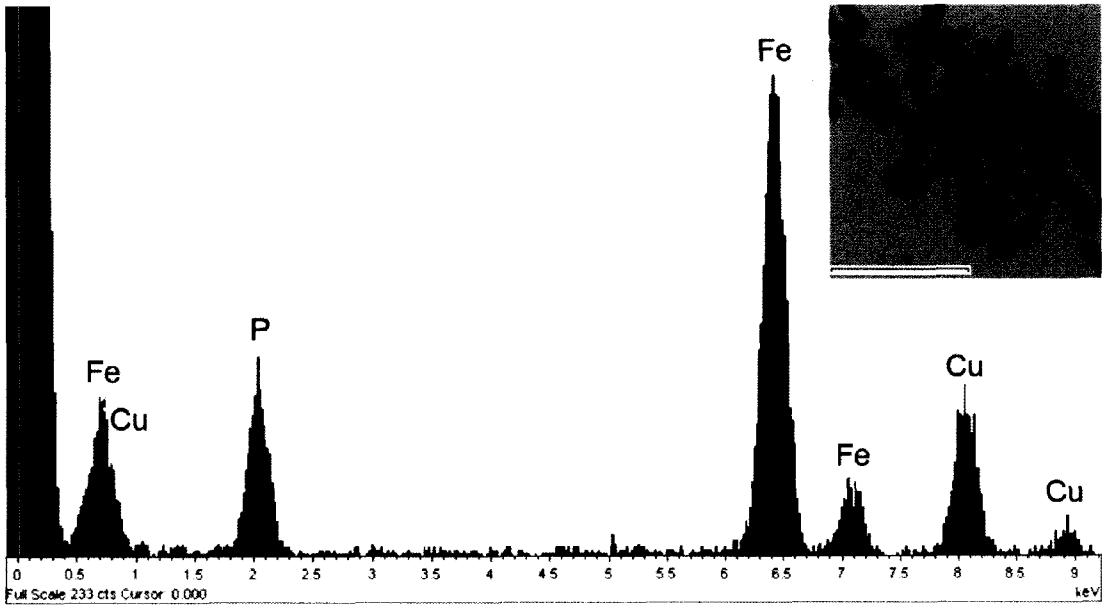

Element	Peak Area	Area Sigma	Weight%	Weight% Sigma	Atomic%
P K	551	44	**20.84**	1.45	32.18
Fe K	1866	71	**79.16**	1.45	67.82

Figure AII.15. Representative EDS analysis of the decomposition of $Fe_4(CO)_{12}(P^tBu)_2$ in 2 mL TOA & 2 mL OA. The yellow box indicates the area of the sample analyzed by EDS. Weight percentage analysis is close to that of Fe_2P (calculated values: 78.3% Fe, 21.7% P).

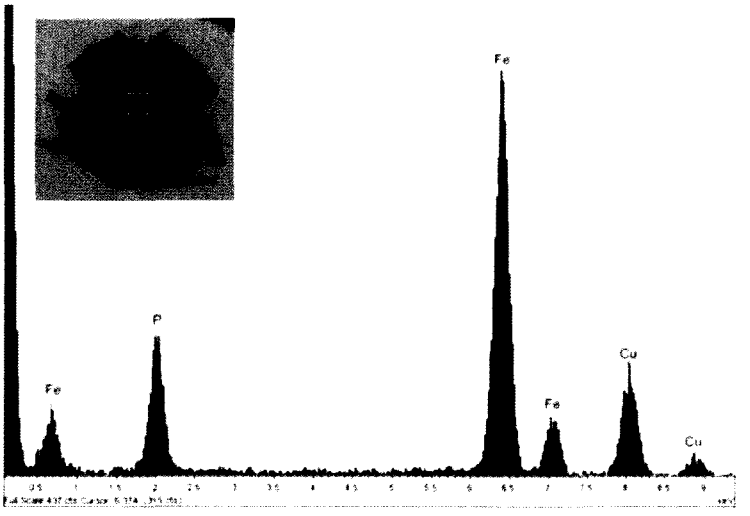

Element	Peak Area	Area Sigma	**Weight%**	Weight% Sigma	Atomic%
P K	1231	66	**20.72**	0.98	32.03
Fe K	4197	105	**79.28**	0.98	67.97

Appendix III. Decomposition of $H_2Fe_3(CO)_9P^tBu$ in a variety of surfactant combinations.

Surfactant	mmol precursor	TEM images
9.6 mL TOA 1 mL OA	0.50	
7 mL TOA 1 mL OA	0.50	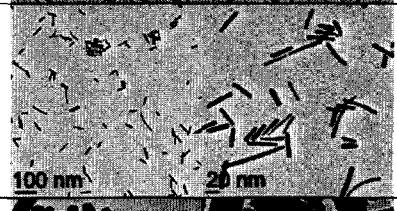
6 mL TOA 2 mL OA	0.50	
4 mL TOA 4 mL OA	0.50	
2 mL TOA 6 mL OA	0.50	
1 mL TOA 7 mL OA	0.50	
8 mL TOA 8 mL OA	0.50	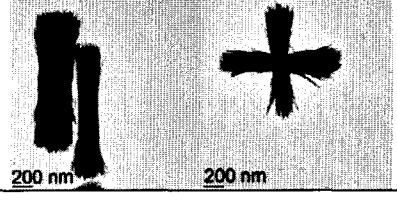

8 mL ODE	0.50	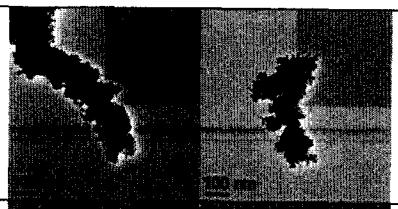
7 mL ODE 0.15 mL OA	0.50	
7 mL ODE 1 mL OA	0.50	
7 mL ODE 1 mL OA	0.47	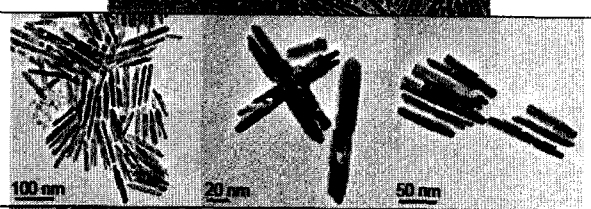
6 mL ODE 2 mL OA	0.50	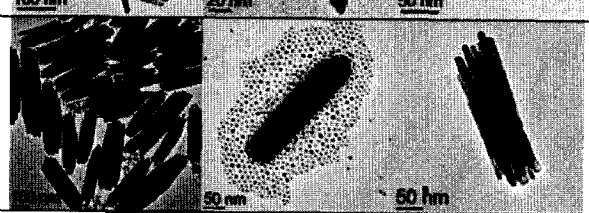
10 mL ODE 1 mL OA	0.50	
1 mL ODE 7 mL OAm	0.50	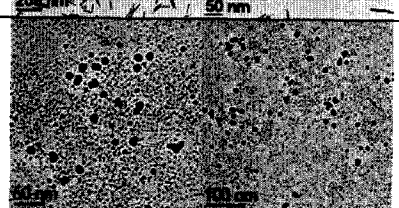
7 mL OAm 1 mL OA	0.50	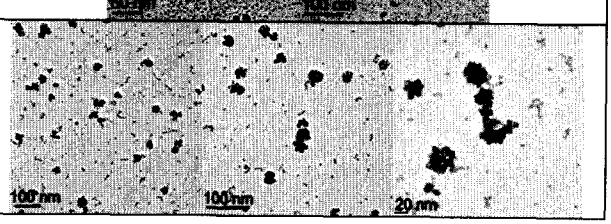

4 mL OAm 4 mL OA	0.50	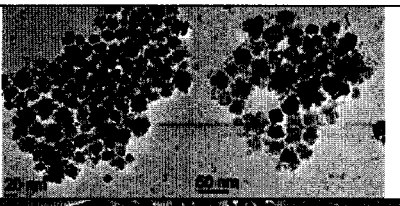
1 mL OAm 7 mL OA	0.50	
10 mL DOE 1 mL OA	0.50	
7 mL DOE 1 mL OA	0.50	
10 mL DOE 0.1 mL OA 0.1 mL OAm	0.50 Injected precursor in ~4 mL DCB.	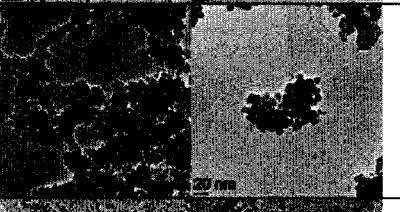
10 mL DOE 0.1 mL OA 0.1 mL OAm	0.50 Combined all reagents at room temperature (no injection).	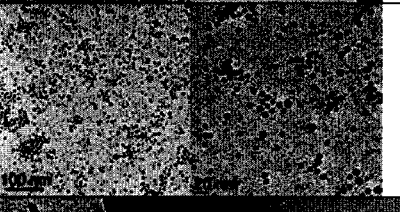
10 mL DOE 1 mL OA	0.50 Injected precursor in 4 mL DCB.	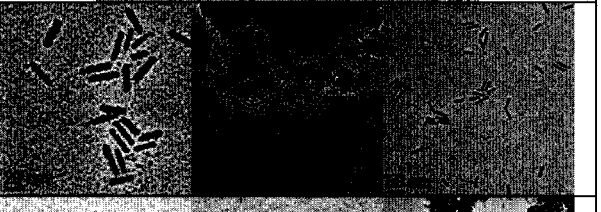
10 mL DOE 1 mL OA	0.50 0.25 mmol dissolved at room temperature, 0.25 mmol injected in 1 mL tridecane.	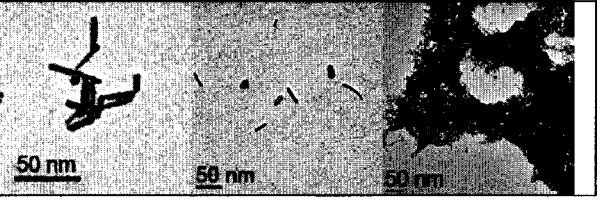

7 mL TOA 1 mL OA	0.25 Trialkylamine variation.	
7 mL TDDA 1 mL OA	0.25 Trialkylamine variation.	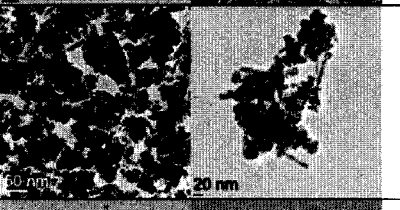
7 mL THA 1 mL OA	0.24 Trialkylamine variation.	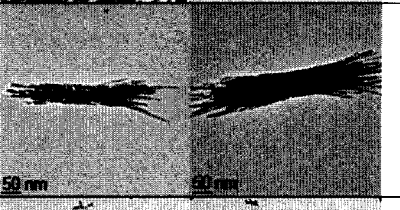
7 mL TDDA 1 mL OA	0.50	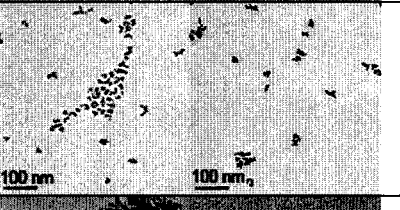
7 mL HDA 1 mL OA	0.50	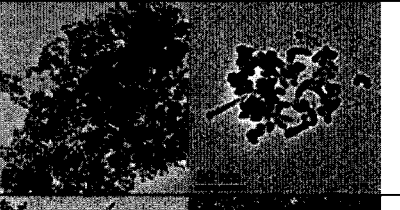
7 mL OOH 1 mL OA	0.50	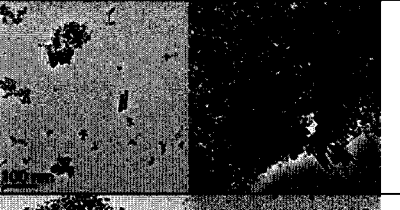
7 mL ODOH 1 mL OA	0.50	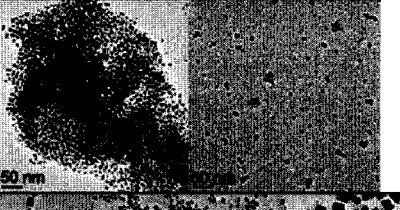
7 mL HDOH 0.15 mL OA	0.50	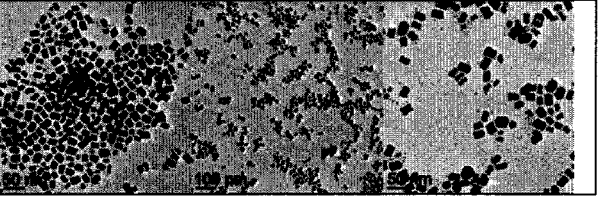

7 mL HDOH 1 mL OA	0.50	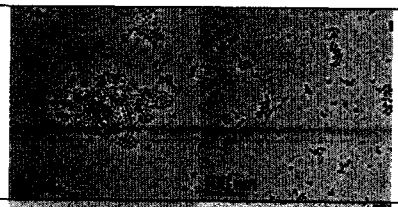
7 mL TOA 0.15 mL OA	0.50	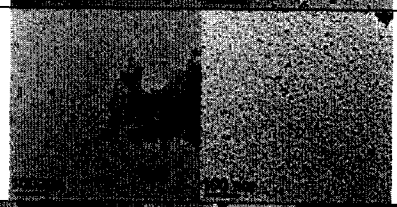
7 mL HDOH	0.50	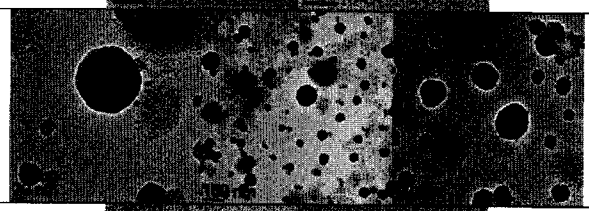
7 mL TOA	0.50	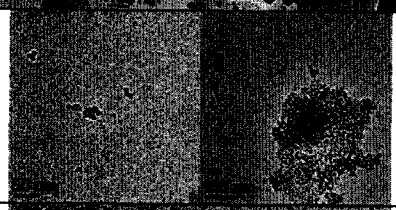
7 mL TOA 1 mL MeOA	0.50	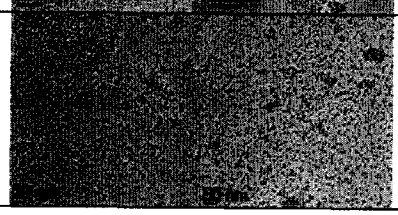

Appendix IV. Supplementary information for Chapter 4.

Figure AIV.1. Summary of the cluster transformations seen for $H_2Fe_3(CO)_9P^tBu$ and $Fe_3(CO)_{10}P^tBu$ in the IR studies.

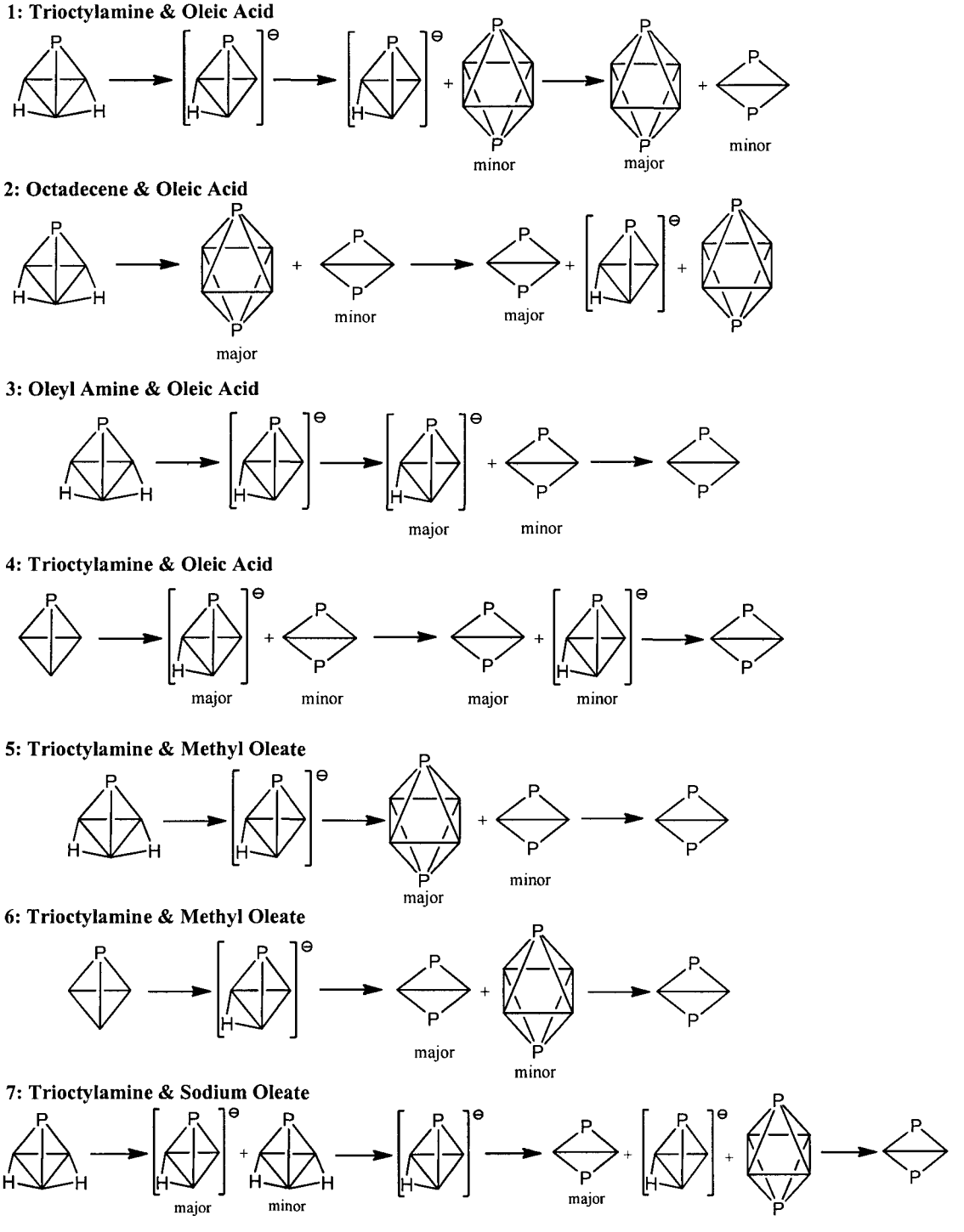

Figure AIV.2. GC-MS data from the bulk decomposition of $H_2Fe_3(CO)_9P^tBu$. The top image shows the GC chromatogram. The MS chromatograms shown are for CO (RT = 1.901 min) and isobutylene (RT = 1.947 min). The small peaks in the GC chromatogram are due to the presence of hexane and methylcyclopentane.

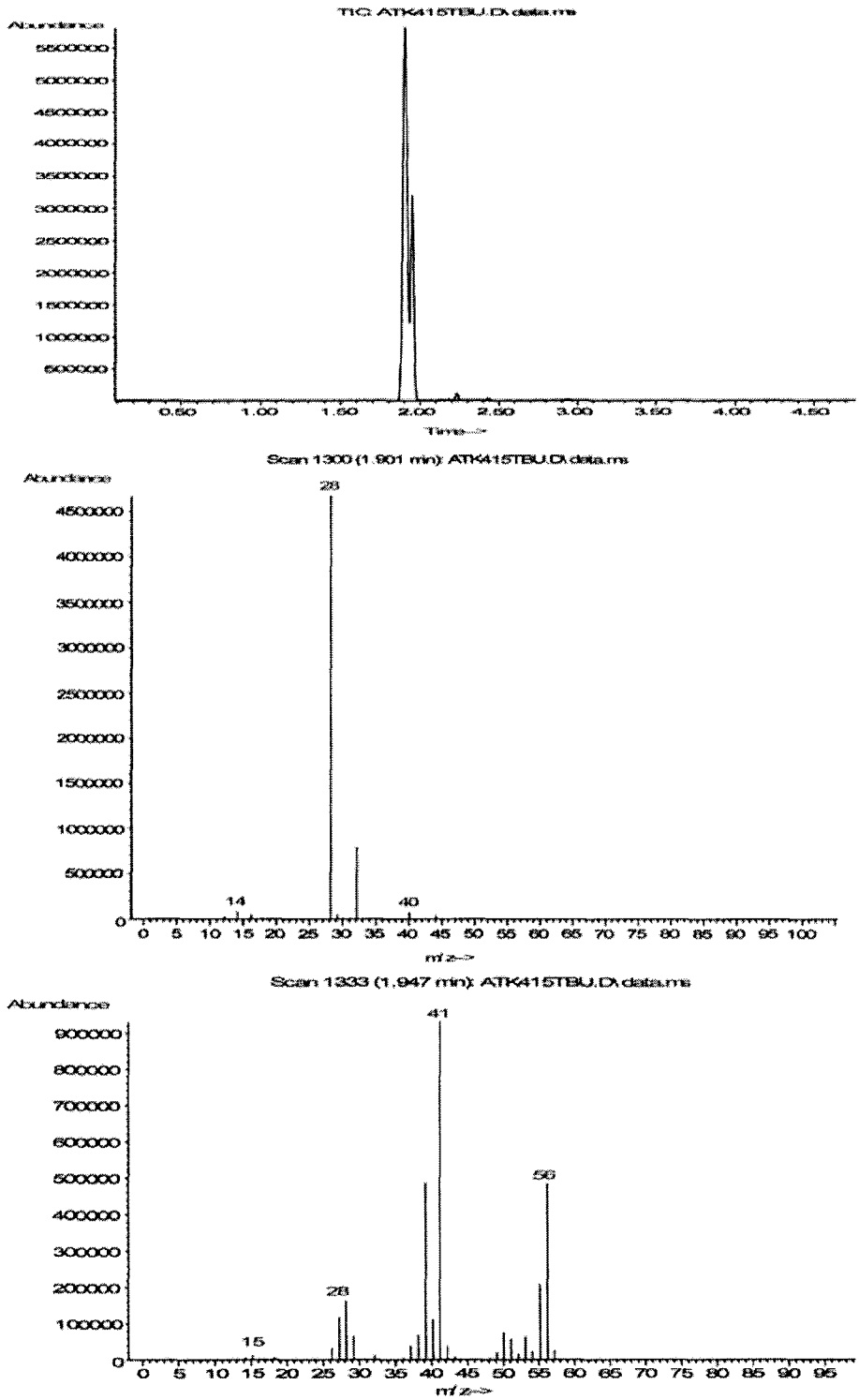

Figure AIV.3. GC-MS data from the bulk decomposition of $H_2Fe_3(CO)_9PPh$. The top image shows the GC chromatogram. The MS chromatograms shown are for CO/CO_2 (RT = 1.907 min) and benzene (RT = 3.051 min). The small peaks in the GC chromatogram are due to the presence of hexane (and its isomers) and methylcyclopentane.

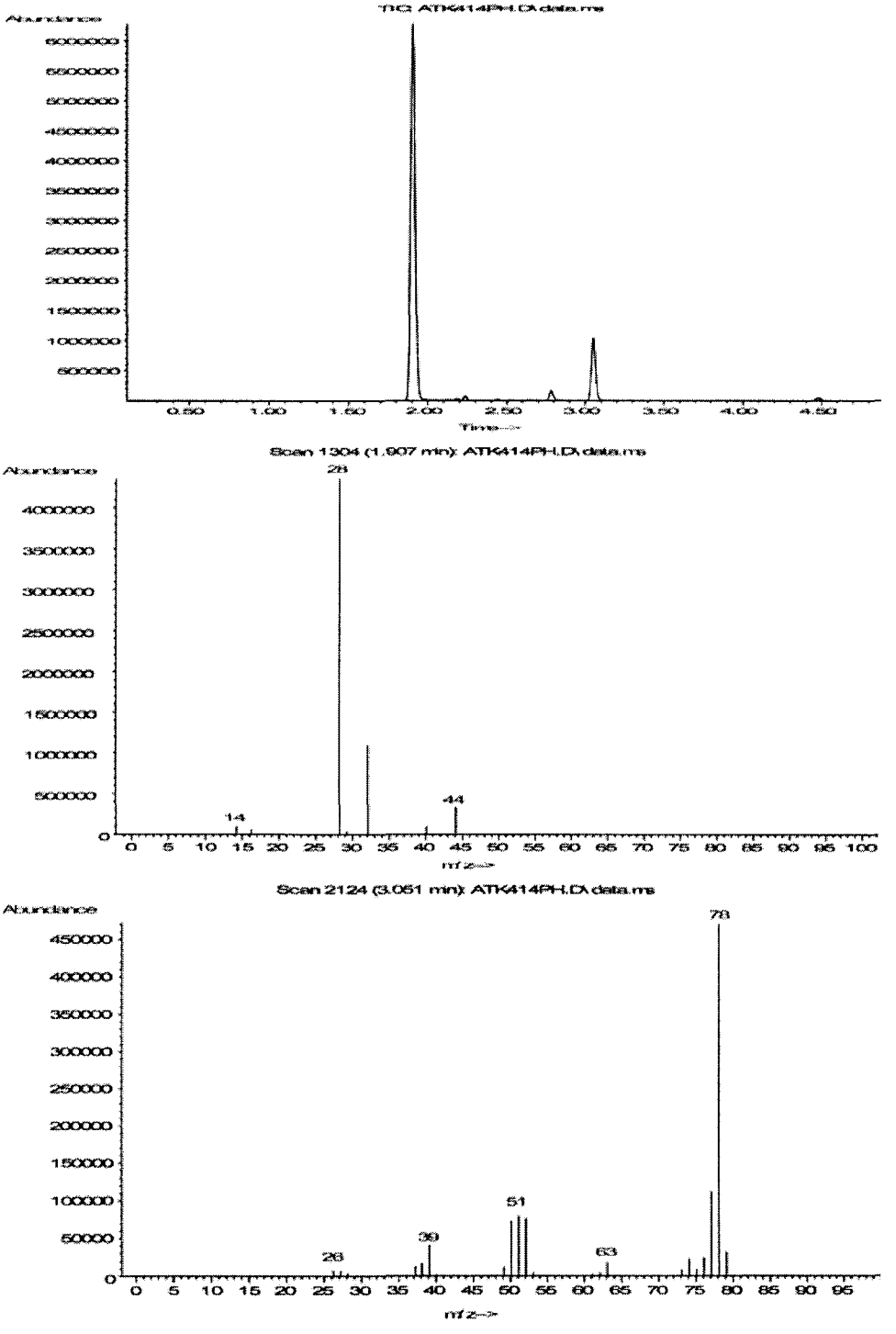

Figure AIV.4. GC-MS data from the bulk decomposition of $Fe_3(CO)_{10}PPh$. The top image shows the GC chromatogram. The MS chromatograms shown are for CO (RT = 1.911 min) and benzene (RT = 3.051 min). The additional peak in the GC chromatogram (RT ~ 2.2 min) is due to the presence of acetone.

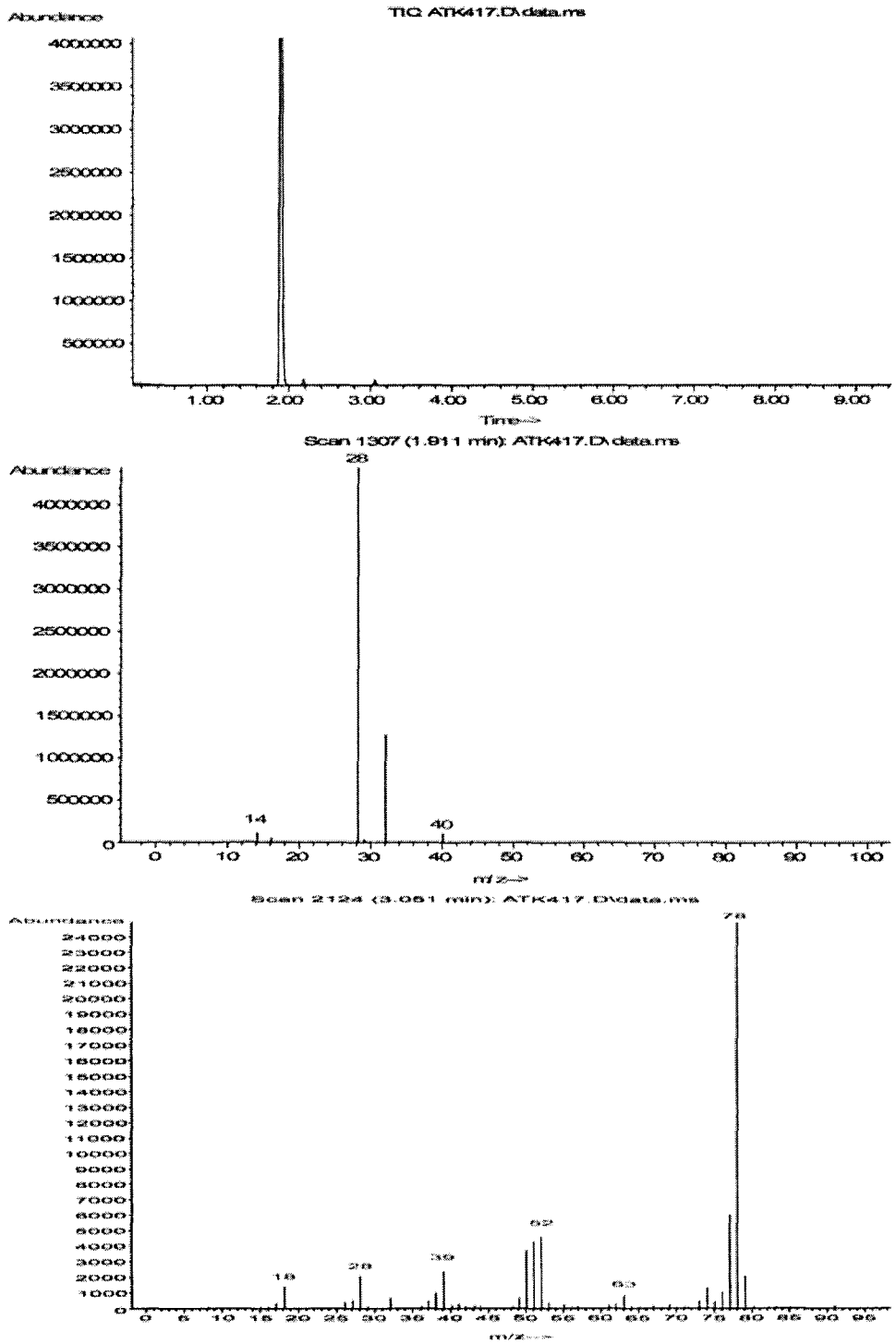

Appendix V. Supplementary information for the decompositions of $H_2Fe_3(CO)_9P^tBu$ with $Mn_2(CO)_{10}$ or $Mn(CO)_5Br$ and the decompositions of $HMn_2(CO)_8PPh_2$.

Decompositions of $H_2Fe_3(CO)_9P^tBu$ with $Mn_2(CO)_{10}$		
$H_2Fe_3(CO)_9P^tBu$ 0.25 g $Mn_2(CO)_{10}$ 0.20 g	7 mL TOA 1 mL OA	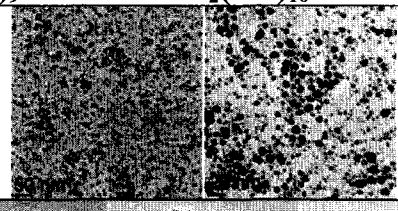
$H_2Fe_3(CO)_9P^tBu$ 0.25 g $Mn_2(CO)_{10}$ 0.20 g	4 mL TOA 4 mL OA	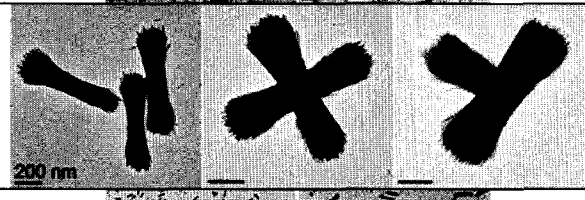
$H_2Fe_3(CO)_9P^tBu$ 0.13 g $Mn_2(CO)_{10}$ 0.10 g	10 mL DOE 1 mL OA inject precursors in 4mL DCB; double injection	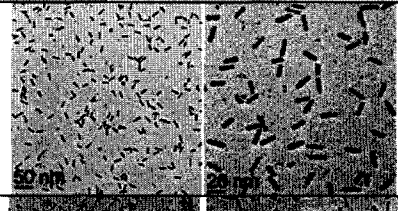
$H_2Fe_3(CO)_9P^tBu$ 0.14 g $Mn_2(CO)_{10}$ 0.11 g	10 mL DOE 1 mL OA No injection, combine at RT	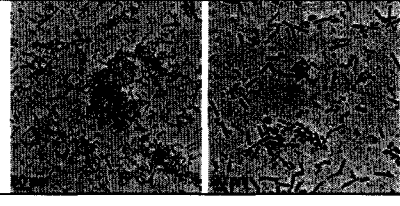
$Mn_2(CO)_{10}$ 0.20 g	10 mL DOE 1 mL OA inject precursor in 2mL DCB	NO NPs
Decomposition of $H_2Fe_3(CO)_9P^tBu$ with $Mn(CO)_5Br$		
$H_2Fe_3(CO)_9P^tBu$ 0.25 g $Mn(CO)_5Br$ 0.40 g	4 mL TOA 4 mL OA	
Decompositions of $HMn_2(CO)_8PPh_2$		
$HMn_2(CO)_8PPh_2$ 0.26 g	4 mL TOA 4 mL OA	NO NPs
$HMn_2(CO)_8PPh_2$ 0.25 g	10 mL DOE 0.1 mL OAm 0.1 mL OA inject precursor in ~3mL DCB	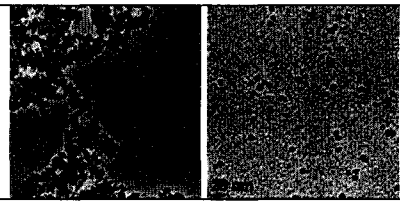

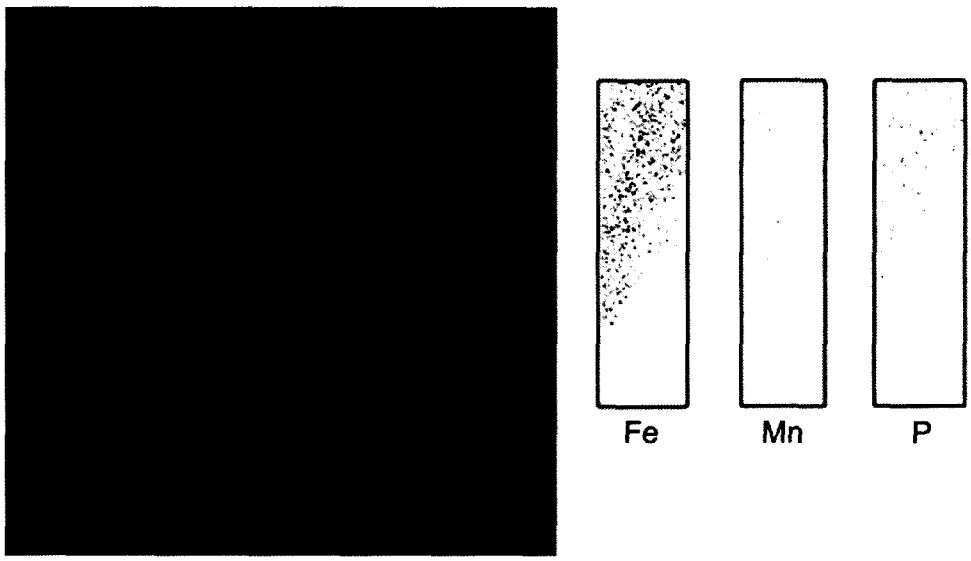

Figure AV.1. Elemental mapping of the split nanorods synthesized from the decomposition of $H_2Fe_3(CO)_9P^tBu$ and $Mn_2(CO)_{10}$ in TOA and OA (4:4).

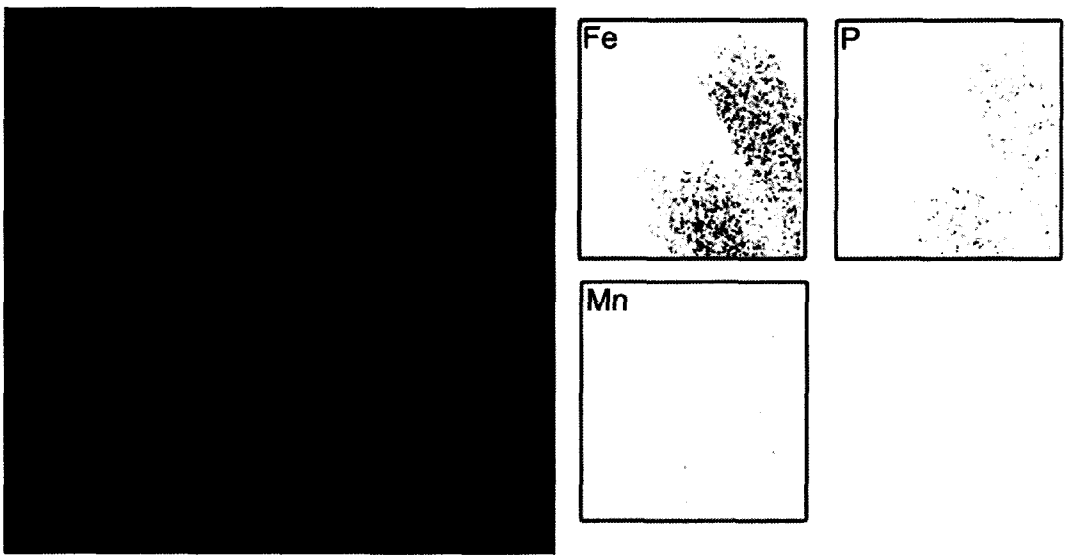

Figure AV.2. Elemental mapping of the split nanorods synthesized from the decomposition of $H_2Fe_3(CO)_9P^tBu$ and $Mn(CO)_5Br$ in TOA and OA (4:4).

Appendix VI. Supplementary information for the gold coating of Fe_2P nanostructures.

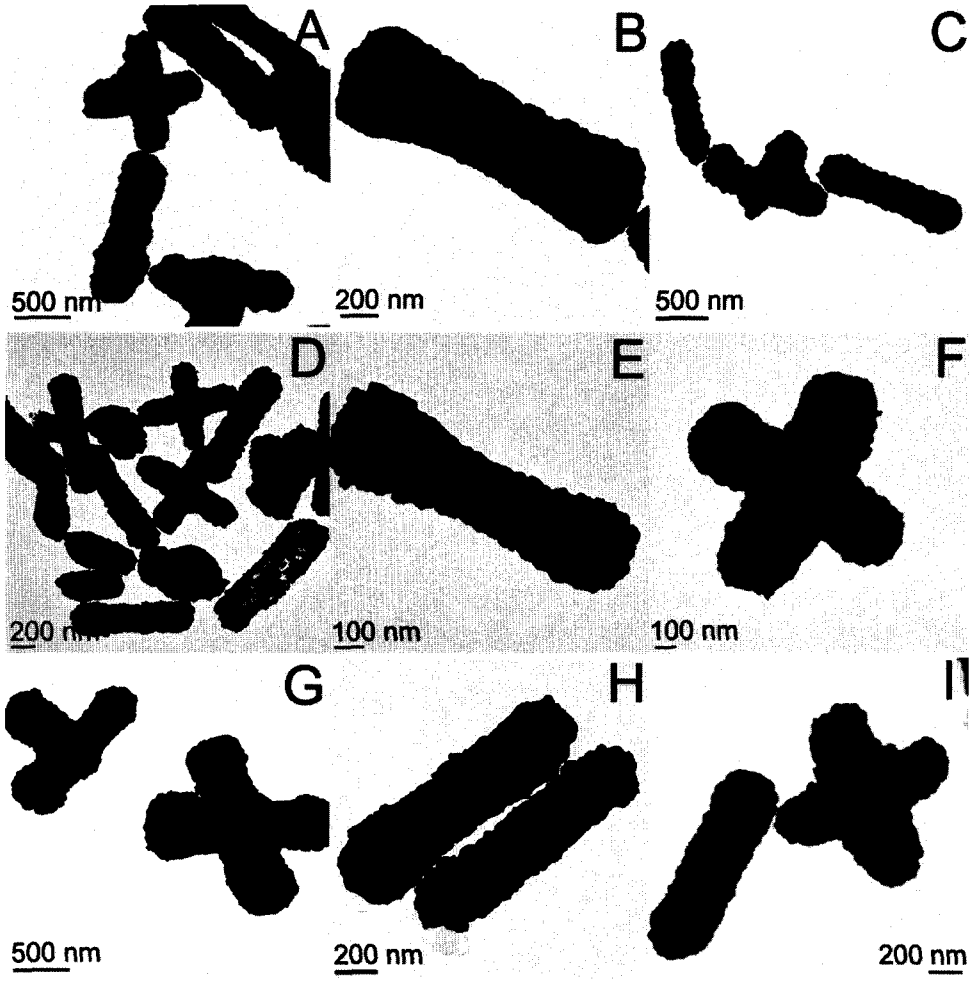

Figure AVI.1. TEM images of Fe_2P-Au structures obtained using CO-reduction. The images shown represent the structures synthesized from 75 μL (A-C), 100 μL (D-F), and 125 μL (G-I) of gold-decorated precursor. Note that in figures D and G, it appears as though some of the particles do not have a complete shell; this is believed to account for the shift back to higher wavelengths of the extinction maximum for the sample synthesized from 100 μL of gold-decorated precursor (see Figure 6.6).

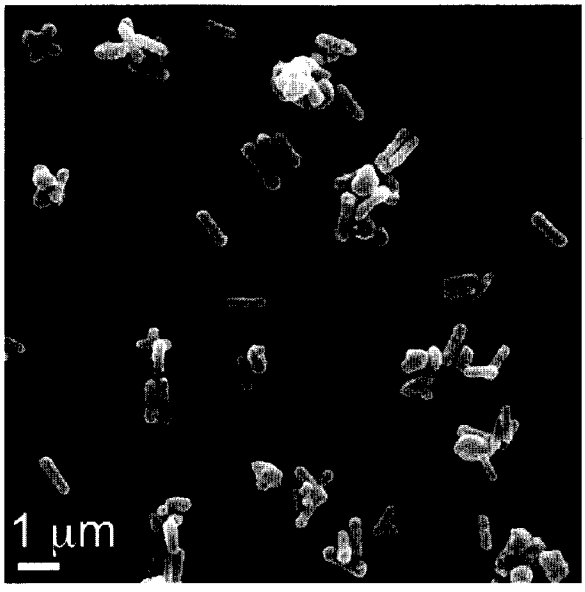

Figure AVI.2. Representative SEM image of the CO-reduced particles, from 50 μL of gold-decorated precursor.

Amount of decorated precursor (μL)	Length (nm)	Width (nm)	Shell Thickness (nm)	Aspect Ratio	λ_{max} (nm)
25	1089 ± 88	323 ± 42	65	3.4	588
50	1065 ± 115	317 ± 53	62	3.4	555
75	1011 ± 90	279 ± 38	43	3.6	542
100	1033 ± 71	246 ± 27	27	4.2	555

Table AVI.1. Summary of the sizing and solution extinction maxima for various sizes of Fe_2P-Au core-shell structures synthesized via CO-reduction. The Au decorated-Fe_2P particles had dimensions of 1051 ± 62 × 193 ± 22 nm (aspect ratio: 5.4, λ_{max} 365 nm).

Anna Kelly
11914 Oakcroft Dr.
Houston, TX 77070

EDUCATION

Rice University, Houston, TX, Doctor of Philosophy in Chemistry (August 2009)
Rice University, Houston, TX, Master of Arts in Chemistry, GPA 3.93 (May 2006)
Loyola University, New Orleans, LA, Bachelor of Science in Chemistry (May 2002)
Graduated *magna cum laude.*

RESEARCH EXPERIENCE

Graduate Research Assistant, Rice University (Fall 2003 – Summer 2009)
- Planned and carried out processes for optimizing the synthesis of magnetic nanoparticles.
- Synthesized organometallic precursors to iron phosphide nanomaterials utilizing inert atmosphere techniques.
- Characterized the morphology and properties of the nanomaterials.
- Presented data effectively via oral and written reports.
- Trained and supervised undergraduate and graduate students.
- Coordinated group meetings and organized lab maintenance.

Undergraduate Research Assistant, National Science Foundation Research Experience for Undergraduates, Texas A&M University, College Station, TX (June – August 2001)
- Conducted research in the area of natural product synthesis.
- Mentored a student participating in the NASA Summer High School Apprenticeship Research Program.

Undergraduate Research Assistant, Loyola University (June 2000 – May 2001)
- Studied catalytic metathesis reactions utilizing vanadium complexes.

TEACHING EXPERIENCE

General Chemistry Lab Teaching Assistant, Rice University (Fall 2003 – Spring 2005)
- Responsible for overseeing weekly labs as well as conducting pre-lab lectures and grading lab reports.

Chemistry Tutor, Academic Resource Center, Loyola University (January 2001 – May 2002)
Organic Lab Assistant, Loyola University (Fall 2001)

SKILLS

Experience in various characterization techniques, including: Fourier Transform Infrared Spectroscopy, Transmission Electron Microscopy, Single Crystal X-Ray Diffraction, X-Ray Powder Diffraction, X-Ray Photoelectron Spectroscopy, UV-Vis Spectroscopy, NMR Spectroscopy, Gas Chromatography - Mass Spectroscopy and Flame Ionization Detection

ACADEMIC SERVICES & ORGANIZATIONS

Rice University Graduate Student Association, Secretary (May 2005 – May 2007)
American Chemical Society, Member (2003 – present)
Dean's Student Advisory Committee, Alternate Member (2000-2001)

AWARDS & HONORS

Harry B. Weiser Research Award in Chemistry (May 2008)
Center for Biological and Environmental Engineering Travel Award (2008)
Dean's Travel Award (2008)
Stephen C. Hofmann Fellowship (2003)
Dean's Scholarship at Loyola University (1998-2002)
Rev. Thomas J. Mulcrone, S.J. Outstanding Student Worker Award (May 2002)
American Institute of Chemists Award (May 2002)
Excellence in Tutoring Award (May 2001)

SELECTED PUBLICATIONS

Levin, C.S.; Hofmann, C.; Ali, T.A.; Kelly, A.T.; Morosan, E.; Nordlander, P.; Whitmire, K.H.; Halas, N.J. "Magnetic-Plasmonic Core-Shell Nanoparticles" *ACS Nano* **2009**, *3*, 1379-1388.

Hofmann, C.; Rusakova, I.; Ould-Ely, T.; Prieto-Centurion, D.; Hartman, K.B.; **Kelly, A.T.**; Lüttge, A.; Whitmire, K.H. "Shape control of new Fe_xO-Fe_3O_4 and $Fe_{1-y}Mn_yO$-$Fe_{3-z}Mn_zO_4$ nanostructures." *Adv. Funct. Mater.* **2008**, *18*, 1-7.

Kelly, A.T.; Rusakova, I.; Ould-Ely, T.; Hofmann, C.; Lüttge, A.; Whitmire, K. H. "Iron Phosphide Nanostructures Produced from a Single-Source Organometallic Precursor: Nanorods, Bundles, Crosses, and Spherulites." *Nano Lett.* **2007**, *7*, 2920-2925.

Whitmire, K.H.; **Kelly, A.T.**; Hofmann, C. "Mononuclear Iron Carbonyls without Hydrocarbon Ligands." Comprehensive Organometallic Chemistry III, 6 (**2006**): 1-76.

Redden, C.; Hofmann, C.; **Kelly, A.**; McHale, M.E.R. "Freshman Chemistry Laboratory Manual." 1st Edition (**2005**).

Poullennec, K.G.; **Kelly, A.T.**; Romo, D. "Highly Diastereoselective Desymmetrizations of Cyclo (Pro, Pro): An Enantioselective Strategy Toward Phakellstatin and Phakellin" *Org. Letters* **2002**, *4*, 2645-2648.

ORAL PRESENTATIONS

Kelly, A.; Rusakova, I.; Whitmire, K.H. "Iron phosphide nanomaterials from molecular precursors." 235th ACS National Meeting, New Orleans, LA, April 10, **2008**.

Kelly, A. "Single Source Precursors to Iron Phosphide Nanomaterials." Invited speaker, Loyola University, New Orleans, LA, September 24, **2007**.

POSTER PRESENTATIONS

Lam, C.; **Kelly, A.**; Whitmire, K.H. "Synthesis and reactions of $HFe_4(\mu_4\text{-}\eta^2\text{-}CH)(CO)_{12}$." 235th ACS National Meeting, New Orleans, LA, April 6-10, **2008**.

Kelly, A.T.; Birdwhistell, K.R.; Dumas, S.A. "A study of Imido Metathesis between carbodiimides and imines catalyzed by $V(NAr)Cl_3$" Undergraduate Poster Session, 52nd Southeast/56th Southwest Combined Regional ACS Meeting, New Orleans, LA, December **2000**.

References

(1) Astruc, D.; Lu, F.; Aranzaes, J. R. *Ang. Chem., Int. Ed.* **2005**, *44*, 7852-7872.
(2) Narayanan, R.; El-Sayed, M. A. *J. Phys. Chem. B* **2005**, *109*, 12663-12676.
(3) Somorjai, G. A.; Blakely, D. W. *Nature* **1975**, *258*, 580-583.
(4) Xiong, Y.; Wiley, B. J.; Xia, Y. *Ang. Chem., Int. Ed.* **2007**, *46*, 7157-7159.
(5) Gregory, D. S. *Adv. Func. Mat.* **2008**, *18*, 1157-1172.
(6) Kan, S.; Mokari, T.; Rothenberg, E.; Banin, U. *Nat. Mater.* **2003**, *2*, 155-158.
(7) Li, L. H.; Ridha, P.; Patriarche, G.; Chauvin, N.; Fiore, A. *Appl. Phys. Lett.* **2008**, *92*, 121102-121103.
(8) Tobia, D.; Winkler, E.; Zysler, R. D.; Granada, M.; Troiani, H. E. *Phys. Rev. B* **2008**, *78*, 104412-104417.
(9) Pereira, A. S.; Rauwel, P.; Reis, M. S.; Silva, N. J. O.; Barros-Timmons, A.; Trindade, T. *J. Mater. Chem.* **2008**, *18*, 4572-4578.
(10) Salazar-Alvarez, G.; Qin, J.; Sepelak, V.; Bergmann, I.; Vasilakaki, M.; Trohidou, K. N.; Ardisson, J. D.; Macedo, W. A. A.; Mikhaylova, M.; Muhammed, M.; Baro, M. D.; Nogues, J. *J. Am. Chem. Soc.* **2008**, *130*, 13234-13239.
(11) Koseoglu, Y.; Kavas, H. *J. Nanosci. Nanotechnol.* **2008**, *8*, 584-590.
(12) Clavel, G.; Willinger, M.-G.; Zitoun, D.; Pinna, N. *Adv. Func. Mat.* **2007**, *17*, 3159-3169.
(13) Leslie-Pelecky, D. L.; Rieke, R. D. *Chem. Mater.* **1996**, *8*, 1770-1783.
(14) Jun, Y.; Lee, J.; Cheon, J. *Ang. Chem., Int. Ed.* **2008**, *47*, 5122-5135.
(15) Douziech-Eryrolles, L.; Marchais, H.; Herve, K.; Munnier, E.; Souce, M.; Linassier, C.; Dubois, P.; Chourpa, I. *Int. J. Nanomed.* **2007**, *2*, 541-550.
(16) Quan, Z.; Li, C.; Zhang, X.; Yang, J.; Yang, P.; Zhang, C.; Lin, J. *Cryst. Growth Des.* **2008**, *8*, 2384-2392.
(17) Zhang, H.-X.; Peng, Q.; Li, Y.-D. *J. Phys. Chem. C* **2008**, *112*, 3272-3282.
(18) Park, J.; Joo, J.; Kwon, S. G.; Jang, Y.; Hyeon, T. *Ang. Chem., Int. Ed.* **2007**, *46*, 4630-4660.
(19) Jun, Y.; Choi, J.; Cheon, J. *Ang. Chem., Int. Ed.* **2006**, *45*, 3414-3439.
(20) Jun, Y.; Jung, Y.; Cheon, J. *J. Am. Chem. Soc.* **2002**, *124*, 615-619.
(21) Cheon, J.; Kang, N. J.; Lee, S. M.; Lee, J. H.; Yoon, J. H.; Oh, S. J. *J. Am. Chem. Soc.* **2004**, *126*, 1950-1951.
(22) Li, Y.; Liu, J.; Wang, Y.; Wang, Z. L. *Chem. Mater.* **2001**, *13*, 1008-1014.
(23) Murray, C. B.; Norris, D. J.; Bawendi, M. G. *J. Am. Chem. Soc.* **1993**, *115*, 8706-8715.
(24) Song, Q.; Zhang, Z. J. *J. Am. Chem. Soc.* **2004**, *126*, 6164-6168.
(25) Manna, L.; Scher, E. C.; Alivisatos, A. P. *J. Am. Chem. Soc.* **2000**, *122*, 12700-12706.
(26) Jun, Y.; Lee, S.; Kang, N.; Cheon, J. *J. Am. Chem. Soc.* **2001**, *123*, 5150-5151.
(27) Lee, S. M.; Jun, Y. w.; Cho, S. N.; Cheon, J. *J. Am. Chem. Soc.* **2002**, *124*, 11244-11245.
(28) Zhang, Y. C.; Qiao, T.; Hu, X. Y.; Wang, G. Y.; Wu, X. *J. Cryst. Growth* **2005**, *277*, 518-523.

(29) Zhang, Y. C.; Wang, G. Y.; Hu, X. Y.; Shi, Q. F.; Qiao, T.; Yang, Y. *J. Cryst. Growth* **2005**, *284*, 554-560.
(30) Koktysh, D.; McBride, J.; Rosenthal, S. *Nanoscale Res. Lett.* **2007**, *2*, 144-148.
(31) Nairn, J. J.; Shapiro, P. J.; Twamley, B.; Pounds, T.; von Wandruszka, R.; Fletcher, T. R.; Williams, M.; Wang, C.; Norton, M. G. *Nano Lett.* **2006**, *6*, 1218-1223.
(32) Malik, M. A.; O'Brien, P.; Helliwell, M. *J. Mater. Chem.* **2005**, *15*, 1463-1467.
(33) Kim, Y.; Jun, Y.; Jun, B.; Lee, S.; Cheon, J. *J. Am. Chem. Soc.* **2002**, *124*, 13656-13657.
(34) Brock, S. L.; Perera, S. C.; Stamm, K. L. *Chem. Eur. J.* **2004**, *10*, 3364-3371.
(35) Stinner, C.; Prins, R.; Weber, T. *J. Catal.* **2001**, *202*, 187-194.
(36) Luo, F.; Su, H.; Song, W.; Wang, Z.; Yan, Z.; Yan, C. *J. Mater. Chem.* **2004**, *14*, 111-115.
(37) Fruchart, D.; Allab, F.; Balli, M.; Gignoux, D.; Hlil, E. K.; Koumina, A.; Skryabina, N.; Tobola, J.; Wolfers, P.; Zach, R. *Physica A* **2005**, *358*, 123-135.
(38) Meyer, A. J. P.; Cadeville, M. C. *J. Phys. Soc. Jpn.* **1962**, *17*, 223-225.
(39) Fujii, H.; Uwatoko, Y.; Motoya, K.; Ito, Y.; Okamoto, T. *J. Phys. Soc. Jpn.* **1988**, *57*, 2143-2153.
(40) Koumina, A.; Bacmann, M.; Fruchart, D.; Soubeyroux, J. L.; Wolfers, P.; Tobola, J.; Kaprzyk, S.; Niziol, S.; Mesnaoui, M.; Zach, R. *Ann. Chim. - Sci. Mat.* **1998**, *23*, 177-180.
(41) Bailey, R. E.; Duncan, J. F. *Inorg. Chem.* **1967**, *6*, 1444-1447.
(42) Kraemer, J.; Redel, E.; Thomann, R.; Janiak, C. *Organometallics* **2008**, *27*, 1976-1978.
(43) Redel, E.; Thomann, R.; Janiak, C. *Chem. Commun.* **2008**, 1789-1791.
(44) Orlov, A.; Roy, A.; Lehmann, M.; Driess, M.; Polarz, S. *J. Am. Chem. Soc.* **2007**, *129*, 371-375.
(45) Schweyer-Tihay, F.; Estournes, C.; Braunstein, P.; Guille, J.; Paillaud, J.-L.; Richard-Plouet, M.; Rose, J. *Phys. Chem. Chem. Phys.* **2006**, *8*, 4018-4028.
(46) Chen, Y.; Hsu, C.; Song, Y.; Chi, Y.; Carty, A. J.; Peng, S.; Lee, G. *Chem. Vap. Deposition* **2006**, *12*, 442-447.
(47) Huttner, G.; Schneider, J.; Mohr, G.; Von Seyerl, J. *J. Organomet. Chem.* **1980**, *191*, 161-169.
(48) Lang, H.; Zsolnai, L.; Huttner, G. *J. Organomet. Chem.* **1985**, *282*, 23-51.
(49) Vahrenkamp, H.; Wucherer, E. J.; Wolters, D. *Chem. Ber.* **1983**, *116*, 1219-1239.
(50) Stamm, K. L.; Garno, J. C.; Liu, G.-y.; Brock, S. L. *J. Am. Chem. Soc.* **2003**, *125*, 4038-4039.
(51) Qian, C.; Kim, F.; Ma, L.; Tsui, F.; Yang, P.; Liu, J. *J. Am. Chem. Soc.* **2004**, *126*, 1195-1198.
(52) Chen, J. H.; Tai, M. F.; Chi, K. M. *J. Mater. Chem.* **2004**, *14*, 296-298.
(53) Koo, J. P. B.; Hwang, Y.; Bae, C.; An, K.; Park, J. G.; Park, H. M.; Hyeon, T. *Ang. Chem., Int. Ed.* **2004**, *43*, 2282-2285.
(54) Veith, M. *J. Chem. Soc., Dalton Trans.* **2002**, 2405-2412.
(55) Carpenter, J. P.; Lukehart, C. M.; Milne, S. B.; Stock, S. R.; Wittig, J. E.; Jones, B. D.; Glosser, R.; Zhu, J. G. *J. Organomet. Chem.* **1998**, *557*, 121-130.

(56) Kelly, A. T.; Rusakova, I.; Ould-Ely, T.; Hofmann, C.; Luttge, A.; Whitmire, K. H. *Nano Lett.* **2007**, *7*, 2920-2925.
(57) Perrin, D. D.; Armarego, W. L. *Purification of Laboratory Chemicals*; 5th ed.; Pergamon Press: New York, 1993.
(58) Deck, W.; Schwarz, M.; Vahrenkamp, H. *Chem. Ber.* **1987**, *120*, 1515-1521.
(59) Hofmann, C.; Rusakova, I.; Ould-Ely, T.; Prieto-Centurión, D.; Hartman, K. B.; Kelly, A. T.; Lüttge, A.; Whitmire, K. H. *Adv. Func. Mat.* **2008**, *18*, 1661-1667.
(60) Tang, J.; Alivisatos, A. P. *Nano Lett.* **2006**, *6*, 2701-2706.
(61) Sunagawa, I. *Crystals: Growth, Morphology, and Perfection*; Cambridge University Press: Cambridge, UK, 2005.
(62) Casula, M. F.; Jun, Y. w.; Zaziski, D. J.; Chan, E. M.; Corrias, A.; Alivisatos, A. P. *J. Am. Chem. Soc.* **2006**, *128*, 1675-1682.
(63) Park, J.; Koo, B.; Yoon, K. Y.; Hwang, Y.; Kang, M.; Park, J.-G.; Hyeon, T. *J. Am. Chem. Soc.* **2005**, *127*, 8433-8440.
(64) Glusker, J. P.; Lewis, M.; Rossi, M. *Crystal Structure Analysis for Chemists and Biologists*; VCH Publishers, Inc.: New York, 1994.
(65) Frank, F. C. *Discuss. Faraday Soc.* **1949**, *5*, 48-54.
(66) Dong, L.; Chu, Y.; Zhang, W. *Mater. Lett.* **2008**, *62*, 4269-4272.
(67) Tian, L.; Yao Tan, H.; Vittal, J. J. *Cryst. Growth Des.* **2008**, *8*, 734-738.
(68) Ota, J.; Roy, P.; Srivastava, S. K.; Nayak, B. B.; Saxena, A. K. *Cryst. Growth Des.* **2008**, *8*, 2019-2023.
(69) Chen, G.-Y.; Dneg, B.; Cai, G.-B.; Zhang, T.-K.; Dong, W.-F.; Zhang, W.-X.; Xu, A.-W. *J. Phys. Chem. C* **2008**, *112*, 672-679.
(70) Keith, H. D.; Padden, F. J. *J. Appl. Phys.* **1963**, *34*, 2409-2421.
(71) Keller, A.; Waring, J. R. S. *J. Polym. Sci.* **1955**, *17*, 447-472.
(72) Granasy, L.; Pusztai, T.; Borzsonyi, T.; Toth, G.; Tegze, G.; Warren, J. A.; Douglas, J. F. *J. Mater. Res.* **2006**, *21*, 309-319.
(73) Nunes, W. C.; Cebollada, F.; Knobel, M.; Zanchet, D. *J. Appl. Phys.* **2006**, *99*, 08N705-703.
(74) Zysler, R. D.; Ramos, C. A.; De Biasi, E.; Romero, H.; Ortega, A.; Fiorani, D. *J. Magn. Magn. Mater.* **2000**, *221*, 37-44.
(75) Dormann, J. L.; Fiorani, D.; Tronc, E. *J. Magn. Magn. Mater.* **1999**, *202*, 251-267.
(76) Hyeon, T. *Chem. Comm.* **2003**, 927-934.
(77) Park, S.-J.; Kim, S.; Lee, S.; Khim, Z. G.; Char, K.; Hyeon, T. *J. Am. Chem. Soc.* **2000**, *122*, 8581-8582.
(78) Yang, J. B.; Xu, H.; You, S. X.; Zhou, X. D.; Wang, C. S.; Yelon, W. B.; James, W. J. *J. Appl. Phys.* **2006**, *99*, 08Q507/501-508Q507/503.
(79) Zhang, G. Q.; Wu, H. P.; Ge, M. Y.; Jiang, Q. K.; Chen, L. Y.; Yao, J. M. *Mater. Lett.* **2007**, *61*, 2204-2207.
(80) Lundgren, L.; Tarmohamed, G.; Beckman, O.; Carlsson, B.; Rundqvist, S. *Phys. Scr.* **1978**, *17*, 39-48.
(81) Fruchart, R.; Roger, A.; Senateur, J. P. *J. Appl. Phys.* **1969**, *40*, 1250-1257.
(82) Bellavance, D.; Mikkelsen, J.; Wold, A. *J. Solid State Chem.* **1970**, *2*, 285-290.

(83) Chandra, R.; Bjarman, S.; Ericsson, T.; Haeggstroem, L.; Wilkinson, C.; Waeppling, R.; Andersson, Y.; Rundqvist, S. *J. Solid State Chem.* **1980**, *34*, 389-396.
(84) Yin, M.; Willis, A.; Redl, F.; Turro, N. J.; O'Brien, S. P. *J. Mater. Res.* **2004**, *19*, 1208-1215.
(85) Wang, H.; Jiao, X.; Chen, D. *J. Phys. Chem. C* **2008**, *112*, 18793-18797.
(86) Yin, Y.; Alivisatos, A. P. *Nature* **2005**, *437*, 664-670.
(87) Knoll, K.; Huttner, G.; Zsolnai, L.; Jibril, I.; Wasiucionek, M. *J. Organomet. Chem.* **1985**, *294*, 91-116.
(88) Woo, K.; Hong, J.; Choi, S.; Lee, H. W.; Ahn, J. P.; Kim, C. S.; Lee, S. W. *Chem. Mater.* **2004**, *16*, 2814-2818.
(89) Shevchenko, E. V.; Talapin, D. V.; Schnablegger, H.; Kornowski, A.; Festin, O.; Svedlindh, P.; Haase, M.; Weller, H. *J. Am. Chem. Soc.* **2003**, *125*, 9090-9101.
(90) Zhang, Y.; Zhu, J.; Song, X.; Zhong, X. *J. Phys. Chem. C* **2008**, *112*, 5322-5327.
(91) Zhu, P.; Wu, W.; Zhou , J.; Zhang, W. *Appl. Organomet. Chem.* **2007**, *21*, 909-912.
(92) Si, R.; Zhang, Y.-W.; You, L.-P.; Yan, C.-H. *Ang. Chem., Int. Ed.* **2005**, *44*, 3256-3260.
(93) Chaubey, G. S.; Barcena, C.; Poudyal, N.; Rong, C.; Gao, J.; Sun, S.; Liu, J. P. *J. Am. Chem. Soc.* **2007**, *129*, 7214-7215.
(94) Zhao, F.; Gao, S. *J. Mater. Chem.* **2008**, *18*, 949-953.
(95) Hou, Y.; Xu, Z.; Sun, S. *Ang. Chem., Int. Ed.* **2007**, *46*, 6329-6332.
(96) Cha, S. I.; Mo, C. B.; Kim, K. T.; Hong, S. H. *J. Mater. Res.* **2005**, *20*, 2148-2153.
(97) Limaye, M. V.; Singh, S. B.; Date, S. K.; Kothari, D.; Reddy, V. R.; Gupta, A.; Sathe, V.; Choudhary, R. J.; Kulkarni, S. K. *J. Phys. Chem. B* **2009**, *113*, 9070-9076.
(98) Bullen, C. R.; Mulvaney, P. *Nano Lett.* **2004**, *4*, 2303-2307.
(99) Wu, H.; Yang, Y.; Cao, Y. C. *J. Am. Chem. Soc.* **2006**, *128*, 16522-16523.
(100) Xie, R.; Rutherford, M.; Peng, X. *J. Am. Chem. Soc.* **2009**, *131*, 5691-5697.
(101) Al-Salim, N.; Young, A. G.; Tilley, R. D.; McQuillan, A. J.; Xia, J. *Chem. Mater.* **2007**, *19*, 5185-5193.
(102) Moulder, J. F.; Chastain, J. *Handbook of x-ray photoelectron spectroscopy : a reference book of standard spectra for identification and interpretation of XPS data*; Physical Electronics Division, Perkin-Elmer Corp.: Eden Prairie, Minn., 1992.
(103) Blanchard, P. E. R.; Grosvenor, A. P.; Cavell, R. G.; Mar, A. *Chem. Mater.* **2008**, *20*, 7081-7088.
(104) Wu, N.; Fu, L.; Su, M.; Aslam, M.; Wong, K. C.; Dravid, V. P. *Nano Lett.* **2004**, *4*, 383-386.
(105) Andelman, T.; Gong, Y.; Polking, M.; Yin, M.; Kuskovsky, I.; Neumark, G.; O'Brien, S. *J. Phys. Chem. B* **2005**, *109*, 14314-14318.
(106) Andelman, T.; Gong, Y.; Neumark, G.; O'Brien, S. *Journal of Nanomaterials* **2007**, *2007*, Article ID 73824.
(107) Nandwana, V.; Elkins, K. E.; Poudyal, N.; Chaubey, G. S.; Yano, K.; Liu, J. P. *J. Phys. Chem. C* **2007**, *111*, 4185-4189.

(108) Saita, S.; Maenosono, S. *Chem. Mater.* **2005**, *17*, 6624-6634.
(109) Lagunas, A.; Jimeno, C.; Font, D.; Sola, L.; Pericas, M. A. *Langmuir* **2006**, *22*, 3823-3829.
(110) de Silva, R. M.; Palshin, V.; Nalin de Silva, K. M.; Henry, L. L.; Kumar, C. S. S. R. *J. Mater. Chem.* **2008**, *18*, 738-747.
(111) Knoll, K.; Huttner, G.; Zsolnai, L.; Orama, O.; Wasiucionek, M. *J. Organomet. Chem.* **1986**, *310*, 225-247.
(112) Vahrenkamp, H.; Wolters, D. *J. Organomet. Chem.* **1982**, *224*, C17-C20.
(113) Stamm, K. L.; Brock, S. L. *J. Alloys Compd.* **2008**, *453*, 476-481.
(114) Bacmann, M.; Fruchart, D.; Chenevier, B.; Fruchart, R.; Puertolas, J. A.; Rillo, C. *J. Magn. Magn. Mater.* **1990**, *83*, 313-314.
(115) Nagase, S.; Watanabe, H.; Shinohara, T. *J. Phys. Soc. Jap.* **1973**, *34*, 908-910.
(116) Kumar, S.; Krishnamurthy, A.; Srivastava, B. K. *J. Phys. D: Appl. Phys.* **2008**, *41*, 055001/055001-055005.
(117) Balli, M.; Fruchart, D.; Gignoux, D.; Tobola, J.; Hlil, E. K.; Wolfers, P.; Zach, R. *J. Magn. Magn. Mater.* **2007**, *316*, 358-360.
(118) Zach, R.; Tobola, J.; Sredniawa, B.; Kaprzyk, S.; Casado, C.; Bacmann, M.; Fruchart, D. *J. Alloys Compd.* **2004**, *383*, 322-327.
(119) Suzuki, T.; Yamaguchi, Y.; Yamamoto, H.; Watanabe, H. *J. Phys. Soc. Jpn.* **1973**, *34*, 911-916.
(120) Fujii, S.; Ishida, S.; Asano, S. *J. Phys. F: Met. Phys.* **1988**, *18*, 971-980.
(121) Jain, S. K.; Kumar, S.; Krishna, P. S. R.; Shinde, A. B.; Krishnamurthy, A.; Srivastava, B. K. *J. Alloys Compd.* **2007**, *439*, 13-17.
(122) Fujii, H.; Hokabe, T.; Fujiwara, H.; Okamoto, T. *J. Phys. Soc. Jpn.* **1978**, *44*, 96-100.
(123) Kumar, S.; Paranjpe, S. K.; Srivastava, B. K.; Krishnamurthy, A. *Phys. Status Solidi A* **1999**, *175*, 693-697.
(124) Yoon, K. Y.; Jang, Y.; Park, J.; Hwang, Y.; Koo, B.; Park, J.-G.; Hyeon, T. *J. Solid State Chem.* **2008**, *181*, 1609-1613.
(125) Jourdain, V.; Simpson, E. T.; Paillet, M.; Kasama, T.; Dunin-Borkowski, R. E.; Poncharal, P.; Zahab, A.; Loiseau, A.; Robertson, J.; Bernier, P. *J. Phys. Chem. B* **2006**, *110*, 9759-9763.
(126) Jourdain, V.; Stéphan, O.; Castignolles, M.; Loiseau, A.; Bernier, P. *Adv. Mater.* **2004**, *16*, 447-453.
(127) Quick, M. H.; Angelici, R. J. *Inorg. Synth.* **1979**, *19*, 160-161, 163.
(128) Iggo, J. A.; Mays, M. J.; Raithby, P. R.; Hendrick, K. *J. Chem. Soc., Dalton Trans.* **1983**, 205-215.
(129) Ha, T. H.; Koo, H.-J.; Chung, B. H. *J. Phys. Chem. C* **2007**, *111*, 1123-1130.
(130) Magnussen, O. M. *Chem. Rev.* **2002**, *102*, 679-726.
(131) Ould-Ely, T.; Prieto-Centurion, D.; Kumar, A.; Guo, W.; Knowles, W. V.; Asokan, S.; Wong, M. S.; Rusakova, I.; Luttge, A.; Whitmire, K. H. *Chem. Mater.* **2006**, *18*, 1821-1829.
(132) Brock, S. L.; Senevirathne, K. *J. Solid State Chem.* **2008**, *181*, 1552-1559.
(133) Ferrando, R.; Jellinek, J.; Johnston, R. L. *Chem. Rev.* **2008**, *108*, 845-910.
(134) Chou, S. Y.; Wei, M. S.; Krauss, P. R.; Fischer, P. B. *J. Appl. Phys.* **1994**, *76*, 6673-6675.

(135) Shukla, N.; Liu, C.; Roy, A. G. *Mater. Lett.* **2006**, *60*, 995-998.
(136) Lu, A.-H.; Salabas, E. L.; Schüth, F. *Ang. Chem., Int. Ed.* **2007**, *46*, 1222-1244.
(137) Jun, Y.-w.; Choi, J.-s.; Cheon, J. *Chem. Commun.* **2007**, 1203–1214.
(138) Cheon, J.; Lee, J.-H. *Acc. Chem. Res.* **2008**, *41*, 1630-1640.
(139) Zhang, X.-B.; Yan, J.-M.; Han, S.; Shioyama, H.; Xu, Q. *J. Am. Chem. Soc.* **2009**, *131*, 2778-2779.
(140) Baruwati, B.; Polshettiwar, V.; Varma, R. S. *Tetrahedron Lett.* **2009**, *50*, 1215-1218.
(141) Mulder, W. J. M.; Koole, R.; Brandwijk, R. J.; Storm, G.; Chin, P. T. K.; Strijkers, G. J.; de Mello Donega, C.; Nicolay, K.; Griffioen, A. W. *Nano Lett.* **2006**, *6*, 1-6.
(142) Kettering, M.; Winter, J.; Zeisberger, M.; Bremer-Streck, S.; Oehring, H.; Bergemann, C.; Alexiou, C.; Hergt, R.; Halbhuber, K. J.; Kaiser, W. A.; Hilger, I. *Nanotechnology* **2007**, *18*, 175101.
(143) Laurent, S.; Forge, D.; Port, M.; Roch, A.; Robic, C.; Vander Elst, L.; Muller, R. N. *Chem. Rev.* **2008**, *108*, 2064-2110.
(144) Jun, Y.-w.; Seo, J.-w.; Cheon, J. *Acc. Chem. Res.* **2008**, *41*, 179-189.
(145) Dobson, J. *Nat. Nanotech.* **2008**, *3*, 139-143.
(146) Wang, L.; Park, H.-Y.; Lim, S. I. I.; Schadt, M. J.; Mott, D.; Luo, J.; Wang, X.; Zhong, C.-J. *J. Mater. Chem.* **2008**, *18*, 2629-2635.
(147) Xu, Z.; Hou, Y.; Sun, S. *J. Am. Chem. Soc.* **2007**, *129*, 8698-8699.
(148) Levin, C. S.; Hofmann, C.; Ali, T. A.; Kelly, A. T.; Morosan, E.; Nordlander, P.; Whitmire, K. H.; Halas, N. J. *ACS Nano* **2009**, *3*, 1379-1388.
(149) Wang, H.; Brandl, D. W.; Le, F.; Nordlander, P.; Halas, N. J. *Nano Lett.* **2006**, *6*, 827-832.
(150) Spuch-Calvar, M.; Pacifico, J.; Pérez-Juste, J.; Liz-Marzán, L. M. *Langmuir* **2008**, *24*, 9675-9681.
(151) Yu; Chang, S.-S.; Lee, C.-L.; Wang, C. R. C. *J. Phys. Chem. B* **1997**, *101*, 6661-6664.
(152) Pérez-Juste, J.; Pastoriza-Santos, I.; Liz-Marzán, L. M.; Mulvaney, P. *Coord. Chem. Rev.* **2005**, *249*, 1870-1901.
(153) Oldenburg, S. J.; Averitt, R. D.; Westcott, S. L.; Halas, N. J. *Chem. Phys. Lett.* **1998**, *288*, 243-247.
(154) Oldenburg, S. J.; Westcott, S. L.; Averitt, R. D.; Halas, N. J. *J. Chem. Phys.* **1999**, *111*, 4729-4735.
(155) Duff, D. G.; Baiker, A.; Edwards, P. P. *Langmuir* **1993**, *9*, 2301-2309.
(156) De Palma, R.; Peeters, S.; Van Bael, M. J.; Van den Rul, H.; Bonroy, K.; Laureyn, W.; Mullens, J.; Borghs, G.; Maes, G. *Chem. Mater.* **2007**, *19*, 1821-1831.
(157) Etgar, L.; Lifshitz, E.; Tannenbaum, R. *J. Phys. Chem. C* **2007**, *111*, 6238-6244.
(158) Frankamp, B. L.; Fischer, N. O.; Hong, R.; Srivastava, S.; Rotello, V. M. *Chem. Mater.* **2006**, *18*, 956-959.
(159) Ghosh, M.; Lawes, G.; Gayen, A.; Subbanna, G. N.; Reiff, W. M.; Subramanian, M. A.; Ramirez, A. P.; Zhang, J.-P.; Seshadri, R. *Chem. Mater.* **2004**, *16*, 118-124.

(160) Somaskandan, K.; Veres, T.; Niewczas, M.; Simard, B. *New J. Chem.* **2008**, *32*, 201-209.
(161) Brinson, B. E.; Lassiter, J. B.; Levin, C. S.; Bardhan, R.; Mirin, N.; Halas, N. J. *Langmuir* **2008**, *24*, 14166-14171.
(162) Caruntu, D.; Cushing, B. L.; Caruntu, G.; O'Connor, C. J. *Chem. Mater.* **2005**, *17*, 3398-3402.
(163) Leff, D. V.; Brandt, L.; Heath, J. R. *Langmuir* **1996**, *12*, 4723-4730.
(164) Prodan, E.; Lee, A.; Nordlander, P. *Chem. Phys. Lett.* **2002**, *360*, 325-332.
(165) Oldenburg, S. J.; Jackson, J. B.; Westcott, S. L.; Halas, N. J. *Appl. Phys. Lett.* **1999**, *75*, 2897-2899.
(166) Prodan, E.; Nordlander, P. *J. Chem. Phys.* **2004**, *120*, 5444-5454.
(167) Prodan, E.; Radloff, C.; Halas, N. J.; Nordlander, P. *Science* **2003**, *302*, 419-422.
(168) Grzelczak, M.; Sánchez-Iglesias, A.; Rodríguez-González, B.; Alvarez-Puebla, R.; Pérez-Juste, J.; Liz-Marzán, L. M. *Adv. Func. Mat.* **2008**, *18*, 3780-3786.
(169) Ni, W.; Kou, X.; Yang, Z.; Wang, J. *ACS Nano* **2008**, *2*, 677-686.
(170) Payne, E. K.; Shuford, K. L.; Park, S.; Schatz, G. C.; Mirkin, C. A. *J. Phys. Chem. B* **2006**, *110*, 2150-2154.
(171) Jana, N. R.; Gearheart, L.; Murphy, C. J. *Adv. Mater.* **2001**, *13*, 1389-1393.
(172) Sando, G. M.; Berry, A. D.; Owrutsky, J. C. *J. Chem. Phys.* **2007**, *127*, 074705.
(173) Lassiter, J. B.; Aizpurua, J.; Hernandez, L. I.; Brandl, D. W.; Romero, I.; Lal, S.; Hafner, J. H.; Nordlander, P.; Halas, N. J. *Nano Lett.* **2008**, *8*, 1212-1218.